UNIVERSITY OF THE WITWATERSRAND, JOHANNESBURG

The nature and characteristics of sulphide mineralisation at the Kamoa - Kakula copper deposit of the Katanga basin, Central African Copperbelt, Lualaba, Democratic Republic of Congo

by

Robert N. Kaemba
(2778312)

Research report submitted in partial fulfilment of the requirement for the degree of Master of Science in Economic Geology from the Faculty of Science at the University of the Witwatersrand,
Johannesburg, South Africa

31st August, 2024

DECLARATION

I declare that this research report is my own, unaided work. It is being submitted for the Degree of Master of Science in Economic Geology at the University of the Witwatersrand, Johannesburg. It has not been submitted before for any degree or examination at any other University.

____

(Signature of Candidate)

31st day of August 2024 at Johannesburg

ABSTRACT

The Kamoa-Kakula deposit is a world-class stratiform copper deposit located in the southern part of the Democratic Republic of Congo (DRC) approximately 25 km from Kolwezi town and close to the border of DRC and Zambia. The ore deposit is in the southern area of the western foreland domain of the Congolese Copperbelt (Central African Copperbelt). The structural setting of the deposit is characterised by the West scarp fault, binding Kamoa to the west whilst it is bounded by faults of the Kansoko Sud trend to the east. The mineral resource footprint of the deposit envelopes the Makulu dome and wraps around the southern edge of the Kamoa dome. The main sedimentary lithologies hosting copper mineralisation are diamictite and interbedded siltstones of the Grand Conglomérat Formation at the base of the Nguba Group overlying sandstones of the Mwashya Subgroup (Roan Group). Previous studies within DRC and Zambia showed that the glaciogenic diamictite (Grand Conglomérat Formation) is a laterally extensive regional marker. The geological interpretation and literature data reveals a distinct stratigraphic correlation of several copper deposits across the Central African Copperbelt confirming multiple occurrences at various stratigraphic levels. Furthermore, this analysis identifies the Fishtie deposit (Lusale basin, Zambia), which occurs on the eastern margin of the Katanga basin, as the closest geological analogue to Kamoa – Kakula.

At Kamoa-Kakula, hydrothermal sulphide mineralisation occurs mainly towards the base of the Grand Conglomérat with the dominant sulphide mineral assemblage composed of pyrite – chalcopyrite – bornite - chalcocite, and minor covellite . Optical microscopy demonstrates the multi-stage crystallisation of few generations of pyrite including the earliest diagenetic framboidal pyrite. The widespread development of the symplectic texture linked to bornite and chalcocite intricate intergrowths and regular rimming of clasts by sulphide overgrowth, as well as the occurrences of framboidal chalcopyrite and bornite argue for the sulphide paragenesis being linked to sulphide replacement. This is consistent with the apparent mineral zonation progressing downwards from pyrite → chalcopyrite → bornite ± covellite → chalcocite. The S isotope variations suggest that a significant portion of S at Kamoa originated from early bacterial sulphate reduction, which resulted in precipitation of fine-grained framboidal and sooty pyrite with the negative $\delta^{34}S$ values as low as -19.9 ‰. The similar, while narrower, range of $\delta^{34}S$ values for chalcopyrite is due to inheritance and homogenization of the S isotopic signature of diagenetic sulphides during ore stage

replacement, whereas the highly negative $\delta^{34}S$ values for chalcocite (down to -35.1 ‰) indicate the subsequent extreme isotope fractionation under low-temperature conditions.

The study includes a comprehensive overview of the regional stratigraphic and geological correlation, in conjunction with detailed mineralogical and isotopic observations, contributing to further understanding of Cu mineralisation at Kamoa-Kakula as well as on a scale of the entire Central African Copperbelt.

TABLE OF CONTENTS

LIST OF FIGURES

LIST OF TABLES

LIST OF ABBREVIATIONS

LITHOLOGY:		GENERAL	
Abbreviation	Description	Abbreviation	Description
SSL	Siltstone	CACB	Central African Copperbelt
SST	Sandstone	DRC	Democratic Republic of Congo
SDT	Diamictite	ZCB	Zambian Copperbelt
SCG	Conglomerate	CCB	Congolese Copperbelt
STRATIGRAPHY:		GC	Grand Conglomérat
Strat code	Nomenclature	PC	Petit Conglomérat
Ng 1.1	Nguba siliciclastics	RAT	Roches Argilo Talqueuses
Ng 1.1.6	Uppermost diamictite	Fm	Formation
Ng 1.1.5	Upper diamictite	FA	Facies
Ng 1.1.4	Upper laminated pyritic siltstone	TCu	Total copper
Ng 1.1.3	Middle diamictite package	Mt	Million metric tonnes
Ng 1.1.2	Lower laminated pyritic siltstone	SHC	Sediment-hosted-copper
Ng 1.1.1	Basal diamictite	S	Sulphur
Ng 1.1.1.3	Upper basal diamictite	SCLM	Sub continental lithospheric mantle
Ng 1.1.1.2	Intercalated siltstone	SDT1	Clast rich diamictite
Ng 1.1.1.1	Lower basal diamictite	SSLPG	Pale green siltstone
R4.2	Mwashya Subgroup	SSLLA	Laminated siltstone with conglomeritic bands
MINERALOGY:		SSLMA	Massive siltstone
Abbreviation	Description	SDT2	Maroon diamictite
Py	Pyrite	SSBLX	Coarse breccia
Cpy	Chalcopyrite	KPS	Kamoa-pyritic-siltstone
Bor	Bornite	DD	Diamond drillhole
Car	Carrollite	BHID	Borehole ID
Cov	Covellite	Wits	Witwatersrand
Cob	Cobaltite	MMU	Microscopy and Microanalysis Unit
Cc	Chalcocite	SEM	Scanning electron microscope
Cu	Copper	SG	Specific gravity
Gal	Galena	SR	Supply risk
Bar	Barite	EI	Economic Importance
Hem	Hematite	ESG	Environmental Social Governance
Mon	Monazite	EU	European Union
Ap	Apatite	UNFCC	United Nations Framework Convention on Climate Change
Ilm	Ilmenite	EV	Electric vehicle

ACKNOWLEDGEMENTS

The Staff at the University of the Witwatersrand, Wits School of Geosciences have been a great source of inspiration. In particular I would like to thank my Research Supervisor, Dr. Marina A. Yudovskaya, for sharing invaluable technical knowledge, as well as for the patience and guidance during this research project – Thank you for the excellent supervision. I appreciate the access and use of the Optical microscopes at the School of Geosciences and use of the Scanning Electron Microscope (SEM) at the Microscopy and Microanalysis Unit (MMU) of the University of the Witwatersrand, amongst other facilities. I am grateful to Prof. Judith Kinnaird, Dr. Paul Nex and Dr. Linda Laccheri for their engaging disposition. I am indebted to the Wits Laboratory staff, particularly Louis Mudalahothe, Caiphas Majola and Samuel Tshabalala, who provided support during sample preparation.

My sincere appreciation goes to Ivanhoe Mines (Kamoa Copper SA.), especially the logistical, administrative and technical staff. Special Thanks is given to George Gilchrist and Franck Twite Banza for the being supportive of this research and for being outstanding hosts at the time. I am Thankful to Prof. Murray Hitzman and Dr. David Broughton for their assistance in this regard. The technical team at Kamoa; Richard, Nestor, Louange, Joseph and Serge, Thanks, I'm grateful for the hospitality and the interesting conversations. I also extend my Thanks to all of the Kamoa core-yard Staff and Papa Phillipe Mabwaka for arranging the timely freight of samples from the DRC to South Africa. I would also like to sincerely Thank my wife Zele, to whom I express gratitude for the motivation, patience and encouragement throughout the period that I pursued further studies, as well as my family and friends for their unwavering support. I am grateful to my parents, Ben and Margaret Kaemba, who made significant sacrifices to ensure I received a good education in my formative years. Last, but certainly not least, Thank you to the late Mr. James Mwale for the inspiring ideas, thoughts and challenging discussions that shaped some of my early opinions about the geology and mineralisation of the Central African Copperbelt.

1 INTRODUCTION

1.1 Environmental and economic background

Over the years, there has been a significant increase of greenhouse gas emissions spanning decades. In particular, nitrous oxide emission was 0.33 ppm in 2017, an increase of 122 %, whilst methane emissions increased by 257 % to 1.86 ppm in 2017 and carbon dioxide increased by 146 % to 405 ppm, from the pre-industrial values (Erickson, 2017). More recently, the most significant effect is by CO_2 emissions and Fig. 1 shows global annual CO_2 emissions from 1940 to 2021, which indicates a total of 37.12 Gt CO_2 (billion metric tonnes) as at 2021 (Statistica, 2023).

Naturally, there are areas contributing to this significant rise of CO_2 emissions more than others and these can be quantified. At present, the sectors contributing the most to this rise in of CO_2 output, amongst others, is the transportation sector due to the combustion of fossil fuels (Erickson, 2017). The solutions in limiting this would therefore involve seeking alternative forms of energy to efficiently decrease the rate at which of CO_2 is being emitted to the atmosphere, whilst still fulfilling transportation needs. One such way of doing this, would be the electrification of vehicles (now commonly referred to as EVs).

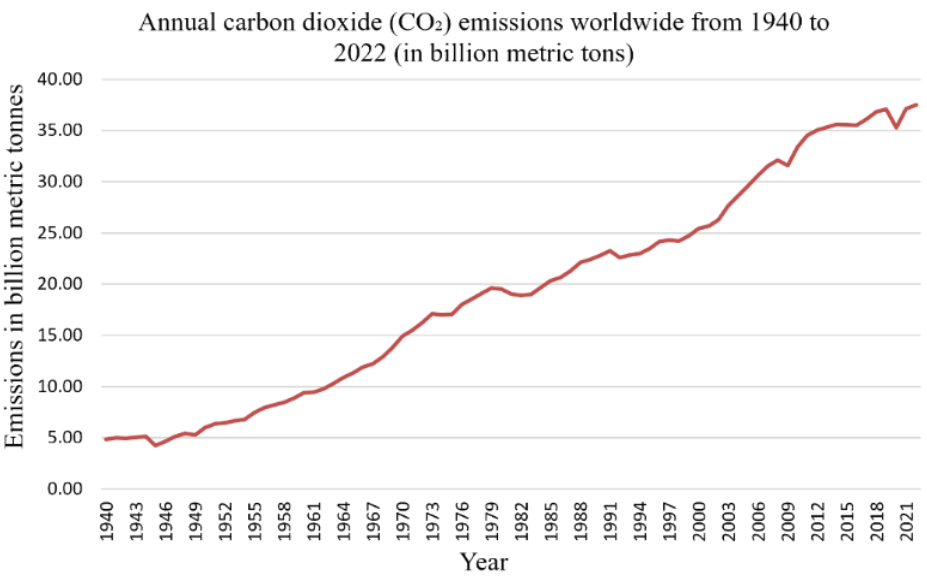

Figure 1: Global annual carbon dioxide (CO_2) emission 1940 to 2022 (Statistica, 2023).

On 12th December 2015, at the U.N. climate change conference in Paris (i.e., COP21), a total of 196 parties adopted a legal International Treaty on climate change known as the Paris Agreement (UNFCC, 2015). Working towards the metrics of this agreement is a key in achieving a reduction in greenhouse gas emissions, in order to make a positive impact to the energy transition. The Paris agreement recognises that intentional global action would be required in order to limit the effects of climate change to 1.5 °C – 2 °C. By limiting (as well as decreasing) the emission of greenhouse gases, the objective would be to reduce emissions by 43 % by 2030 (UNFCC, 2015). Other key areas that can make a contribution to the reduction of greenhouse gas emissions, is the substitution of the use of coal (and natural) gas to produce electricity, with alternatives such as wind and solar (Erickson, 2017). Therefore, in order to achieve a decarbonised economy, an understanding of the raw materials required to produce e.g., electric vehicles, wind and solar energy components, is necessary. This is to determine where the supply of the raw materials for this will be recovered from.

As a result of the forecasted increase in demand in commodities, the World Bank (amongst other organisations) conducted an analysis of the alternative forms of energy, and the respective commodities that would be required. To achieve a low carbon future, commodities such as lithium, cobalt and graphite will require production to be increased to levels of approximately 400% of current levels, and other commodities such as copper will see an overall increase in production (Hund et al., 2023). This is because of the technologies in which these commodities are applied. By 2050, copper will have significant demand from the application of solar photovoltaic (PV) components, wind turbines and concentrated solar power (CSP) parts (Hund et al., 2023), in addition to its application in electric vehicles and industrialisation. This highlights the significance of copper and subsequently, the current and forecasted supply have been reviewed to determine whether sufficient supply will meet demand of the technologies required to achieve these commitments of the Paris agreement.

Critical metals are commodities at risk of depletion due to factors such as diminishing resources, being mined as a companion product, its complexity of processing, environmental factors and risks associated to supply restrictions (Graedel et al., 2012). Results from the 2023 European Union (EU) criticality assessment are shown by Fig. 2, which illustrates commodities supply risk plotted against economic importance. Whilst copper sits below the supply risk (SR) threshold, it is considered a strategic raw material due to its economic importance and varied technological applications that may contribute to the green transition. As shown by the critical raw materials supply risk vs economic importance scatter plot, critical raw materials are those that have a component of supply risk as well as economic importance, whilst strategic raw materials are those that may not necessarily have a high risk of supply, however, are used in a wide range of applications and have a high level of economic importance.

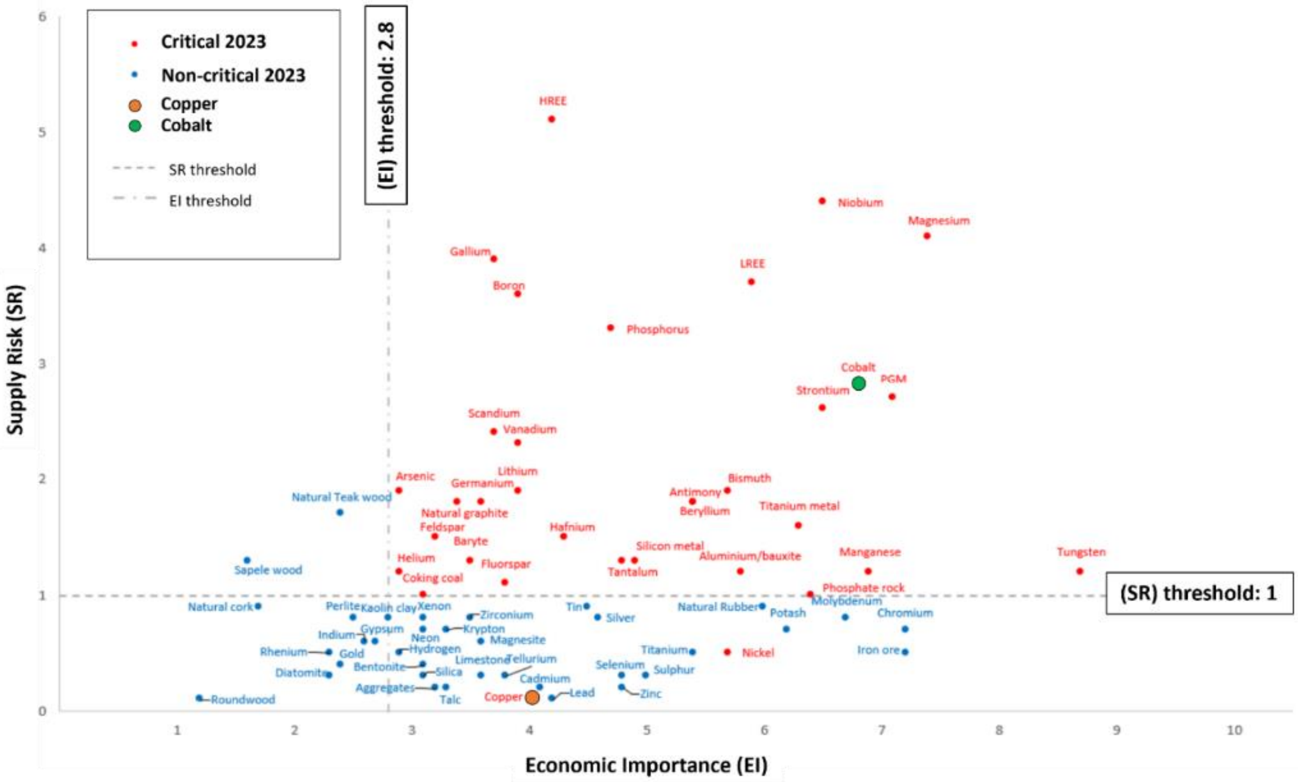

Figure 2: Scatter plot of critical raw materials, supply risk vs economic importance (modified after Grohol and Veeh, 2023).

1.2 Copper supply

Copper projects reaching development have been hindered historicaly by a number of reasons. These range from resistance to capital expenditure, inappropriate allocation of resources, introduction of Environmental Social Governance (ESG) operation framework and a limited pool of high-quality projects being available (Kettle, 2021). As a result, a shortfall of approximately 15 Mt may be experienced by the year 2040, at which stage a forecasted demand of approximately 40 Mt will be reached (Fig. 3).

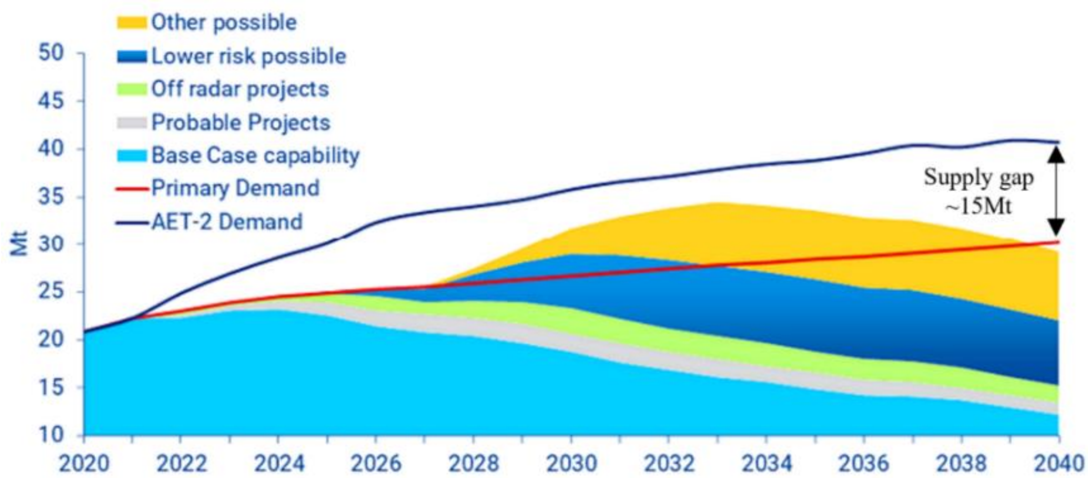

Figure 3: Demand for copper from 2020 forecast to 2040 (Kettle, 2021).

Other aspects to consider in bridging this gap is the global supply, with respect to mining and processing of copper (Fig. 4). This can help identify bottlenecks in the copper supply-chain. For example, in countries where copper Mined > Refined, consideration should be made with respect to developing or increasing the refining capacity in these localities, which can directly increase supply efficiency.

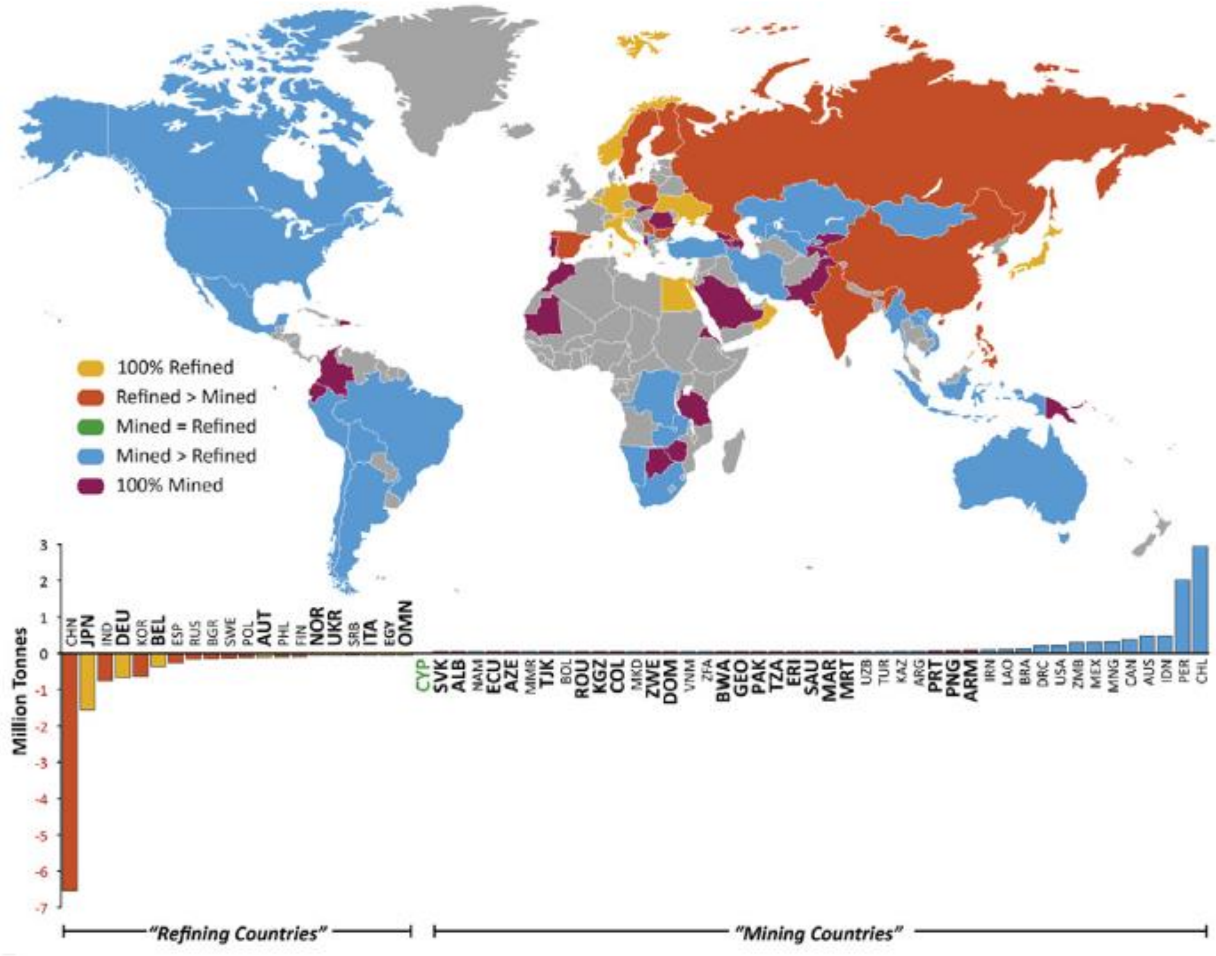

Figure 4: Global distribution of copper mining and localities refining (McNulty and Jowitt, 2021).

1.3 Cobalt supply

The primary research focus of this study will be the occurrence of copper in the Central African Copperbelt, however, it is important to mention the occurrence and economic implications of cobalt in the region. This is due to the current wide-ranging applications of cobalt in its use in batteries, superalloys, cemented carbides and diamond tools. The main deposit types, main contributors, uses of cobalt and production are shown by Fig. 5 and Fig. 6. The pie charts shown by Fig. 5 a illustrates the importance of sediment hosted Cu-Co deposits and their contribution to the global metal budget. Whilst, Fig. 5 b, highlights the DRC as the main producer of cobalt, Fig. 5 c shows a pie chart indicating the main uses of cobalt.

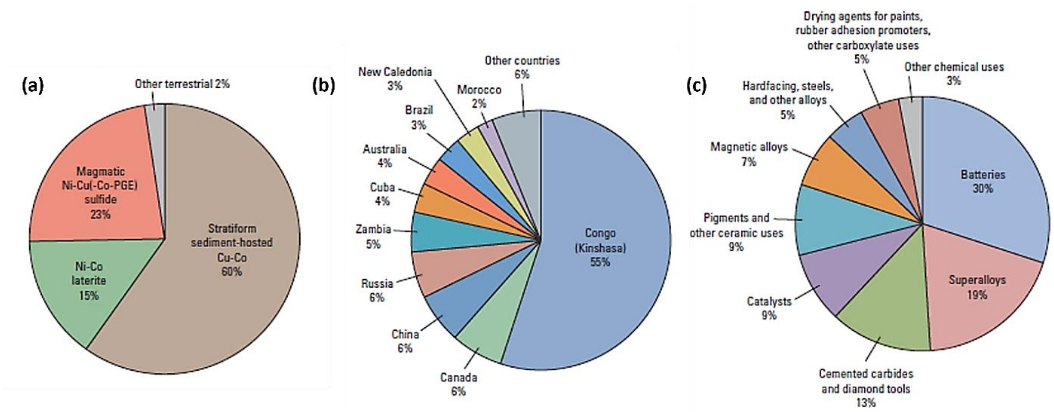

Figure 5: Types of deposits producers and uses of cobalt (Slack et al., 2017).

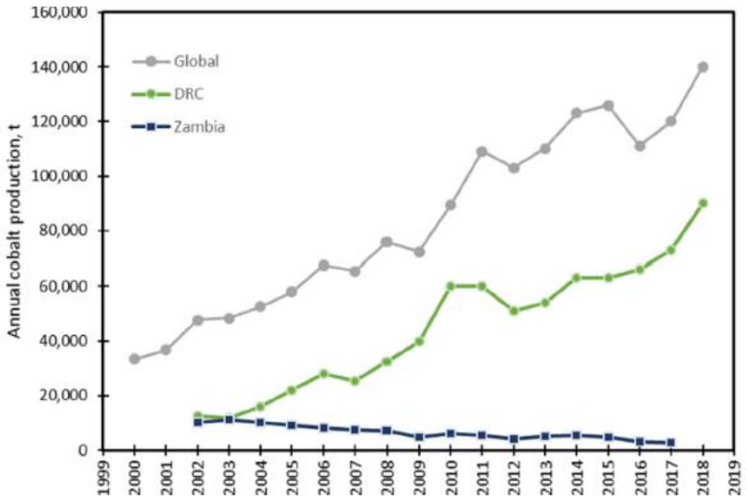

Figure 6: Production of cobalt from 1999 to 2019 (Crundwell et al., 2020).

The common cobalt sulphide minerals are carrollite $Cu(Co,Ni)_2S_4$, pentlandite $(Fe,Ni,Co)_9S_8$, linnaeite (Co_3S_4), and siegenite $(Co,Ni)_3S_4$ (Slack et al., 2007). Economic grades of Co are associated to Cu-Co deposits occurring predominantly within dolomites and dolomitic shales of allochthonous facies in the DRC (Congolese Copperbelt - CCB). These occur at an average Co:Cu ratio of 1:13, with the highest occurrences in the southern parts of the Lufilian arc at a ratio of 3:1 (Cailteux et al., 2005).

A lower Co:Cu ratio is exhibited in the south-eastern parts of the Lufilian, extending into Zambia (Zambian Copperbelt - ZCB), where lower average ratios of around 1:57 are observed (Cailteux et al., 2005). Earlier observations suggest a cobalt association to the ore-shale, as well as upper parts of the Lower Roan, occasionally extending to the Upper Roan of the Katangan succession (Annels and Simonds, 1984).

1.4 Models tested

The Katanga basin is a mature metallogenic province, with occurrences of sediment hosted Cu ± Co ore deposits controlled by lithology and upper crustal basin-dome architecture (Cailteux et al., 1994; Selley et al., 2018). Mineralisation formed initially during early or late diagenesis, with the next major mineralisation stage culminating during the late Proterozoic metamorphism associated to the Lufilian orogeny. Several syn- to post-orogenic polymetallic Cu-Ag deposits also occur in the CACB (Muchez et al., 2007).

These stages are generally accepted but the role of each specific process contributing to each deposit is a source of debate. This research project aims to further understand the nature and characteristics of sulphide mineralisation. This is to be achieved by studying alteration styles and S isotopic compositions of sulphides in several profiles through the ore zones of the Kamoa – Kakula copper deposit hosted by siltstones and diamictites. The previous isotope study by Schmandt (2013) suggested that sulphide sulphur was derived from diagenetic pyrite, whereas other studies placed a focus on the nature and lithological controls of Cu sulphides within the diamictite (Twite, 2016 ; Turner et al., 2023). Results from Turner et al. (2023) demonstrated that disseminated sulphides within the diamictite matrix and within siltstone exhibited coarse-grained crystalline sulphide gangue 'caps' (rounded rims close to clasts) and 'beards'(elongated-stretched rims), observed on the edges of clasts. The implication of this suggests two stages of mineralisation: (1) an early-phase producing disseminated mineralisation and (2) a late-phase remobilising Cu from the matrix on the clast edges (Turner et al., 2023). It is possible that the early-phase of mineralisation occurred prior to orogenic compression, whilst the late-phase occurs during the Neoproterozoic Lufilian compression.

Earlier studies support a syn-orogenic origin for copper sulphides based on evidence from the strain fringes and strain shadows and their relationship with copper mineralisation (Twite et al., 2020) that suggests a single phase of deformation resulting in coaxial deformation that is responsible for strain fringe and strain shadow growth under high temperature conditions. The main evidence of this, is the occurrence of copper within the strain fringes and strain shadows, suggesting syn-orogenic new growth and/or remobilisation and recrystallisation of sulphides. This idea is consistent with the later proposal by Turner et al., (2023), which made observations of mineralised 'caps' and 'beards' on the clast edges.

The models to be investigated include;

- Study the S isotopic compositions to test the diagenetic sulphur source model
- Test the syn-orogenic model by characterising mineralisation present
- Investigate the hypothesis of early and late-stage mineralisation

1.5 Aims and Objectives

The Central African Copperbelt (CACB) is a premier sediment hosted Cu-Co province hosting numerous orebodies. These ore bodies have formed in a variety of contrasting settings and exhibit a diverse range of alteration and mineralisation assemblages. This geological and metallogenic history provides an opportunity to further the understanding of the geological setting and processes responsible for the significant mineralisation in the region. This Research project places a focus on the occurrence of mineralisation at the Kamoa – Kakula copper deposit located in the western foreland area of the Democratic Republic of Congo (DRC). The aim is to improve our understanding of the geological and stratigraphic setting in which this deposit occurs, understand the source of sulphur, determine the ore-forming processes that cause mineralisation and the main characteristics exhibited by the sulphide mineralisation. Ultimately, this will substantiate a favoured mineralisation model based on the obtained data and interpretations in this study, as well as previous literature. The key aims and objectives are summarised below;

- Regional comparison and correlation between mineral occurrences and deposits in the Zambian Copperbelt (ZCB) and Congolese Copperbelt (CCB).
- Core logging and underground mapping to understand the local stratigraphy and position of stratiform mineralisation.
- Analysis of mineral associations at macro- and microscopic levels to interpret paragenetic relationships and stages of mineralisation. Optical and electron microscope observations will be used.
- Evaluation of sulphur sources for the different stages of mineralisation using in-situ mass-spectrometric analysis of the S isotope ratios in discrete sulphide grains via laser sampling.
- Analysis of geophysical data to constraint characteristic responses of sulphides and contrasting lithologies using forward-modelling of gravity, magnetics and resistivity methods.

2 REGIONAL GEOLOGICAL SETTING – KATANGA BASIN

2.1 SHC Deposits worldwide

Early workers through the 1970s and 1980s recognised the sediment-hosted copper (SHC) type deposits, as a group of mineral deposits predominantly associated with sedimentary basin development (Fig. 7) (Zientek et al., 2014). These deposits are located at the boundary between red beds and shallow-marine shales, siltstones, sandstones or carbonates with mineralisation confined to reduced horizons, at which the precipitation of metals occurs (Hitzman et al., 2010). Exploration for SHC deposits is generally associated to these sedimentary settings, where the aforementioned configuration of sediments occurs.

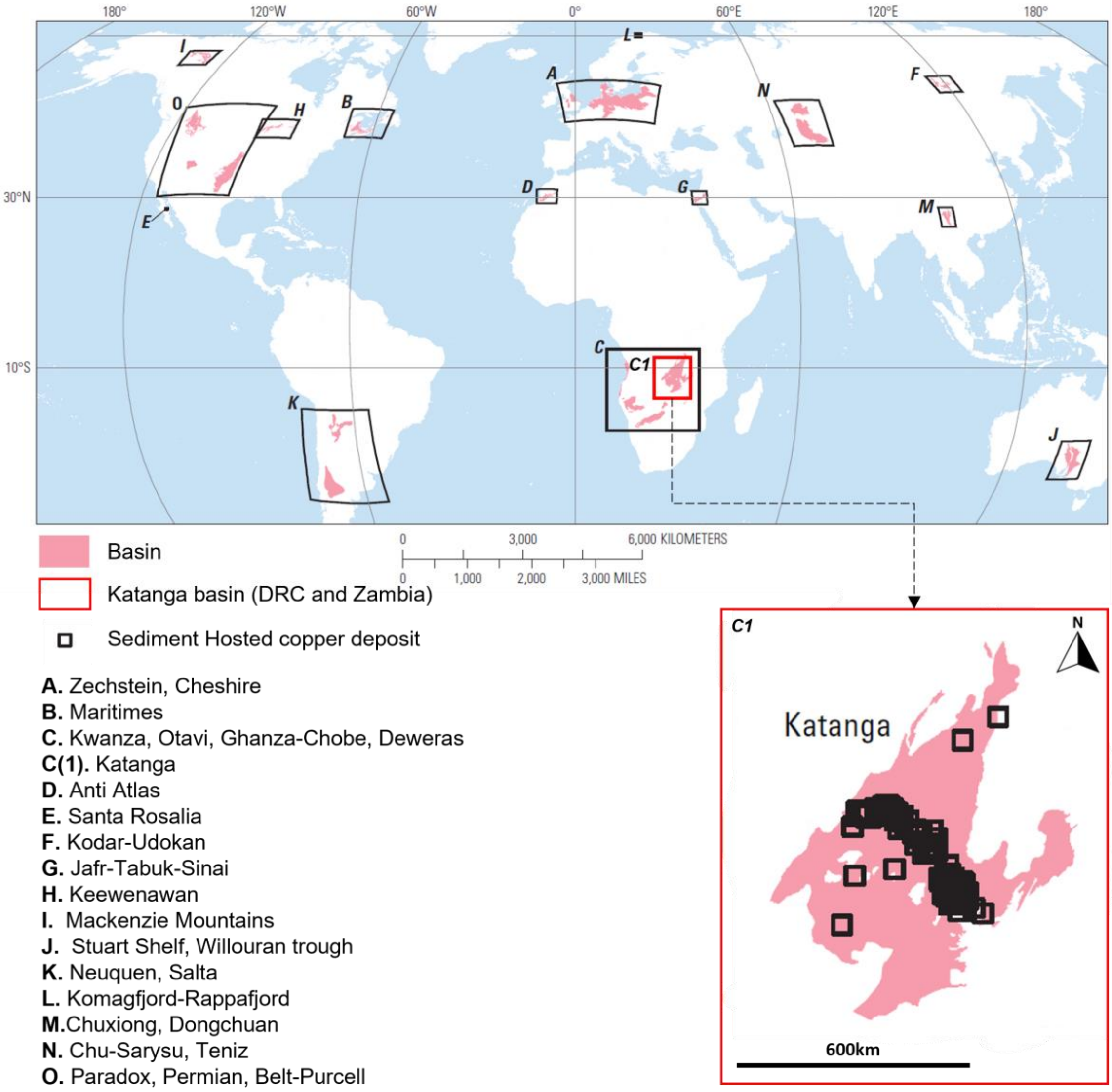

Figure 7: Global sediment hosted copper basins (modified after Zientek et al., 2014).

Whilst a high number of the copper mineral systems produce small sub-economic copper deposits, four main basins on Earth host giant sedimentary hosted copper deposits (Hitzman et al., 2010). These main basins are detailed from 1 through 4, below:

1. Katangan basin of the CACB (Neoproterozoic)
2. Kupferschiefer, Zechstein basin of Europe (Permian)
3. Devonian to Carboniferous Chu-Sarysu basin of Kazakhstan (i.e., Dzhezkazgan deposit, after Lur'ye and Gablina, 1982)
4. Paleoproterozoic Kodar - Udokan basin of Siberia

Other notable basins with significant Cu resources are the Mesoproterozoic Keweenaw basin associated to the mid-continent rift of the Northern America (i.e., White Pine) and the Neoproterozoic-Cambrian basin of Afghanistan i.e., Aynak (Hitzman et al., 2010). This signifies the widespread distribution of sedimentary basins globally and their association to copper mineralisation.

In 2014, the USGS conducted a study with a focus on SHC deposits worldwide including the SHC deposits of the CACB. The two areas concerned were the Congolese Copperbelt (CCB) and Zambian Copperbelt (ZCB). Table 1 shows the main areas globally, that host large copper deposits of the sediment-hosted stratabound type. Whilst the resource estimations are historical, the volume of copper resources shown by the Table 1, signifies the economic importance of the Katanga basin as a source of copper.

Table 1: Global SHC deposits and their resources (after Zientek et al., 2014)

Area	**Deposits**	**Resources (million metric tons)**	**% identified resource**
Global	205	310	100
Basin: Katangan	85	150	50
Basin: Zechstein	10	79	25
Chu – Sarysu basin	8	28	9
Kodar – Udokan basin	2	20	6

2.2 Regional tectonic setting

Regionally, the tectonic evolution of the Katanga basin is associated to the assembly (~1300 – 900 Ma) and break-up (~800 Ma) of the supercontinent Rodinia, the collision of east and west Gondwana and widespread continental rifting that occurred ~825 Ma to 740 Ma (Li et al., 2008; Bogdanova et al., 2009; Vérard, 2021). The orogenic event of interest that follows the amalgamation of these continental domains is the Pan-African Orogeny occurring between ~870 Ma to ~500 Ma and resulting in the formation of several mobile belts, which surrounded the older cratons (Kröner and Stern, 2004). This collision of east and west Gondwana, resulted in the Lufilian and Zambezi orogenies, during which the Lufilian arc and the Central African Copperbelt were formed (Fig. 8 a - c). This shows the final assembly of east and west Gondwana occurring between 650 Ma to 510 Ma (Squire and Keays, 2023).

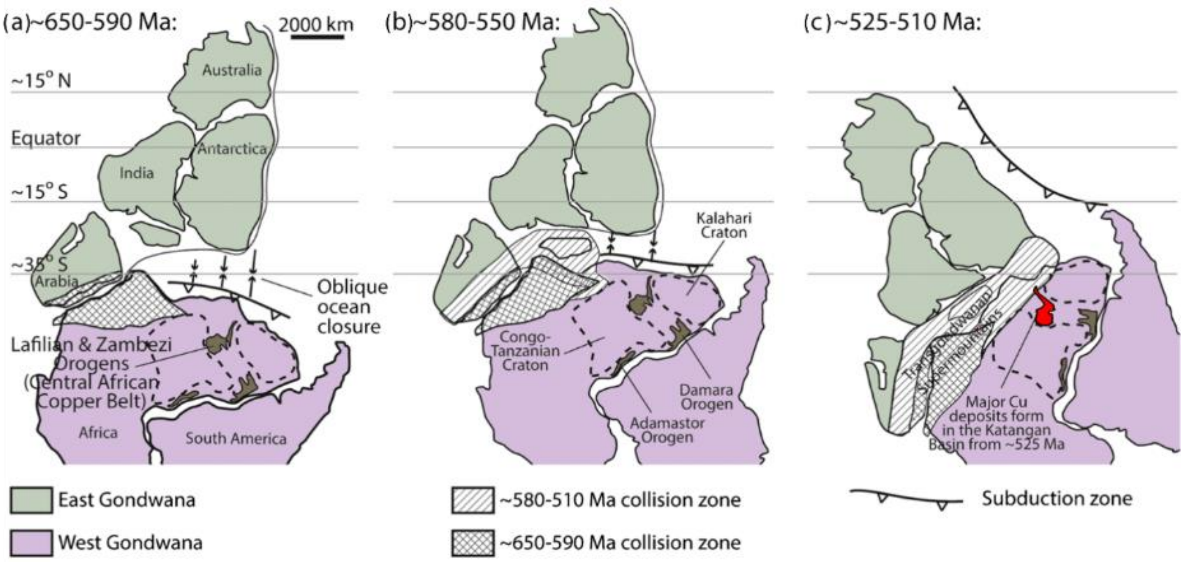

Figure 8: Tectonic evolution of east and west Gondwana (Squire and Keays, 2023).

Widespread rifting may have caused crustal thinning, providing potential access for ore bearing fluid migration. Several methods can be used to model and understand the nature of the sub continental lithospheric mantle (SCLM). The use of high-resolution shear wave tomography has been applied to map the modification of SCLM (Fig. 9) and identify zones of mantle upwelling and crustal thinning with the objective of determining the evolution of upper lithospheric domains (Begg et al., 2009). The sequence of tectonic events related to the region of interest are rifting, collision and orogenic closure.

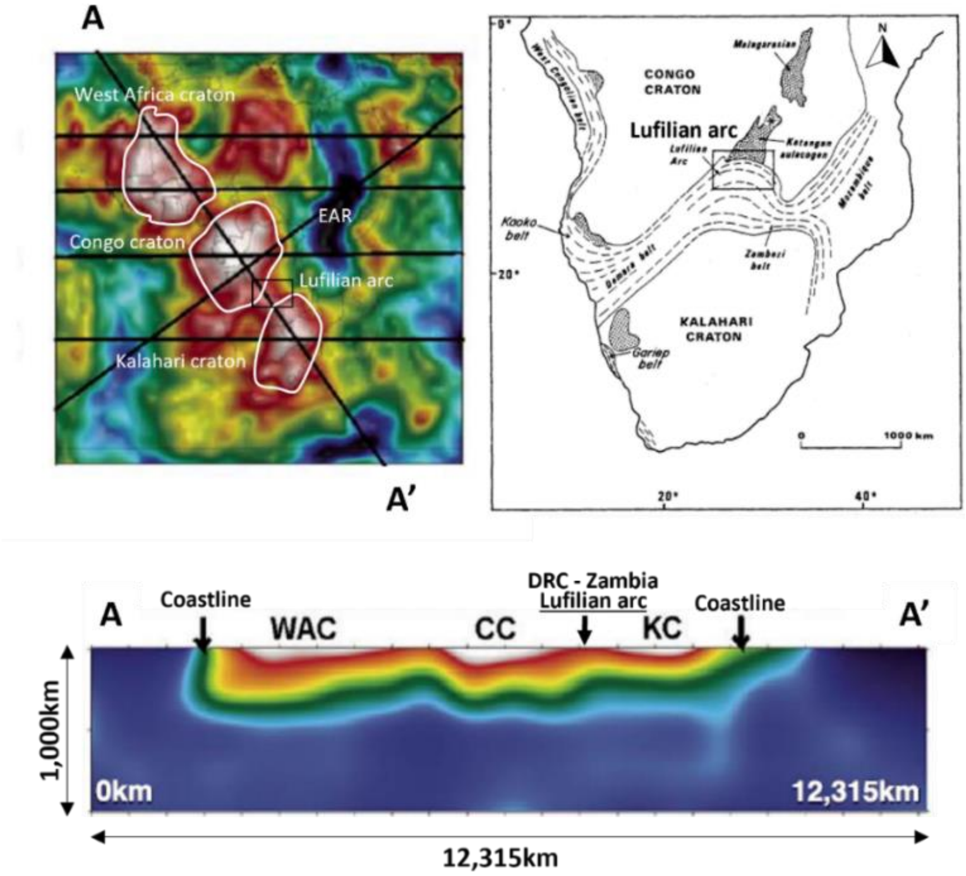

Figure 9: Seismic tomography and tectonic setting of the Lufilian arc (Kampunzu and Cailteux, 1999; Begg et al., 2009).

The tomography modelling by Begg et al., (2009) supports the configuration of the Congo and Kalahari cratons and the development of the Lufilian arc, along with the resultant mobile belts (Damara, Zambezi and Mozambique) as proposed by Kampunzu and Cailteux (1999). These resultant mobile belts that form i.e., the Zambezi, Damara and Mozambique belts, are all proximal to the Lufilian arc. The application of tomography models can be particularly useful to identify areas in which sedimentary basins can occur as a result of upwelling mantle (after collision, before rifting) interacting with upper crustal levels.

Kröner and Stern (2004) and previous workers, recognised a series of deformational episodes from rifting through to orogenic closure, arc and micro-continent accretion, until the final suture to form Gondwana. The main events that affected the Katanga basin include early rifting, causes localised basin faults, extension and magmatism, whilst basin inversion and deformation are recorded ~595 – 490 Ma and metamorphism to the upper greenschist facies ~530 Ma (Selley et al., 2005; Hitzman et al., 2012). This extension – compression tectonic convergence led to northward folding and thrusting, which deformed the succession, producing the structural setting favourable to promote mineral system development.

2.3 Regional Structural setting

The Congolese Copperbelt exhibits a higher-level structural complexity as compared to the Zambian Copperbelt. This can largely be attributed to halokinesis occurring within the time period 1050 Ma – 650 Ma, in which deposition of the lower parts of the Katanga succession was followed by the emplacement of mega–breccias and salt diapirs due to folding and thrusting (Cailteux et al., 2018). The configuration, which has formed as a result of the north–directed folding and thrusting deformation events, resulted in the Katangan basin arrangement illustrated by the simplified interpretation below (Fig. 10). This shows a more detailed configuration of the Katanga basin and surrounding mobile belts. The interpretation of the structural setting of the Katanga basin is associated to an intracratonic rift basin opening (in the area between the Congo and Kalahari cratons) and the widening of the basin can be attributed to proto-oceanic rift stage, along with later collision of the Kalahari and Congo craton (Cailteux and Putter, 2019). These events result in the arrangement and structural domains namely, the Lufilian foreland, External fold and thrust belt, Domes Region, Synclinorial belt and Katanga high.

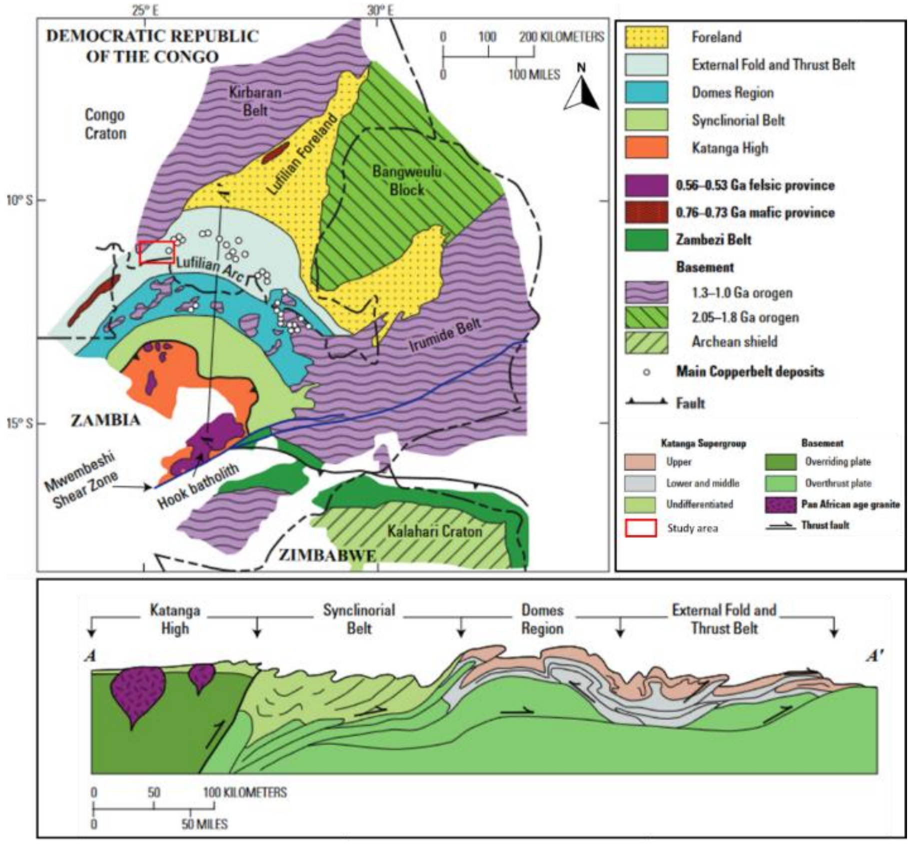

Figure 10: Simplified regional structural interpretation across the CACB (Zientek et al., 2014, modified after Porada 1989; Porada and Berhorst 2000).

2.4 Regional Stratigraphy

The Katanga Supergroup is made up of continental metasedimentary units with limited mafic intrusions (Cailteux et al., 1994). The Katangan succession can be broadly divided into the Roan Group, which is overlain by the Nguba Group, with the Kundelungu Group overlying the Nguba Group, all of which sit above the Archean to Mesoproterozoic granitic basement (Batumike et al., 2007; Selley et al., 2018). Correlation between the stratigraphy of the CCB, the ZCB and the Northwest Province (Zambia) is generally possible as shown by Fig. 11 (Hitzman et al., 2012).

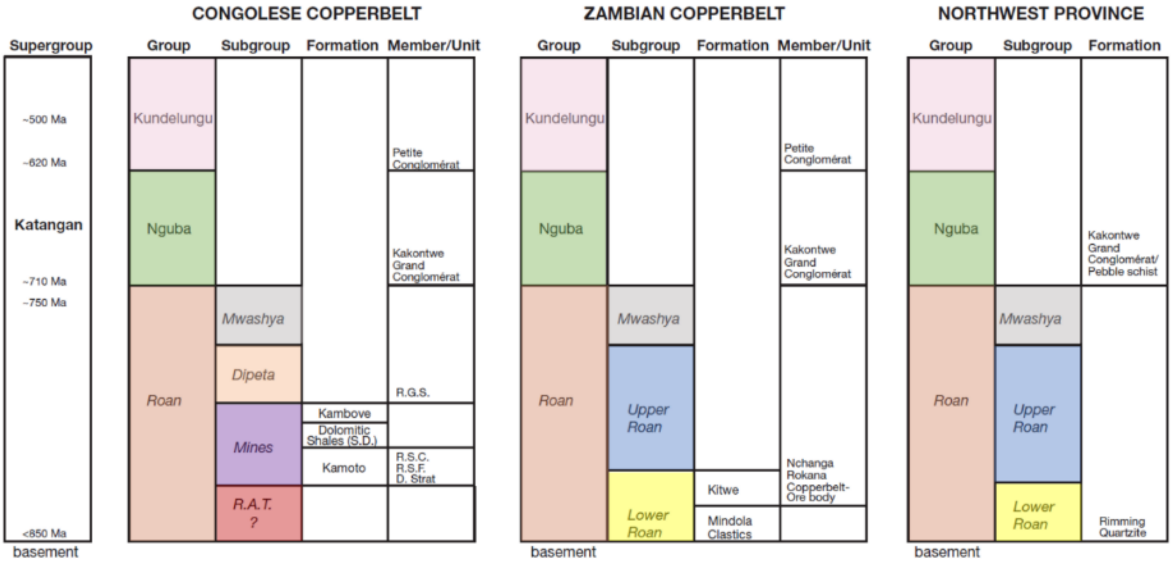

Figure 11: Katanga succession in the CCB, ZCB and NWP (Hitzman et al., 2012).

The Roan Group is dominated by evaporitic sequences of a lacustrine environment overlain by a series of carbonate and siliciclastic sequences of the Nguba Group and Kundelungu Group, indicative of proto-oceanic and epi-continental depositional settings. In the CCB, the Roan Group is subdivided into the R.A.T. (Roches Argilo Talqueuses), Mine Series, Dipeta and Mwashya Subgroups. The Nguba Group and Kundelungu Group are regressive sequences with diamictites at the base (Cailteux et al., 1994). The diamictite units at the base of the Nguba Group (Grand Conglomérat Fm.) and Kundelungu Group (Petit Conglomérat Unit) are correlated to the Sturtian glaciation (717 to 659 Ma Grand Conglomérat Fm.) and the younger Marinoan glaciation (645 to 635 MaPetit Conglomérat Unit) (Hitzman et al., 2012; Hoffman et al., 2017). These diamictites are overlain by cap-carbonates referred to as Kaponda, Kakontwe, Kipushi and Lusele respectively (Batumike et al., 2007; Kampunzu et al., 2009). Above the carbonate associated to the Grand Conglomérat (carbonates of Kakontwe Fm.), are proto-oceanic rift sequences comprising of carbonates, siltstones and shales (of the Nguba Group). Overlying the cap carbonate associated to the Petit Conglomérat (Lusele Fm), is an epi-continental succession comprised of sandstones, carbonates, siltstones and shales of the Kundelungu Group (Batumike et al., 2007; Kampunzu et al., 2009).

The Katanga basin has a curved-symmetrical form with a sedimentary package of approximately 11 km of stratigraphy towards the north and around 2 km at the basin margins (Selley et al., 2018). This variability in thickness within the basin is believed to reflect the extensional growth of the basin. Whilst these general geometries were relatively well preserved through orogenesis, halokinesis causes local complexities. The areas affected by salt tectonism (mainly observed in the DRC) occur in the centre of the basin, as well as towards the north of the basin, whilst the southern area is less affected by salt tectonics although metamorphism is of higher grade due to thrusting, folding and burial (Selley et al., 2018).

2.5 Metamorphism

Regional metamorphic grades of the CACB range from prehnite-pumpellyite to amphibolite facies, with high pressure eclogites and whiteschists occurring in the Domes Region (Kampunzu and Cailteux, 1999; Selley et al., 2005). Subduction of oceanic lithosphere, results in eclogite formation at ~600 Ma. Whilst, garnet-amphibolites and biotite-kyanite-garnet gneisses are indicative of whiteschist metamorphic facies within the Lufilian arc (John et al., 2004). This indicates peak metamorphic conditions of about 750 ±25 °C. This is related to the final continental collision between the Congo and the Kalahari cratons at ~530 Ma, coincident with the assembly of Gondwana (John et al., 2004).

The tectonic evolution of the Pan-African Lufilian Arc plays a role in the development of the regional metamorphic regime of the Central African Copperbelt (CACB). The illustration below, Fig. 12, shows the tectonic evolution following the collision between east and west Gondwana (which is intricately associated to the formation of Lufilian Arc) commencing from (a) the dispersal of Rodinia forming an ocean basin, to (b) subduction of oceanic lithosphere bringing together the Kalahari and Congo cratons (closure of ocean basin), (c) collision of the Kalahari and Congo cratons and (d) uplift and cooling within the suture zone between the two cratons.

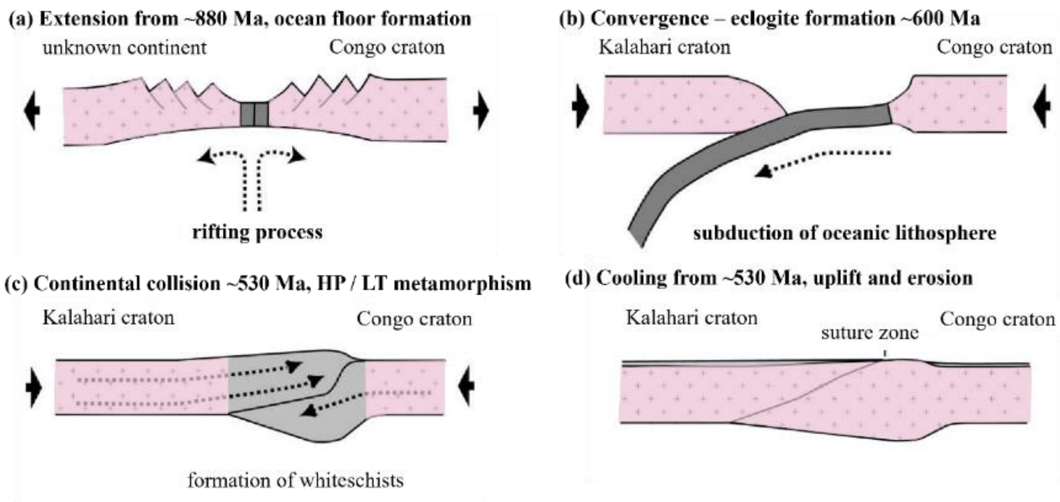

Figure 12: Illustration of the proposed evolution of the Pan-African Lufilian Arc–Zambezi Belt orogen (John et al., 2004).

The extension of the rift basin at the onset of the Pan-African orogeny resulted in the formation of a passive continental margin (Porada and Berhorst 2000). Subsequently, eclogites formed at around 600 Ma as a result of the converging of the oceanic lithosphere associated to the Congo and Kalahari cratons. This was superseded by the formation of the talc – kyanite whiteschist assemblages at around 530 Ma linked to peak metamorphic conditions of 750°C ± 25°C at 13 ± 1 kbar (John et al., 2004). In order to consolidate these observations, a generalised interpretative P/T path for the Central African Copperbelt metamorphism was compiled (Fig. 13). This illustrates the metamorphic domains of the CACB according to the understanding of the regional metamorphism. Additionally, the P/T path of a CACB eclogite sample of Gt-Omph-Amp-Qtz-Rt (paragenesis 1) and Gt-Cpx-Amp-Pl-Qtz-Ilm (paragenesis 2) is shown in Fig. 14 (François et al., 2018), demonstrating the wide range of regional metamorphic conditions.

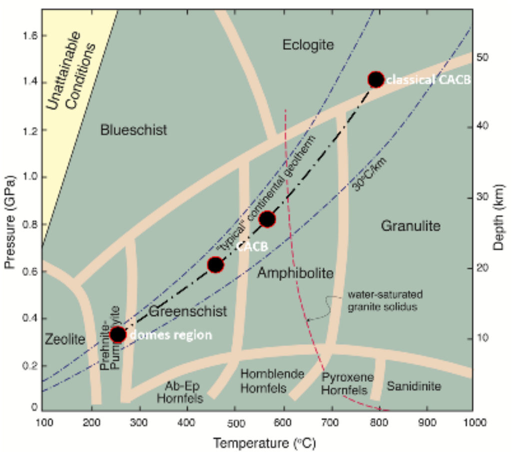

Figure 13: Illustration of CACB metamorphism P/T path (modified after Winter, 2020).

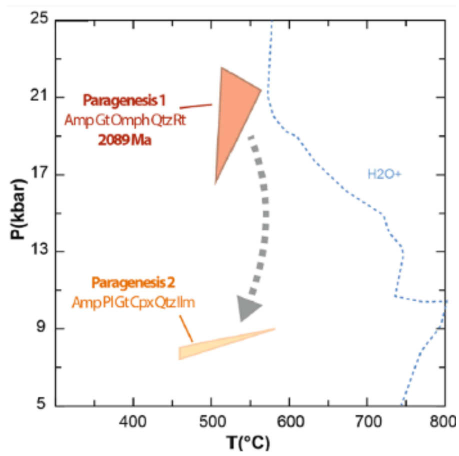

Figure 14: Eclogite metamorphism P/T path for the CACB (François et al., 2018).

This interpretation is related to observations of prehnite – pumpellyite to amphibolite facies, with high pressure eclogites and whiteschists (Kampunzu and Cailteux,1999; Selley et al., 2005). Other studies in the Zambian Copperbelt (ZCB) by Sillitoe et al., (2017) report that rock samples from Chambishi southeast and Mufulira deposits exhibit greenschist facies metamorphism, whereas the mineral associations of the amphibolite facies are observed in samples from Sentinel and Mujimbeji deposits. Peak metamorphism occurs around 530 Ma (Kampunzu et al., 1999; Selley et al., 2005; Hitzman et al., 2012) and the formation of eclogites is associated to the subduction of oceanic lithosphere at around 600 Ma (John et al., 2004). The dominance of sericite and chlorite in the western part of the CACB supports the notion that rocks in the region has been metamorphosed to lower greenschist facies (François, 1974; Hitzman et al., 2012). The observation of ubiquitous chlorite (Schmandt, 2013) suggests that rocks occurring locally at the Kamoa – Kakula study area have also undergone weak to moderate metamorphism to lower greenschist facies.

2.6 Alteration

Alteration in the Central African Copperbelt occurs at a regional scale and is associated to permeability, the availability of sulphur and the nature in which lithologies react to the redox reaction that occurs between the between oxidised and reduced facies (Fay and Baryon, 2012). The alteration assemblages can act as an indicator of the potential association to Cu – Co mineralisation and the pathways that the metal-bearing fluids may have taken, as well as their subsequent interaction with host rocks. This type of framework can be used to differentiate between deposits or regions. In the northern part of the Katanga basin, at the Tenke-Fungurume district (Democratic Republic of Congo), anhydrite and dolomitic alteration is predominantly observed with episodic introduction of silica alternating with dolomite (Fay and Baryon, 2012). Other types of alteration present at this location include magnesian, chlorite, potassic and sodic alteration (Mambwe et al., 2017). In the central parts of the CACB, the observation by Selley et al., (2005), highlights the occurrence of hydrothermal albite and K-feldspar alteration. The Nchanga deposit (Zambia) exhibits the hydrothermal alteration mineral assemblages comprising dolomite, chlorite, sericite, rutile and phlogopite, amongst others (McGowan et al., 2006). In the far eastern area of the CACB, the presence of K-feldspar surrounding ankerite grains as well as albite alteration (Hendrickson et al., 2015) is noted in the diamictite hosted Fishtie deposit (Zambia). At

Kamoa – Kakula, hydrothermal alteration assemblages involve potassic, magnesian and chlorite alteration (Schmandt et al., 2013).

2.7 Mineralisation

It is widely accepted that Copperbelt disseminated mineralisation occurred during diagenesis primarily through oxidation-reduction reactions within a rift setting, whilst the vein associated mineralisation is interpreted to have occurred as a result of remobilisation of disseminated sulphides due to orogenesis (Selley et al., 2005; Hitzman et al., 2010; Sillitoe et al., 2017). There has also been recognition of two generations of copper and cobalt mineralisation, the first diagenetic phase associated to the hydrothermal fluid temperatures of around 15 to 220°C and salinity of 11.3 to 20.9 wt.% NaCl, whilst the second phase is associated to the temperatures of 70 to 385°C and salinity of 35 to 45.5 wt.% NaCl (El Desouky et al., 2016). Fluid inclusion assemblage studied at Kamoa – Kakula demonstrated temperatures in the range of 210°C to 240°C with final and eutectic melting observed at -20°C and 45°C respectively, indicating a Na-Ca brine that is associated to salinities of ~23 – 26 wt % NaCl wt eq. (Schmandt, 2013).

The regional stratiform Cu ± Co mineralisation, which is predominantly diagenetic in origin, has also been observed to be epigenetic, as well as hypogene – as is the case of Zn-Pb-Cu and Cu-Ag-Au mineralisation occurring in Nguba Group carbonates and Kundelungu Group clastics. These superimposed assemblages are likely to occur due to remobilisation of mineralisation in the Roan Group (Batumike et al., 2007). This demonstrates that base-metal mineralisation occurs as a result of varied conditions within the Katanga basin, at multiple stratigraphic positions. A compilation by Selley et al., (2018) (Fig. 15) illustrates the occurrence and spatial distribution of these deposits showing the additional occurrence of other multi-commodity deposits including those with U-Ni-Co (Au-PGE), Cu-U, Cu ± Ni and Cu (Mo-Au) mineralisation.

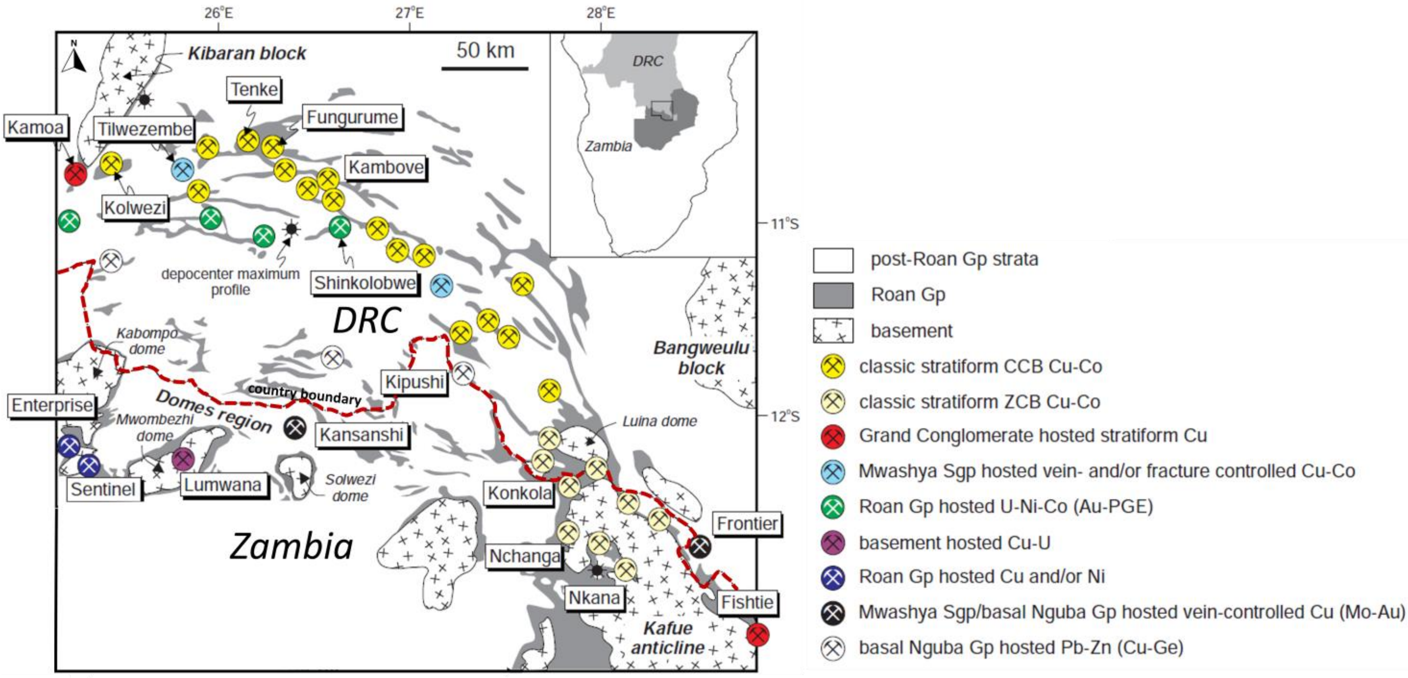

Figure 15: Mineral deposits of the CACB (Selley et al., 2018).

Orogenesis and metamorphism have had a distinct effect on the timing and ages of Cu-Co mineralisation in the CACB. The tectonic evolution plays an important role in the metallogeny of the region, which is associated to the onset of rifting, subsequent sedimentation, renewed rifting, synorogenic sedimentation, deformation during the Lufilian, with later cooling and uplift (Hitzman et al., 2010). Studies by Sillitoe et al., 2017 used Re-Os isotope geochemistry as the dating methodology to constraint the timing of mineralisation. Their results indicate that sulphide mineralisation occurred in Zambia at 534.4 ± 2.2 – 524.8 ± 2.2 Ma (Lumwana), 512.4 ± 1.7 – 502.4 ± 1.2 Ma (Kansanshi) and 525.7 ± 3.4 Ma (Nkana), whilst further Re-Os dating results from the DRC revealed the timing of sulphide mineralisation to occur at ~645 ± 15 Ma (Musoshi) and in two stages at Kamoto at 682 ±28 – 230 ± 36 Ma and 821 ± 51 – 762 ± 33 Ma (Sillitoe et al., 2017). This spectrum of results supports the proposal that Cu-Co mineralisation is largely associated to the Lufilian orogeny, which triggered multiple stages of sulphide mineralisation. Mainstage mineralisation is accepted to occur at around 570 – 520 Ma, associated to the age of the emplacement of the Hook batholith, coincident with the orogenic peak at 530 Ma (Selley et al., 2005; Sillitoe et al., 2017). The timing of mineralisation derived from Re-Os dating suggests that Cu-Co mineralisation generally occurs as a result of the dissolution of evaporites and subsequent circulation of ore bearing fluids within the Katanga basin (Sillitoe et al., 2017; Saintilan et al., 2018). Evidence of this is disseminated, nodular mineralisation and bedding parallel mineralisation, with mineralisation styles exhibiting strain from tectonism (Sillitoe et al., 2017; Twite et al., 2019). Sillitoe et al., (2015) provided a schematic representation of the basin architecture and the ore deposits that are formed (Fig. 16). This generalised illustration depicts the evolution of the Katanga sedimentary basin and the deformation occurring during rifting and subsequent basin inversion. As a result, sediment hosted copper deposits form in the Mesoproterozoic and Paleoproterozoic basement along with the Neoproterozoic sediments. This highlights the temporal link between mineralisation and the Paleoproterozoic to Mesoproterozoic basement, related to initial / renewed rifting of the basin, due to crustal extension (Fig. 16, 1; Fig 16, 2 a-b) whereas mineralisation in the Neoproterozoic sedimentary sequences is associated to the inverted rift sequence, due to crustal contraction (Fig. 16, 2 c-d).

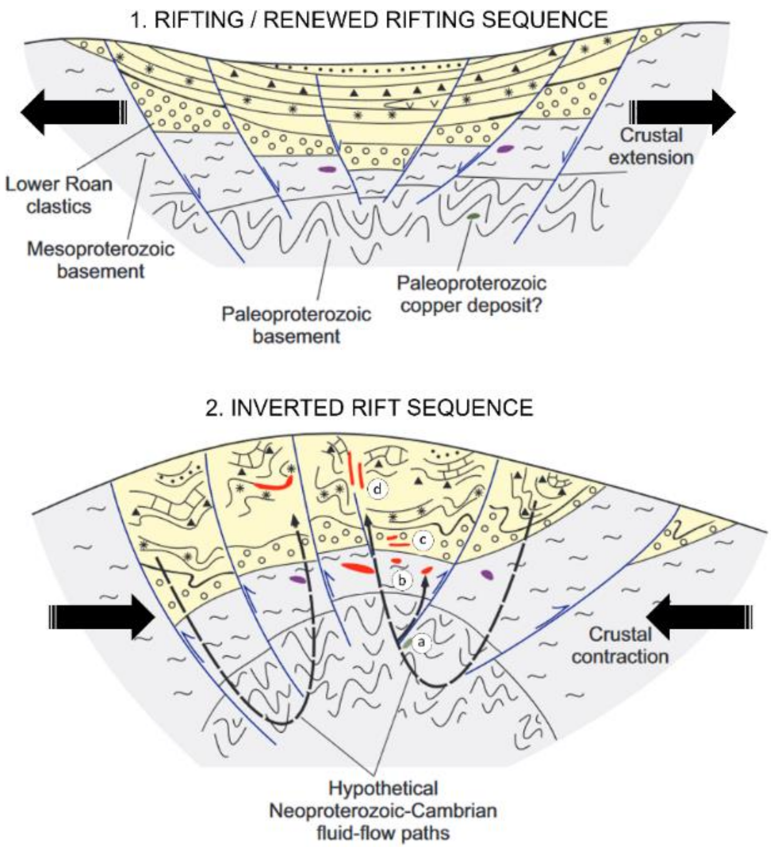

Figure 16: Katanga basin architecture and position of mineralisation (modified after Sillitoe et al., 2015).

3 PROJECT LOCATION AND LOCAL GEOLOGY

3.1 Project Location

The Kamoa – Kakula deposit is a sedimentary hosted copper deposit located in the Katanga basin, in the Central African Copperbelt (CACB) Lualaba Province, in the Democratic Republic of Congo (DRC). It is located approximately 25 km west of Kolwezi (Fig. 17). The discovery of the Kamoa – Kakula deposit was a result of a combination of exploratory methods such as geochemical soil sampling, stream sediment sampling, airborne magnetic surveys, radiometric surveys as well as drilling (Broughton and Rogers, 2010). The geological setting is associated to the intracratonic rift basin opening (in the region between the Congo and Kalahari cratons) and widening of the basin, attributed to proto-oceanic rift stage (Cailteux and Putter, 2019). Kamoa – Kakula is located in an unconventional setting to the DRC, east of the deposits occurring within the Mine Series of the Roan group. It is located on the western boundary of the Katanga basin.

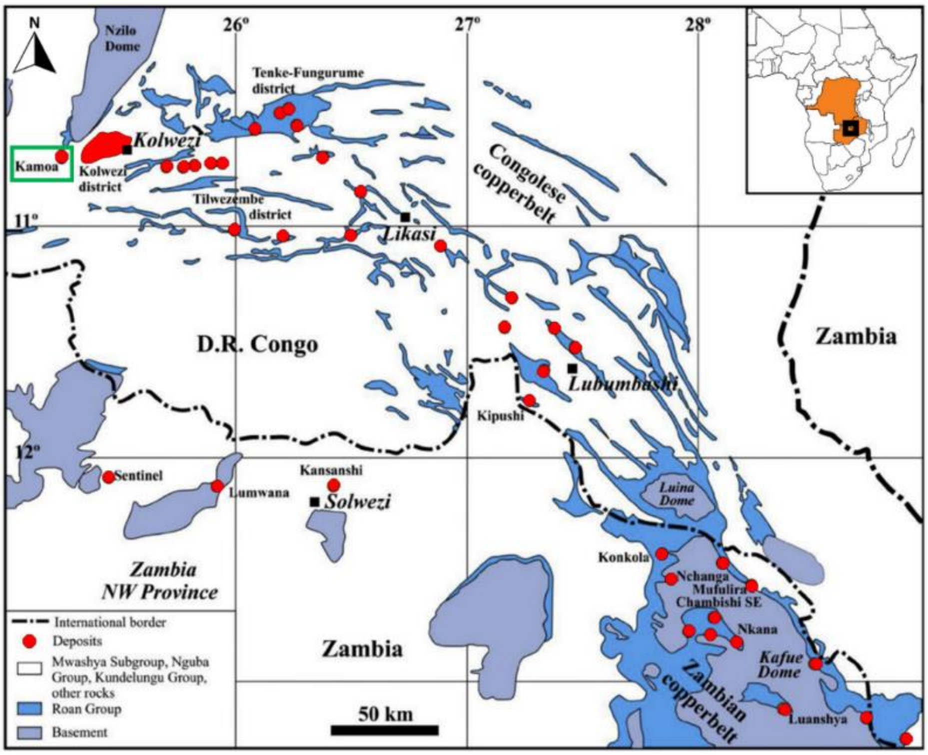

Figure 17: Simplified geological map of Central African Copperbelt, CACB (after François, 1973).

3.2 Kamoa Sub-basin facies and Local geology

The Kamoa deposit occurs within the Kamoa sub-basin, in the western foreland, Katanga basin. The local succession is part of the Katanga succession and its depositional environment is associated to rifting and sedimentological processes. Whist it is widely accepted that the Grand Conglomérat is associated to the Sturtian glaciogenic event, defined above, an alternate proposal suggests that the formation of the sub-basin occurs as a result of initial rifting, followed by fault – related mass flow of conglomerates as a result of faulting and seismic activity (Kennedy et al., 2019). The basin palaeoenvironment (Fig. 18) shows the progressive depositional evolution of the Kamoa sub-basin as occurring in 3 phases, with these phases producing facies FA1 to FA7.

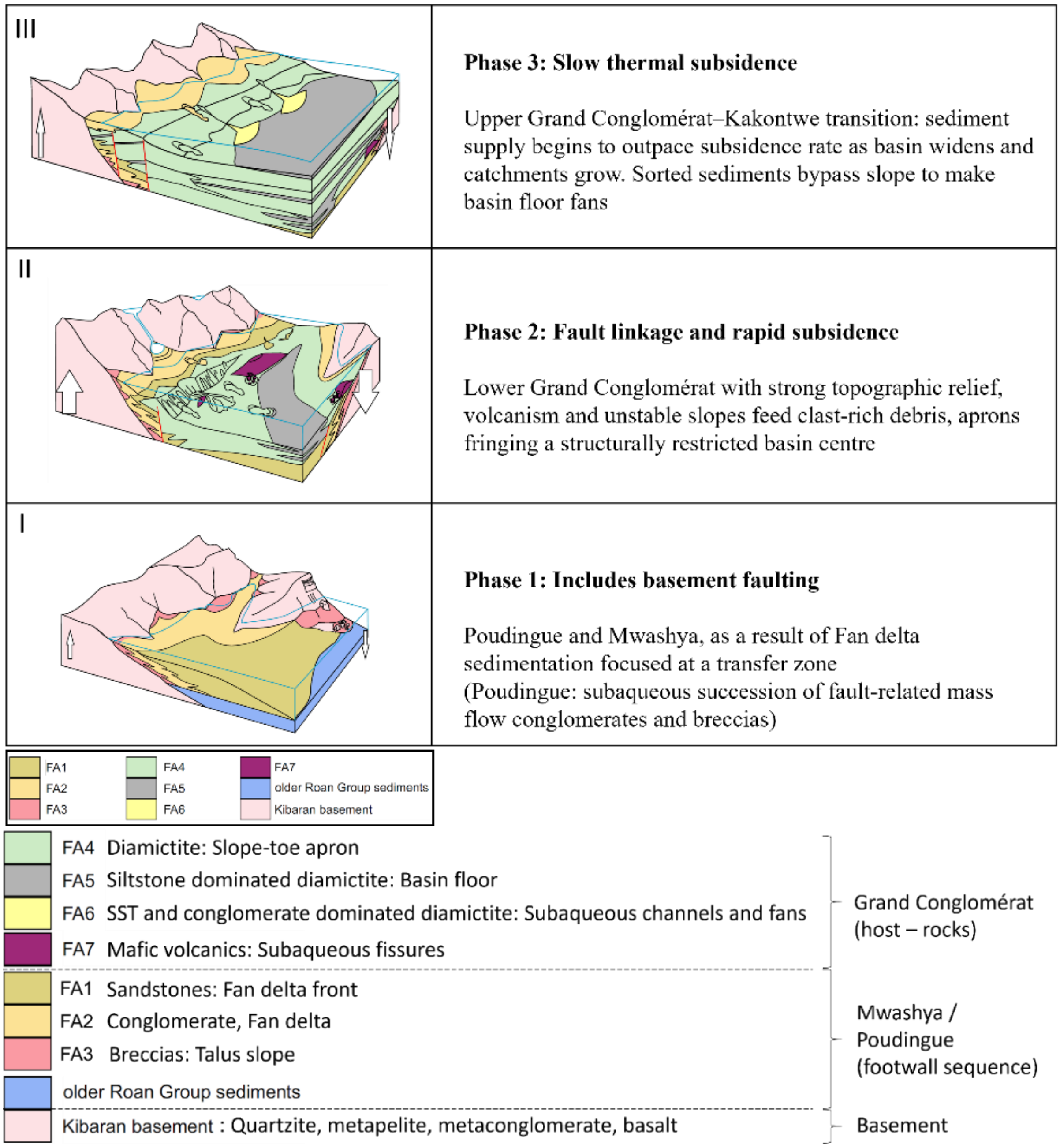

Figure 18: Phases of the Kamoa sub–basin sedimentary development (Kennedy et al., 2019).

The depositional model is interpreted to position Facies 1 to Facies 7 overlying older Roan Group sediments and Kibaran basement. Facies 1 (Mwashya Subgroup) comprises a sandstone likely deposited at the front of a fan delta, whilst Facies 2 (conglomerates and interbedded sands) and Facies 3 (predominantly quartzite) of the Mwashya subgroup, suggest an influx of coarser grained sediment. Kennedy et al., 2019 suggest that Facies 4 through Facies 7 (Grand Conglomérat) form as a result of debris flows and are dominantly diamictite with varying degrees of coarseness with the exception of Facies 5, which is siltstone dominant and also comprises a pyrite-rich siltstone. The lithologies local to Kamoa include

Kibaran basement, a basal (Roan) conglomerate (Poudingue), Mwashya sandstones and diamictite of the Grand Conglomérat Fm. (Broughton and Rogers, 2010). The Kamoa copper deposit is proximal to the Kamoa and Makulu domes and the west scarp fault (Fig. 19). The NE-SW west scarp fault causes a distinct west-down offset on the western part of the deposit and thickness variations of lithologies, whilst the NE-SW Kansoko Sud trend exhibits east-down normal displacement (Twite, 2016; Schmandt et al., 2012).

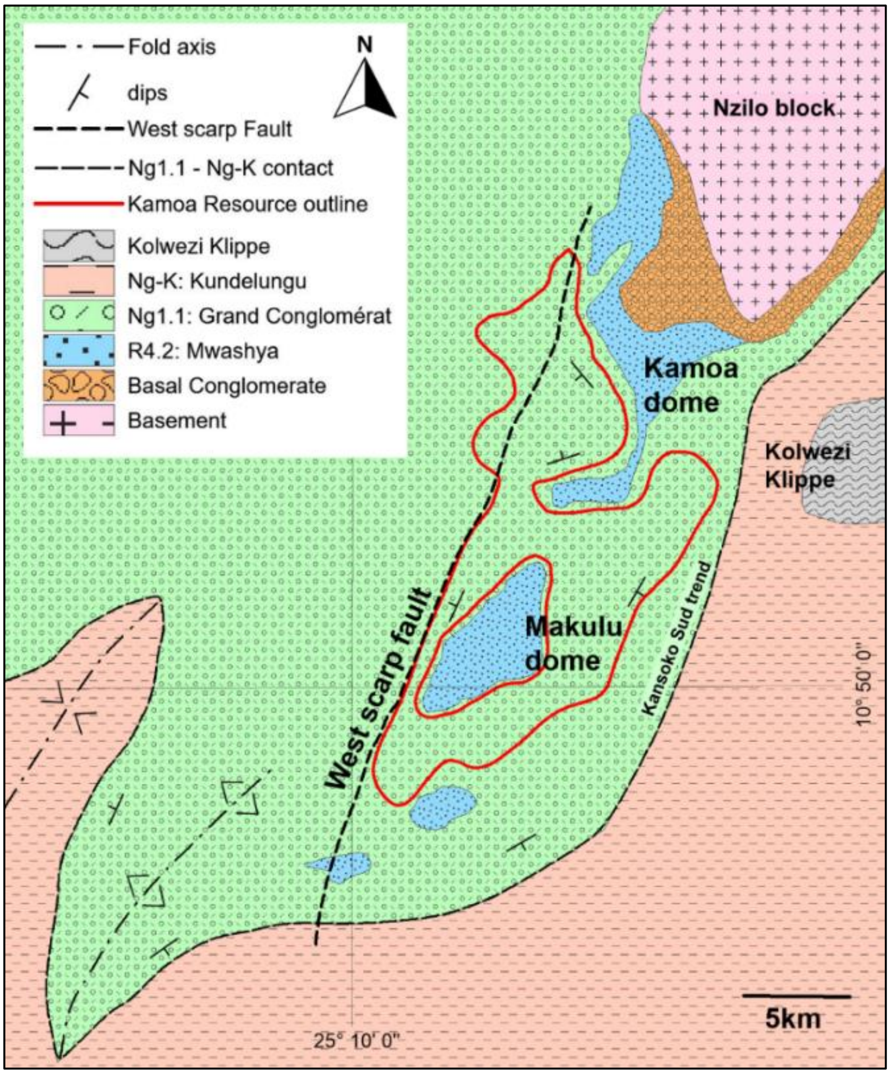

Figure 19: Local geology of Kamoa (modified after Broughton and Rogers, 2010; Twite et al., 2019).

The local geological setting at Kamoa – Kakula has been delineated by systematic geological and exploratory techniques and drilling, which have constrained the local geology. At prospect scale, the Nzilo block is present and represents a basement inlier proximal to the local Roan Group (R4.2; Mwashya Subgroup) sedimentary succession which comprises of iron-rich sandstones as well as conglomerate, this is overlain by a diamictite (R1.1; Grand Conglomérat Fm.) succession that has internal variability (Broughton and Rogers, 2010), this sub-division of diamictite is further detailed in Section 5.2 (Kamoa-Kakula stratigraphy). As shown by Fig. 19 this sequence is overlain by Ng-K; Kundelungu, whilst the Kolwezi Klippe is observed on the eastern part of this geology surface expression. The Cu deposit is closely associated to the Makulu and Kamoa domes, bound by the West scarp fault to the west and the Kansoko Sud trend to the east (Twite, et al., 2019).

4 METHODOLOGY

4.1 Literature review and preparation for field visit

An appropriate research methodology to address the scope of the Research project, which is to investigate the nature and characteristics of sulphide mineralisation at the Kamoa – Kakula deposit, was developed (Fig. 20). A review of existing literature was the initial method of determining the scope of the project. The Katangan stratigraphy and understanding of ore genesis was studied by Bowen and Gunatliaka in 1976, improving upon initial studies conducted by Mendelsohn (1961), as well as Binda and Mulgrew (1974). From 1922 to 2000, various direct and indirect exploratory methods were conducted in the CACB (Simabwachi, 2022). At the project area, in 2004, Ivanhoe Mines and their Contractors, executed an exploration programme in the DRC with initial activities involving conventional stream sediment sampling which exhibited results >3,500 ppm Cu, soil geochemistry with proven anomalies >500 ppm Cu and airborne geophysical surveys that discriminated the magnetic Grand Conglomérat Fm. (Broughton and Rodgers, 2010). Studies by Schmandt (2013) and Twite (2016) identified the dominant sulphide mineral assemblage comprising of pyrite, chalcopyrite, bornite and chalcocite, also proposing a distinguishable mineral zonation. Subsequently robust 3D modelling techniques were applied conforming to the lithological constraints and controls of mineralisation (Gilchrist, 2019). The literature review was further advanced in conjunction with site staff, and later refined during the course of the field visit in the DRC. Preparation for the field visit included discussion of the aims of the project with Ivanhoe Geologists as well as identification of appropriate drillholes, respective prospects and sections. Kakula, Kakula west, Kansoko Centrale, and Kansoko Sud were selected as the study areas upon discussion. This literature review of historic and recent geological information was used to understand the geological history in the regional and local context in order to better conceptualise this study as well as to provide input to the regional stratigraphic correlation carried out focusing on correlation of ore deposits in the Zambian Copperbelt and Congolese Copperbelt.

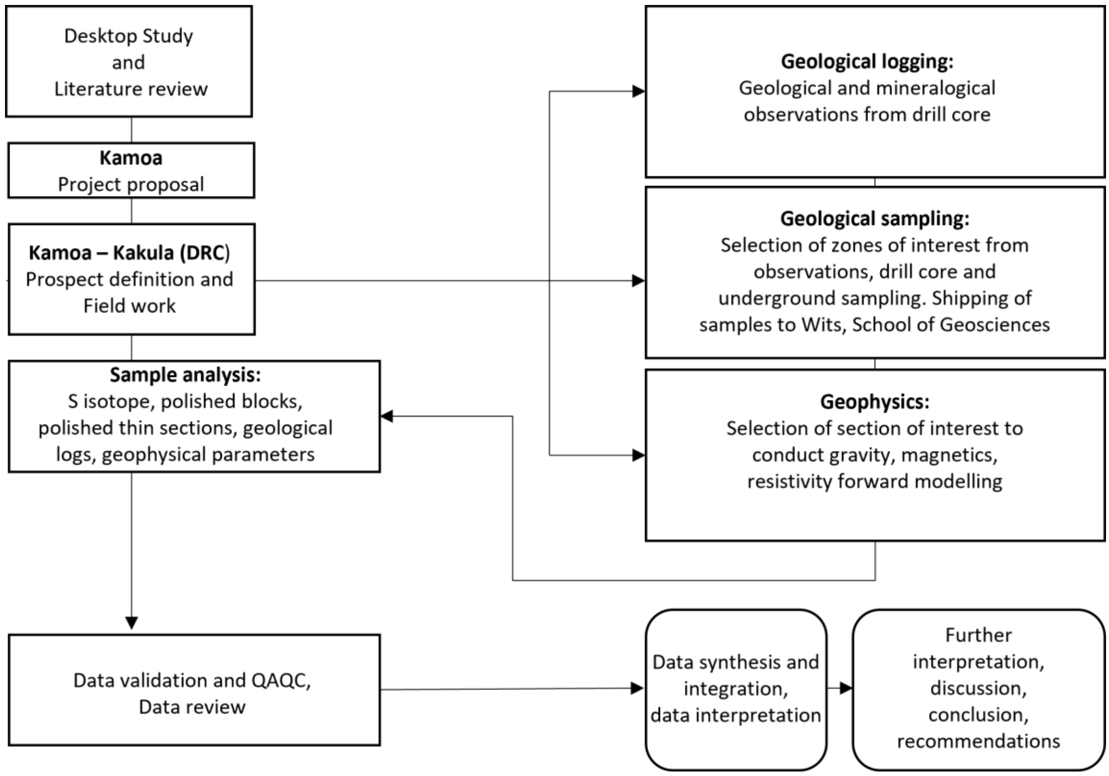

Figure 20: Flowchart of the methodology designed and applied in this study.

4.2 Geological logging and sample collection

Geological logging was conducted during a field visit to Kamoa – Kakula. The selection criteria was based on spatial distribution of prospect areas, host rock lithology, mineralisation style, mineralised zones with grade > 2.5 % TCu, identifying zones with the potential to make an informative paragenetic relationship, occurrence of sulphide grains and representative samples from zones with grade < 2.5 % TCu. Based on this criterion, four prospect areas were selected and the following procedure was followed with some help from site managers and technicians;

(1) drill core retrieval and layout; drill core laid out on logging tables;
(2) geological logging of drillholes, observing weathering state, colour, colour intensity, grainsize, structure, lithology, alteration and mineralogy;
(3) taking photos and sampling of mineralised zones; observations in relation to mineralogy, mineralisation type and style, increasing / decreasing abundance, marking of drill core, sample bagging in polyethylene plastic bags, sample mark in core tray;
(4) core cutting of samples; cutting of sample by electric core-saw, bag sample in polyethylene plastic zip-lock bag, return excess sample, boxing samples for dispatch;

The representative samples from mineralised zones were taken from the aforementioned prospect areas and a total of eight drillholes were selected and sampled (Table 2). Following the mentioned steps, the samples then were placed into sample boxes and prepared for freight from the Democratic Republic of Congo to the School of Geosciences, University of the Witwatersrand, Johannesburg, South Africa.

Table 2: Project drillholes for this study

BHID	Project	Prospect
DKMC_DD1039	Kamoa - Kakula	Kakula
DKMC_DD1044	Kamoa - Kakula	Kakula
DKMC_DD571	Kamoa - Kakula	Kansoko Centrale
DKMC_DD624	Kamoa - Kakula	Kansoko Centrale
DKMC_DD627	Kamoa - Kakula	Kansoko Centrale
DKMC_DD1179	Kamoa - Kakula	Kakula West
DKMC_DD952	Kamoa - Kakula	Kansoko Sud
DKMC_DD956	Kamoa - Kakula	Kansoko Sud

4.3 Underground sampling

A traverse was conducted at the Kakula Mine, Kakula north decline, in order to contextualise the relationship between lithologies, structure, nature of lithology contacts and mineralisation from exposed underground rock faces. During the mapping visit, 11 samples were collected in order to make further lithological and mineralogical observations. The discriminant factors for the selection of the areas investigated, were;

(1) mineralised lithologies
(2) lithologies proximal to mineralisation
(3) lithologies distal to mineralisation

Mineralised horizons at Kakula Mine – Kakula north decline are associated to a cut-off of > 2.5 % TCu and samples that were selected, were chosen by host rock lithology, their position within the profile that was traversed, areas of visible mineralised and areas absent of visible mineralisation (Table 3).

Table 3: Samples collected from Kakula Mine

No. Samples	Project	Locality
11	Kakula Mine	Kakula North decline: multiple samples from six stratigraphic levels

Subsequently the drillhole and underground samples were compiled into a batch of samples that were shipped to University of the Witwatersrand, School of Geosciences, Johannesburg, South Africa as well as to the Laboratory of Stable Isotopes of the Far East Geological Institute, Russian Academy of Sciences, Vladivostok, Russia.

4.4 Reflected and transmitted light microscopy

An optical microscope (Olympus BX41) was used for transmitted light microscopy at the University of the Witwatersrand, School of Geosciences. This was used to study representative polished thin sections and polished blocks. The polished blocks were prepared from the samples by (1) cutting each specimen to size and selecting a representative area with sulphides (2) mounting fragments within epoxy resin (3) grinding of the block to remove any uneven surfaces (4) polishing to make plane visible. Subsequently, allowing for study and mapping by reflected light microscopy for further in situ analysis of the compositions of representative sulphide grains. A total of 10 polished blocks were prepared from samples collected (Table 4), with each polished block containing 5-6 fragments of the samples from the various prospect areas.

Table 4: Polished blocks prepared for this study

Polished block	**BHID Samples**			
Block 1	DKMC_DD624	DKMC_DD956		
Block 2	DKMC_DD624	DKMC_DD956	DKMC_DD1044	
Block 3	DKMC_DD1044			
Block 4	DKMC_DD624	DKMC_DD627	DKMC_DD1044	
Block 5	DKMC_DD571	DKMC_DD624	DKMC_DD627	DKMC_DD1044
Block 6	DKMC_DD571	DKMC_DD627		
Block 7	DKMC_DD956	DKMC_DD1039	DKMC_DD1044	
Block 8	DKMC_DD571	DKMC_DD627	DKMC_DD956	DKMC_DD1039
Block 9	DKMC_DD571	DKMC_DD627	DKMC_DD956	DKMC_DD1039
Block 10	DKMC_DD571	DKMC_DD624	DKMC_DD1039	DKMC_DD1044

A total of 30 polished thin section samples were prepared (Table 5) across the eight drillholes. In this method, rock samples were mounted to a core saw and 30 µm sized thin section slices were prepared. These were placed between glass slides measuring 27 x 46 mm and secured in place by epoxy resin. One sample was fragmented in the process of thin section sample preparation.

Table 5: Thin sections prepared from samples in this study

Prospect	Sample BHID or Location		
Kakula	DKMC_DD1039 (2)	DKMC_DD1044 (2)	
Kansoko Centrale	DKMC_DD571 (3)	DKMC_DD624 (3)	DKMC_DD627 (3)
Kakula West	DKMC_DD1179 (5)		
Kansoko Sud	DKMC_DD952 (4)		
Kakula North decline	Underground (8)		

4.5 Scanning electron microscope

Polished thin sections were reviewed at the Microscopy and Microanalysis Unit (MMU) of the University of the Witwatersrand. A TESCAN VEGA Scanning Electron Microscope (SEM) was used for this analysis. A narrow beam of electrons is emitted by the SEM, which scans the sample pixel by pixel and as such the uniformity (and potential obstructions) of the surface of the sample is of importance. The main principle of the SEM are as follows;

- Secondary (low energy electrons) electrons emitted from the atoms of the sample
- Electrons from the SEM beam bounce off the sample, and these high energy backscattered electrons are received by the SEM
- The electrons from the SEMs electron beam interact with the atoms of the sample and create an X-ray that determines the sample composition, which is then displayed

Samples were identified from polished thin sections with sufficient sulphide grains present to identify and interpret the paragenetic relationship. A total of 33 photomicrographs of polished thin sections from four drillholes were reviewed on the SEM (Table 6). These polished thin sections are taken from three prospect areas namely Kansoko Centrale, Kakula and Kansoko Sud. The samples are from mineralised zones of drillholes DKMC_DD571, DKMC_DD627, DKMC_DD952 and DKMC_DD1044.

Table 6: Polished thin sections analysed by SEM

Sample No.	Prospect	No. Samples
DKMC_DD571	Kansoko Centrale	8
DKMC_DD627	Kansoko Centrale	8
DKMC_DD952	Kansoko Sud	10
DKMC_DD1044	Kakula	7

4.6 Sulphur isotopes

The sulphur isotope systematics is widely used to determine the sulphur isotopic variations observed in the geological record and infer the sources of sulphur. This involves the measurement of the stable isotopes ^{32}S, ^{33}S, ^{34}S, and ^{36}S and subsequent interpretation of results to understand the sulphur cycle (Johnston, 2011). The measurement of sulphur isotopes provides a basis for understanding the depositional environment from the Archean to present day. The most abundant sulphur isotopes are ^{32}S and ^{34}S (Farquhar and Wing, 2003).

This method is applicable to the project area, with the objective of further understanding the genesis and evolution of sulphides within the Kamoa – Kakula deposit. Isotope ratio mass-spectrometry with laser-ablation (LA) sampling and fluorination was used for multiple S isotope analysis of sulphides in the Laboratory of Stable Isotopes of the Far East Geological Institute, Russian Academy of Sciences, Vladivostok (Velivetskaya et al., 2019). An ultraviolet femtosecond LA system (NWR Femtosecond UC with laser Pharos 2mJ-200-PP and harmonics module HE-4Hi-A) was used to produce a laser crater of 80 µm in diameter and 40 µm in depth. Laser-generated aerosol sulphide particles were converted to SF_6 (~12–13 nmol) via reaction with BrF_5 at 350°C. The SF_6 was purified by means of a cryogenic trap system and introduced into the ion source of a Thermo Scientific MAT 253 isotope ratio mass spectrometer using a gas injection interface. Sulphur isotope ratios were measured by monitoring masses 127 ($^{32}SF_5^+$), 128 ($^{33}SF_5^+$), 129 ($^{34}SF_5^+$), and 131($^{36}SF_5^+$). The results are presented in per mil on the Vienna Cañon Diablo Troilite (V-CDT) scale as per conventional notation:

$$\delta = (R_{sample} / R_{standard} - 1) \times 1000$$

where R_{sample} and $R_{standard}$ are S isotope ratios for a sample. A total of 110 discrete sulphide grains were analysed by Laser Ablation Isotope Ratio Mass Spectrometry (Table 7). Of the 110 analytical points, six points returned insufficient signal from the analysis due to hematite inclusions, with the remaining 104 analyses reported. No signals of mass-independent S isotope fractionation were detected during the analyses.

Table 7: Drillholes and number of samples analysed for sulphur isotope study

BHID	Prospect area	No. Samples	Not reported
DKMC_DD571	Kansoko Centrale	20	1
DKMC_DD624	Kansoko Centrale	21	1
DKMC_DD627	Kansoko Centrale	19	1
DKMC_DD956	Kansoko Sud	8	-
DKMC_DD1039	Kakula	10	-
DKMC_DD1044	Kakula	26	3

4.7 Geophysics – forward modelling

Geophysical forward modelling allows for the adjustment of model parameters by the interpreter until a representative model is produced graphically, whilst inverse modelling (inversion) relies on computed algorithms from a set of field parameters (Dentith and Mudge, 2014). During the modelling process, these techniques required a number of iterations, interpretation and knowledge of the subsurface, whilst the inversion process required less intervention by the interpreter than the forward modelling. Input parameters were applied, using knowledge of the lithologies and mineralisation present, the outputs were then reviewed and where applicable, inverse models produced. These were then analysed and parameters adjusted where appropriate and the process was repeated until as close to representative results were achieved (Fig. 21).

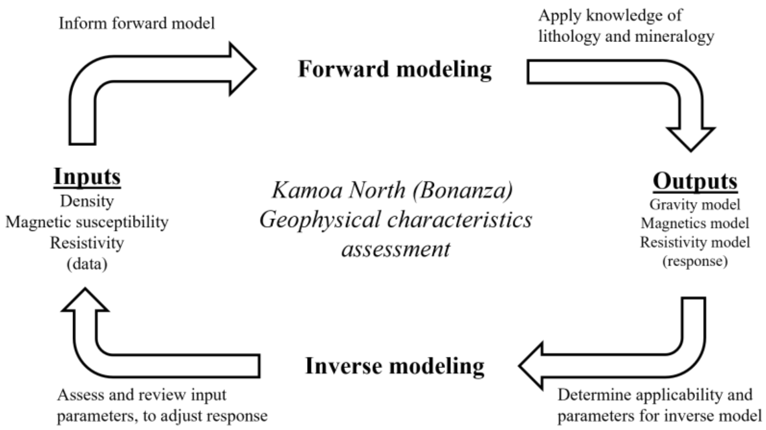

Figure 21: Compiled workflow of Kamoa North geophysical forward modelling applied in this study.

Drillholes from a section at Kamoa were selected for the purpose of forward modelling, to analyse the geophysical characteristics of sulphide mineralisation, selected based on the occurrence of sulphide mineralisation and appropriate host rocks. Five drillholes, from Section 306700 E (Kamoa north bonanza zone) were used for the forward modelling (Table 8). The process of forward modelling was applied to the gravity, magnetics and resistivity methods, using density data from Kamoa and reference magnetic susceptibility and resistivity values. These values were subsequently used to model the respective geophysical response in software packages Grav2dc v2.0, Mag2dc and Res2dMod v2.2 (software by Cooper, 1997).

Table 8: Drillholes used in the geophysical forward modelling study

BHID	Prospect	Section
DKMC_DD1450	Kamoa North - bonanza	306700 E
DKMC_DD1484	Kamoa North - bonanza	306700 E
DKMC_DD1491	Kamoa North - bonanza	306700 E
DKMC_DD1565	Kamoa North - bonanza	306700 E
DKMC_DD1571	Kamoa North - bonanza	306700 E

4.7.1 Gravity modelling

The principle of gravity forward modelling considers the gravitational field, in relation to a mass originating from a particular point, taking into account Newtons law of gravitation, related to the force between medium (F) being proportionate to the product of their mass (mM) and inverse to the square root of their distance (r):

$$F = G\frac{mM}{r^2}$$

where G = 6.67384 × 10^{-11} m^3 kg^{-1} s^{-2} is the universal gravitational constant (Hirt, 2016). The evaluation of gravity therefore relies on assessment of a body's mass – density distribution. The density measurements used for this study are from the aforementioned five drillholes. Density (specific gravity) measurements are taken at a frequency of every 1 m. These density values will be modelled in Grav2dc to produce a gravity forward model.

4.7.2 Magnetics modelling

The earths magnetic field is approximately 50,000 nT and variations of geological origin ordinarily do not exceed 10,000 nT, therefore variations due to magnetic minerals within the subsurface can be large (Dentith and Mudge, 2014). As these variations are uncommon, the magnetic susceptibility properties of rocks and minerals can be used to determine anomalous variations in the subsurface. Additionally, several types of magnetisation (absent of the geomagnetic field i.e., remnant magnetisation) may occur (Cooper, 1997).

The effect of magnetic material on the earths magnetic field can be modelled with the following equation:

$$M = \chi H = \chi(H_0 + H_s)$$

where the magnetic field (H) is present, along with the magnetisation (M), associated to a magnetic body (Lelièver and Oldenburg, 2006). Reference values of magnetic susceptibility of lithologies present, within drillholes on Section 306700 E, will be used. The main lithologies present in drillholes on the section modelled are, the middle diamictite (Ng1.1.3), Kamoa pyritic siltstone (Ng1.1.2), basal diamictite (Ng1.1.1) and Mwashya sandstone (R4.2). The magnetic susceptibility values will be used in Mag2dc to produce a magnetics forward model.

4.7.3 Resistivity modelling

The resistivity method is applied to understand the ability of the subsurface layers to allow current to flow through the various layers. Assuming these layers are horizontal, the resistivity of a body or material, (ρ), is a measure of how well the material retards the flow of current (Herman, 2001). This method uses this characteristic to determine the variability of resistivity or inversely, conductivity, within the subsurface. An artificial current is introduced to the subsurface, and electrodes measures the potentials, to determine the extent of current received (Telford et al., 1990). Resistivity is a function of ohms law (1), and the resistivity formulation of the current density (2), can be expressed as:

$$V = IR \qquad (1)$$

$$J = \sigma E = \frac{1}{\rho} E = -\frac{1}{p} \nabla V \qquad (2)$$

where J represents current density, E the electric field vector, V the electric potential, σ is the conductivity and the resistivity is represented by ρ (Herman, 2001). Reference resistivity values of the different lithologies present within drillholes on Section 306700 E (i.e., aforementioned Ng1.1.3, Ng1.1.2, Ng1.1.1 and R4.2 units) will be used and subsequently modelled in Res2dMod to produce a resistivity forward model.

4.8 Mineral systems approach

The mineral system approach will be used to evaluate the various components within this study. The mineral systems concept was developed to better understand the processes that influence the occurrence and distribution of ore deposits. The concept was initiated by previous workers such as Wyborn et al. in 1994, with improvements later made by Knox-Robinson and Wyborn in 1997. The concept was further developed by Hronsky and Groves (2008), which was further built upon by McCuaig and Hronsky (2014). Whilst the approach has been historically applied to the petroleum industry, the approach has become a widely accepted methodology for mineral deposit targeting (Groves et al., 2022). The definition of a mineral system can be considered as the integration, understanding and application of the geological components involved in the formation of mineral deposits initiating from development of ore bearing fluids from a source, through to the ore bearing fluid migration, accumulation and concentration (Wyborn et al., 1994). This can be attributed to the expression (and prediction) of the essential components of ore forming processes that occur at multiple spatial scales, driven by recognisable features from regional and local scale geoscientific datasets (McCuaig and Hronsky, 2014). These features can be represented by lithospheric architecture, tectonic triggers, district fertility, geochemical indicators, depositional sites and crustal level preservation (Occhipinti et al., 2016). Recognising and interpreting the indicators of ore forming processes is important, subsequently linking these to available datasets in order to create a hypothesis that can be tested, or to support the rationale for generation of additional data that may be needed in order to reach a decision point. The system places an emphasis on the process, rather than the genetic models. Several iterations of the approach have been made, underpinned by the view that ore forming processes can be analysed through a staged approach by reviewing characteristics of the source of metals and its transition from its source to form an ore deposit, this can be expressed by the ore endowment formula:

$$\text{ORE ENDOWMENT} = F \times A \times G \times P$$

where the source of metals or fertility is denoted (F), lithospheric architecture (A), the geodynamic setting (G) and the preservation (P), relating to the preservation of an economic ore deposit i.e., preservation from weathering and other geological processes (Megill, 1988; Groves et al., 2022). The way in which these components are configured, relate to the source of ore bearing fluids, lithospheric plumbing, tectonic evolution and setting, as well as post ore uplift, exhumation and potential cover sequences (Groves et al., 2022). The intersection of these components is where ore genesis occurs (Fig. 22). Whilst the petroleum and mineral system have similarities, components of the mineral system can be quite complex, requiring the presence of appropriate geodynamics, fertility, transient events, architecture and preservation (Fig. 23).

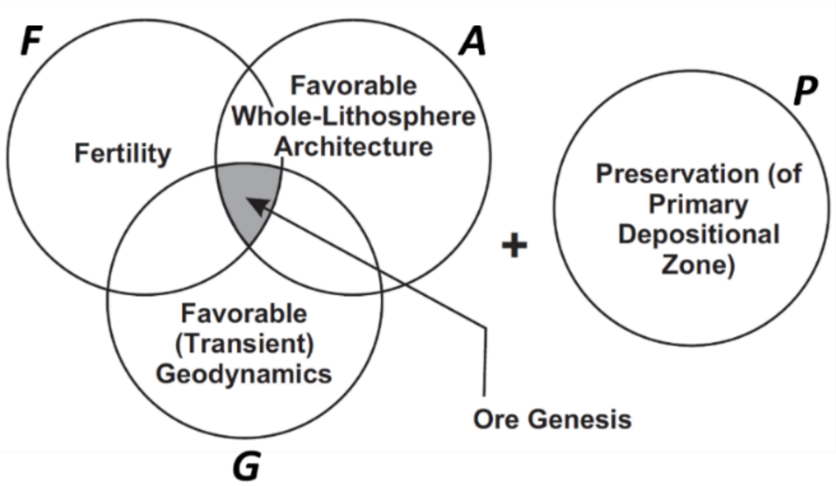

Figure 22: Mineral system components (McCuaig and Hronsky, 2014).

(a) PETROLEUM SYSTEM

(b) MINERAL SYSTEM

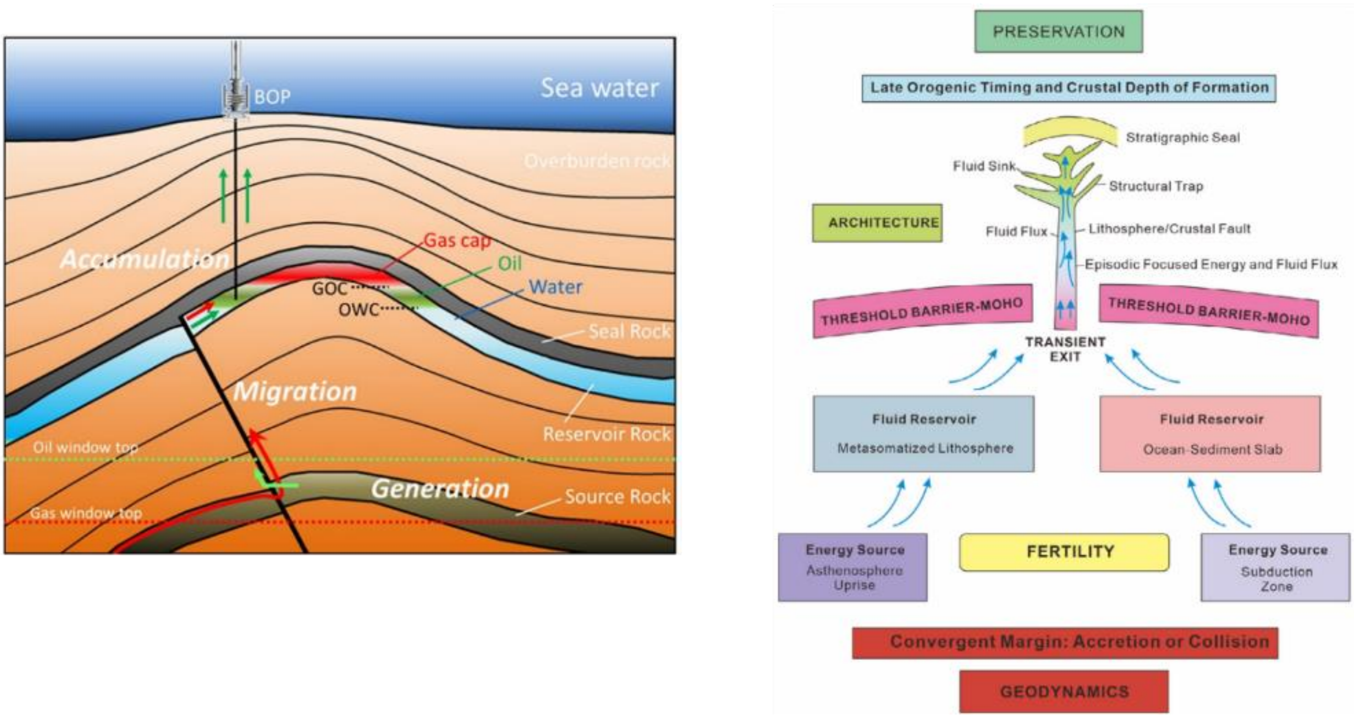

Figure 23: Mineral system framework; (a) petroleum system and (b) mineral system (JOGMEC, 2013; Groves et al., 2022).

Due to the tectonic history of the study area, this approach will be relevant during data integration and interpretation for this study. The rationale for using this approach is to better understand the structural framework (amongst other components), which may be crucial to ore forming processes that may exploit the presence of deep-seated structures, which could act as fluid conduits for metal-bearing oxidising brines. A schematic diagram (Fig. 24) illustrates the development of basement structures, emphasising the criticality of the recognition of vertical (or sub-vertical) accretionary structures in the lithosphere, that may not have very obvious surface expressions but are associated to mineral deposits (McCuaig and Hronsky, 2014). The development of such structures occurs over time and can have implications to ore bearing fluid migration and economic deposit formation.

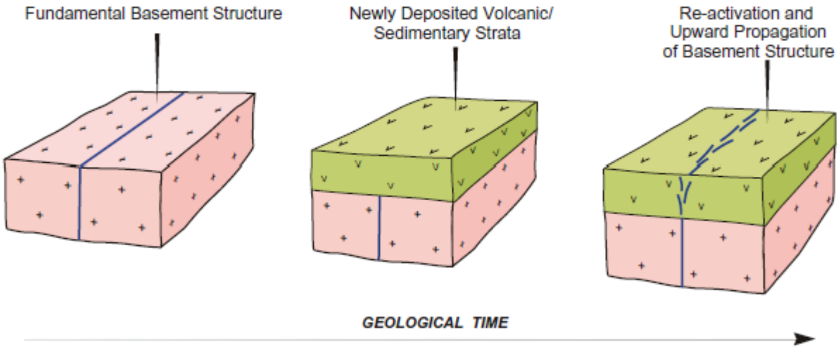

Figure 24: Development of basement structures over geological time (McCuaig and Hronsky, 2014).

5 RESULTS

The Kamoa – Kakula Mine lease is delineated into 13 prospect areas (Fig. 25). The drillholes that have been assessed are situated in four of the thirteen prospect areas (Table 9). A variety of methods and analyses have been carried out in this study in order to achieve the aims and objectives of the study. For regional geological context, a regional geological review making stratigraphic setting comparisons of ore deposits in the CACB in Zambia (ZCB) and DRC (CCB) has been conducted.

Table 9: Project drillholes

BHID	Project	Prospect
DKMC_DD1039	Kamoa - Kakula	Kakula
DKMC_DD1044	Kamoa - Kakula	Kakula
DKMC_DD571	Kamoa - Kakula	Kansoko Centrale
DKMC_DD624	Kamoa - Kakula	Kansoko Centrale
DKMC_DD627	Kamoa - Kakula	Kansoko Centrale
DKMC_DD1179	Kamoa - Kakula	Kakula West
DKMC_DD952	Kamoa - Kakula	Kansoko Sud
DKMC_DD956	Kamoa - Kakula	Kansoko Sud

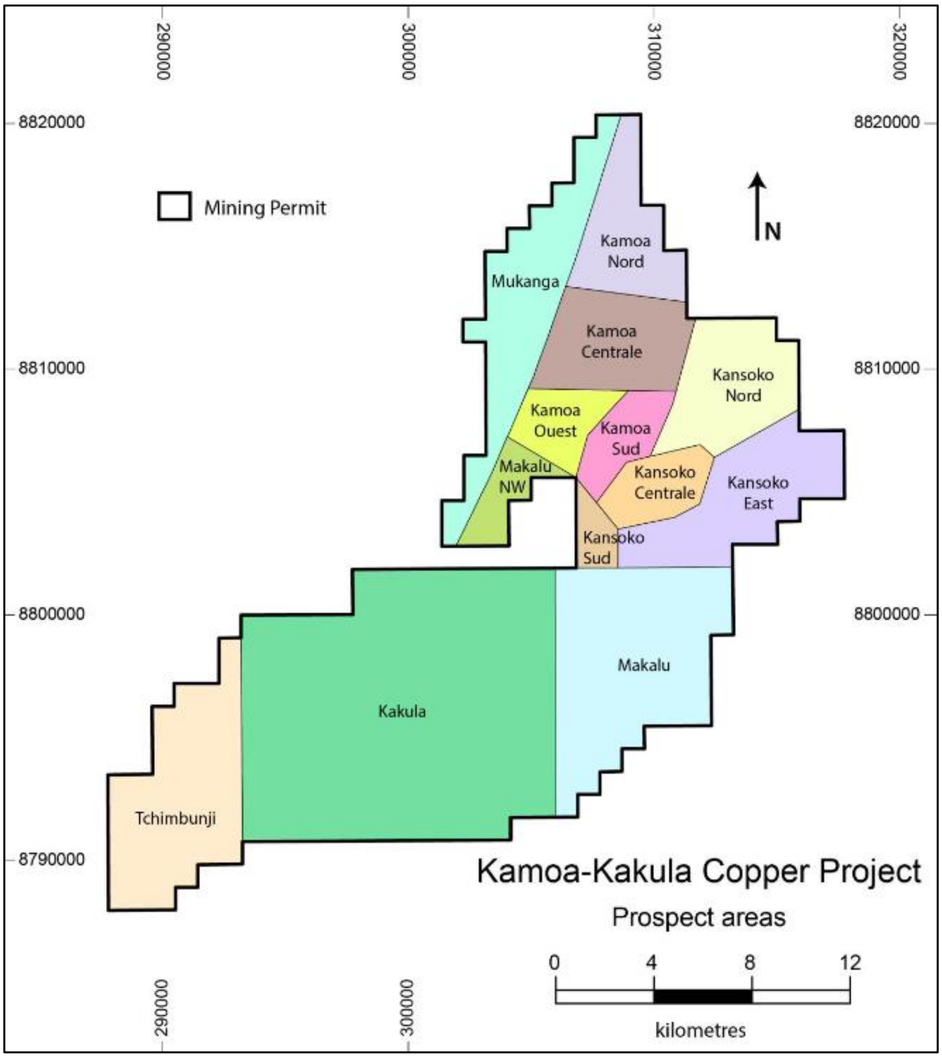

Figure 25: Location of Mining permit prospect areas at Kamoa – Kakula (OreWin, 2023).

5.1 Regional geological correlation

Regional geological correlation was carried out from the west of the Katanga basin, commencing at the study area (Kamoa – Kakula, DRC), through to the Lusale basin (Fishtie deposit, Zambia) in the eastern margin of the basin. A total of 17 ore deposits have been reviewed with respect to their location in the basin (Fig. 26) and a summary of the stratigraphic position of the host rocks was produced (Table 10). The location map shows the footprint of the Katanga basin and the location of the following deposits; (1,2) Kamoa – Kakula; DRC, (3) Kolwezi; DRC, (4) Tenke Fungurume; DRC, (5,6) Sentinel and Enterprise; Zambia (7) Lumwana; Zambia (8) Kansanshi; Zambia, (9) Kipushi; DRC and Zambia, (10) Lubambe; Zambia, (11) Chingola A & C; Zambia (12) Nchanga; Zambia, (13) Mufulira; Zambia (14) Frontier; DRC, (15) Lonshi; DRC, (16) Itawa; Zambia (17) Fishtie (Lusale sub-basin); Zambia.

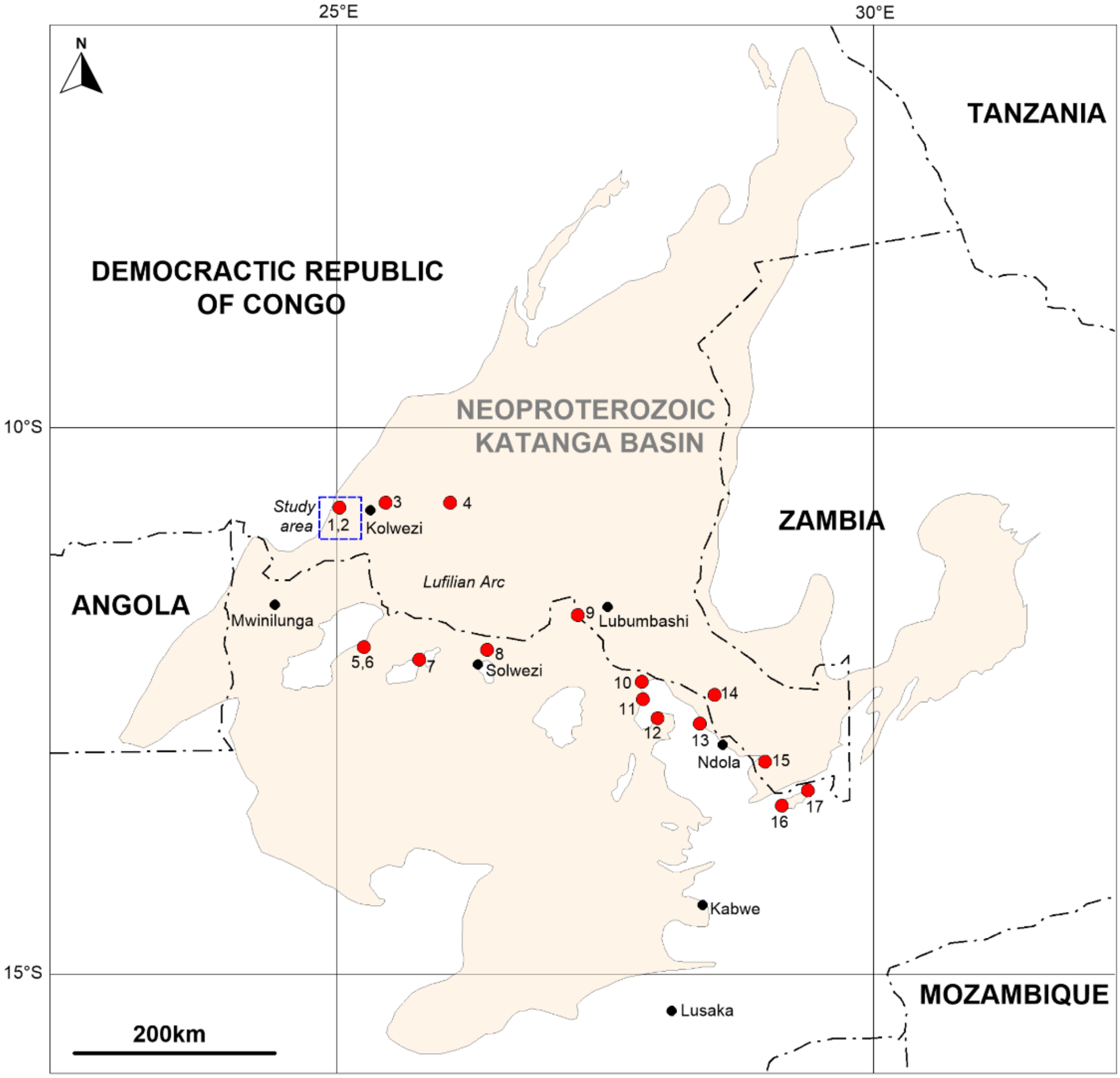

Figure 26: Plan map showing the location of copper deposits , part of the regional stratigraphic correlation study. This displays the location of CACB copper deposits reviewed for their copper ore deposit stratigraphic level, summarised by Table 10 (No. 1 to 17). Katanga basin outline modified after USGS Scientific Investigations report 2010–5090–T.

The selected deposits reviewed in the regional correlation are taken from both the Congolese Copperbelt (CCB) and Zambian Copperbelt (ZCB) across of the width of the Katanga basin. Mineralisation occurs at multiple levels of the CACB stratigraphy (Table 10; Fig. 27), with ore deposits observed in the lower parts of the CACB stratigraphy (i.e., Upper and Lower Roan) e.g., Nchanga, through to deposits in the Nguba group, e.g., Kamoa, Kansanshi.

Table 10: Deposits part of the NW-SE regional stratigraphic correlation from Kamoa-Kakula Cu deposit, this study (DRC – western Katanga basin margin) to Fishtie Cu deposit (Zambia – eastern Katanga basin margin). Literature sources contributing to geological and stratigraphic interpretation are indicated underneath this Table.

No.	Deposits	Location	Stratigraphic position of Host rocks
1	Kamoa - Kakula (Kitoko)	Western Foreland, CCB (basin-margin; west)	Grand Conglomérat Fm.
2	Kamoa - Kakula		
3	Kolwezi	Congolese Copperbelt	Kolwezi Klippe (Roan Group)
4	Tenke Fungurume		Mwashya and Upper Fungurume / Mine Series (Roan Group)
5	Sentinel	Domes Region, ZCB	Mwashya
6	Enterprise		Lower Roan
7	Lumwana		Basement (+ Lower Roan thrust sheets)
8	Kansanshi		Grand Conglomérat, Mwashya
9	Kipushi	CCB and ZCB	Grand Conglomérat Fm.
10	Lubambe	Zambian Copperbelt	Lower Roan
11	Chingola A & C		Lower Roan
12	Nchanga		Lower Roan
13	Mufulira (East Kafue anticline)		Upper and Lower Roan
14	Frontier	Congolese Copperbelt (basin-margin; east)	Mwashya / Upper part of the Upper Roan
15	Lonshi		Upper part of the Upper Roan (2003); Grand Conglomerat – Kaktontwe horizon (2012)
16	Itawa (DDHIT26)	Zambian Copperbelt (basin-margin; east)	Stratigraphy from Nguba to Mindola clastics Fm (observation of evaporites in the Upper Roan)
17	Fishtie (Lusale sub-basin)		Kakontwe - Grand Conglomérat transitional horizon

[1,2] Broughton and Rogers, (2010); Ivanhoe, (2023); This study (2024)

[3] Yantambwe and Cailteux, (2019)

[4] Schuh et al., (2012); Mambwe et al., (2017)

[5,10,12,12,13] Sillitoe et al., (2017)

[6] Capistrant et al., (2015)

[7] Bernau, (2007)

[8] Broughton et al., (2002); Hitzman et al., (2012); Broughton, (2014); MacIntyre, (2019)

[9] Batumike et al., (2007)

[14] Hitzman et al., (2012); Porter, (2015)

[15] Stephens and Newall (2003); Hitzman et al., (2012) Hendrickson et al., (2015);

[16] Bull et al., (2011); Broughton., (2014)

[17] Hendrickson et al., (2015)

The regional correlation within this study mainly focused on deposits in stratigraphic positions around the Lower Roan Group, Nguba Group and Mwashya Subgroup level, therefore occurrences above this level were not considered. It is important to mention that copper deposits can occur at higher stratigraphic levels within the Katangan stratigraphy. An example of this is the stratabound epigenetic Cu-Pb-Zn sulphide deposit, Dikulushi, which occurs in the Kiubo Fm, Ngule Subgroup of the Kundelungu Group (Kampunzu et al., 2009). Geochronology from volcanic breccia (Nguba Group) in Mwinilunga (Zambia) provides a SHRIMP U–Pb zircon age of 735 ± 5 Ma, pointing towards the Grand Conglomérat Fm. (diamictite) exhibiting a Sturtian glaciation association (Master and Wendorff, 2011). The Petit Conglomérat is likely the equivalent to the Ghaub diamictite and Maieberg Formation in the Otavi Group, Damara Orogen (Namibia) and is dated at 635.5 + 1.2 Ma, suggesting a Marinoan glaciation association (Hoffmann et al., 2004). The compiled stratigraphic column (Fig. 27) shows the regional stratigraphy hung from the Grand Conglomérat Fm. to illustrate the correlation between the Congolese Copperbelt (DRC) and Zambian Copperbelt (Zambia).

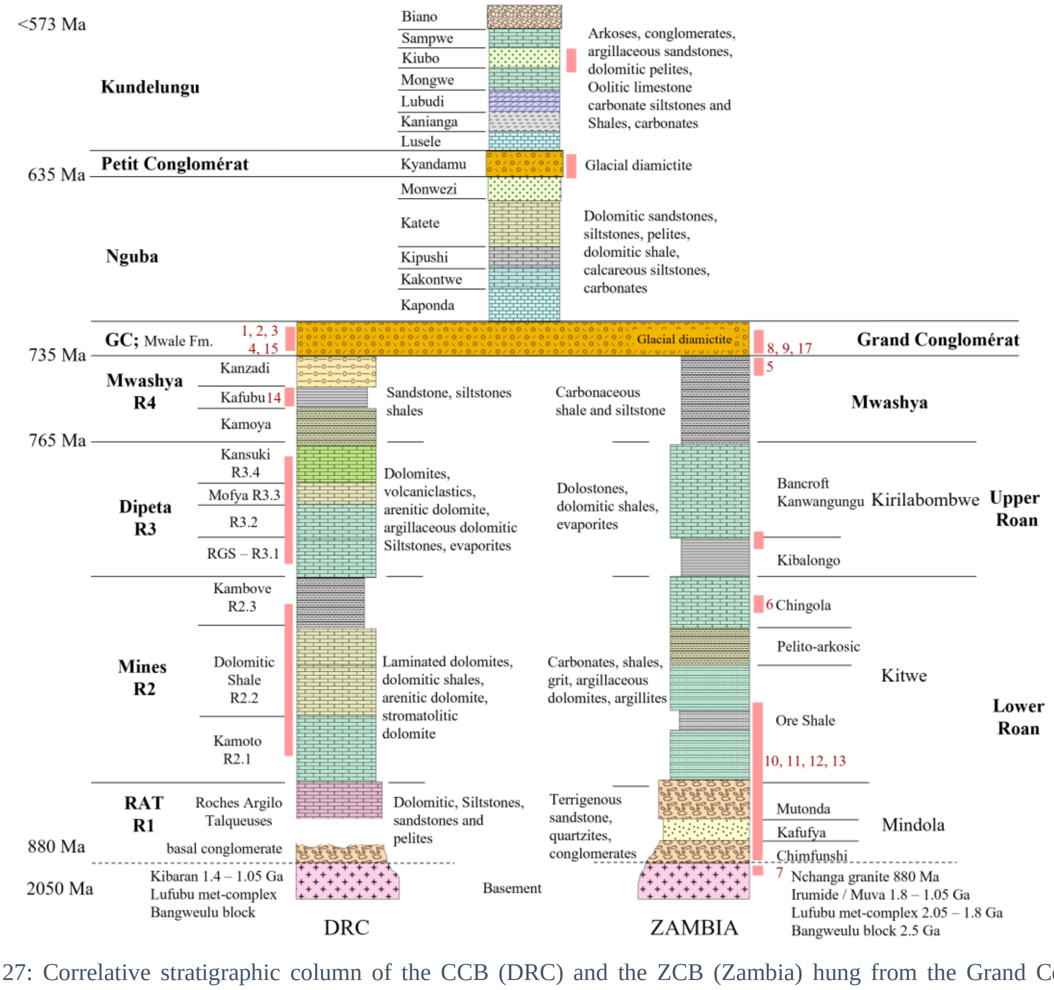

Figure 27: Correlative stratigraphic column of the CCB (DRC) and the ZCB (Zambia) hung from the Grand Conglomérat Fm. (glacial diamictite). Compiled from sources; François, 1973; Cailteux et al., 1994; Kampunzu and Cailteux, 1999; Batumike et al., 2007; Kampunzu et al., 2009; Hitzman et al., 2012; Selley et al., 2018. Age dates taken from Kampunzu et al., 2009; Hitzman et al., 2012; Porter, 2015. Stratigraphic positions of ore deposits (red bars with deposit number) indicated in Table 10 with sources cited.

5.2 Kamoa-Kakula stratigraphy

Extensive diamond core drilling has been conducted at the study area (Kamoa – Kakula) by Ivanhoe Mines, with a total of 2,260 drillholes (±764,000 metres) drilled as of July, 2023 (Ivanhoe Mines, 2023). This has well-constrained the local stratigraphic understanding. The Grand Conglomérat nomenclature is widely accepted as Ng1.1, whilst the underlying Mwashya sandstone is R4.2. Based on lithological characteristics, Ng1.1 is subdivided to Ng1.1.1 (basal diamictite) through to Ng1.1.6 (uppermost diamictite). The representation of this is shown by local (Kamoa) stratigraphic column (Fig. 28). Copper mineralisation in the Congolese Copperbelt is known to dominantly occur within the R2 (Mines-Subgroup) whilst mineralisation at Kamoa – Kakula occurs within the Nguba Group, in subdivisions of the basal diamictite, Ng.1.1.1. These mineralised subdivisions are Ng1.1.1.1; lower basal diamictite, Ng.1.1.1.2; intercalated siltstone / sandstone and Ng1.1.1.3; upper basal diamictite, as well as Ng1.1.2; lower laminated pyritic siltstone / sandstone. A total of eight drillholes were selected from Kakula, Kakula west, Kansoko centrale and Kansoko Sud with subsequent geological logging and sampling carried out, with results summarised in Fig. 29 to Fig. 35.

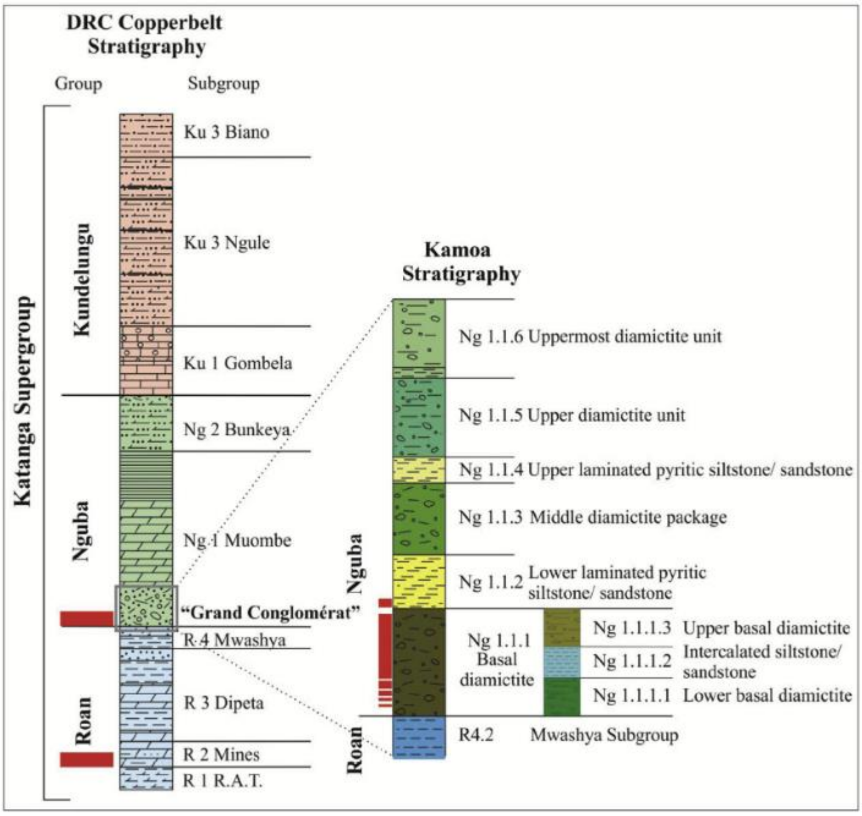

Figure 28: CCB stratigraphy and Kamoa stratigraphic column (Batumike et al., 2007; Twite et al., 2019).

5.2.1 Sandstone and Lower basal diamictite (R4.2 and Ng1.1.1.1)

The sandstone is the lowermost unit at the Kamoa deposit and is a medium-grained sandstone that is predominantly feldspathic, also containing quartz and mica. Occasional sparse pyrite is observed with minor amounts of laminated siltstone. The overlying basal diamictite is coarse-grained comprises 25 – 30% of poorly sorted subrounded to subangular quartz, shale and mafic clasts. This unit can occasionally have a greenish tinge.

Figure 29: Contact of R4.2 sandstone and lower basal diamictite from DKMC_DD627 at 500.00 m.

5.2.2 Intercalated siltstone (Ng1.1.1.2)

The intercalated siltstone is a fine-grained light to medium to dark, grey siltstone. Massive and occasionally weakly laminated, medium to coarse-grained sandstone interbeds of variable (cm – m) thicknesses occur within this unit. Disseminated sulphides are also observed within the intercalated siltstone, which is permissible, as the unit occurs within the mineralised zone at Kamoa – Kakula.

Figure 30: Intercalated siltstone and sandstone from DKMC_DD952 at 132.50 m.

5.2.3 Upper basal diamictite (Ng.1.1.1.3)

The upper basal diamictite is a medium- to coarse-grained, light to medium grey diamictite with silt and chlorite common within the matrix. It comprises 10 – 20% poorly sorted clasts of quartz and lithic fragments. Whilst the clasts are poorly sorted, they occasionally show weak alignment to bedding, which may reflect original conditions due to water reworking. The clasts within the basal diamictite are less densely distributed, in comparison to the lower basal diamictite.

Figure 31: Upper basal diamictite from DKMC_DD1039 at 221.00 m.

5.2.4 Lower laminated pyritic siltstone (Ng1.1.2)

The lower laminated pyritic siltstone is commonly referred to in local nomenclature as the 'Kamoa-Pyritic-Siltstone' or KPS. It is a fine grained, well laminated siltstone, with occasionally sandy layering. It has a higher pyrite content (10 – 25%), than adjacent lithologies. This pyrite can be disseminated but is dominantly distributed parallel to bedding.

Figure 32: Laminated pyritic siltstone from DKMC_DD1179 at 98.00 m.

5.2.5 Middle diamictite (Ng1.1.3)

The middle diamictite is a coarse-grained, medium to dark grey diamictite. The clast distribution is moderate to dense, comprising around 25 – 35 % of the whole rock with mm- to cm- scale angular to sub–angular shaley, dolomitic and mafic clasts. It has an argillaceous matrix, with occasional chlorite within the matrix. The clast proportion is greater than the proportion in the basal and upper basal diamictites. Finely disseminated pyrite can be observed within the matrix and close to the edges of clasts.

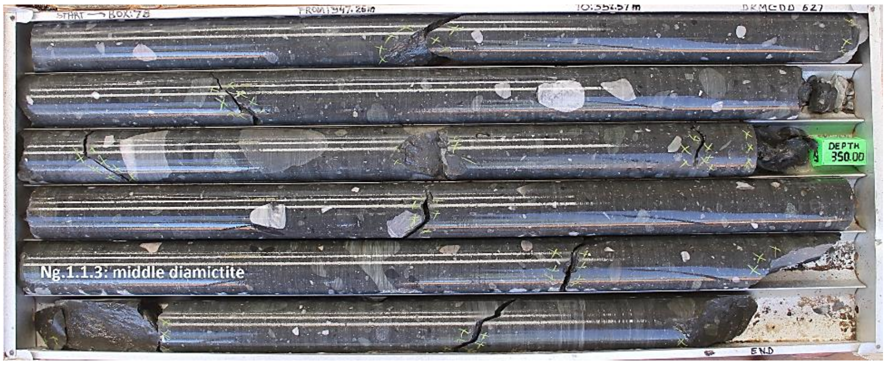

Figure 33: Middle diamictite from DKMC_DD627 at 350.00 m.

5.2.6 Upper laminated pyritic siltstone (Ng1.1.4)

The upper laminated pyritic siltstone is a fine-grained, well-laminated light to medium grey siltstone with occasional minor mm-scale clasts. There are occasional fine to medium sandy bands occurring at dense and occasionally sparse cm-scale intervals. Disseminated pyrite is common within this siltstone, estimated at 10 – 20%. Pyrite also occurs dominantly aligned to bedding, greatest at what appears to be reduced zones (dark grey intervals) within the unit. The unit is graded upward with the coarser parts of the unit occurring at its base.

Figure 34: Upper laminated pyritic siltstone and sandstone from DKMC_DD624 at 80.00 m.

5.2.7 Upper diamictite (Ng1.1.5)

The upper diamictite is a medium grained grey – green diamictite. It is clast poor, with clast distribution estimated to be around 10%. The clasts are sub-angular to close to rounded and there is a distinct increase in mafic clasts. Quartz clasts are commonly observed, as well as dolomitic clasts. Trace amounts of pyrite can be observed within the matrix, with some occurring at clast edges. The upper diamictite has distinctly lower density distribution of clasts in comparison to its counterparts, the lower basal, upper basal and middle diamictite.

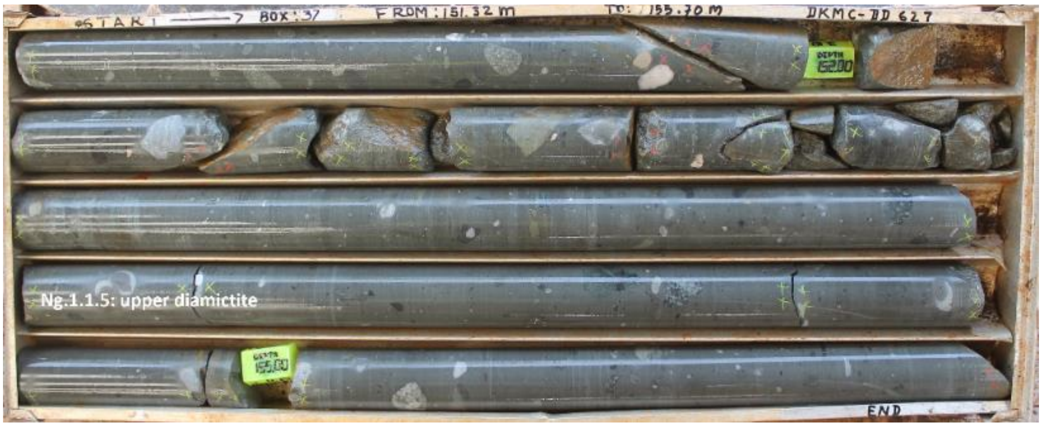

Figure 35: Upper diamictite from DKMC_DD627 at 152.00 m.

5.3 Underground mapping traverse

Kakula Mine is located in the southwest portion of the Kamoa Mine Lease (Fig. 36). The Kakula North decline provides access to the area in which the traverse was conducted. A traverse through the profile of the deposit was carried out and a summary of lithologies is provided (Fig. 37 and Table 11). The lithologies encountered (referred to according to Kakula Mine nomenclature) are the maroon diamictite (SDT2) overlying the massive siltstone (SSLMA), which sits directly about the laminated siltstone (SSLLA), separating this to the bottom parts of the sequence is a coarse breccia (SSLBX), followed by a pale green siltstone (SSLPG), which overlies the clast-rich diamictite (SSLPG). At a cut off of 2.5%TCu, the mineralised units are the SDT2, SSLMA, SSLLA, SSLBX and the top parts of the pale-green siltstone.

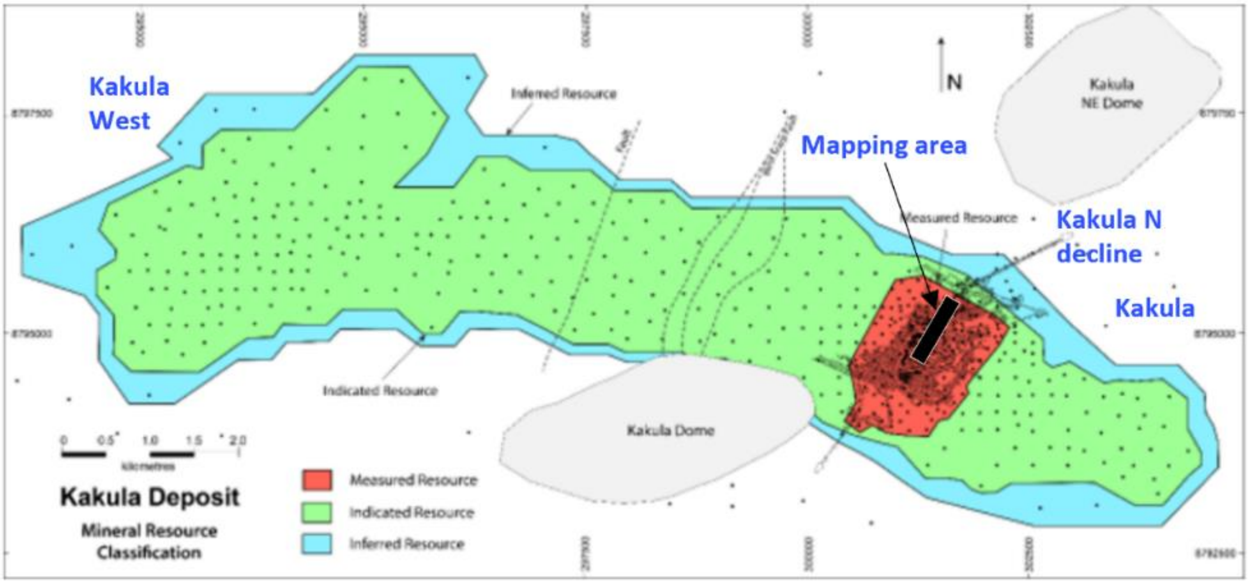

Figure 36: Location of Kakula Mine and Kakula N decline (Ivanhoe Mines, 2023).

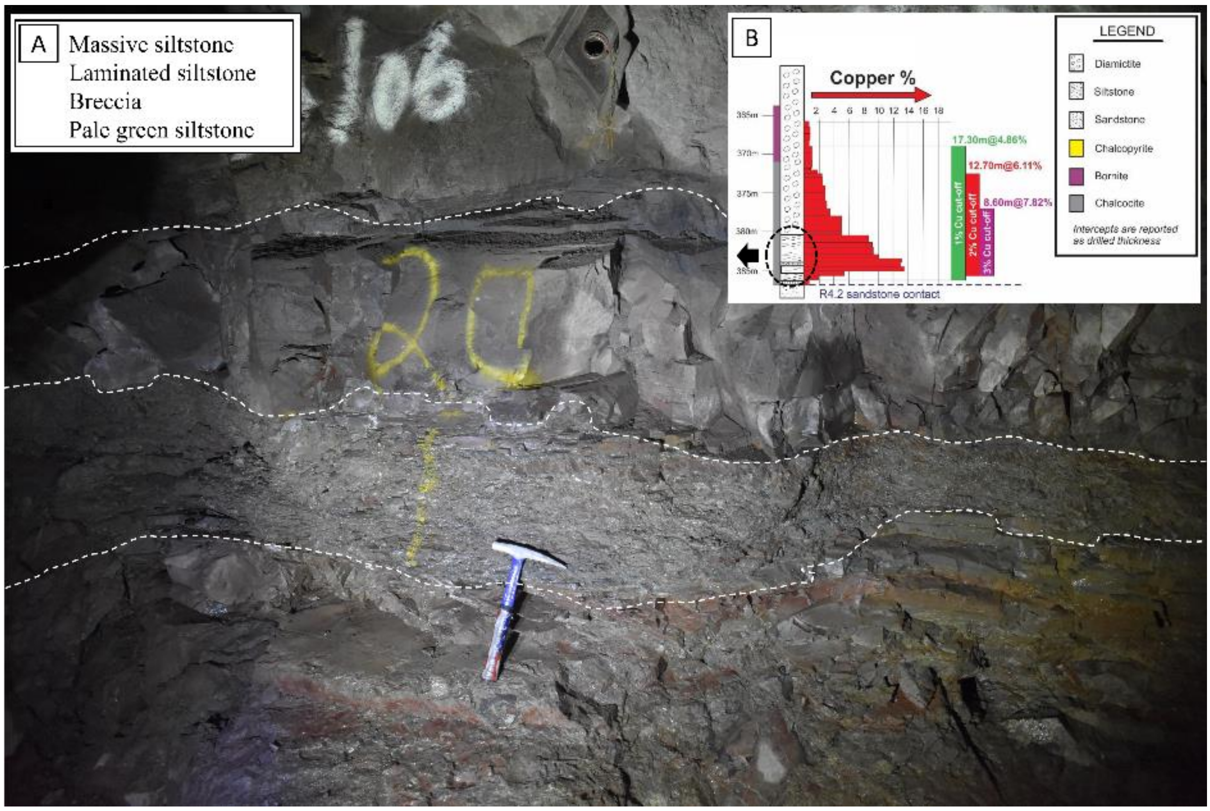

Figure 37: Photograph of underground profile at Kakula North decline, Kakula – taken during this study (A) From base; pale green siltstone, breccia, laminated siltstone, massive siltstone (B) Downhole log of representative borehole from Kakula illustrates that the high-grade interval of the package occurs within the siltstone sequences, proximal to the underlying R4.2 sandstone. Downhole log (B) taken from Ivanhoe Mines press release dated 8th September, (2019), cited in reference list.

Table 11: Representative underground samples from Kakula Mine; Kakula North decline (this study). Displayed in order of Kakula stratigraphy, from clast rich diamictite (SDT1) at the base of the sequence to overlying maroon diamictite (SDT2).

Sample	Description
	Maroon diamictite (SDT2): Medium to coarse grained, medium grey to maroon diamictite. Around 25 – 30% subangular to angular clasts of siltstone and occasional mafic clasts. Weak to moderate hematite alteration. Moderate copper mineralisation, in lesser amounts compared to underlying lithologies.
	Massive siltstone (SSLMA): Fine to medium grained, light to medium grey – green siltstone. Weakly bedded, massive with moderate to high copper mineralisation. Pervasive bands of mm – cm scale chalcocite stringer veinlets, creating a mesh network of chalcocite veinlets, weak chlorite alteration.
	Laminated siltstone, with conglomeritic bands (SSLLA): Fine grained, medium to light grey siltstone with occasional conglomeritic / breccia bands towards base. Conglomeritic / breccia bands contain angular to sub angular clasts predominantly of siltstone. Disseminated, parallel to bedding and clast-rim chalcocite mineralisation.
Breccia (SSLBX)	
	Pale green siltstone (SSLPG): Fine grained, medium to pale green siltstone. moderately to well mm scale bedded, with occasional dark grey to green bands aligned to bedding. Occasional crenulation of bedding. Weak to moderate mineralisation, increasing towards contact with overlying lithology.
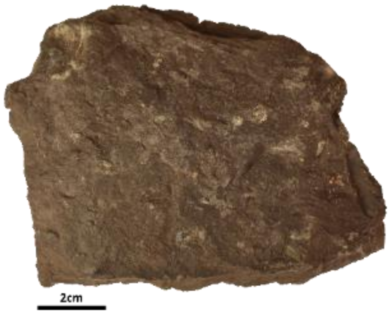	Clast rich diamictite (SDT1): Medium to coarse grained maroon-grey diamictite. Around 30% subangular to subrounded clasts, predominantly sandstone and quartz fragments. Occasional mafic clasts. Trace amounts of sub-economic chalcocite. Very weakly mineralised compared to overlying lithologies.

5.4 Petrography

5.4.1 Reflected light microscopy

Observations from photomicrographs in plane and cross-polarised reflected light of polished thin sections taken from borehole DKMC_DD1044, Kakula (Fig. 38 a - f) show a mineral assemblage that is predominantly bornite and chalcocite. The images are taken from the following lithologies and depths: (a) 319.20m, intercalated siltstone Ng1.1.1.2; (b) 336.40m, lower basal diamictite Ng1.1.1.1; (c) 343.70m, intercalated siltstone Ng1.1.1.2; (d) 322.70m, lower basal diamictite Ng1.1.1.1; (e) 343.70m, intercalated siltstone Ng1.1.1.2; and (f) 333.40m, lower basal diamictite Ng1.1.1.1. The photomicrographs shows: (a) bornite within the top part of the sample, with irregular edges, whilst chalcocite replacing bornite occurs in the bottom and right of the sample with equal proportions of bornite to chalcocite; (b) predominantly chalcocite replacing bornite in the central part of the sample (c) predominant chalcocite following a curvilinear orientation of host silicates (d) anhedral chalcopyrite intergrowing with euhedral to corroded pyrite (e) predominantly chalcocite, with smaller grains wrapping around the larger chalcocite grain (f) predominantly chalcocite (70%) with lesser amounts of bornite (30%), with relics preserved in the central parts of the chalcocite grains and in symplectites.

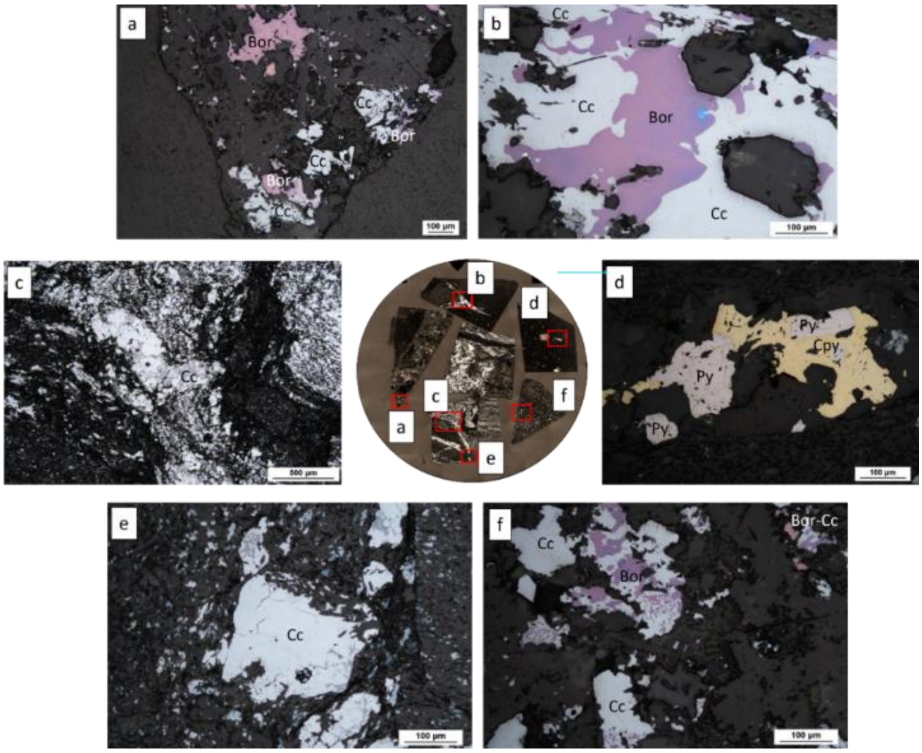

Figure 38: PP reflected light photomicrographs from DKMC_DD1044 at 319.20 m to 343.70 m.

Observations from photomicrographs in plane-polarised reflected light of a sample taken from the Kansoko Centrale prospect (Fig. 39 a - d) show a mineral assemblage that is predominantly composed of chalcopyrite and pyrite. Observations in the images are taken from the following drillholes and depths (a) DKMC_DD627; 474.70m, Ng1.1.2, lower laminated siltstone (b) DKMC_DD627; 488.80m, within Ng1.1.1.3, upper basal diamictite (c) DKMC_DD624; 288.50m within Ng1.1.2, lower laminated siltstone and (d) DKMC_DD627; 492.50m, within Ng1.1.1.3, upper basal diamictite. The Figure 39 shows (a) euhedral pyrite (nomenclature given: Py2) in the top part of the sample, surrounded by ball-like grains of framboidal pyrite (nomenclature given: Py1). Within groundmass of Py1 are occasional crystals of Py2; (b) grains of sub-rounded to anhedral chalcopyrite Cpy (100 µm x 150 µm) are in the top right of the sample, along with sub-rounded to euhedral pyrite (Py2) to the right of the sample, surrounded by rounded grains of pyrite (Py1); (c) euhedral crystals of pyrite (Py2) surrounded by framboidal grains of pyrite (Py1); (d) massive chalcopyriteCpy rimmed by subhedral pyrite (nomenclature; Py4) and euhedral carrollite (Car) crystals.

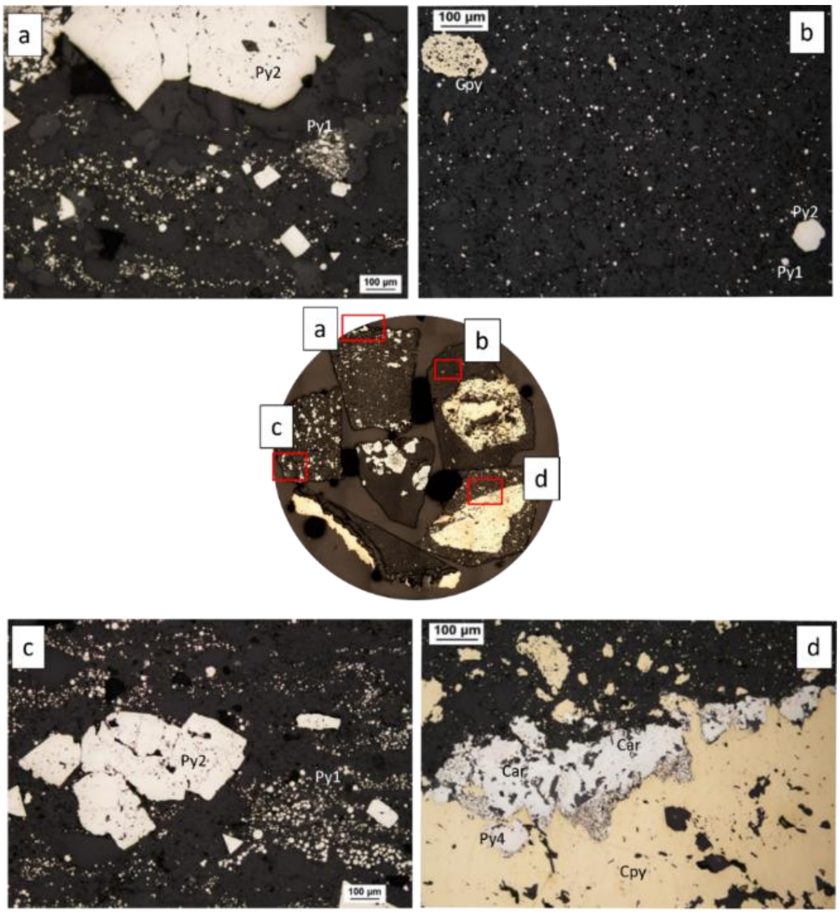

Figure 39: PP reflected light photomicrographs from DKMC_DD627 at (a) 474.70m, (b) 488.80m and (d) 492.50m and DKMC_DD624 (c) at 288.50m. Cpy – chalcopyrite, Py – pyrite, Car – carrollite.

5.4.2 SEM-BSE microscopy

Observations from SEM-BSE images of sample taken at 492.50 m within the upper basal diamictite (Ng1.1.1.3) in DKMC_DD627, Kansoko Centrale (Fig. 40 a - d) shows a mineral assemblage that is dominantly pyrite and chalcopyrite. The SEM-BSE image show (a) clast-like chalcopyrite grains with irregular margins floating in a chlorite-smectite-quartz matrix along with quartz clasts. The chalcopyrite grains have crude vertical alignment and envelopes of chlorite or silica and a relic pyrite inclusion is also visible in the central chalcopyrite grain; (b) chalcopyrite (as the main Cu-mineral) with both sharp and corroded margins of anhedral grains. Well-developed euhedral carrollite crystals (50 – 100 µm) contains multiple microinclusions of galena whereas pyrite is brecciated and partly replaced by fine-grained bladed chlorite; euhedral carrollite metacrystals contains inclusions of galena and silicate in image (c) with higher magnification sphalerite and xenotime occur in a quartz-chlorite-smectite (sericite) matrix; (d) anhedral chalcopyrite within a sericite-chlorite matrix with marcasite after decomposed pyrite. Grains of galena are included into a carrollite metacrystal whereas a chlorite needle crosscuts all sulphides.

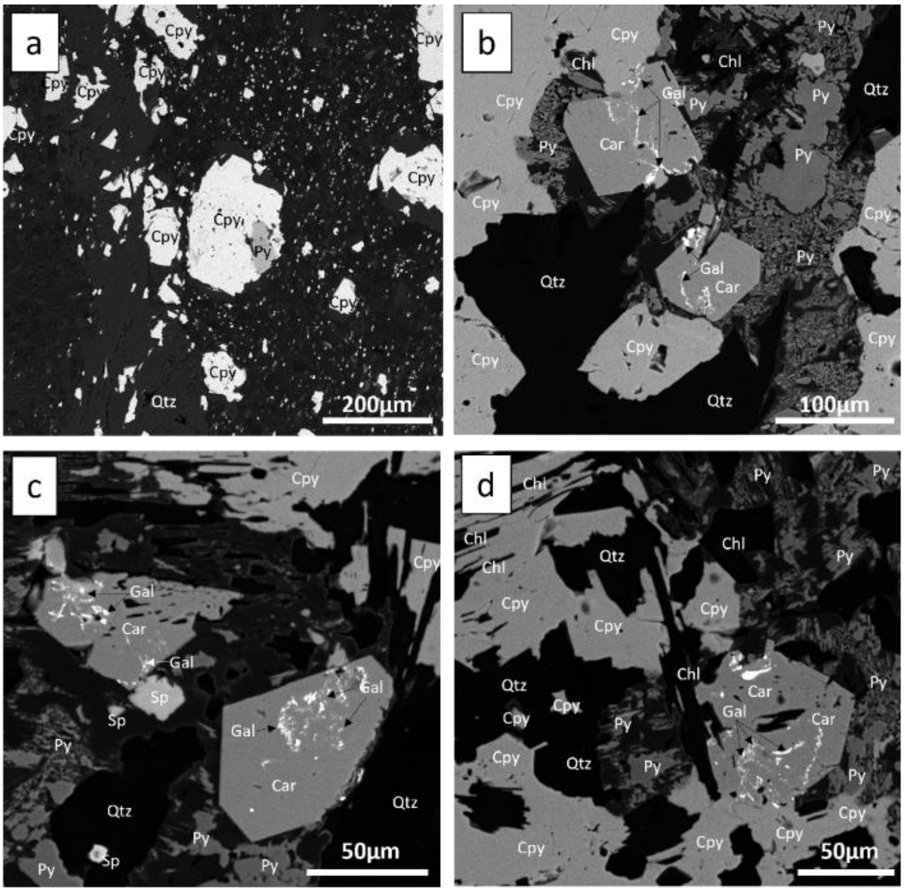

Figure 40: SEM-BSE photomicrographs from DKMC_DD627 at 492.50 m.

Observations from SEM-BSE images of a sample taken at 492.50 m within the upper basal diamictite (Ng1.1.1.3) in DKMC_DD627, Kansoko Centrale (Fig. 41 a - b) shows a mineral assemblage that is dominantly chalcopyrite in close proximity to monazite. Observations from image (a) shows silicate inclusion in chalcopyrite, which appears to be sitting within a smectite-chlorite matrix. An adjacent monazite grain exhibits distinct texture of late diagenetic growths with multiple silicate inclusions, which were trapped, and a very narrow discontinuous rim of metamorphic overgrowth. In the Fig. 41 b, a detrital monazite core (approximately 50 – 60 µm in diameter) is overgrown by a porous darker rim, which is, in turn, surrounded by a narrow discontinuous metamorphic rim of micro-crystals with euhedral faces.

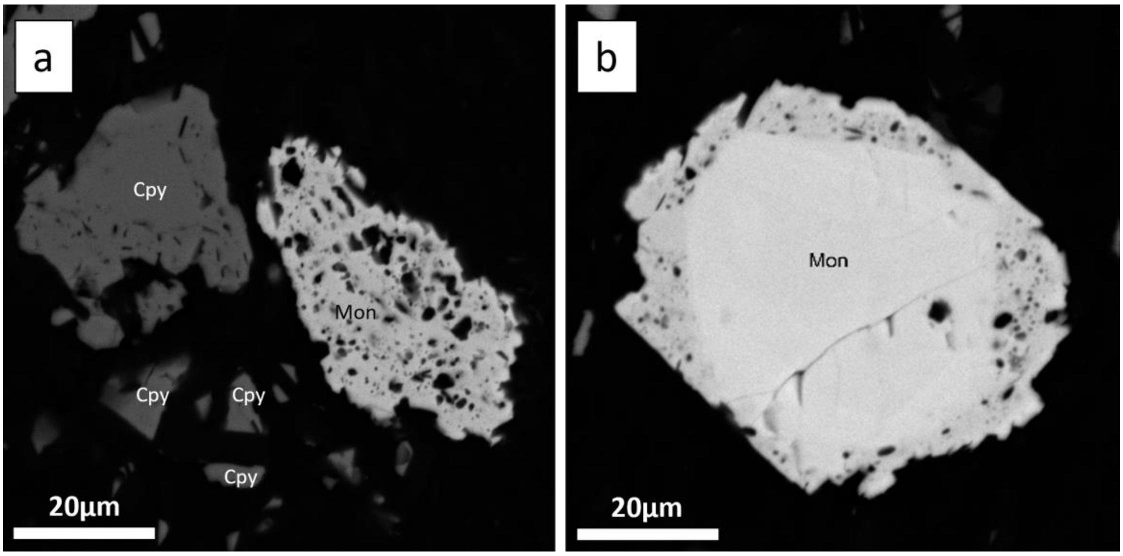

Figure 41: SEM-BSE photomicrographs from DKMC_DD627 at 492.50 m.

Observations from SEM-BSE images of a sample taken at 319.20m within the intercalated siltstone Ng1.1.1.2 in DKMC_DD1044, Kakula (Fig. 42 a - d) shows a mineral assemblage that is dominantly bornite and chalcocite. Observations from image; (a) exhibits the widespread development of symplectic texture of bornite and chalcocite intimate intergrowth; (b) at a scale of 50 µm, the section shows a symplectic texture within a bornite – chalcocite dominant association, there is also a strong corrosion at the margin of the original bornite grain; (c) is dominantly chalcocite and bornite in symplectic intergrowth (d) shows a central 100 µm x 250 µm grain of bornite replaced by symplectic intergrowths at the top and the bottom of the grain with homogeneous chalcocite in the right.

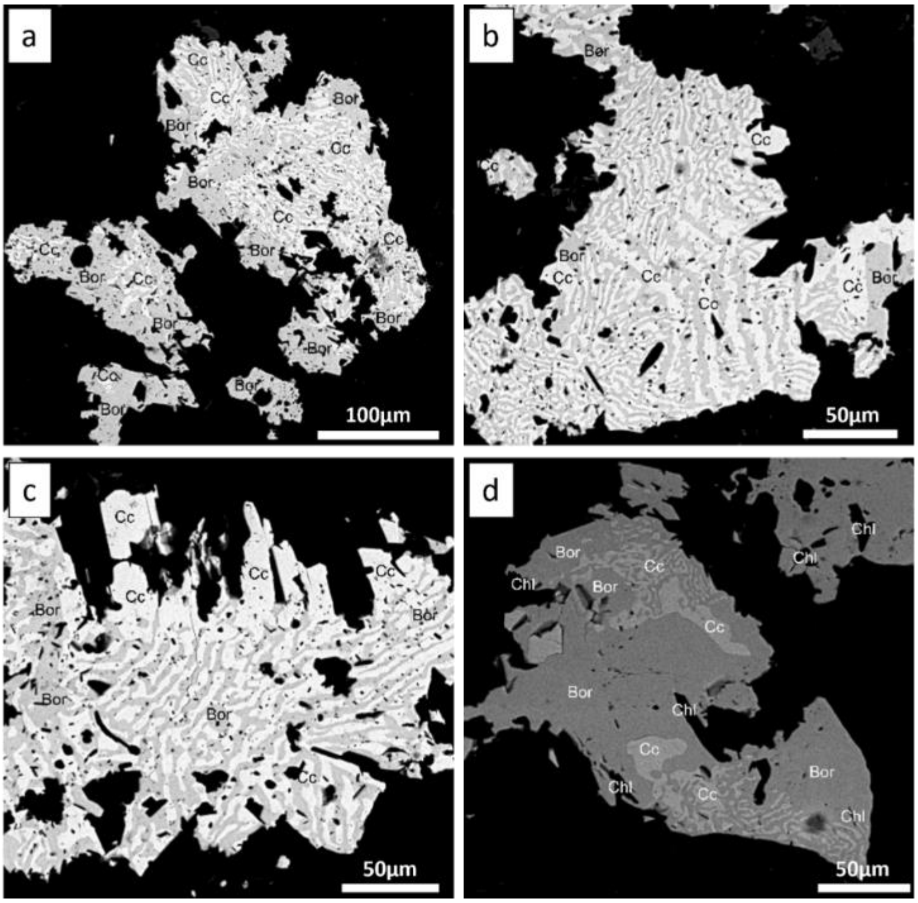

Figure 42: SEM-BSE photomicrographs from DKMC_DD1044 at 319.20 m.

5.5 Sulphur isotopes

The analysis of sulphur isotopes was conducted in order to determine a potential source of sulphur related to the genesis and evolution of sulphides within the Kamoa – Kakula deposit. A total of 104 reported results from in situ sulphide grains were obtained from the Far East Geological Institute, Russian Academy of Sciences, Vladivostok. Grains of four pyrite generations i.e., Py1, Py2, Py3, Py4, and chalcopyrite in the diamictite (Grand Conglomérat Fm.) were analysed along with bornite, chalcocite, covellite and cobaltite within the fine-grained siltstones, clast supported conglomerates, and matrix supported diamictites. The pyrite generations were recognised based on the observations in polished sections: Py1 – framboidal and sooty pyrite of the diagenetic origin; Py2 – recrystallised diagenetic pyrite in the inclusion-rich cores of euhedral crystals; Py3 – homogeneous euhedral crystals without inclusions and rims around the Py2 cores; Py4 – euhedral pyrite in an association with chalcopyrite. The results of these samples (Fig. 43 to Fig. 45) show a wide range of $\delta^{34}S$ values with the lowest observed from chalcocite (-35.1 ‰) in siltstone of DKMC_DD624

(Kansoko Centrale) and the highest from pyrite (22.4 ‰) in diamictite of DKMC_DD1044 (Kakula). Framboidal and sooty diagenetic Py1 shows a relatively narrow range of $\delta^{34}S$ values from -20 to -10 ‰, whereas Py2 show a wider range from -13 to 20 ‰. Euhedral pyrite without inclusion-rich cores (Py3) of the metamorphic rims, overgrowing the earlier generation of pyrite (Py2) with inclusion-rich cores, has $\delta^{34}S$ values like those of the related cores ranging from -10 to 22.4 ‰. Their overlapping values suggest their formation within the same stage of crystallisation, therefore, their values are shown in the same plot. The latest generation of pyrite (Py4) from the ore assemblage with chalcopyrite is characterised by 3 analytical points with two $\delta^{34}S$ values falling within a range of -8.1 to -14.4 ‰ and a single $\delta^{34}S$ value at 8.5 ‰.

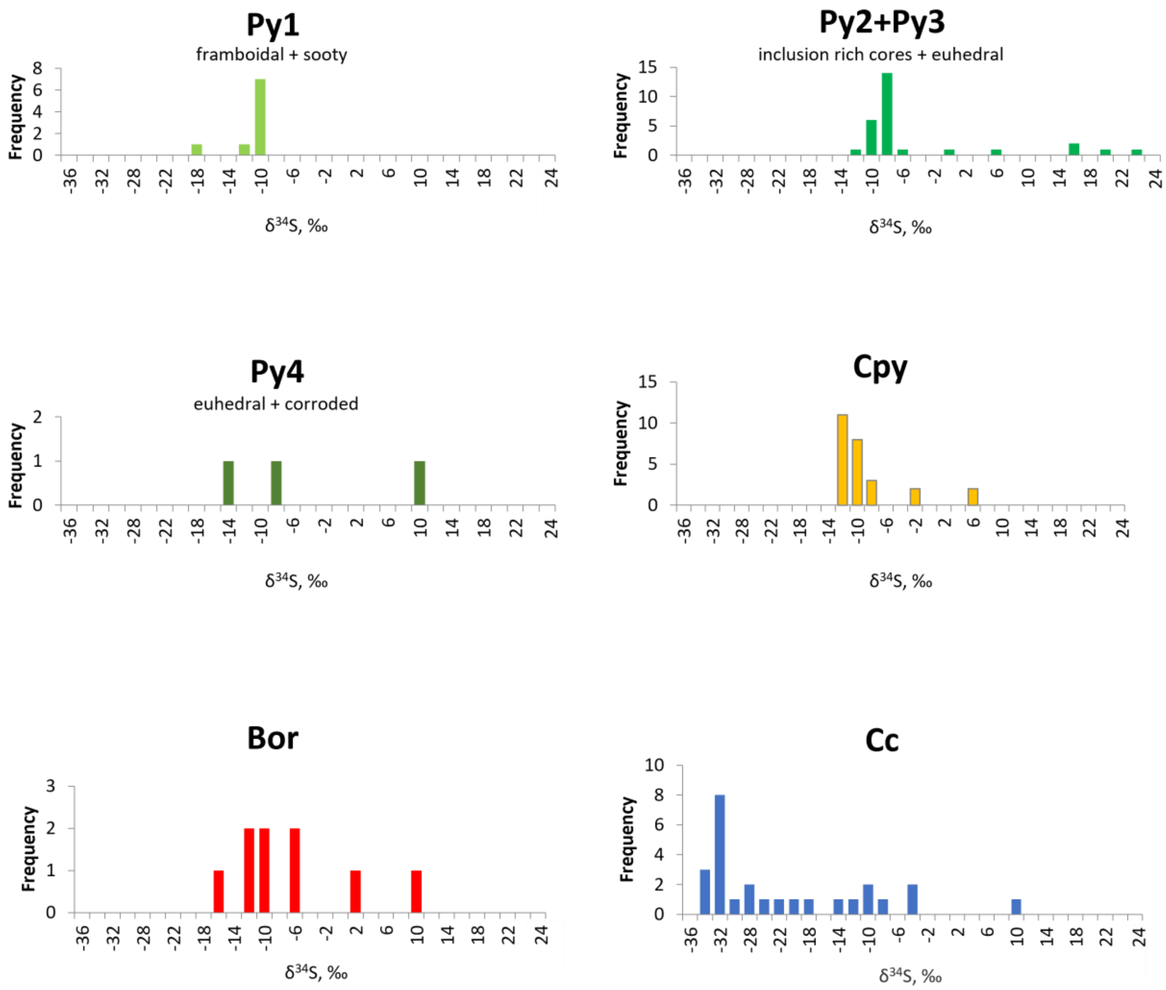

Figure 43: Frequency histograms of individual sulphide minerals $\delta^{34}S$ sulphur isotopic data. Samples of pyrite generations – Py1, Py2+Py3 and Py4, samples of chalcopyrite – Cpy, bornite – Bor and chalcocite – Cc.

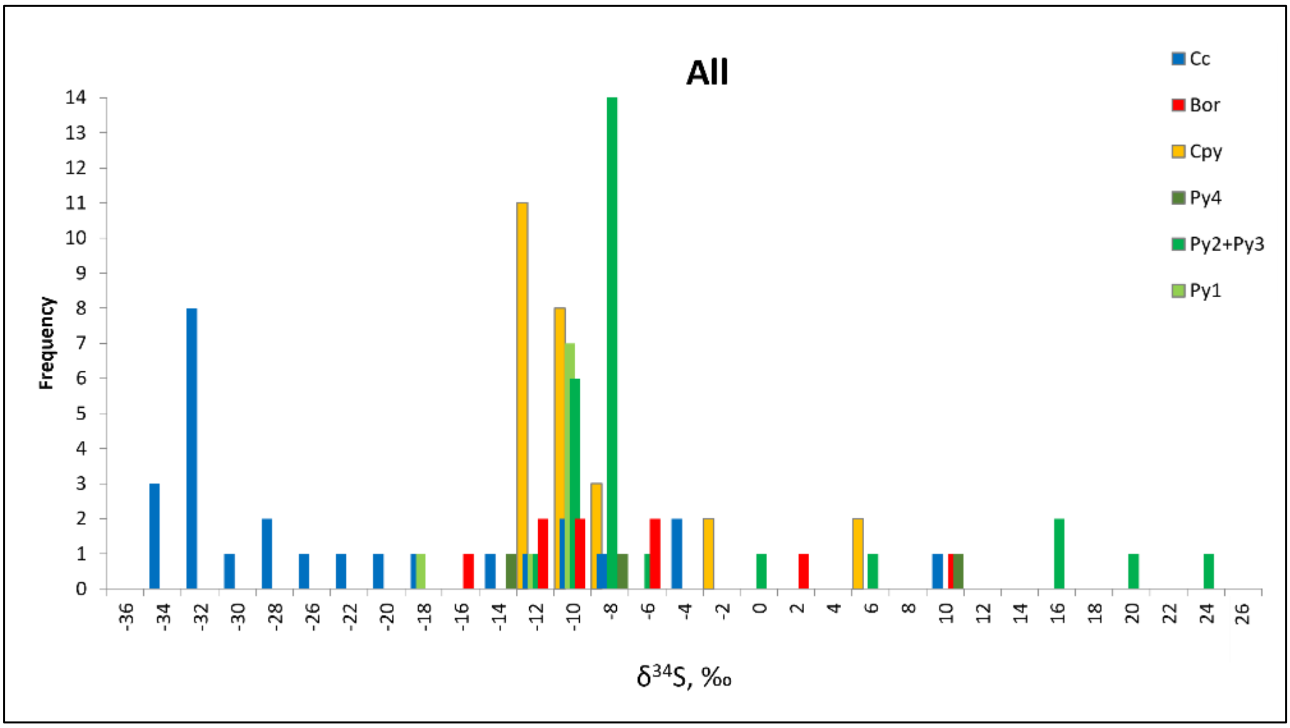

Figure 44: Frequency histogram of sulphide minerals δ^{34}S sulphur isotopic data (all samples). Samples of pyrite generations – Py1, Py2+Py3 and Py4, samples of chalcopyrite – Cpy, bornite – Bor and chalcocite – Cc.

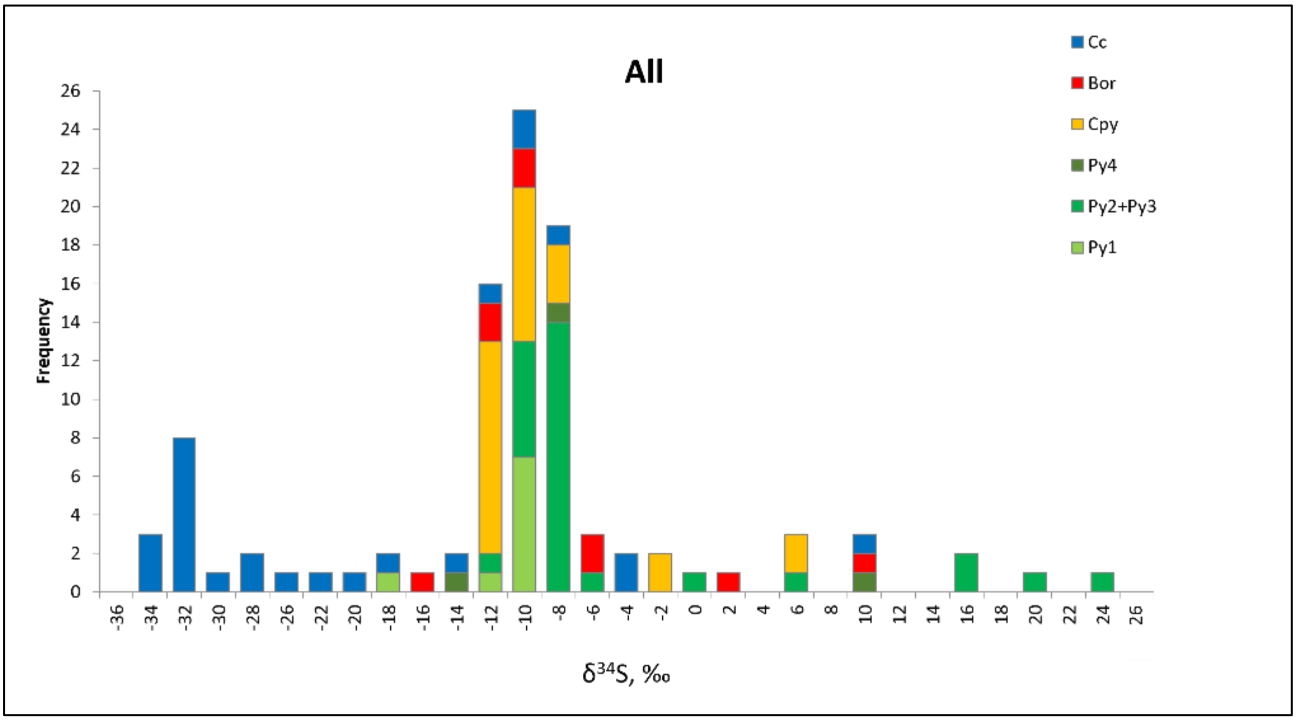

Figure 45: Frequency stacked histogram of sulphide minerals δ^{34}S sulphur isotopic data (all samples). Samples of pyrite generations – Py1, Py2+Py3 and Py4, samples with chalcopyrite – Cpy, bornite – Bor and chalcocite – Cc.

5.6 Geophysics

The local geology at Kamoa comprises of sedimentary sequences, mainly diamictite and siltstones (Grand Conglomérat Fm. of the Nguba Group) overlying an immature silty-sandstone, of the Mwashya Subgroup. Intercalated within the diamictite unit is a pyritic shale, also within the Grand Conglomérat. Drillholes from a selected N-S section (306700 E) taken from Kamoa North ('bonanza zone') have been used to review the geophysical characteristics of the lithologies and sulphide mineralisation (Fig. 46 and interpretative geological cross section in Fig. 47).

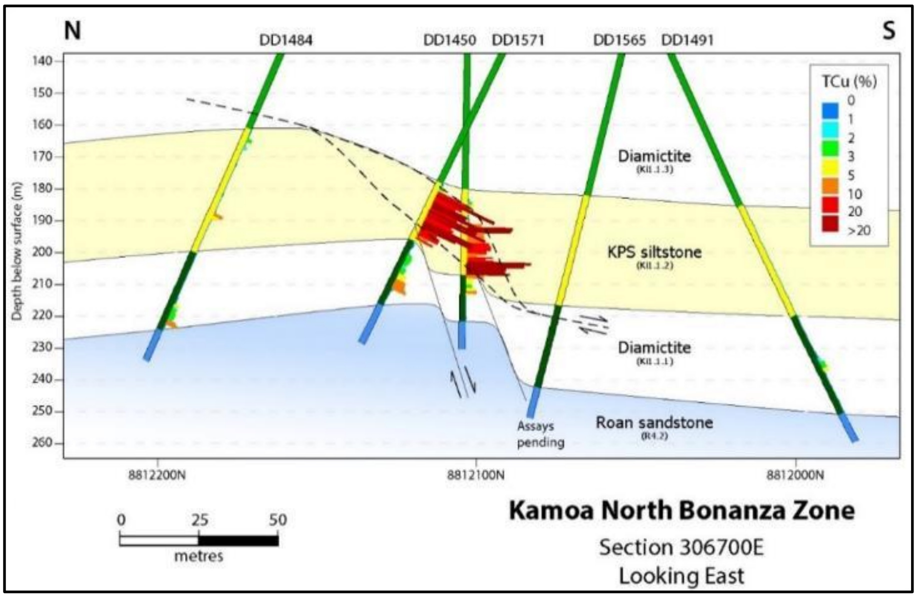

Figure 46: Kamoa North, bonanza zone, section (Ivanhoe Mines, 2021).

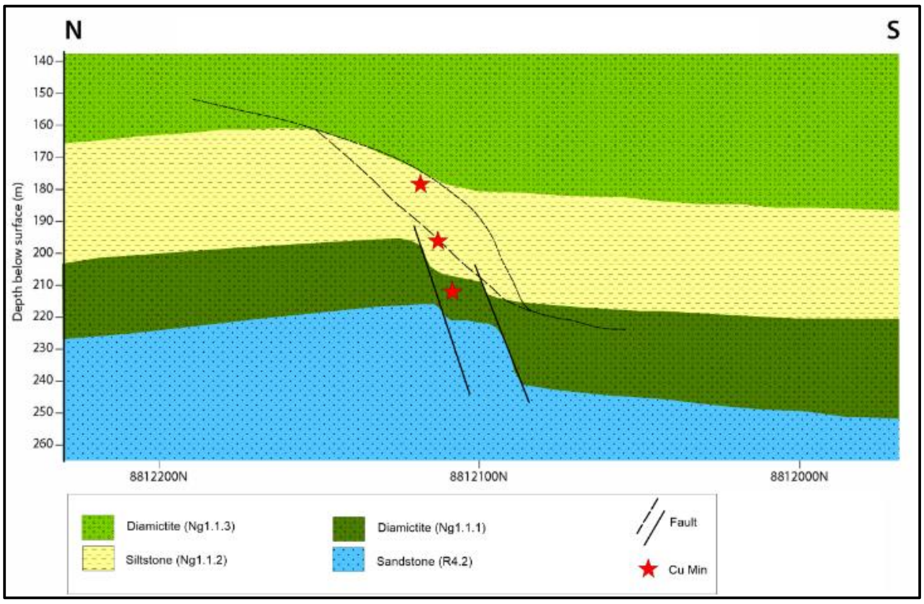

Figure 47: Geological cross-section interpretation of Kamoa north (bonanza zone), this study.

High-grade Cu mineralisation (> 10 % TCu) is observed within the KPS, with lesser amounts observed within the basal diamictite (> 2 % TCu). The sulphide mineralisation style is disseminated sulphide, as well as surrounding clasts (Fig. 48).

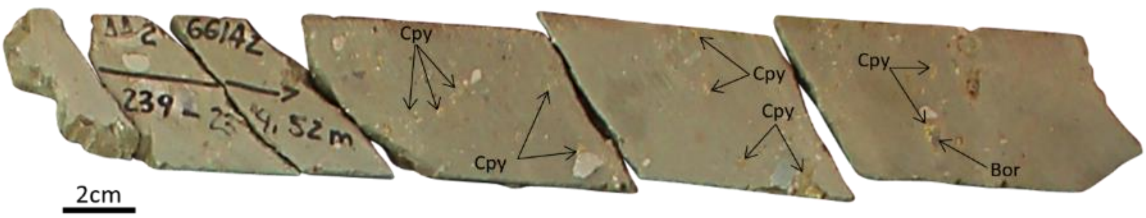

Figure 48: Core from mineralised intercept in DKMC_DD1571; 239.00m (Kamoa N). Cpy – chalcopyrite; Bor – bornite.

The measurements for specific gravity (SG) are taken at 1 m intervals throughout the mineralised intervals for the drillholes on section 306700 E Kamoa North. Using these downhole results from the SG measurements (Fig. 49), average density values were obtained. Also displayed is the downhole plots are TCu assay vertical histogram and downhole assays of Fe content (by pXRF analysis) within the mineralised zone. These average density values, along with reference values for magnetic susceptibility and resistivity (Table 12) were used to produce geophysical forward models.

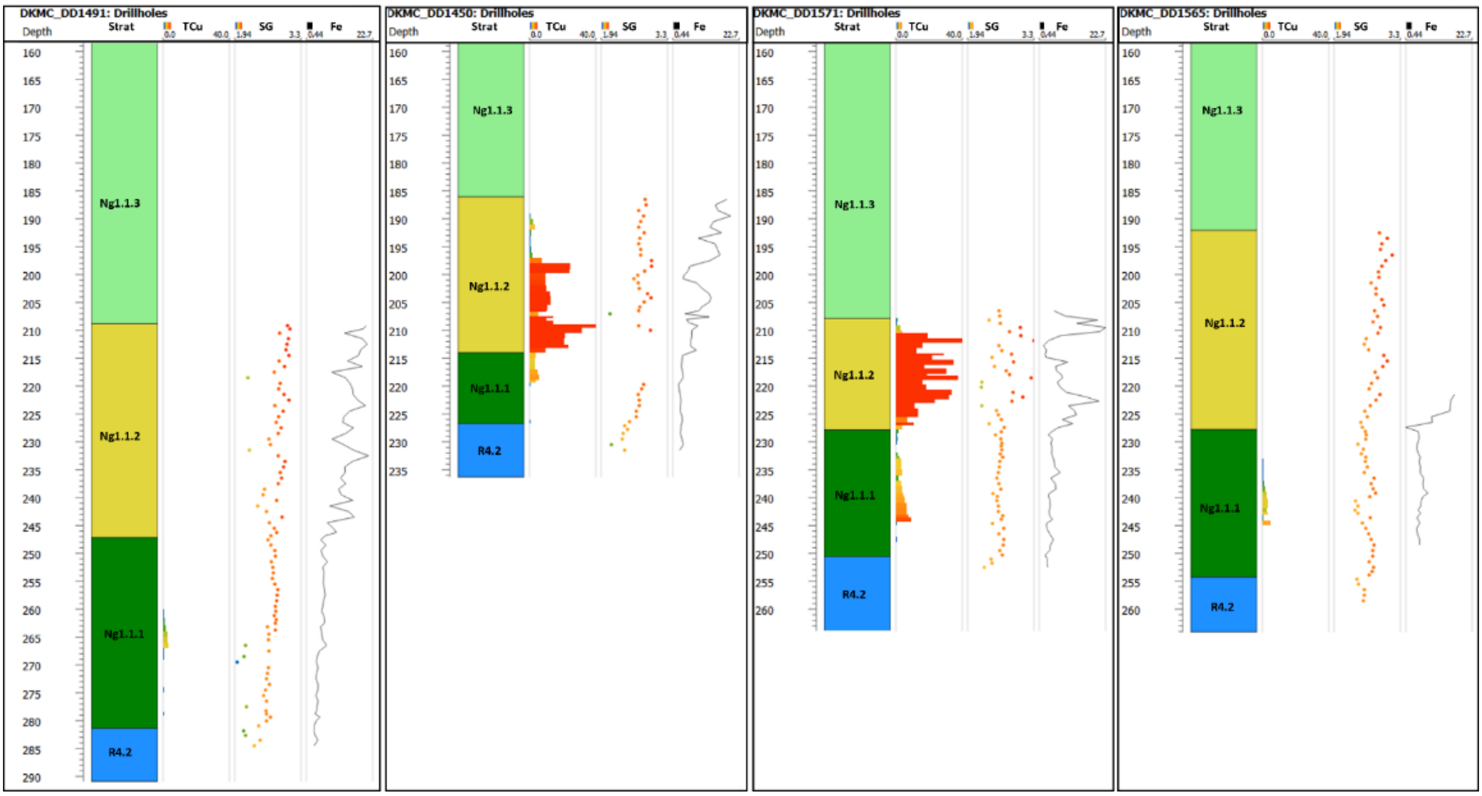

Figure 49: Downhole plots of TCu, SG and Fe at Kamoa N (bonanza zone).

Table 12: Lithological units and mineralised zone parameters - with forward model values

Lithology	Stratigraphy	Density (g/cm^3)[1]	Mag-susc (SI)[2]	Resistivity (Ω·m)[3]
Diamictite	Ng1.1.3	2.4	0.003	10,000
KPS - shale	Ng1.1.2	2.7	0.002	2,000
Diamictite	Ng1.1.1	2.5	0.003	10,000
Sandstone	R4.2	2.35	0.0009	4,000
Mineralised zone		3	0.3	0.3

[1]Average Kamoa N density values; Telford et al., (1990) [3] Abidin et al., 2011; Sucipta et al., (2019)

[2] Dentith and Mudge, (2014)

6 DISCUSSION

6.1 Zambia and DRC stratigraphy

6.1.1 Geological setting

The Neoproterozoic Central African Copperbelt is one of the largest Cu-Co provinces in the world. The source of mineralisation in the region remains debateable with the main contention revolving from syngenetic to diagenetic models as well as hydrothermal and diagenetic models (Cailteux et al., 2005). The process of economic ore body formation relies on the oxidised metal bearing fluids being transported by a conduit, through an aquifer, past a redox boundary through upper crustal levels to reduced horizons, triggering sulphide precipitation (Hitzman et al., 2010). These fluids are normally low to moderate temperature and moderate to highly saline ore bearing fluids (Hitzman et al., 2010). The long period of sedimentation (880 - 540Ma), forms the Katanga Supergroup of the Katanga basin. The Supergroup has a thickness of ~11 km, whilst the thickness on the edges of the basin are relatively thinner (Selley et al., 2018). The Katanga basin straddles the boundary between Zambia and DRC, therefore the stratiform Cu-Co deposits occur within the Zambian Copperbelt (ZCB) and Congolese Copperbelt (CCB). One of the key differences with the deposits of the CCB is the occurrence of breccias as a result of salt diapirism (halokinesis). The timing of the disruption of salt occurs around 765 – 735 Ma associated to extension and magmatism (Hitzman et al., 2012; Selley et al., 2018). The peak of orogenesis occurred around 530Ma, which is coincident with main stage mineralisation, which occurred at around 570 – 520Ma (Sillitoe et al., 2017). The results herein, through the aforementioned methodology, attempts to assess the geological differences and similarities in the regional context within the Central African Copperbelt and the nature and characteristics of sulphide mineralisation, with a focus on the Kamoa – Kakula copper deposit in the Democratic Republic of Congo.

6.1.2 Regional stratigraphic correlation (deposit 1 to deposit 17)

A series of deposits were identified for a regional geological correlation from the CCB to the ZCB. This takes into consideration the temporal position of mineral deposits in the region and the attributes associated to; the local and regional fertility of a particular domain, the intracratonic basin architecture, structural configuration, preservation potential and the hydrological basin characteristics. Despite facies variations, the clastic sedimentary sequences within the Katanga basin are known for their extensive lateral continuity. It is this characteristic that has been used to identify mappable stratigraphy to determine regional differences and similarities across the Katanga basin.

The Kamoa – Kakula and Kitoko deposits (Table 10: 1-2) are located proximal to the Western Foreland region and are stratiform sediment-hosted copper deposits occurring in the CACB fold and thrust belt structural domain of the CCB, DRC. At Kamoa – Kakula the geological setting of the deposit is characterised by underlying Mwashya Subgroup oxidised hematitic sandstone, overlain by a package of diamictite belonging to the 735 Ma Grand Conglomérat Fm. (Nguba Group), with mineralisation hosted in basal diamictite and interbedded siltstones (Broughton and Rogers, 2010). The main difference in the geological setting between the Kamoa – Kakula deposit and the Kitoko deposit, which both host copper mineralisation in the diamictite, is that the Grand Conglomérat Fm. at Kitoko unconformably overlies (and is in contact with) the Kibaran basement, as opposed to Mwashya Subgroup sandstone at Kamoa – Kakula (Ivanhoe, 2023). The Kolwezi district (Fig. 50 a; Table 10: 3) east of Kamoa – Kakula has been described as a series of thrust nappes, which are a result of compression during the Lufilian orogeny (François, 1973; Pirard and Hatert, 2008; Yantambwe and Cailteux, 2019). The structural complexities are a result of NE-SW verging thrust faults (Kansoko and Kansuki trends), affecting the stratigraphy (Twite, 2016; Yantambwe and Cailteux, 2019; Twite et al., 2019). Yantambwe and Cailteux (2019) further describe the area to be dominated by local occurrences of allochthonous megabreccias comprising Dipeta Subgroup (R-3) and Mines Subgroup (R-2) rocks, which host copper mineralisation, surrounded by younger lithologies such as Grand Conglomérat Fm. amongst others. These are understood to correlate to the Upper Roan, Zambia (to Dipeta) and Lower Roan - Kitwe Fm, Zambia (to Mines Series) respectively (François, 1973; Cailteux et al., 1994; Kampunzu and Cailteux, 1999; Batumike et al., 2007).

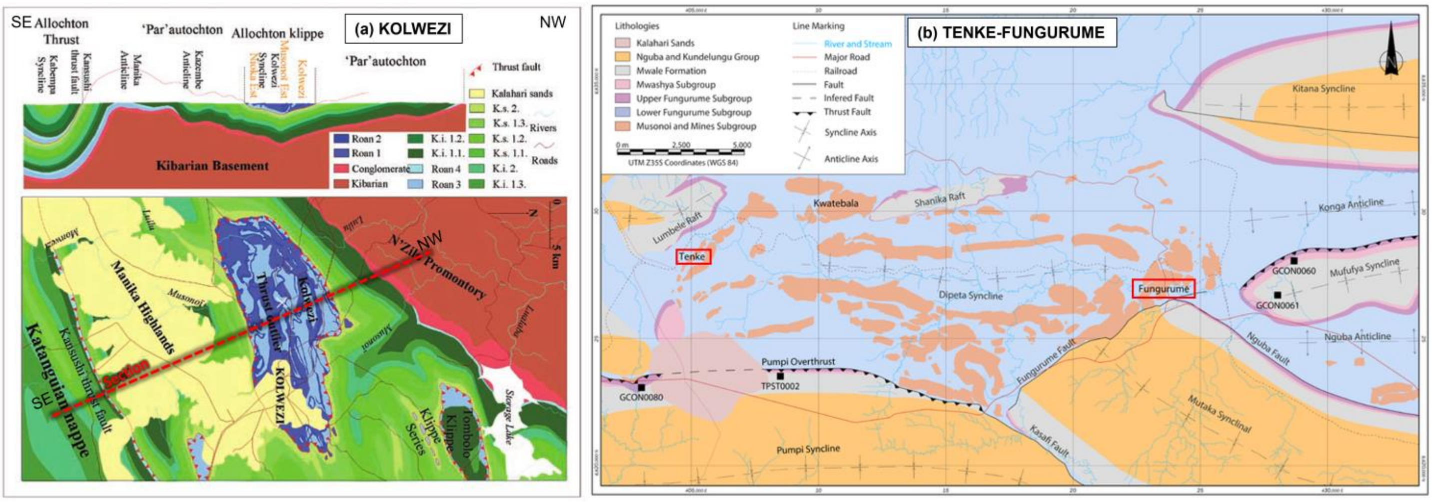

Figure 50: Geological map of the Congolese Copperbelt (a) Kolwezi area and (b) Tenke Fungurume area (Pirard and Hatert, 2008; Mambwe et al., 2020).

The Tenke Fungurume district, DRC (Fig. 50 b; Table 10: 4) is further east of Kolwezi and the tectonic setting of this sediment-hosted copper district has also been affected by structural deformation due to the Lufilian orogeny. This deformation (folding and thrusting / halokinesis, during the Lufilian) results in the formation of over 100 allochthonous blocks, with close to 15 of these blocks being mineralised within the Mines Series of the Roan Group (Schuh et al., 2012). The geological setting is similar to that of the Kolwezi district, with younger stratigraphic units (Kundelungu, Nguba and Roan Groups) surrounding the Mines Series Subgroup allochthons. This geological configuration is not common based on observations of the deposits reviewed in the ZCB. The regional tectonic evolution involves initial regional extension, further subsequent extension, followed by compression and basin inversion (Selley et al., 2005). The Domes region is a structural domain that forms during the north-directed deformation of the arcuate Lufilian arc and the Sentinel, Enterprise, Lumwana and Kansanshi (Table 10: 5-8) sediment- hosted copper-gold and nickel deposits occur within this domain. These deposits host mineralisation at different stratigraphic positions. The Sentinel Cu deposit is hosted within an intensely folded phyllite located at the edge of the Kobompo dome and is suggested to occur at the Upper Roan Group (Mwashya Subgroup) stratigraphic position, whilst the proximal hydrothermal Ni ± Cu Enterprise deposit occurs within metasedimentary rocks of the Lower Roan Group, at a lower stratigraphic position (Steven and Armstrong 2003; Capistrant et al., 2015; Hitzman et al., 2012). The Lumwana Cu (± Co, ± U) deposit is located on the Mwombezhi dome and is hosted within kyanite-bearing, amphibolite facies schist to gneisses (basement) that have been deformed by thrusting (Steven and Armstrong 2003; Bernau et al., 2013). Kansanshi Cu-Au deposit is a structure-controlled vein-hosted deposit, which is hosted by recumbently folded metasedimentary rocks at the base of the Nguba Group within formations metamorphosed to amphibolite facies (Broughton et al., 2002; Hitzman et al., 2012; MacIntyre, 2019). Whilst this stratigraphic level is similar to the setting at Kamoa, the Mwashya Subgroup (underlying the Grand Conglomérat) at Kansanshi comprises shale rather than sandstone and has a distinctly different structural configuration. The Kipushi Zn-Cu-Pb deposit, DRC and Zambia, (Table 10: 9) is located north of the Domes region, proximal to a NW-SE trending anticline and axial breccia (Grand Lambeau; Kiubo Fm). It is hosted within dolomitic argillites and shales of the Kakontwe, Kipushi and Katete (Serie Recurrent) Formations, which overlie the Kaponda Fm and Mwale Fm; Grand Conglomérat, Nguba Group (Kampunzu et al., 2009). This geological setting is close to to that at Kamoa, although it differs due to complex structural regime resulting in the emplacement of the axial breccia (fault breccia). Southeast of Kipushi are the ZCB deposits (Zambia): Lubambe, Chingola A& C, Nchanga and Mufulira (Table 10: 10-13). These deposits occur in the lower parts of the ZCB stratigraphy as described in the Section 5.1 (Fig. 27). Mineralisation is hosted within the basal conglomerate of the Lower Roan Group, with the exception of Mufulira, where mineralisation is hosted within dolostone of the Upper Roan Group, in addition to the basal conglomerate (Hitzman et al., 2012; Sillitoe et al., 2017). These deposits (10-13) are located stratigraphically lower than the Kamoa deposit. Frontier and Lonshi Cu deposits (Table 10: 14-15), east of the Kafue anticline, are hosted in the Mwashya Subgroup (shale) and at Lonshi, it is now presumed to be at the Grand Conglomérat (diamictite) level (Hitzman et al., 2012; Hendrickson et al., 2015). This is comparable to Kamoa, with the exception of the mineralisation occurring in the Mwashya Subgroup. Further east at the Itawa prospect (Table 10: 16) is the most complete stratigraphy proximal to Lusale sub-basin comprising Lower Roan basal conglomerate, upward to the Nguba Group, exhibiting rapid thickness changes and distinct evaporites in the Upper Roan (Bull et al., 2011). The Fishtie Cu deposit (Table 10: 17), Lusale sub-basin, hosts Cu mineralisation in carbonates of the Kakontwe Fm. and Grand Conglomérat, which overlie basement schists and quartzites (Hendrickson et al., 2015). The geological setting at Fishtie is similar to Kamoa and representative of the far eastern basin margin. The main difference is that quartzite underlies the Grand Conglomérat, as opposed to Mwashya sandstone, observed at this position at Kamoa. A schematic basin-scale interpretation from deposit (Table 10: 1) to deposit (Table 10: 17), shows lateral continuity of the CACB stratigraphy (Fig. 51) with subordinate lithological variations.

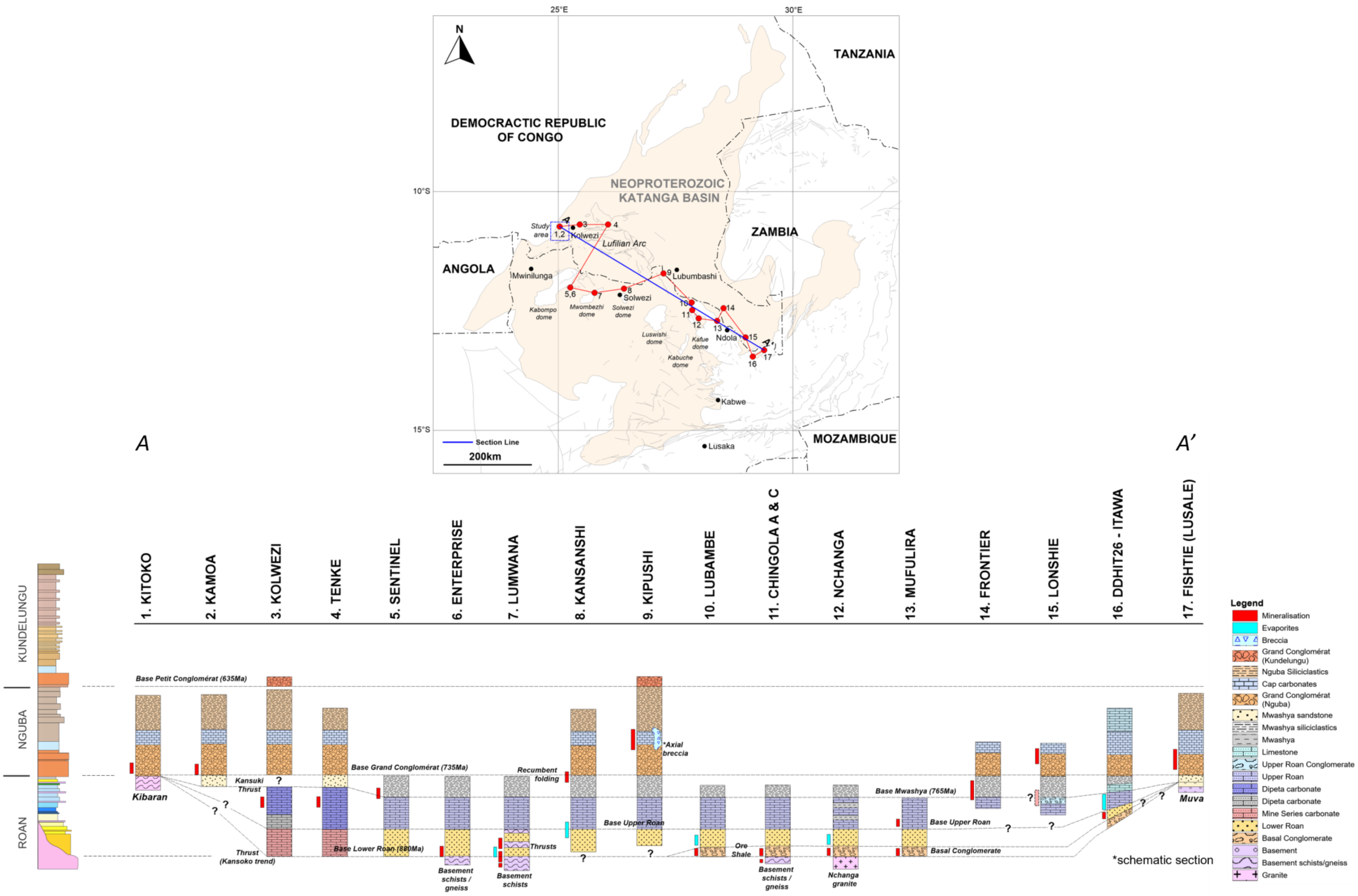

Figure 51: Katanga basin stratigraphic correlation section A – A' showing generalised deposit stratigraphy and position of mineralisation. From study area (Kamoa – Kakula Cu deposit, DRC) in the northwest i.e., deposit 1: Kitoko, which is in the Western Foreland of the Congolese Copperbelt (CCB), to the southeast at deposit 17: Fishtie Cu deposit, Zambia, which is in the Eastern Foreland of the Zambian Copperbelt (ZCB). This section has been compiled using observations and interpretation from the study area, as well as observations and interpretation from the sources that are cited underneath Table 10. The outline of the Katanga basin is modified after United States Geological Survey (USGS) Scientific Investigations report 2010–5090–T.

6.1.3 Grand Conglomérat Formation correlation

The Grand Conglomérat Formation is a geologically significant marker horizon and can host moderate to large-scale sediment hosted copper (SHC) deposits. This pan-glacial formation comprises poorly sorted, subrounded to subangular clasts and spans approximately 65,000 km^2 (Cahen, 1978; Batumike et al., 2007; Selley et al., 2018). The diamictite is made up of polymictic clasts of quartz, siltstone – shale, schists and granitic fragments (Master and Wendorff, 2011). Studies that have been conducted within the Katanga basin investigate the origin of the Grand Conglomérat Fm making regional comparisons from various locations, paying close attention to similarities and contrasting characteristics. Earlier studies correlate the debris flows and diamictites (Grand Conglomérat) to the Sturtian glaciation and relate this to the extensional breakup of the Rodinia (Hoffman, 1999). Whilst its glacial origin is supported by the distinct textures, spatial distribution, clast variability and age association to the Sturtian glaciogenic event, the processes involved have been a source of debate. Kennedy et al., (2019) suggests that whilst glaciation may have played an important role in sediment input to the Kamoa – Kakula area, the diamictite was further re-mobilised by mass-flow / sediment-slump processes.

From geological drill core logging conducted in this study, the nature and composition of the clasts within the diamictite (Grand Conglomérat) of the study area appears to be polymictic. This is observed from clast fragments and dropstones in the diamictite comprising quartz, mafic and lithic clasts and fragments, that are commonly subrounded to subangular (Fig. 52 A). Approximately 200 km SE of the study area, in the Domes region of the ZCB, is the Kansanshi Cu-Au deposit where sub-rounded to subangular clasts within Grand Conglomérat are composed of dominantly quartz, dolomite as well as argillaceous and granitic rocks (Broughton et al., 2002; MacIntyre, 2019). This varies from the Kamoa – Kakula area, as the morphology of the clasts at the Kansanshi Cu-Au deposit are elongated (Fig. 52 B). This comes as a result of regional deformation during the Lufilian orogeny associated to north directed thrusting and local kilometric scale recumbent folding (Broughton et al., 2002; Selley et al., 2005). Diamictite studied at the Fishtie deposit (~400 km SW of Kansanshi) revealed subrounded to subangular quartz, mafic, carbonate and lithic fragments with no preferred orientation (Fig. 52 C-D) (Hendrickson, 2013; Simusokwe, 2021), which is similar to Kamoa diamictite. These observations favour close correlation of the diamictite (Grand Conglomérat Fm) observed at Kamoa – Kakula in the western margin of the Katanga basin, with that at the Fishtie deposit at the eastern margin (Fig. 52 A to D).

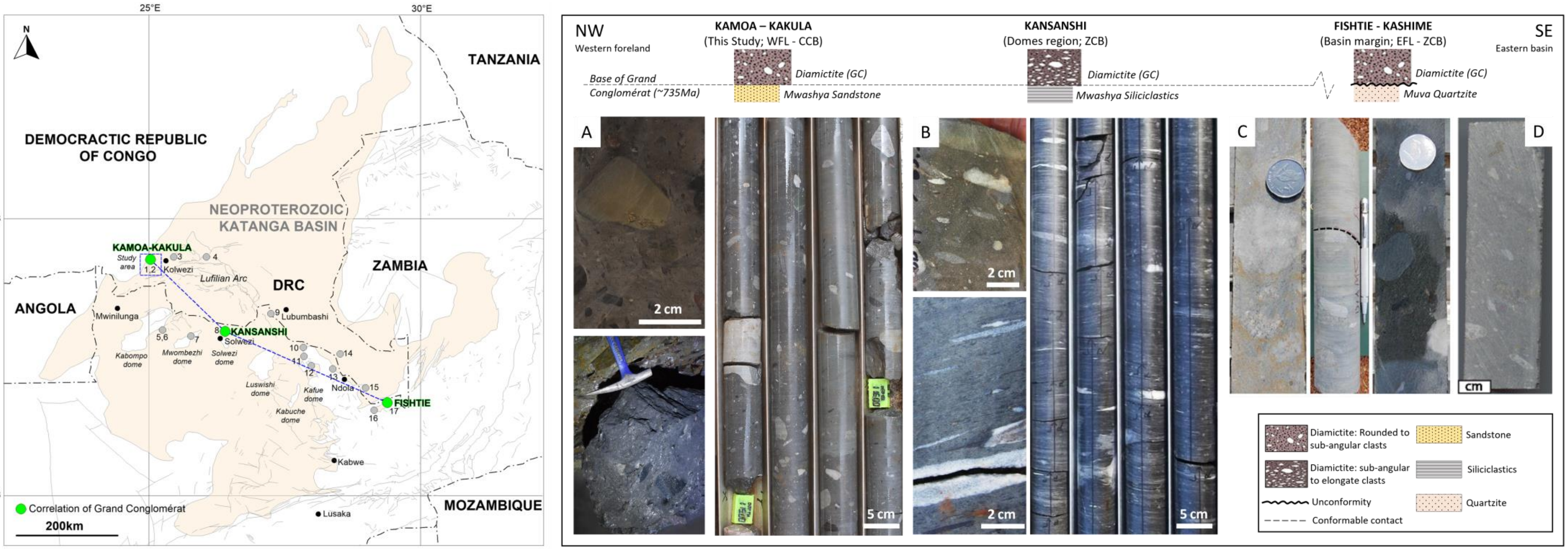

Figure 52: Regional geological setting and observations of the Grand Conglomérat Fm (diamictite) from northwest, central and southeast of the Katanga from three localities. Locality (A) Kamoa – Kakula Cu deposit (this study) diamictite samples from, clock-wise, DKMC_DD1044 at 319.20 m, DKMC_DD571 from 115.54 m to 119.00 m, and Kakula North underground boulder showing rounded, sub-rounded and sub-angular clasts, (B) Kansanshi Cu-Au deposit (McIntyre, 2019) showing sub-rounded to sub-angular deformed, elongated clasts and (C; D) Fishtie Cu deposit (Hendrickson, 2013; Simusokwe, 2021) showing rounded, sub-rounded and sub-angular clasts. CCB – Congolese Copperbelt, ZCB – Zambian Copperbelt, WFL – Western Foreland, EFL – Eastern Foreland, GC – Grand Conglomérat.

6.2 Mineralisation processes

6.2.1 Mineral System Model

Sediment-hosted copper (SHC) deposits form within sedimentary basins of the world, which in most instances have been affected by some level of deformation. The SHC deposit type has been discovered in most continents (Section 2.1, Fig. 7) and in the Central African Copperbelt, the long period of sedimentation along with structural complexity associated to Lufilian orogeny created a favourable framework for SHC-type mineralisation. The major components of the SHC mineral system include (i) a "source" of sulphur and metals transported by oxidised brine or fluid, (ii) a heat source that can act as a thermal "driver", (iii) a conduit(s) in which the ore bearing fluids are transported (by growth faults and secondary fault networks) acting as a "pathway", (iv) a chemical or physical "trap" that triggers the precipitation of sulphides and (v) relatively impermeable overlying strata which caps the system acting as a "seal" (Hitzman et al., 2005; Hitzman et al., 2010).

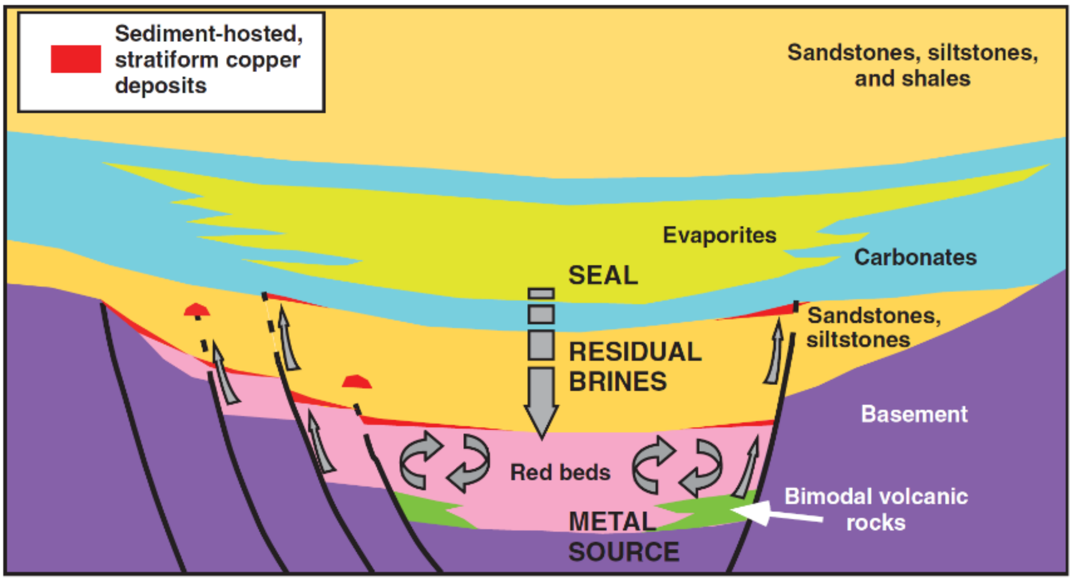

Figure 53: Schematic cross section of a closed sediment hosted copper system (Hitzman et al., 2010).

The most favourable sedimentary basin configuration of the SHC-type mineral system seems to be a closed system (Fig. 53). A closed system can be capped by carbonates containing evaporites or other appropriate lithology of similar characteristics. This "seal" allows for the extended precipitation of sulphides to form larger ore bodies, as opposed to an open system with restricted development of seal lithologies. The open mineral system configuration promotes the early evacuation of ore bearing fluids and as a result forms smaller ore bodies due to limited preservation potential in comparison to an open system. The spatial parameters of these systems can be highly variable and of particular interest to this study, the Katanga stratigraphy can be up to ~11 km in thickness (Selley et al., 2005; Dewaele et al., 2006). It is proposed that the formation of the SHC-type mineral deposits relies on the availability of a saline brine (in the range of around 9-16 wt.% NaCl eq.) to strip, dissolve and transport copper in solution under suitable Eh-PH and temperature variations i.e., low temperature conditions for diagenetic sulphide crystallisation (i.e., < 100 °C) and around 200 °C for late sulphide formation and a reduced medium for the reaction responsible for the precipitation of ore sulphides to occur (Dewaele et al., 2006; Cailteux et al., 2005).

The mineral systems approach requires favourable geodynamics, fertility, architecture and preservation potential of a region (McCuaig and Hronsky, 2014). Occhipinti et al., (2016) highlights the importance of the geochemical indicators. The geodynamic event is the Lufilian orogeny, creating the distinct structural domains and architecture allowing for fertile ore bearing fluids access to upper crustal levels. At Kamoa, two significant N-NE trending faults and the West Scarp fault are noted, along with a tendency for high grade mineralisation to occur proximal to the Mupaka fault (Broughton and Rogers, 2010; Parker et al., 2013; Twite et al., 2019). These components are illustrated by Fig. 54, which shows the fertility (F) (Kakula north underground sample), the geodynamics (G) – illustrated by the regional Lufilian arc structural interpretation (after Porada 1989) and the local architecture (A) illustrated by the simplified lithological block model (Twite et al., 2019).

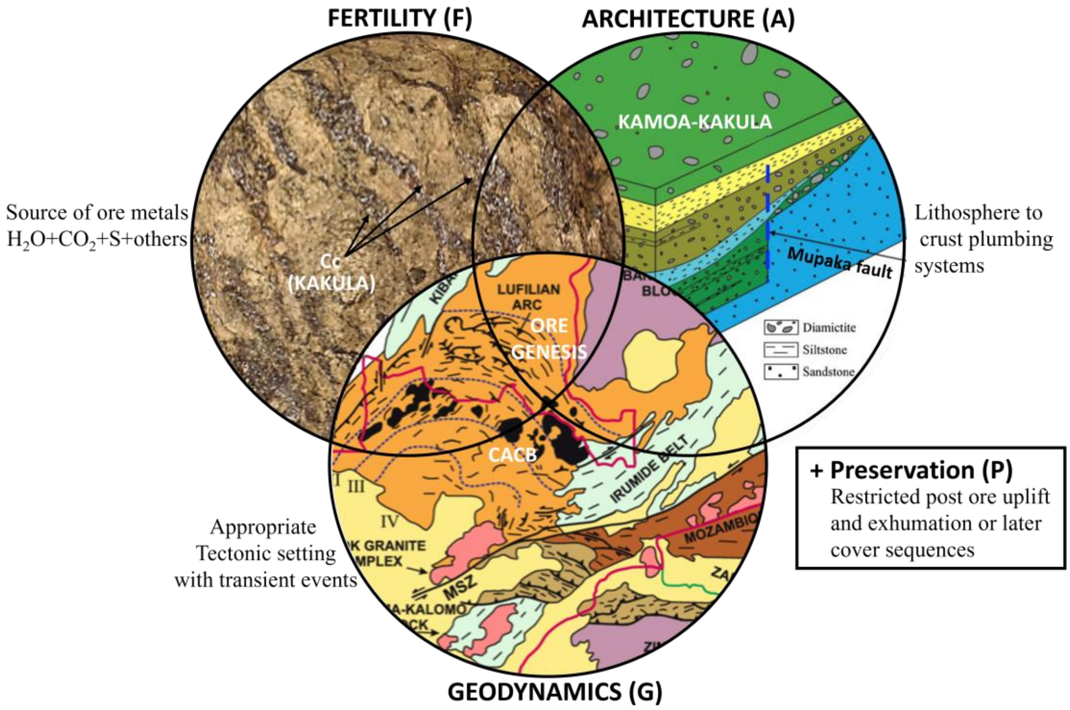

Figure 54: Kamoa - Kakula FAG mineral system Venn diagram (created using concept of McCuaig and Hronsky, 2014).

6.2.2 Mineralogy

Mineralogy within the SHC type of deposits is diverse. The style of mineralisation is generally considered as disseminated, vein type and stratiform, which can occur with metasomatic sulphide replacement forming mineralisation surrounding clasts or lithofragments (Cox et al., 2003; Dewaele et al., 2006). This precipitation of metal exploits a redox boundary and is controlled by the presence of a permeable aquifer, sufficient biogenic or abiogenic sulphides, a reductant such as organic shale, gas (e.g., CH_4) or bitumen (Cox et al., 2003; Dewaele et al., 2006) and earlier sulphide accumulations. Below the pyritic (FeS_2), zone, common copper mineralogy in SHC type deposits that are likely applicable to this study, in a paragenetic sequence, include: chalcopyrite ($CuFeS_2$), bornite (Cu_5FeS_4), digenite (Cu_9S_5), djurleite ($Cu_{31}S_{16}$) and chalcocite (Cu_2S) and these minerals can form a distinct mineral zonation (Fig. 55). These are ordered from least abundant in copper content (by copper to sulphur ratio) to the most abundant (Hayes et al., 2015). Other minerals can include sphalerite, galena and native copper (Cox et al., 2003), and results from optical microscopy conducted in this study, identifies most of these minerals except djurleite.

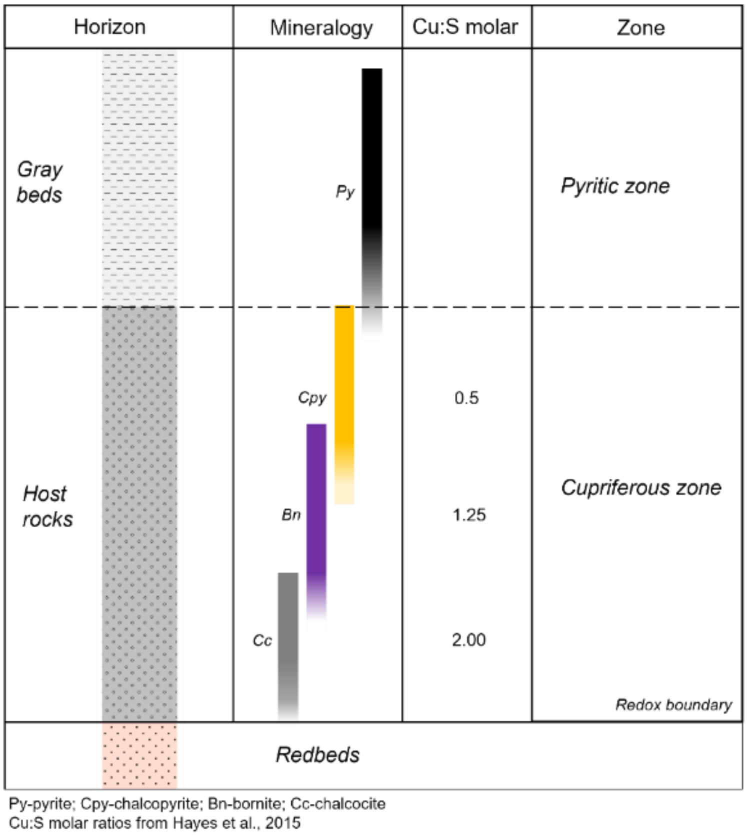

Figure 55: Typical SHC type Py → Cpy → Bn → Cc zonation (modified after Brown, 2018).

6.3 Mineralisation: Kamoa–Kakula

6.3.1 Mineralisation setting and characteristics

The main sulphide mineral assemblages observed from this study are (1) pyrite-dominant and (2) chalcopyrite-bornite-chalcocite with minor pyrite (Fig. 56). These different styles of mineralisation can be seen in Fig. 56 A and B; disseminated, bedded and overgrowing clasts mineralisation, Fig. 56 B, C, D; disseminated, overgrowing and replacement of clasts, Fig. 56 E; pervasive breccia-like mm-cm scale veinlets, and Fig. 56 F; banded replacement mineralisation of bedding. The proportions within the mineral assemblages are consistent with the previous studies (Twite, 2016; Twite et al., 2019), which approximated the distribution of economic minerals at Kamoa – Kakula to be chalcopyrite (~50%), bornite (~30%) and chalcocite (~20%).

The observation of sphalerite and galena in lesser amounts, in addition to rock-forming sericite, chlorite, quartz, specularite and rutile are also observed (Schmandt et al., 2013; Turner et al., 2023). Twite et al. (2020) further noted the variations of fine- to coarse-grained disseminated mineralisation, as well as the mineralised strain shadows and strain fringes surrounding clasts and proposed that the latter texture is indicative of coaxial deformation associated with structural events. This style of mineralisation is also observed in this study at Kansoko Centrale (DKMC_DD627) and although less common, observed at Kakula West (DKMC_DD1179). Chalcopyrite, bornite and chalcocite in the strain shadows are common within the basal diamictite and associated to gangue minerals such as quartz, mica, chlorite, hematite and carbonate recrystallised under stress (Fig. 57 c - e). Mineralisation aligned to bedding is prevalent within the intercalated siltstones (Fig. 56 A) and in the siltstone clasts within the diamictites. Turner et al., (2023) refer to this sulphide texture within the basal diamictite at Kamoa as ‘caps’ (equivalent to strain fringes) and ‘beards’ (equivalent to strain shadows) when compared to the observations by Twite et al., (2020). Whilst economic mineralisation is not observed to be hosted within underlying Mwashya Subgroup sandstone of the Roan Group, specular hematite and trace amounts of bornite and chalcocite (linked locally to native copper) are observed within the transition horizon from the Mwashya sandstone, towards the overlying Grand Conglomérat diamictite (Twite, 2016). Photomicrographs from optical microscopy from this study are displayed in Fig. 57 to Fig. 60, followed by the key observations and interpretation.

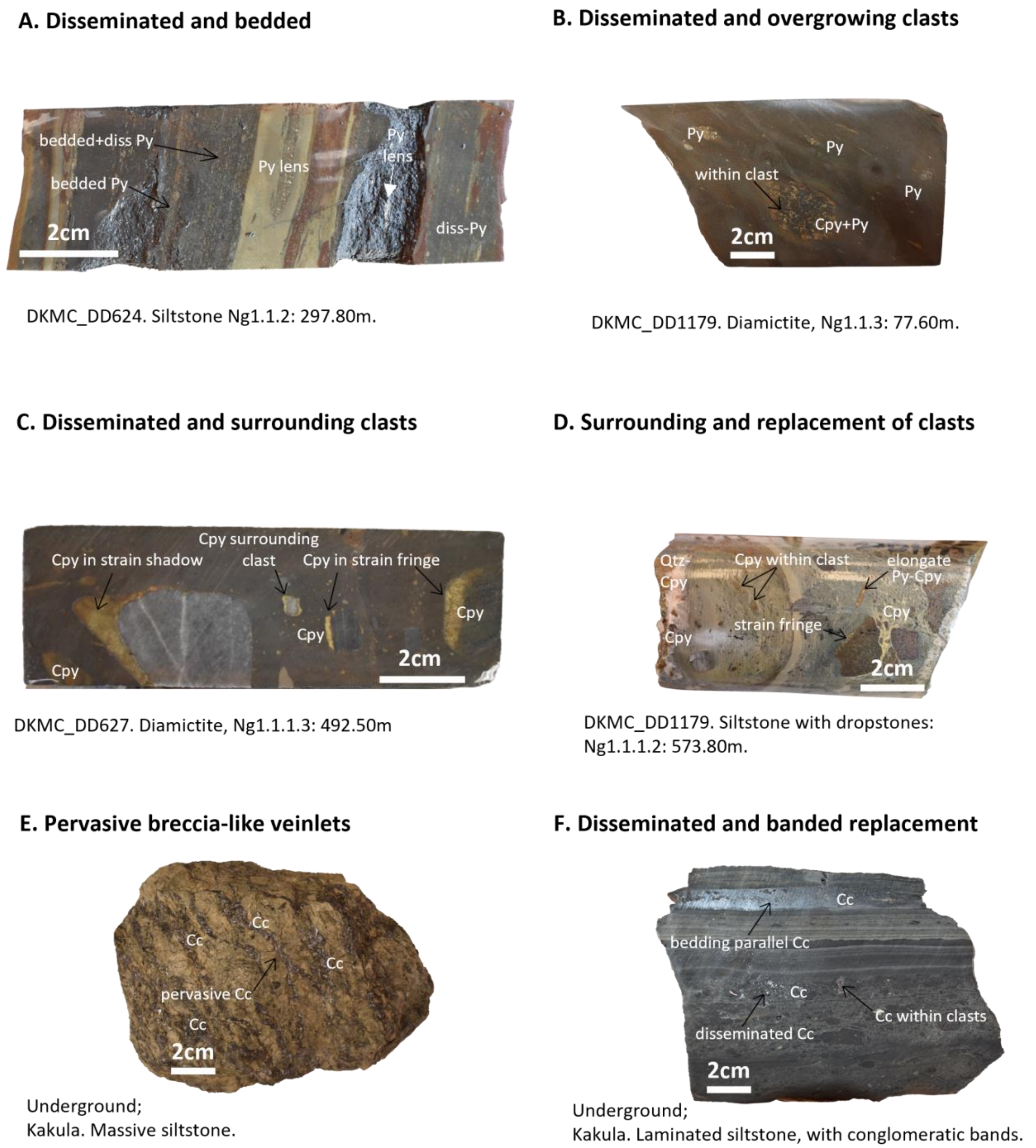

Figure 56: Styles of mineralisation observed at Kamoa (A) Disseminated mineralisation aligned to bedding in DKMC_DD571, (B) pervasive breccia-like within clasts in DKMC_DD1179, (C) surrounding and overgowing clasts in DKMC_DD627, (D) overgrowing and replacement of clasts in DKMC-DD1179, (E) pervasive mm-cm scale veinlets from Kakula underground (F) banded ore after sedimentary bedding from Kakula underground. Py - pyrite, Cpy - chalcopyrite, Cc - chalcocite, Qtz - quartz.

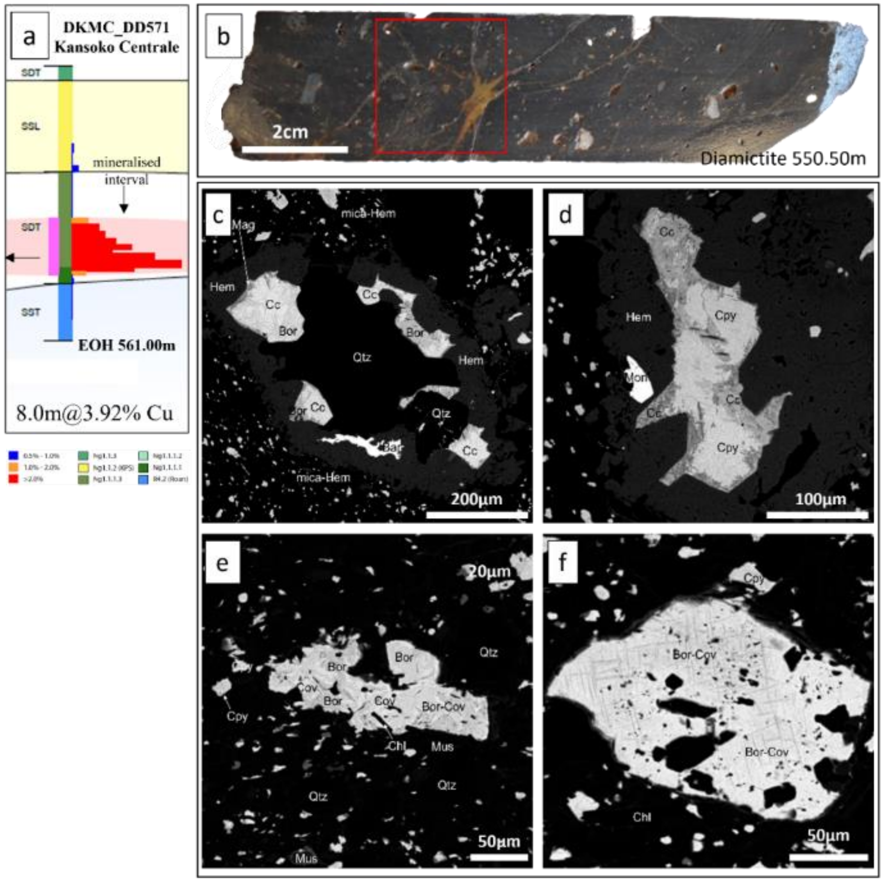

Figure 57: SEM-BSE photomicrographs from DKMC_DD571 at 550.50m (a) Downhole schematic geological log (b) image of core sample (c) irregular Cc and Bor, proximal mica-Hem matrix with bar within matrix, all surrounding Qtz grain in centre (d) Cpy rimmed by Cc with corroded edges within Hem matrix, Mon inclusion within Hem matrix (e) assemblage of Bor – Cov + distal granular Cpy within Qtz-Chl-mica matrix (f) Bor-Cov lamella within original Bor grain ~100µm with corroded edges, distal irregular Cpy in Chl matrix. Cpy – chalcopyrite, Bor – bornite, Cc – chalcocite, Cov – covellite, Bar – barite, Chl – chlorite, Hem – hematite, Qtz – quartz, Mus – muscovite mica, Mon – monazite.

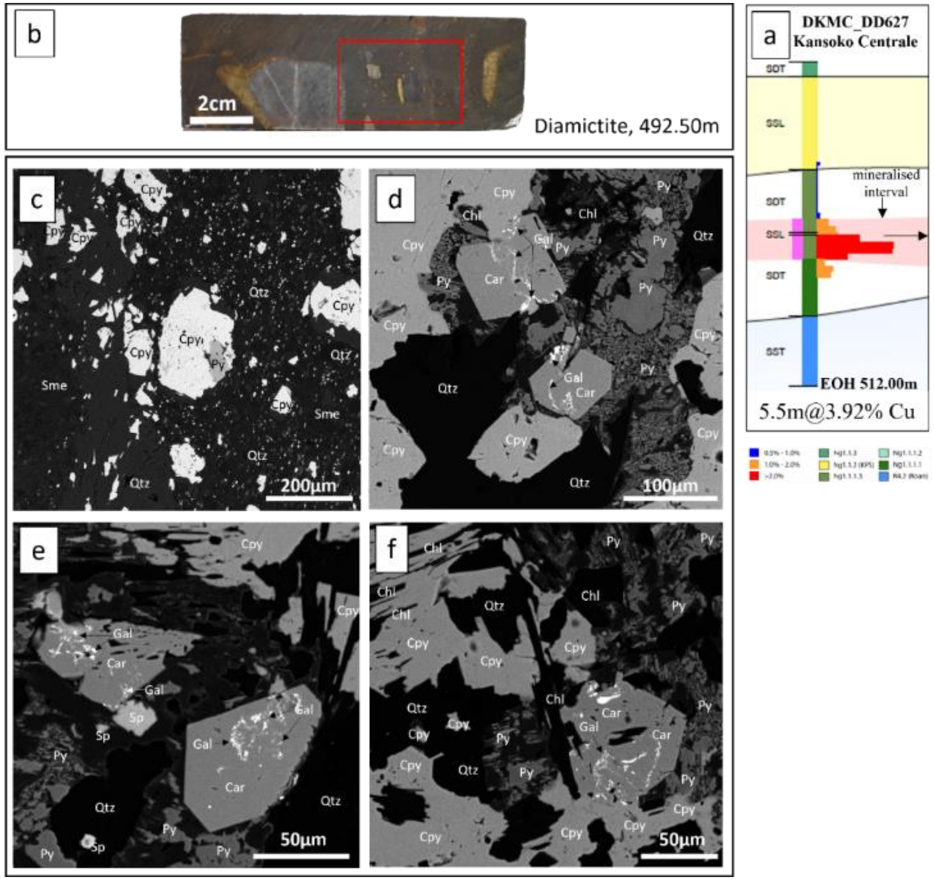

Figure 58: SEM-BSE photomicrographs from DKMC_DD627 at 492.50m (a) Downhole schematic geological log (b) image of core sample (c) Cpy with irregular margins within crudely aligned (Chl)-Sme-Qtz matrix (d) sub-angular Cpy + Car, µm-scale veinlets of Gal within Car crystals. Irregular and medium grained disseminated Py occurring within Qtz-Chl matrix (e) Py with corroded margins, Sp in matrix and Chl-Sme + Gal, irregular Qtz (f) Euhedral Car + interstitial gal surrounded by disseminated Py and Qtz-Chl matrix. Irregular shaped Cpy with corroded edges, adjacent to irregular Qtz. Cpy – chalcopyrite, Car – carrollite, Py – pyrite, Qtz – quartz, Sme – smectite, Chl – chlorite, Gal – galena, Sp – sphalerite.

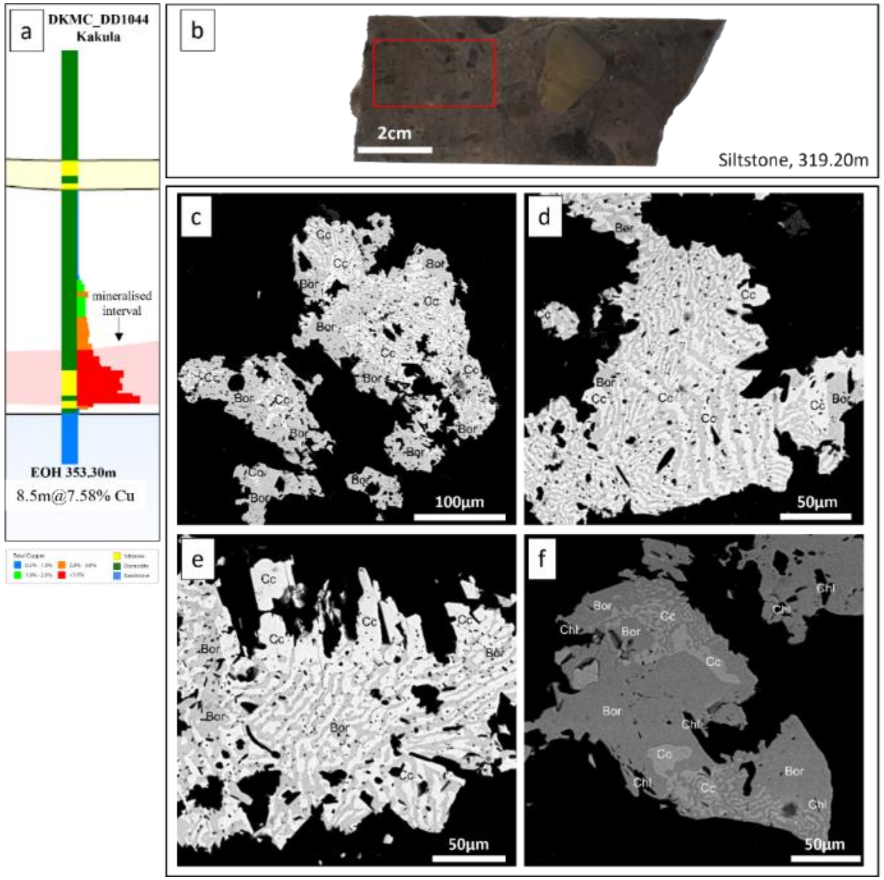

Figure 59: SEM-BSE photomicrographs from DKMC_DD1044 at 319.20m (a) Downhole schematic geological log (b) image of core sample (c) two grains Bor + Cc, myrmekitic texture showing replacement of Bor by Cc (d) myrmekitic texture, dominantly Cc with minor Bor (e) Bor + Cc in a myrmekitic texture, edges show dominant Cc (f) dominantly Bor grain with elongate development of Chl, bottom right and upper central parts indicate development of myrmekitic texture with Cc. Bor – bornite, Cc – chalcocite, Chl – chlorite.

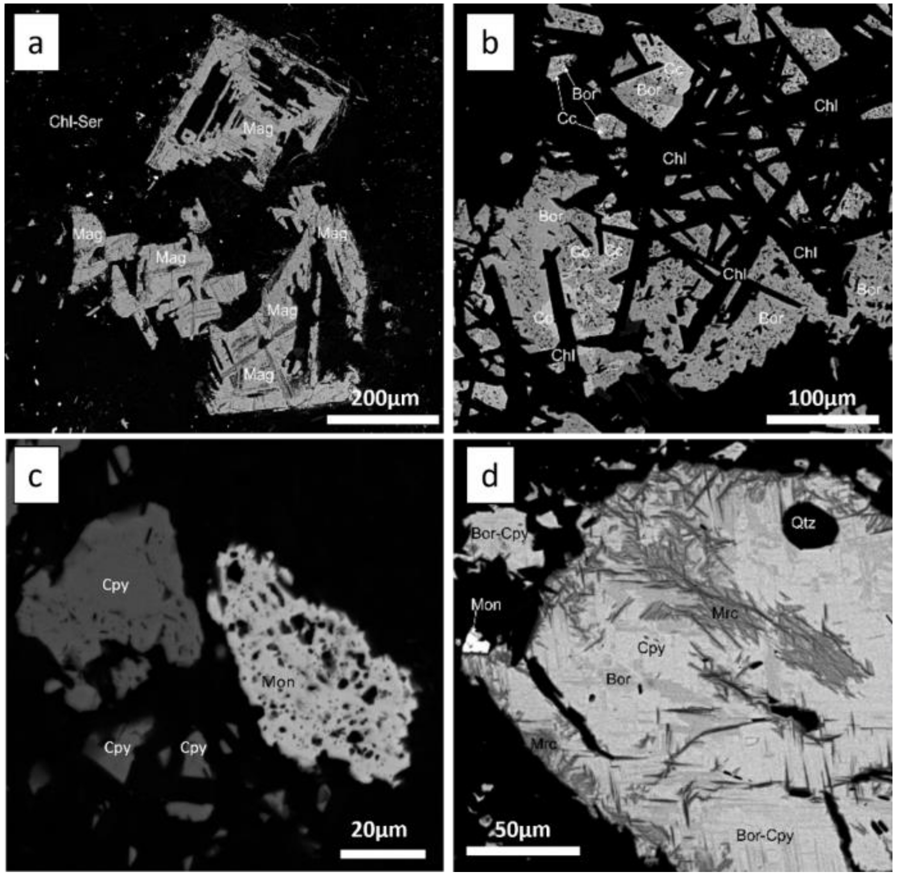

Figure 60: SEM-BSE photomicrographs. From DKMC_DD1044 at 319.20m; (a) skeletal crystals surrounded by Chl-Ser matrix (b) Bor + Cc as indicated within cross cutting elongate Chl disruptive overprint. From DKMC_DD627 at 492.50; (c) Cpy within silica rich matrix, Mon grain around 8 µm x 10 µm in size with solution cavities, altered edges and fresh central part. From DKMC_DD571 at 550.50m; (d) Bor-Cpy replacement. with Mrc along crenulate grain margins and infilling fractures. Bor – bornite, Cc – chalcocite, Mag – magnetite, Chl – chlorite, Ser – sericite, Qtz – quartz, Mrc – marcasite, Mon – monazite.

The mineralised intervals of DKMC_DD571 at 550.50m (within diamictite), Kansoko Centrale (Fig. 57 c – f), is composed of chalcopyrite, bornite, covellite and chalcocite. Anhedral barite 50 – 300 µm in size (Fig .57c) intragranular within a hematite-smectite-silica clasts and surrounding matrix is observed. Barite is a common gangue mineral within hydrothermal systems (Castroviejo, 2023) although sulphate minerals such as barite could be a product of late-stage oxidation. Alternatively, this can occur as relics of primary sedimentary sulphates, as barite is more resistant to dissolution in comparison to easily remobilised gypsum and anhydrite. The relics of anhydrite in the Mwashya Subgroup footwall at Kamoa were reported by Schmandt et al., (2013), who interpreted these as relics of evaporitic sulphates. The gangue association of chlorite, carbonate and sericite in the studied sample is consistent with greenschist facies conditions of metamorphism. Hematite after detrital magnetite is widely developed whereas detrital apatite and monazite are accessory. The zoned, symplectic and lamellar textures of chalcopyrite in the sulphide intergrowths (Fig. 57 e) suggests continuous hydrothermal alteration, with distinct consecutive replacement by bornite, covellite and chalcocite (Fig. 57 f). The image also shows that the original bornite grain (> 100 µm) has been converted into covellite during this hydrothermal alteration. The corroded margins and internal texture in the grain reflect the intensity of this replacement. A thin chlorite-silica rim around the sulphide grains suggests synmetamorphic growth.

A smectite-(sericite)-quartz-chlorite gangue assemblage (Fig. 58 c) composes the matrix of mineralised interval of DKMCDD_DD627 at 492.50m (within diamictite), Kansoko Centrale. The bedded texture suggests original sedimentary stratification of an argillaceous matrix in a poorly sorted diamictite. Chalcopyrite with sharp and corroded margins and chlorite-quartz-carbonate intergrowths and inclusions dominate this mineralised zone. Diagenetic framboidal pyrite is absent, whereas coarse-grained pyrite (Py3 and Py4) is present as inclusions in chalcopyrite and is locally decomposed into a fine-grained mix of dispersed secondary pyrite, marcasite and silicates. The chalcopyrite grains seem to be confined to the central part of dispersed sulphides avoiding the areas with semi-decomposed pyrite and euhedral carrollite crystals. The carrollite metacrysts ~50 – 100 µm in size include silicates and disseminations of galena and, supposedly, form at expense of decomposing earlier pyrite (Py3) (Fig. 58 d – f). The galena disseminations and micro-veinlets are associated with sphalerite crystals in the matrix. Hematite after detrital magnetite is common whereas micrograins of detrital xenotime are very rare. The observed texture of major pyrite and chalcopyrite is typical of the sediment-hosted copper deposits (Sillitoe and Gappe, 1984; Sillitoe, 2010). Secondary marcasite could be later destabilised at low-temperature processes, although at temperatures of >300 °C, it may be associated to Cu-Co-Ni mineralisation (Castroviejo, 2023). The ore mineral assemblage at Kakula varies slightly to those observed in the samples from Kansoko Centrale as illustrated in photomicrographs of a sample from mineralised interval of DKMC_DD1044 at 319.20m, within siltstone (Fig. 59 c - e and Fig. 60 a - d). The gangue assemblage is composed predominantly of chlorite with common relic euhedral and skeletal magnetite grains, accounting for 5 - 10 % of the area. Detrital magnetite displays typical magmatic texture of a Ti - rich magnetite, decomposed into magnetite and ilmenite where magnetite is replaced by hematite and goethite, whilst ilmenite is transformed into leucoxene and rutile. The abundance of chlorite and detrital magnetite suggests a mafic precursor for these fragments in the sediments. This is consistent with the occurrence of common chlorite pseudomorphs, after pyroxene, with hematite developed along cleavage and outlines of the grains revealing their primary morphology. Bornite is the main hypogene copper sulphide here with the widespread symplectic texture indicative of bornite being replaced by chalcocite (Fig. 59 c - e). The consequent lamellar and irregular diffusion-type replacement by covellite and late-stage chalcopyrite is also observed. The mineral zonation at Kamoa is well developed and distinct. It can be clearly observed in drillhole DKMC_DD1044 (Kakula). This drillhole contains a mineralised intercept of 8.5m @ 7.58% Cu and reveals a zonation transitioning from pyrite to chalcopyrite through to bornite and chalcocite; this supports the replacement transitions explained earlier (Fig. 61).

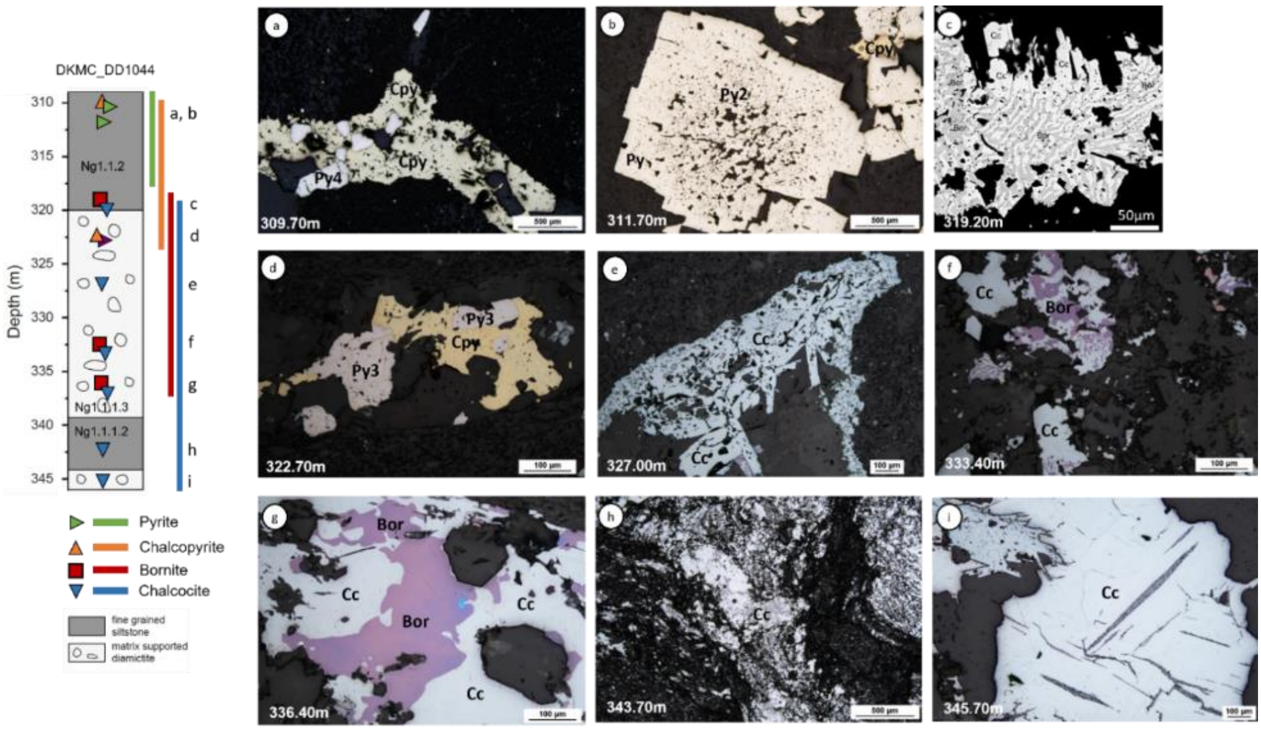

Figure 61: Mineral zonation interpretation for drillhole DKMC_DD1044 (Kakula) from 310.00 m.

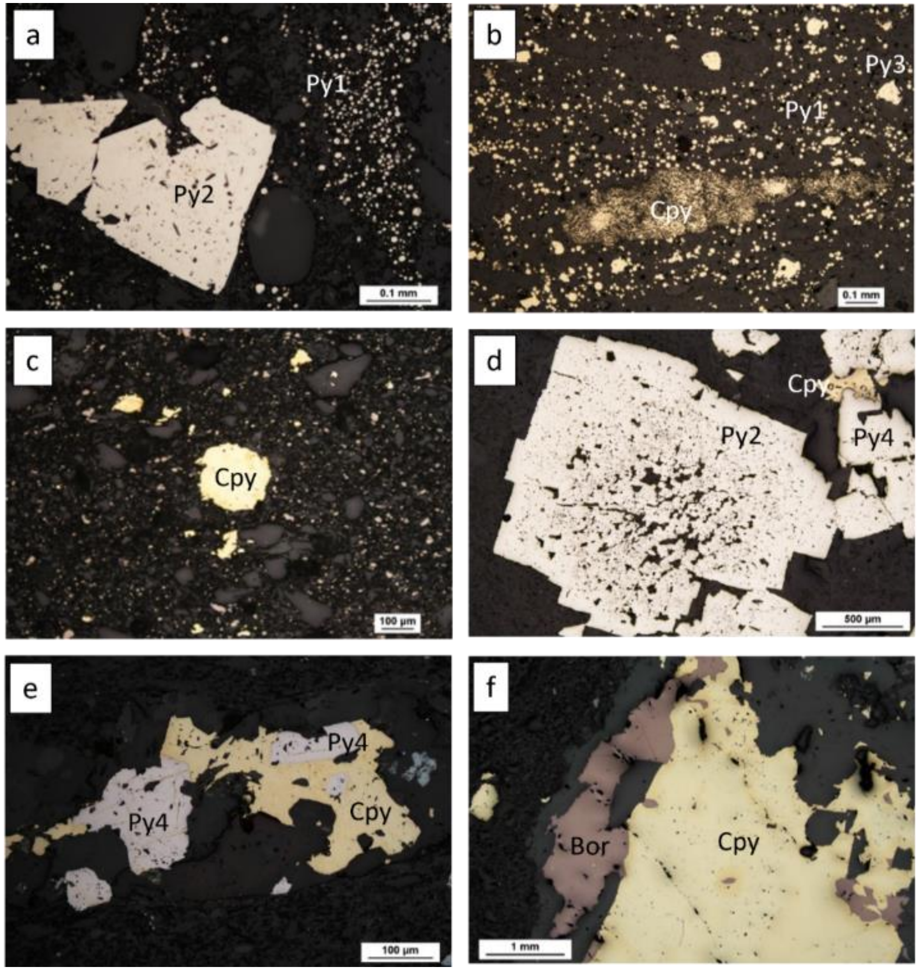

Figure 62: PP reflected light photomicrographs (a) From DKMC_DD624 at 298.80m framboidal Py and Euhedral Py (b) DKMC_DD956 at 274.5 Cpy surrounded by framboidal Cpy (c) DKMC_DD956 at 278.00m Cpy surrounded by recrystalising Py, likely secondary, along with disseminated Cpy (d) DKMC_DD1044 at 311.70m Cpy replacement of euhedral Py (e) DKMC_DD1044 at 322.70m Cpy with corroded edges, replacing Py (f) DKMC_DD627 at 498.30m predominantly Cpy with corroded edges, with Bn replacing Cpy at edges. Fram Py – framboidal pyrite, Py – pyrite, Cpy – chalcopyrite, Bor – bornite.

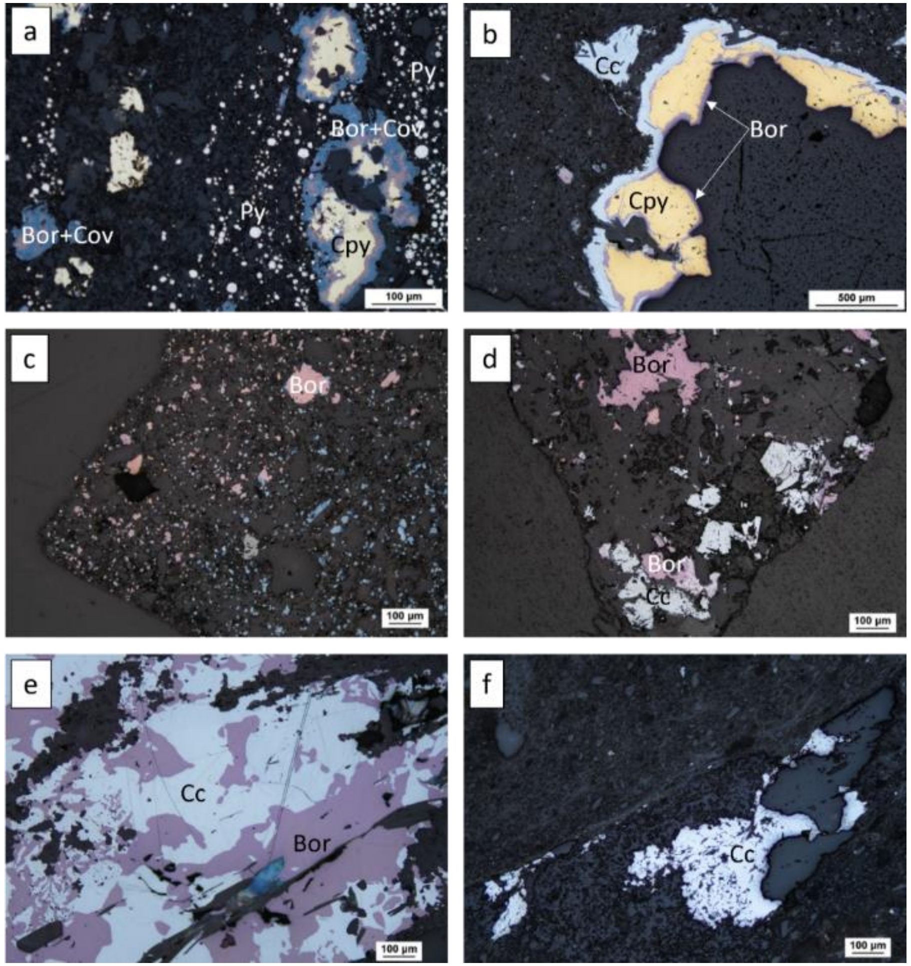

Figure 63: PP reflected light photomicrographs (a) DKMC_DD624 at 303.10m Cpy rimmed by growth textures of Bor and Cov (b) From DKMC_DD624 at 304.50m Cpy, with irregular rim of replacement by Bor, and irregular rim of replacement by Cc (c) DKMC_DD571 at 550.50m fine grained, granular and disseminated style of Bor (d) DKMC_DD1044 at 319.20m replacement of Bor by Cc (e) DKMC_DD1044 at 328.80m widespread replacement of Bor by Cc (f) DKMC_DD1039 at 344.90m well developed Cc with corroded edges and granular, fractured internal texture, showing crude alignment. Cpy – chalcopyrite, Bor – bornite, Cc – chalcocite, Cov – covellite.

Prior to the SEM and S isotope analysis, sulphide mineralisation at Kamoa was reviewed by reflected light microscopy in polished sections and polished blocks prepared for the laser sampling . This was carried out with the objective of characterising the textural relationships and determining the sulphide generations. Initial observations were focused at the Kakula, Kansoko Centrale and Kakula prospects (Fig. 62 a - f), with further comparisons between economic sulphide mineralisation of the Kansoko Centrale and Kakula prospects (Fig. 63 a - f) predominantly based on the samples from the pyritic siltstone, Ng1.1.2 and basal diamictite, Ng1.1.1 (Table 13 and Table 14).

Table 13: Mineral assemblage of sulphide grains from Fig. 62 a - f

BHID	Depth (m)	Lith	Strat1	Strat2	Prospect	Sulphide assemblage
DKMC_DD624	298.8	SSL	Ng1.1.2		Kansoko Centrale	Py1-Py2-Py3
DKMC_DD956	274.5	SDT	Ng1.1.1	Ng1.1.1.3	Kansoko Sud	Py1-Py3-Cpy
DKMC_DD956	278	SDT	Ng1.1.1	Ng1.1.1.3	Kansoko Sud	Py-Cpy
DKMC_DD1044	311.7	SSL	Ng1.1.1	Ng1.1.1.2	Kakula	Py2-Cpy
DKMC_DD1044	322.7	SDT	Ng1.1.1	Ng1.1.1.1	Kakula	Py4-Cpy
DKMC_DD627	498.3	SDT	Ng1.1.1	Ng1.1.1.1	Kansoko Centrale	Cpy-Bor

SSL – siltstone, SDT – diamictite, Py – pyrite, Cpy – chalcopyrite, Bor – bornite.

Table 14: Mineral assemblage of sulphide grains from Fig. 63 a - f

BHID	Depth (m)	Lith	Strat1	Strat2	Prospect	Sulphide assemblage
DKMC_DD624	303.1	SSL	Ng1.1.2		Kansoko Centrale	Bor-Cov
DKMC_DD624	304.5	SDT	Ng1.1.1	Ng1.1.1.3	Kansoko Centrale	Cpy-Bor-Cc
DKMC_DD571	550.5	SDT	Ng1.1.1	Ng1.1.1.3	Kansoko Centrale	Bor-Cov
DKMC_DD1044	319.8	SSL	Ng1.1.1	Ng1.1.1.2	Kakula	Bor-Cc
DKMC_DD1044	328.8	SDT	Ng1.1.1	Ng1.1.1.1	Kakula	Bor-Cc
DKMC_DD1039	344.9	SDT	Ng1.1.1	Ng1.1.1.1	Kakula	Cc

SSL – siltstone, SDT – diamictite, Cpy – chalcopyrite, Bor – bornite, Cov – covellite, Cc – chalcocite.

The lithologies that host mineralisation are diamictite and siltstone that occur within the basal unit. An assemblage of densely distributed, fine-grained rounded grains of framboidal pyrite (Py1) sub-micron to 10 µm in size and euhedral pyrite with inclusion-rich core (Py2) and inclusion-poor rim (Py3) are observed at Kansoko Centrale (Fig. 62 a). A similar dense configuration of framboidal chalcopyrite (Cpy) with similar size parameters to that observed for framboidal pyrite, suggest that chalcopyrite replaced pyrite framboids (Fig. 62 b) in the laminated siltstone at Kansoko Sud. Similar textures, as a result of the replacement of framboidal pyrite by chalcopyrite, are not uncommon and were reported in DDH194 drilled at Kamoa (Schmandt, 2013). The development of framboidal pyrite is redox dependant process and is therefore an indicator of past anoxic environment conditions (Sweeney and Kaplan, 1973; Wilkin et al., 1996). The mottled growth texture of chalcopyrite (Fig. 62 b) is likely related to an accumulation of sooty pyrite among framboids that were replaced by later chalcopyrite. Framboidal chalcopyrite is rare as it mostly occurs as anhedral, rounded as well as anhedral angular grains, with outlines resorbed and crosscut by matrix silicates, mostly chlorite (Fig. 62 c). Widespread development of the later pyrite (Py3 and Py4) generations, including those incorporating framboidal pyrite (Py1), have been noted at Kakula (Fig. 62 a and d). The inclusion-rich Py2 is overgrown by Py3 with euhedral faces, although locally exhibiting skeletal and corroded morphology. The latest pyrite generation (Py4) appears to be intimately associated to chalcopyrite crystallisation. The Py4 grains may appear as corroded relics in chalcopyrite (Fig. 62 e), but may also be found as a rim along the margins of chalcopyrite aggregates. The replacement of chalcopyrite by bornite occurs at the grain margins, as observed from a sample from Kansoko Centrale (Fig. 62 f). Both bornite and chlorite replace the chalcopyrite grain along the margins.

Sulphide grains from drillholes DKMCDD_DD571 and DKMC_DD624 show two distinctly varying textures of replacement (Fig. 63 a and b). An anhedral chalcopyrite grain, is rimmed by bornite and covellite (due to replacement) occurring in the moderately corroded grain margin (Fig. 63 a), whilst framboidal pyrite occurs in the surrounding groundmass. The framboidal pyrite indicates the initial reducing conditions and its survival and unchanged morphology suggests that chalcopyrite did not replace Py1 and did not use the components of local Py1, but was instead built from externally derived elements. Covellite occurs in sediment-hosted copper systems usually in minor amounts and usually forms during the supergene enrichment stage (Castroviejo, 2023) replacing bornite. Another sample of mineralised laminated siltstone taken at 304.50 m depth that is 1.40 m from the previous one (at 303.10 m depth). This reveals a somewhat similar, whilst different, pattern of replacement (Fig. 63 b). Figure 63 b shows similar grain-margin replacement textures, with the left-side of the chalcopyrite grain exhibiting replacement by chalcocite, whilst the right-side of the chalcopyrite grain exhibits replacement by bornite. Complete replacement by chalcocite is observed in a 250 μm sized grain in the top right of the photomicrograph. This particular intergrowth (Fig. 63 b) forms as a chalcopyrite-silicate strain fringe at the edge of a silicate rock fragment (bottom right). The internal rim of bornite is directly adjacent to the clast whereas the outer rim is bounded by syn-metamorphic silicates, crystallised under the strain in the pressure shadow. It may be interpreted as evidence of post-peak timing of bornite and chalcocite replacement of syn- peak metamorphic chalcopyrite.

Consecutive sulphide replacement textures are common in other sedimentary basins of the world. In particular, intergrowth of chalcocite, bornite and pyrite are noted in the cupriferous zone of sediment-hosted copper deposits of the Kupferschiefer-Zechstein sedimentary succession of Poland that is characterised by a pyritic – Zn – Pb – Cu zonation and hematite zones overlying red beds (Oszczepalski et al., 2019). A disseminated texture in a transitional zone between disseminated bornite and covellite is noted at Kansoko Centrale (Fig. 63 c). Within this assemblage, larger anhedral grains of bornite (20 – 80 μm) are associated with spherical and sub-spherical much smaller bornite grains, which look like replaced framboids, although their morphology is strongly deformed. Some of bornite grains are replaced by minor chalcocite, whereas in the covellite-dominant zone, chalcocite is present as relics among covellite. A few framboidal relics are observed among covellite grains. The replacement of bornite by chalcocite is more apparent at Kakula and observed in DKMC_DD1039 and DKMC_DD1044 (Fig. 63 d and e). The symplectic texture of the grains suggests a diffusive replacement with no final equilibrium achieved. It indicates that at some stage bornite became unstable but the diffusion rate was too slow to reach an equilibrium and complete replacement in this case. At the same magnification level, a sample from drillhole DKMC_DD1039 at 344.90 m depth shows dominant chalcocite completely replaced bornite, which in its turn has replaced chalcopyrite (Fig. 63 f). This figure shows a strain fringe composed of quartz and chalcocite attached to an elongated rock fragment in a laminated siltstone. Anhedral quartz crystallised at the very end of the fringe whereas covellite is also distributed along the lamination cleavage. The ubiquitous chalcocite replacement appears to be a major characteristic of the Kakula prospect.

Based on these observations, generalised stages of mineralisation and a sulphide paragenetic sequence is proposed (Fig. 64). The mineral composition of primary lithologies is highly diverse as diamictites encompass the fragments of various magmatic, metamorphic and sedimentary rocks all contributing to the diverse assemblage of detrital minerals, in which relics of zircon, monazite and titanomagnetite are the most obvious. However, these assemblages are out of the scope of this study. The diagenetic to syngenetic sulphide assemblage of the stage 1 mineralisation mainly includes framboidal and finely disseminated sooty pyrite (Py1). A contribution of diagenetic copper accumulation is not obvious from the observed associations, as all copper minerals show features of replacement of pre-existing protolith. The framboidal chalcopyrite and bornite seem to be a result of replacement of primary pyrite (Py1) framboids. The metamorphic assemblage of the stage 2 mineralisation includes major chalcopyrite and pyrite (Py2+Py3+Py4). The degree of mineralisation and recrystallisation of sulphides is likely related to the spatial proximity to the fluid pathways. The proximal facies at peak metamorphic conditions are characterised by the most intense recrystallisation of ore minerals (chalcopyrite, pyrite and Co sulphides), metamorphic rock-forming minerals (chlorite, quartz, carbonates and sericite) and accessory minerals of fluid-mobile elements (metamorphic overgrowth on detrital monazite, xenotime and zircon). The mineralisation in stage 3 may correspond to a retrograde metamorphic stage with decreasing temperature, increasing Cu/S ratio in fluid that results in chalcopyrite replacement by bornite, covellite and chalcocite. The chalcocite-dominant assemblage includes also abundant hematite (specularite) indicating oxidised conditions. The formation of covellite, native copper, copper sulphates and chrysocolla happened during the stage 4 associated to supergene alteration under acid conditions due to decomposing sulphides.

The pyritic zone in the upper parts of the host rock package is transitioning from the lower pyritic siltstone (Ng1.1.2) to the upper basal diamictite (Ng1.1.1.3), where framboidal pyrite and sooty pyrite are crystallised and replaced by chalcopyrite, transitioning to the cupriferous zone. Subsequently, chalcopyrite is replaced by bornite (± chalcocite) downwards within the cupriferous zone. Subsequently bornite is replaced by chalcocite (± covellite), within the lower basal diamictite. Lastly chalcocite becomes the main mineralisation style towards the bottom parts of the host rock package (base of lower basal diamictite; Ng1.1.1.1) and this is proximal to the redox boundary with the underlying Mwashya sandstone (R4.2). It is likely that some overlap between the sulphide assemblages exists within the vertical mineral zonation profile. This regular zonation, typical of the SHC deposits, is consistent with thermodynamic modelling of sulphate-rich copper-bearing brines encountering a reduced pyritic horizon (Ripley et al., 1985) with zonation formed within a single stage due to fluid depletion in copper. Their model suggests that an ore fluid was initially within the chalcocite stability field and reacted with pyrite to produce chalcocite. As fluid became exhausted due to chalcocite precipitation the fluid entered the bornite and eventually chalcopyrite stability fields. The sustained flow of the same copper-rich fluid, results in continuous replacement of earlier bornite and chalcopyrite by chalcocite and bornite shifting the front of the reactions ahead. Within this model, all copper minerals are consequently formed within the same stage of mineralisation. In an open system with continuous long-lasting flow of fluid in equilibrium with chalcocite, all iron could be replaced by copper with an eventual formation of monomineralic chalcocite bodies as seen in Kansoko. This model, however, does not agree with the visual absence of pyrite (or its relics) in diamictite at the base of the mineralised zone unless sedimentary pyrite was totally destroyed and replaced. Initial high Cu/S and Cu/Fe in the fluid are also inconsistent with the limited chalcocite occurrences in some Kamoa prospects, where the main ore type is chalcopyrite (e.g., Kansoko Sud). In the next chapter, the obtained S isotope data are used to verify these models.

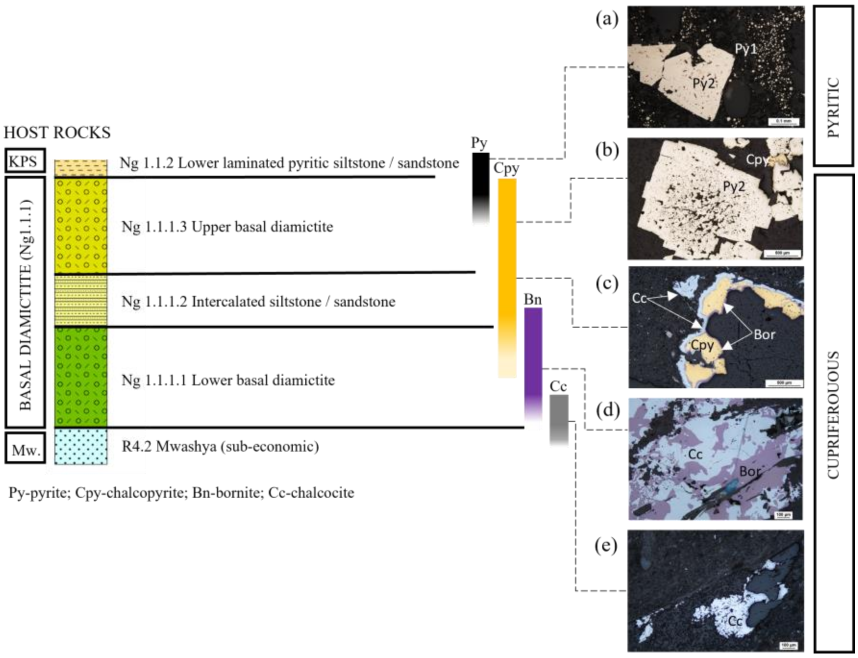

Figure 64: Generalised sulphide paragenesis at Kamoa-Kakula deposit. Strat-column modified after Broughton and Rogers, (2010); Twite, (2016). (a, b) pyrite zone – DKMC_DD624 at 298.80m and DKMC_DD1044 at 311.70m (c) chalcopyrite zone – DKMCDD624 at 304.50m, (d) bornite zone – DKMCDD1044 at 339.20m, (e) chalcocite zone – DKMC_DD1039 at 344.90m. Py1 – framboidal pyrite, Py 2 – anhedral pyrite, Cpy – chalcopyrite, Bor – bornite, Cc – chalcocite.

6.4 Sulphur isotopes

Sulphur isotope data from in-situ analyses of grains of pyrite, chalcopyrite, bornite, chalcocite and other sulphide species are presented in this report. These sulphides occur in the Kamoa-Pyritic-Siltstone (KPS) and basal diamictite (Ng1.1) within fine-grained siltstones, clast-supported diamictites and matrix supported diamictites. Chalcocite was observed to be preferentially enriched within diamictites with a mud and silty matrix. Downhole Cu was plotted to understand the relationship between Cu and the sulphur isotopic variations. In most cases Cu has a positive correlation with depth, therefore, the Cu-enriched intervals are encountered at deeper depths into the sedimentary formations. In some chalcocite-dominant sections a negative $\delta^{34}S$ correlation with Cu is established that correlates with the vertical mineral zonation, exhibited by the sulphide species variations downhole (Fig. 65 to Fig. 70).

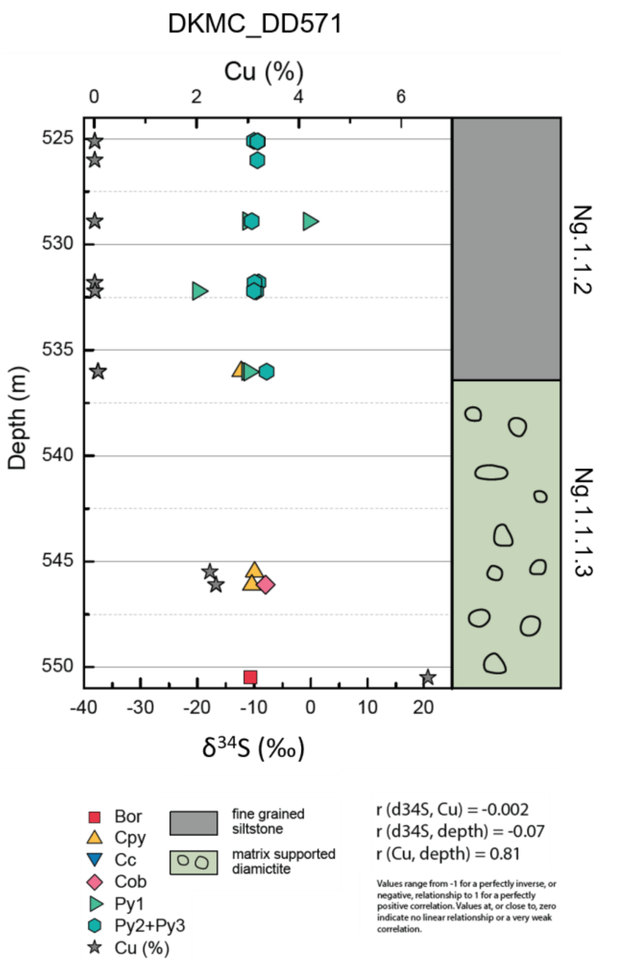

Figure 65: $\delta^{34}S$ variations in sulphides from DKMC_DD571, Kansoko Centrale. Bn – bornite; Cpy – chalcopyrite; Cc – chalcocite; Cob – cobaltite; Py1, Py2+Py3, pyrite generations; Cu% – copper assays.

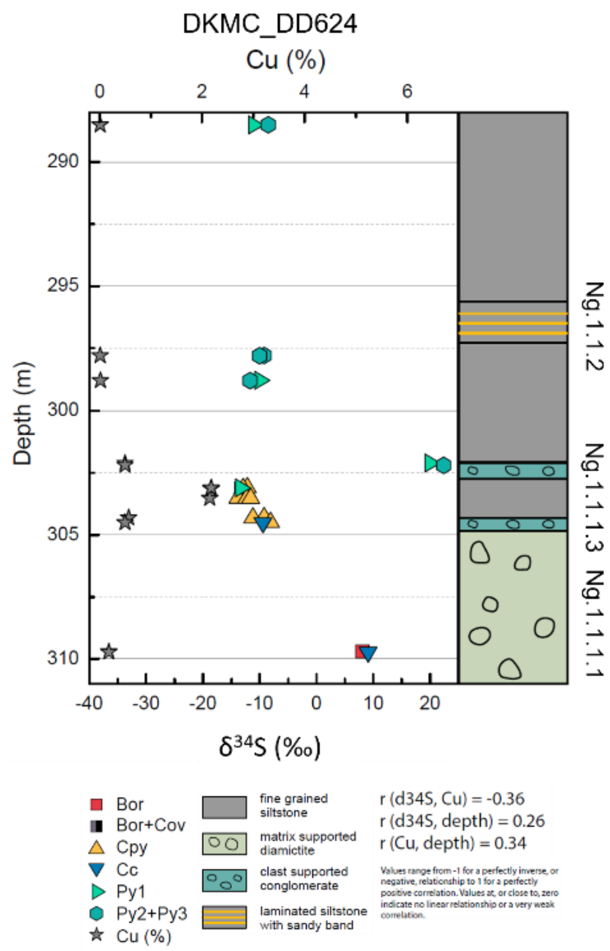

Figure 66: $\delta^{34}S$ variations in sulphides from DKMC_DD624, Kansoko Centrale. Bn – bornite; Cov – covellite; Cpy – chalcopyrite; Cc – chalcocite; Py1, Py2+Py3, Py4 – pyrite generations; Cu% – copper assays.

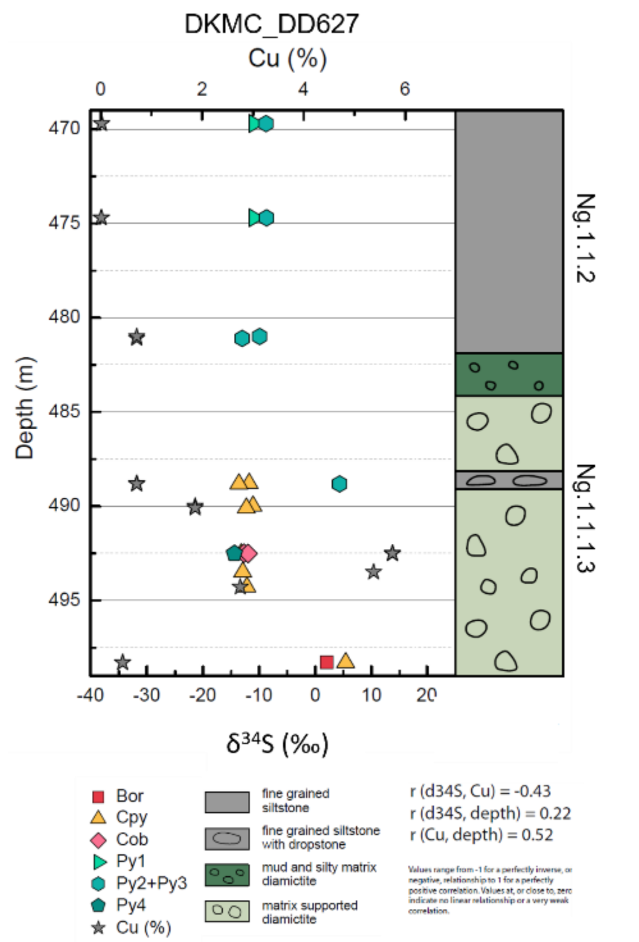

Figure 67: $\delta^{34}S$ variations in sulphides from DKMC_DD627, Kansoko Centrale. Bn – bornite; Cpy – chalcopyrite; Cob – cobaltite; Py1, Py2+Py3, Py4 – pyrite generations; Cu% – copper assays.

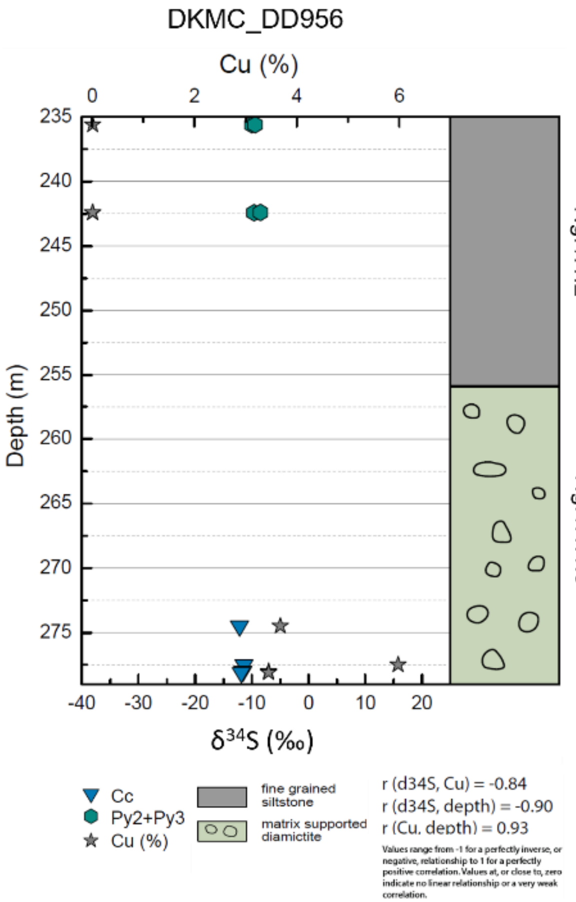

Figure 68: $\delta^{34}S$ variations in sulphides from DKMC_DD956, Kansoko Sud. Cpy – chalcopyrite; Py2+Py3 – pyrite generations, Cu% – copper assays.

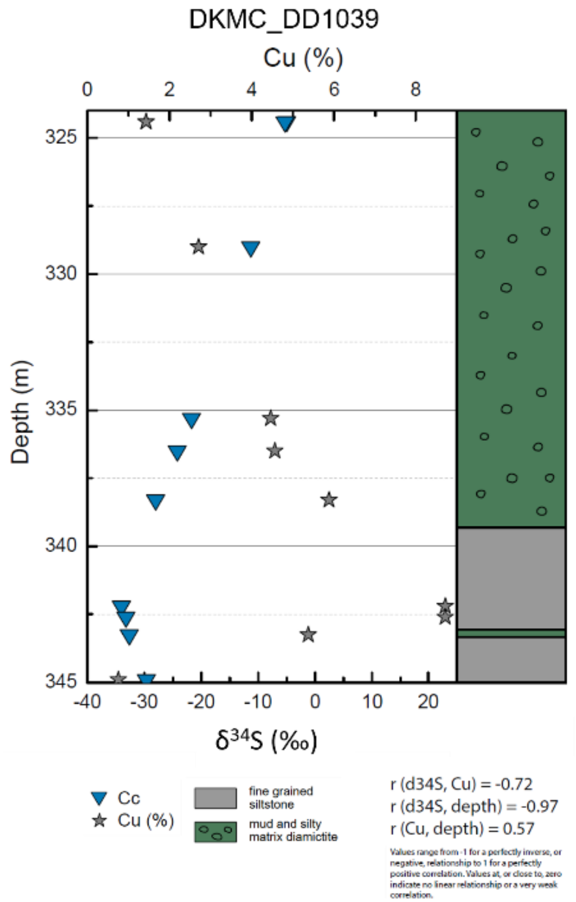

Figure 69: $\delta^{34}S$ variations in sulphides from DKMC_DD1039, Kakula. Cc – chalcocite; Cu% – copper assays.

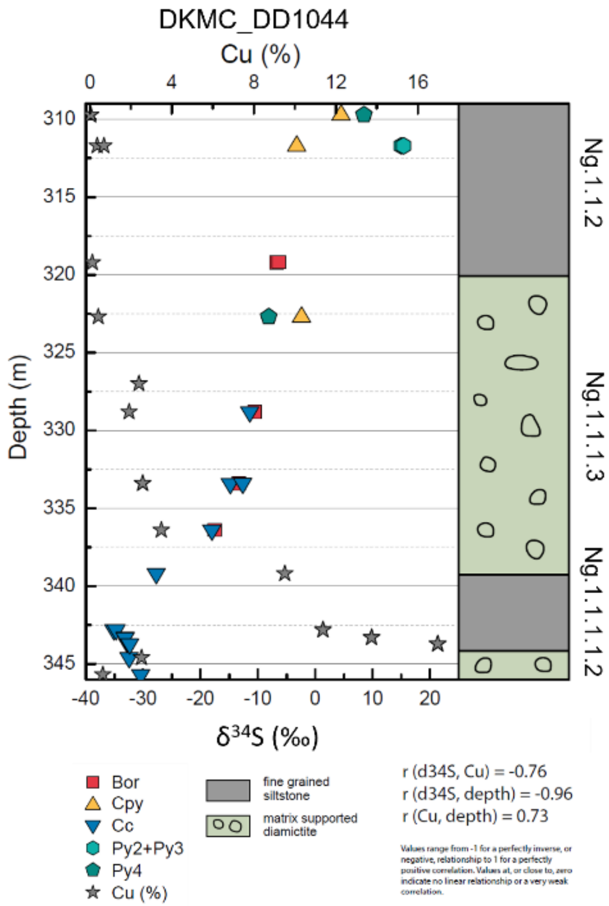

Figure 70: $\delta^{34}S$ variations in sulphides from DKMC_DD1044, Kakula. Bn – bornite; Cpy – chalcopyrite; Cc – chalcocite; Py2+Py3, Py4 – pyrite generations; Cu% – copper assays.

A review of the S isotope data indicates that Py1 within the fine-grained siltstones displays predominantly negative $\delta^{34}S$ values between -19.9 and -10 ‰ that supports biogenic reduction. This range is narrower but similar to the range from -11 to +3 ‰ reported for diagenetic pyrite by Schmandt et al., (2013) who used the microdrilling technique for sampling and favoured a sulphate reduction origin for this pyrite. The second-stage inclusion-rich pyrite (Py2) with the cores and coarse-grained pyrite (Py3) are both similarly enriched in the heavy S isotope within the wider range from -13.0 to 22.4 ‰. Most of samples show a small irregular difference in $\delta^{34}S$ values for co-existing diagenetic and metamorphic pyrite not exceeding 1 - 3 ‰. In the borehole DKMC_DD571 the difference, however, may reach up to 10 ‰ indicating an absence of equilibrium. Pyrite generation Py4, associated with chalcopyrite within the matrix-supported diamictites, shows predominantly negative $\delta^{34}S$ values between -14.4 and -8.1 ‰, although a single analysis within the fine-grained siltstones indicates a higher value equal to 8.5 ‰ (DKMC_DD1044, Kakula).

All obtained values fall within the modern and ancient sedimentary pyrite values (Seal, 2006), and if the isotopically light signature of the pyrite is likely a product of biogenic reduction, then the later pyrite generations that are irregularly enriched in heavy isotope may be a consequence of isotope fractionation or an input of isotopically heavy sulphur from sulphate-bearing fluid. Bornite sampled within the matrix supported diamictite displays mixed $\delta^{34}S$ values ranging from -17.5 to 8.1 ‰, with a bornite + covellite sample showing a low value of -13.2 ‰. Chalcopyrite in siltstones mostly displays consistent negative $\delta^{34}S$ values of between -12.9 to -8.1 ‰ with a few compositions enriched in the heavy isotope within the range from -3.2 to +5.4 ‰. Analyses of chalcopyrite from matrix supported diamictites also yielded similar negative $\delta^{34}S$ values that range from -13.2 to -12.4 ‰, while those from fine-grained siltstones with dropstones fall into the similar range between -13.6 and -11.8 ‰. As a whole, chalcopyrite shows the most homogeneous S isotope composition that may be interpreted as evidence of achieving an equilibrium with the fluid, which transported isotopically homogeneous sulphur. Cobaltite within matrix supported diamictites shows predominantly negative $\delta^{34}S$ values ranging between -12.7 and -8.0 ‰, similar to co-existing chalcopyrite. The most drastic sulphur isotopic variations are exhibited by the sulphur isotope compositions of chalcocite. Chalcocite within the fine-grained siltstones predominantly exhibits extremely low $\delta^{34}S$ values between -35.1 and -29.6 ‰. Chalcocite from matrix-supported diamictites shows negative $\delta^{34}S$ values within a range of -34.0 and -9.4 ‰, with a single analysis indicating a higher value equal to 9.1 ‰ (DKMC_DD624). Chalcocite from the diamictite with a mud and silty matrix is enriched in the light sulphur isotope with $\delta^{34}S$ values between -28.0 and -5.0 ‰. At Kakula, the S isotope composition of chalcocite shows a regular trend of upward enrichment in the heavy isotope with the lowest $\delta^{34}S$ values observed at the base of the orebody regardless the host lithology (Fig. 69 and Fig. 70). This trend should be a result of abiogenic reduction and isotope fractionation, as we did not envisage a participation of bacteria at the stage of chalcocite replacement, which may explain the mechanism for fractionating the S isotopes.

As a whole, ore sulphides at Kamoa exhibit both a relatively homogeneous distribution of sulphur isotopes (in chalcopyrite and bornite) and large-scale isotope fractionation resulting in highly negative values in chalcocite-enriched orebodies. Recent sulphur isotope studies offer a deeper understanding of the geochemical processes involved in the formation of the SHC deposits in the Zambian and Congo Copperbelt (Fig. 71). Hendrickson et al., (2015) studied the Fishtie copper deposit (Lusale basin) in Zambia and proposed that copper sulphides enriched in the heavy S isotope were derived from thermochemical reduction of Neoproterozoic seawater sulphate. Schmandt et al., (2013), at Kamoa, suggested that most of the sulphur in the copper sulphides was derived from earlier formed diagenetic iron sulphide, emphasising the role of early hydrothermal activity in the region. Burnard et al., (1993) studied the Nampundwe deposit in the south-central part of the Katanga basin in Zambia at which distinct pyritic sheets occur and suggested diverse sources of sulphur, including mixing processes and changes in fractionation related to the physical and chemical conditions at the time of precipitation. Studies by Qiaofan et al., (2021) focused on the S isotope compositions of chalcopyrite and bornite within the main ore body of the Chambishi deposit (Zambia). Their findings suggest that sulphur was derived from early diagenetic sulphide originated by reduction of seawater sulphate. Sulphides occurring within the sediment-hosted copper (SHC) deposits of the Central African Copperbelt show an extremely wide range of $\delta^{34}S$ variations (Dechow and Jensen, 1965; Schwarcz and Burnie, 1973; Ohmoto, 1986; Okitaudji-Lokoho, 1989; Sweeney et al., 1986; Annels, 1989; Sweeney and Binda, 1989; McGowan et al., 2003; Lerouge et al., 2005; Selley et al., 2005; Haest et al., 2009) although the highly negative $\delta^{34}S$ values for chalcocite in this study are reported for the first time. The wide range of sulphur isotopic variations are consistent with sulphur isotopic data obtained from other SHC deposits over the world (Bechtel et al., 2001; Burnie et al., 1972).

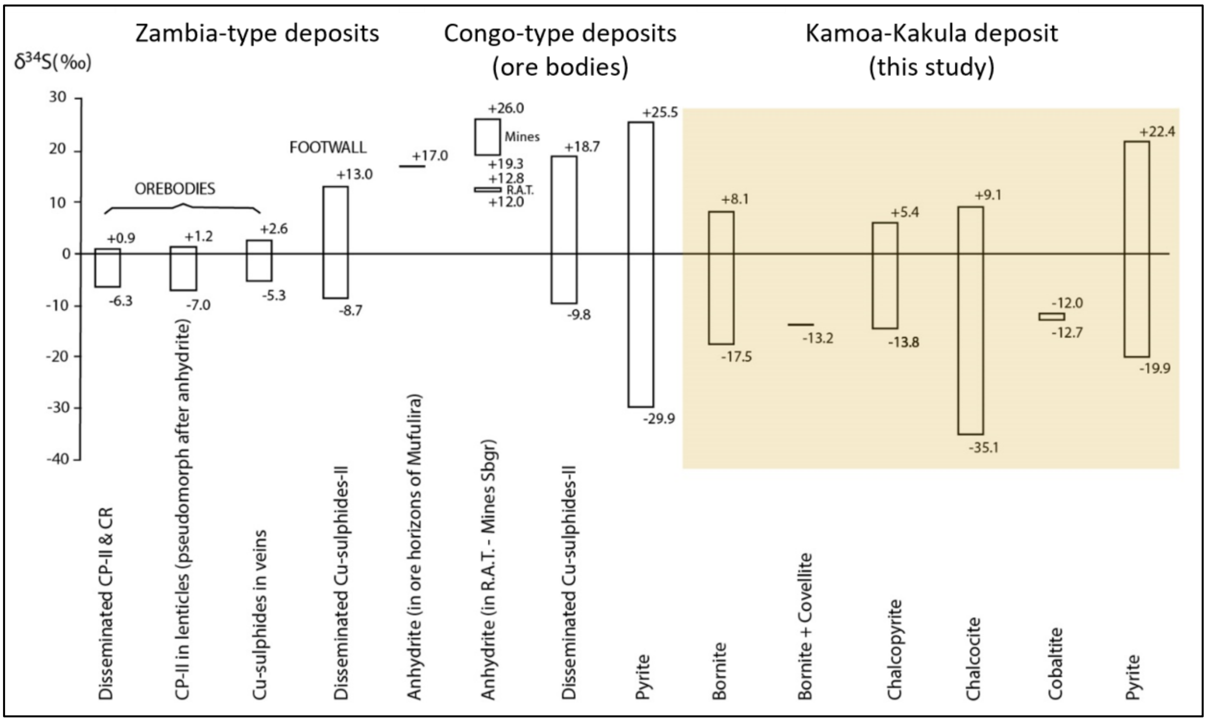

Figure 71: Comparison of $\delta^{34}S$ values for sulphides / sulphates from selected studies from Zambia and DRC deposits. In Zambia, sulphides from the ore shale, footwall and veins at Konkola, sulphates from Mufulira ore horizons (data from Sweeney et al., 1986; Cailteux et al., 2005). In DRC from Kamoto, Kambove - Ouest, Luswishi, Etoile, Ruashi; data from Okitaudji, 1989 and Lerouge et al., 2004), and data for this study (Kamoa – Kakula). CP – chalcopyrite; CR – carrollite.

The sulphur isotopic variations observed from the S isotope data from this study, supports the previous conclusion reached by Schmandt et al., (2013). In particular, the similarity of the S isotope compositions of pyrite and main-stage chalcopyrite and bornite suggest an inheritance of diagenetic S at consequent replacement. However, the S isotope composition of later pyrite generations (within the siltstone), indicates contribution from a source enriched in the heavy S isotope. The highly negative values recorded for ore chalcocite, for the first time, indicate extreme S isotope fractionation during the low-temperature process of replacement.

6.5 Geophysics

An airborne magnetics survey ~200 km southeast of the study area, in Northwestern Province – Zambia, executed by First Quantum Minerals (FQM) in 1997 and 1998 was reviewed to provide regional context. The airborne survey image is taken from Colorado School of Mines PhD Thesis by James Barron (2003). The survey covered 26,429 line-km at azimuth of 0°, line spacing of 200m and control lines at azimuth 090° with 2000 m spacing (Barron, 2003 – flown by FQM, 1998). The reduced to pole (RTP) processing method of this airborne survey reveals a variety of magnetic anomalies of; coarse, irregular, circular, clustered, elongate and broad characteristics. A distinct magnetic anomaly delineates the Solwezi dome and this response is likely to be associated with the ‘rimming quartzite’, a talc-kyanite-hematite bearing quartz-mica schist (Bernau, 2007; Broughton, 2014; MacIntyre, 2019). Other distinguishable anomalies from the survey include graphitic shales, mafic rocks, large scale structures, siliciclastic geometries exhibiting folding and domal features, as well as basement signatures (Fig. 72 and Fig. 73). This briefly highlights the significance of geophysical surveys to the region and its relevance to geological understanding and interpretation.

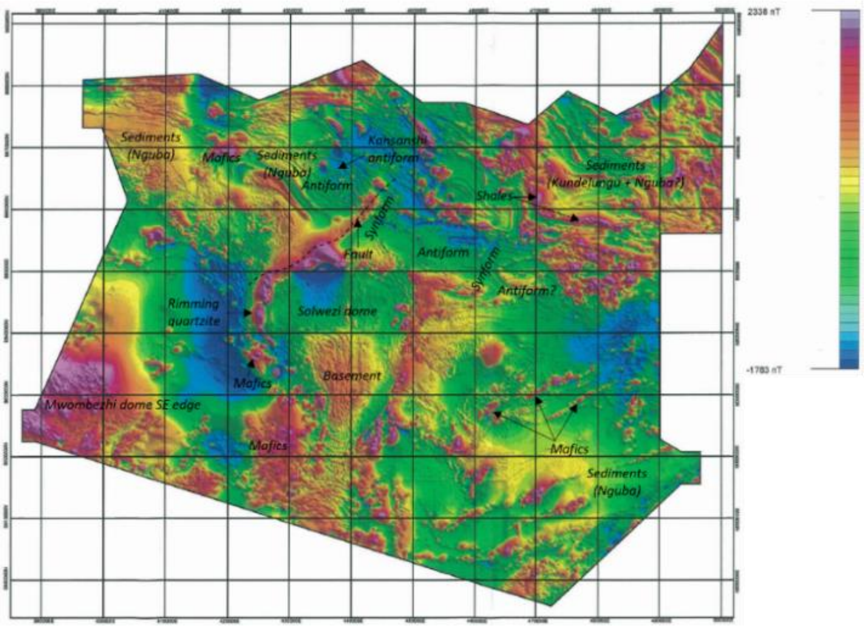

Figure 72: Reduced to the pole magnetic (RTP) map of the Solwezi area in the Northwestern Province of Zambia. The magnetic intensity ranges are from; 2338nT to -1783nT (Source: Barron, 2003. PhD Thesis, p.45. – flown by FQM, 1998).

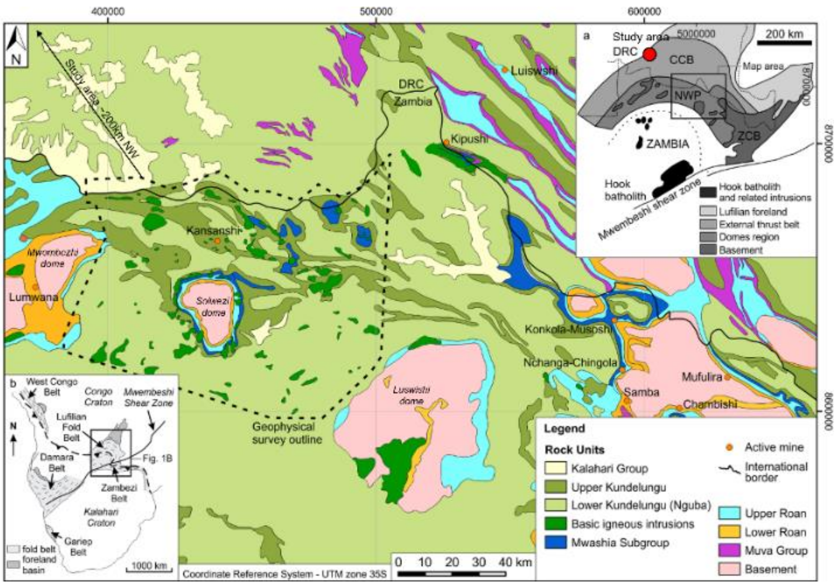

Figure 73: Geological interpretation of the Central African Copperbelt in the Northwestern area of Zambia proximal to DRC border ~200km southeast of study area (Bacha et al., 2023, modified after Barron 2003; Hitzman et al., 2012; Selley et al., 2018).

6.5.1 Kamoa North (bonanza zone); geophysical forward modelling

A North-south section (306700 E), from Kamoa North ‘bonanza zone’ (Fig. 74 and Fig. 75) was selected with the objective of applying geophysical forward modelling techniques. Provided by these images is the spatial context of the location of Kamoa North, as well as lithologies, interpreted faults and the position of observed mineralisation (i.e., within the diamictite; Ng1.1.1 and the siltstone; Ng1.1.2). Methods such as gravity, magnetics, resistivity, and induced polarisation (IP) are well known geophysical methods proven to contribute to understanding the geometric and compositional characteristics within the sub-surface and are collected from surface or airborne (Telford et al., 1990).

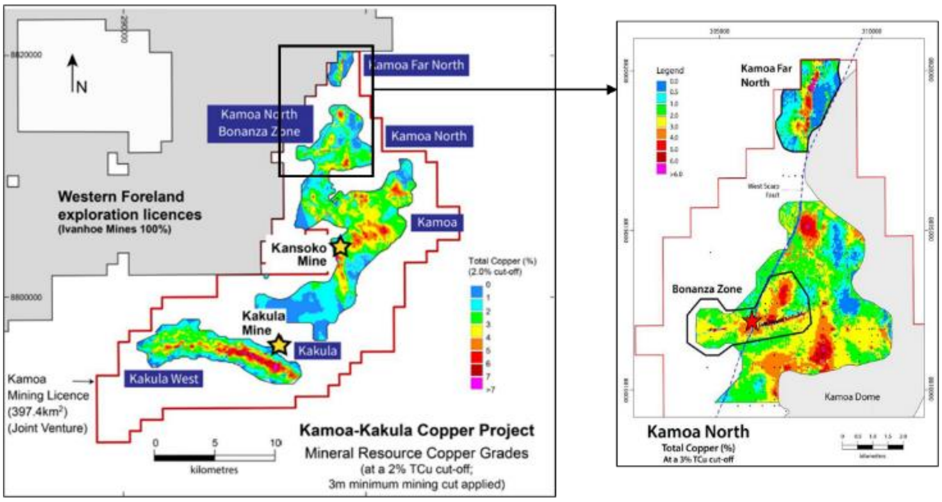

Figure 74: Copper grades by location at Kamoa - Kakula and location of bonanza zone (Ivanhoe, 2023).

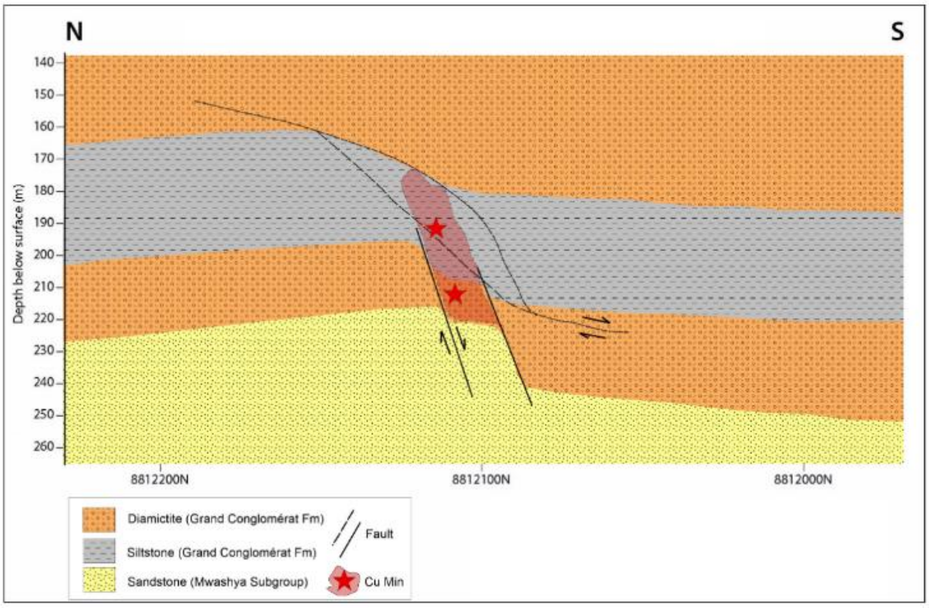

Figure 75: Kamoa north bonanza zone interpreted geological cross-section (compiled for this study).

6.5.2 Gravity

The gravity model for Section 306700 E (Kamoa north 'bonanza zone') was produced using density contrasts shown by Table 15. This shows the average density values by lithology from SG measurements taken from drillholes on this section, along with calculated density contrast values. The minimum value a gravimeter can detect is 0.04 mGal, therefore the response of material with gravity measurements above this value can be modelled. The forward gravity model was modelled in grav2dc (Fig. 76). The forward model produces a positive gravity anomaly with an intensity of 2.36 mGal, overlying the position of the sulphide zone. This zone has a density contrast to surrounding lithologies (basal diamictite and KPS) of 0.75. The sulphide zone has a higher density than surrounding rocks and it is this characteristic that enables the forward model to produce the positive geophysical gravity anomaly that is observed.

Table 15: Density values and density contrasts for grav2dc forward model

Unit	Density[1]	Density contrast
Diamictite	2.3	-0.05
KPS - shale	2.7	0.35
Diamictite	2.5	0.15
Mineralised body	3.1	0.75
Sandstone	2.35	background

[1]Average density values from Kamoa North SG measurements (Section 5.6; Fig. 49)

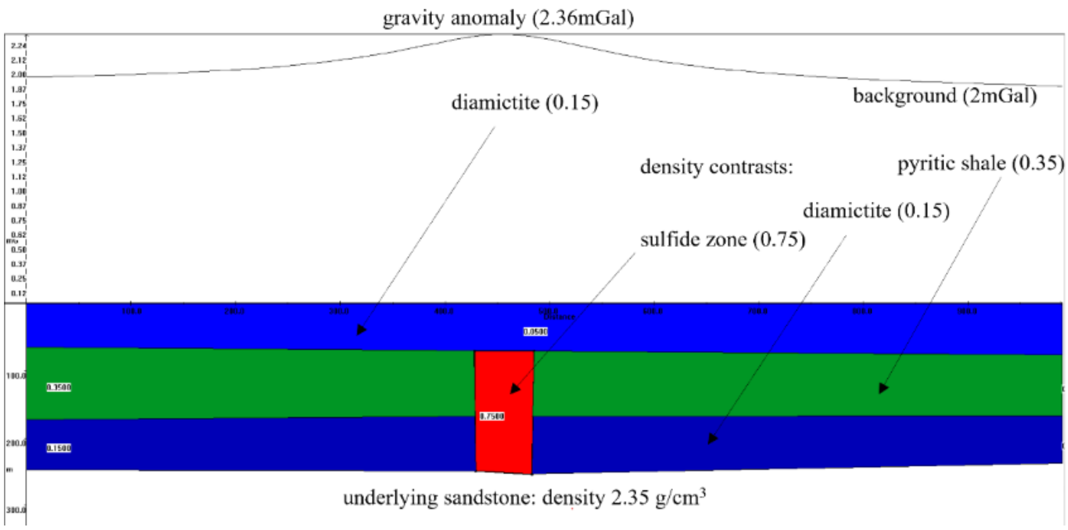

Figure 76: Kamoa north 'bonanza zone' gravity forward model section (grav2dc).

The gravity response shown by section illustrated in Fig. 76, indicates that the gravity geophysical technique would be suitable to determine zones hosting dense sulphides. The technique would be less effective in areas where the sulphides and lithologies are laterally extensive as the method would be less effective due to this broad and lateral extent. Disturbance may also be caused by thick overburden that may mask the gravitational response.

6.5.3 Magnetics

Average magnetic susceptibility values were obtained for the purposes of magnetics forward modelling (Table 16). Subsequently a magnetics forward-model was produced in mag2dc (Fig. 77). From this model a positive magnetic anomaly of ~350 nT was observed directly overlying the modelled sulphide zone. This anomaly results from the contrasting magnetic susceptibility values of the sulphide mineralised zone in comparison to the surrounding sedimentary rock units (diamictite and shale). For the purposes of this model, the background lithology of sandstone is not displayed.

When the sulphide zone depth was varied within mag2dc (made deeper), the amplitude of the anomaly reduced. This implies that the anomaly is strongest when the sulphide zone is closest to surface. For regional interpretation, as exhibited by the profile, magnetics would be a suitable survey method and could provide context to the potential position of sulphide bodies in the subsurface, as well as graphitic shale packages. It is important to note that this method responds to magnetic minerals and therefore an understanding of the specific mineralogy occurring in an area is required. This characteristic is what produces an anomaly in the mag-profile of a forward model, due to thee contrasting magnetic susceptibilities against the host rocks.

Table 16: Mag-susc mag2dc forward model parameters

Unit	Mag Susceptibility[1]
Diamictite	0.003
KPS - shale	0.002
Diamictite	0.003
Mineralised body	0.2
Sandstone	0.0009

[1]Morgan, (2012); Dentith and Mudge, (2014)
[2]Magnetic model parameters generated in CrowdMag calculator

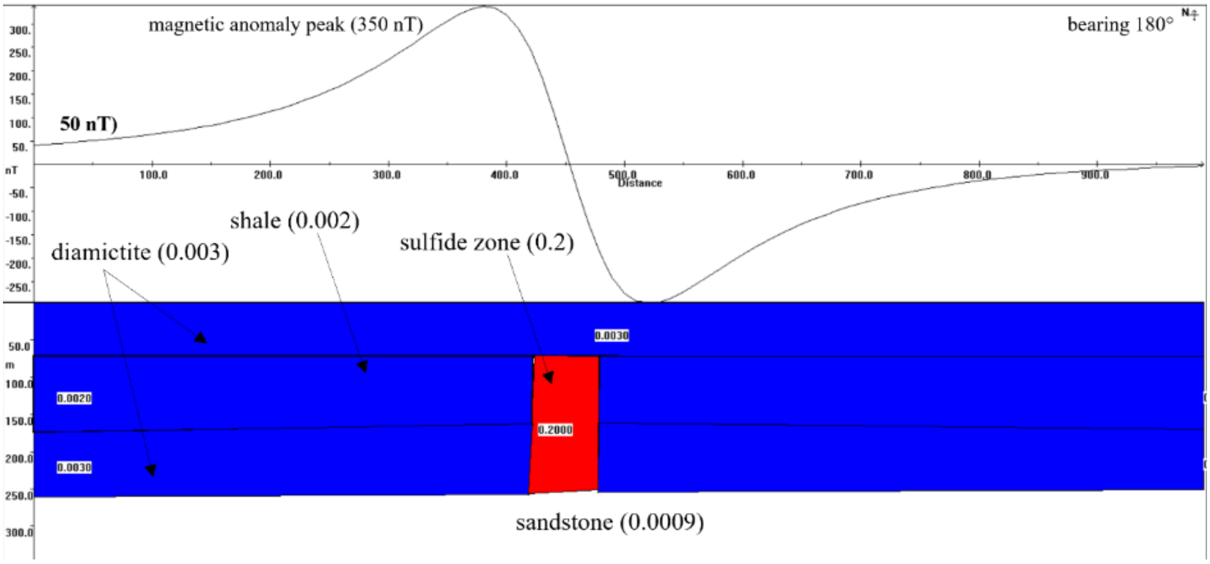

Figure 77: Kamoa North 'bonanza zone' magnetics forward-model section (mag2dc).

6.5.4 Resitivity

This method measures the electrical resistivity of a particular area in the subsurface . Resistivity values for lithotypes were obtained and input into res2Dmod as the resistivity parameters (Table 17). These values were then used in res2Dmod and numerous iterations and resistivity survey array configurations were tested. The most appropriate array for the forward model was the Wenner beta array. The resistivity pseudo-section of Section 306700E, Kamoa north 'bonanza zone' (Fig. 78) shows a highly negative resistivity anomaly. This is due to the characteristic low resistivity (high conductivity) properties of the sulphide zone (0.3 Ω·m), and higher resistivity of surrounding rocks. It was observed that the anomaly is broader than expected and this may be attributed to the occurrence of unmineralised rock types and overburden that overlie the sulphide zone. Due to the conductive nature of the sulphide zone and reasonable magnetic susceptibility contrast with surrounding lithologies, this confirms that the resistivity technique is effective.

Table 17: Resistivity res2Dmod forward model parameters

Unit	Resistivity (Ω.m)[1]
Diamictite	10,000
KPS - shale	2,000
Diamictite	10,000
Mineralised body	0.30
Sandstone	4,000

[1]Abidin et al., (2011); Sucipta et al., (2019)

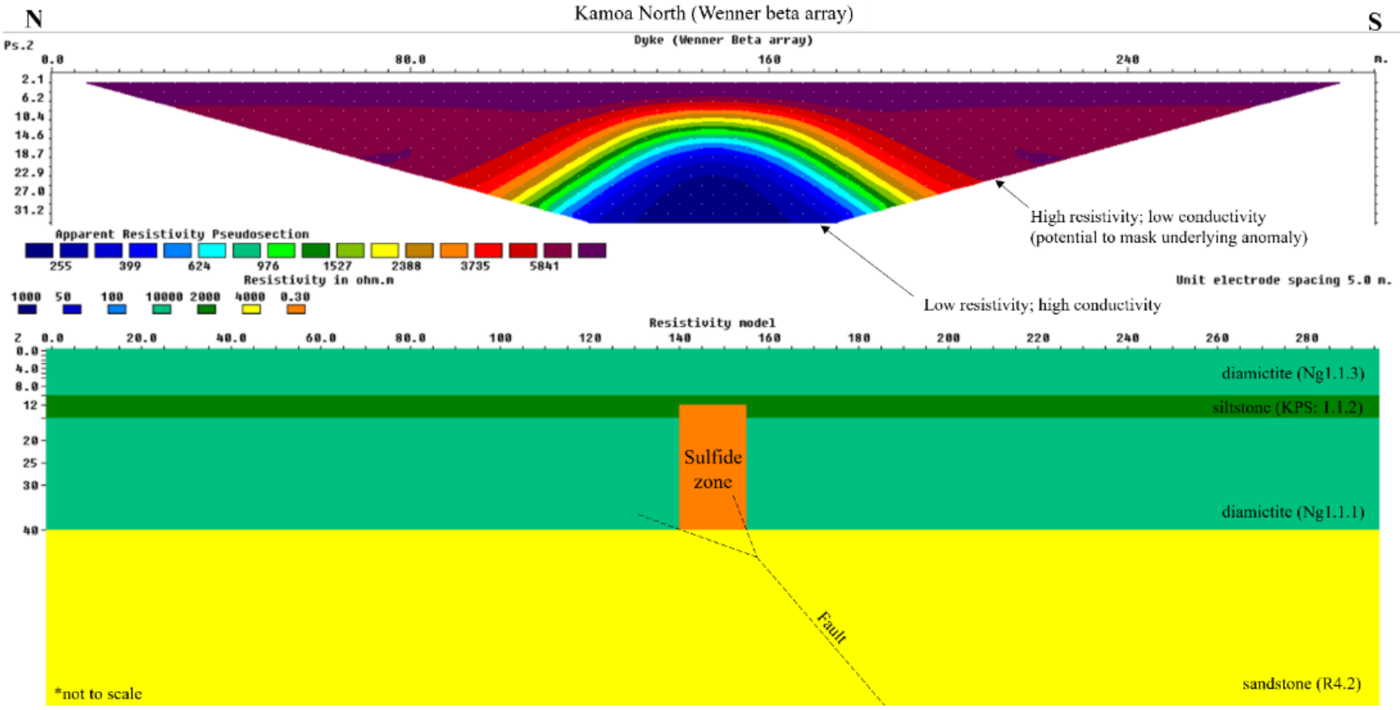

Figure 78: Kamoa North 'bonanza zone' resistivity forward-model pseudo section (Res2Dmod).

6.5.5 Application of geophysical techniques

The application of geophysical techniques continues to be widely applied in Mining and Exploration, relying on the contrasting subsurface physical properties. The regional geology of the Katanga basin (Central African Copperbelt) is dominated by sedimentary sequences (Hitzman, 2005; Hitzman et al., 2012) of variable densities, physical properties and mineralogical features. The mineral assemblages that have been described in this study highlight the occurrence of pyrite, chalcopyrite, bornite and chalcocite as the dominant sulphide assemblage, whilst magnetite has also been observed. Therefore, the properties of this mineralogy would have an effect on the usefulness of geophysical techniques. The gravity technique would be best suited to determine contrast in subsurface densities and whilst contrasts between sedimentary packages may be indistinct, sulphide bodies, intrusions, salt and sandstone horizons may be detected due to this variance in density. Since the Domes region of the Central African Copperbelt (in Zambia) forms as result of north directed folding and thrusting associated to the Pan-African Lufilian orogeny (Selley et al., 2005) this causes the occurrence of the basement-highs and, to the north, the halokinetic structures. Domal structures associated to the basement topography are the most targeted structural setting for copper mineralisation in this part of the region (Broughton et al., 2002; MacIntyre, 2019). The juxtaposition of basement against sediments creates a geological setting where large scale density contrasts between basement and adjacent sediments can be observed and used to target dome structures, by a variety of geophysical techniques.

Other geological settings include the regions dominantly affected by salt-tectonics (halokinesis) mainly observed in the DRC (Cailteux et al., 2005; Selley et al., 2005) and can similarly create architectural settings of contrasting rock properties. These contrasting features and complex geological architecture create anomalies that can be investigated by geophysical techniques. The application of magnetics and resistivity can aid the detection of mineralised ore bodies or magnetic lithologies within the subsurface or brought to surface by geodynamic or transient events. The mineralisation process as described by Hitzman et al., (2010) highlights the necessary components of a mineral system, which can include mobile reductants, hydrocarbons or reduced carbonaceous shales to promote and trigger sulphide precipitation. This may result in formation of magnetic minerals or reduced environments, distinct from the surrounding rocks.

Additional techniques such as seismic reflection e.g., were applied at the Kansanshi Cu-Au deposit, Domes region. This data was acquired using 10 m shot and receiver spacing (28 Hz geophones) and a SIST-type seismic source (FQM 2013; reported by Malehmir and Juhlin, 2023). This demonstrated that seismics can be an effective method to improve our understanding of the geological structures near surface as well as at deeper levels to decipher the structural regime that controls and concentrates mineralisation.

6.5.6 Mineralisation model

At Kamoa – Kakula sulphide mineralisation, inclusive of economic copper sulphides, are preferentially hosted within the basal conglomerate, intercalated lithologies and the Kamoa-Pyritic-Siltstone. The process of mineralisation at Kamoa (Fig. 79) involves the migration of metal bearing oxidised brines through a permeable aquifer, i.e., the Mwashya Subgroup sandstone. The migration of these fluids occurs through pathways, faults such as the Mupaka fault and / or faults associated to the Kansoko Sud trend, amongst other growth faults. Subsequently the chemical precipitation of sulphides occurs upon these sulphate bearing fluids crossing the redox boundary towards reduced facies. This precipitation of sulphides occurs within the reduced horizon. The reduced horizon is the diamictites and siltstones (KPS) of the Grand Conglomérat Fm.

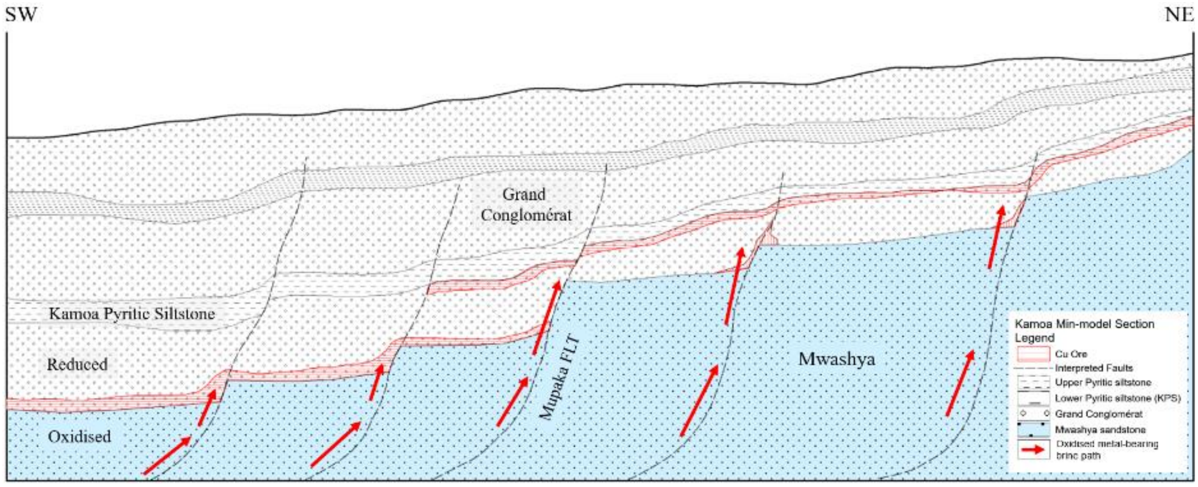

Figure 79: Schematic section showing the mineralisation model at Kamoa (redox-reaction conceptual model created after Hitzman et al., 2005; Broughton and Rogers, 2010; Hitzman et al., 2010; Schmandt, 2013; Twite, 2016; Twite et al., 2019).

The stratigraphy hosting the Fishtie Cu deposit in the Lusale sub-basin in the Central province of Zambia is underlain by basement schists and quartzites of the Muva Supergroup (Fig. 80). Whilst earlier discussions highlighted the similarities in the geological setting of Fishtie and Kamoa, the ore-bearing Grand Conglomérat Fm. at Kamoa is instead underlain by Mwashya Subgroup sandstone of the Roan Group. The Fishtie deposit is hosted within dolostone (Kakontwe Fm) overlying diamictite and siltstones (Grand Conglomérat) stratigraphically towards the base of the Nguba Group (Hendrickson, 2013; Simusokwe, 2021). The model of its formation involves the precipitation of sulphide mineralisation due to the redox conditions arising from the transport of ore bearing fluids from the lower parts of the Lusale sub-basin through high-angle faults to the reduced package of diamictite and siltstones in the upper parts of the stratigraphy (Hendrickson, 2013; Hendrickson et al., 2015; Simusokwe, 2021). A similar fault and redox-reaction controlled model that involves the migration of ore-bearing fluids through an aquifer to reduced sedimentary sequences (diamictites and siltstones) of the Grand Conglomérat is also suggested for Kamoa (Broughton and Rogers 2010; Schmandt, 2013; Twite, 2016; Twite et al., 2019).

The Fishtie deposit is mainly a copper-sulphide (with lesser copper oxide) deposit and is positioned closer to surface than Kamoa. As a result, in addition to hypogene sulphide mineralisation, supergene copper-oxide mineralisation is observed within the Kakontwe Fm., overlying the Grand Conglomérat (Hendrickson, 2013; Hendrickson et al., 2015).

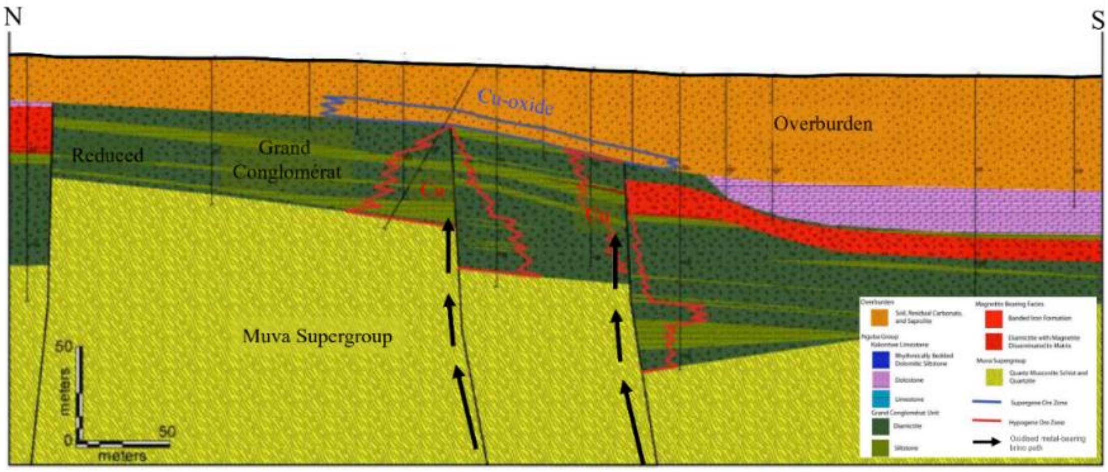

Figure 80: Schematic section showing the mineralisation model at Fishtie (after Hendrickson, 2013).

The model of stratiform sulphide mineralisation within the sedimentary environment involves the movement of hydrothermal fluids through appropriate structural and geodynamic settings. The subsequent redox reaction processes that occur between oxidised and reduced facies, triggers the precipitation of copper sulphides (Cailteux et al., 2005; Hitzman et al., 2005; Selley et al., 2005; Hitzman et al., 2010; Heinrich and Candela, 2013; Hitzman et al., 2012). This is the supported model and process responsible for the occurrence sulphide mineralisation at Kamoa – Kakula. The ore paragenesis within the Neoproterozoic Central African Copperbelt is dominated by Cu – Co sulphide speciation. This mineralisation has several indicators that suggest that the sulphide mineralisation is associated to early diagenetic and late diagenetic processes, with tectonism and metamorphism controlling additional fluid input, as well as remobilisation of primary mineralisation resulting in sulphide enrichment (Cailteux et al., 2005; Hitzman et al., 2005). Understanding the fluid migration pathways, accumulation, concentration and the integration of the geological, geophysical, geochemical and geoscientific datasets is of significant importance. This is in addition to understanding mineral system components such as regional fertility, lithospheric architecture, geodynamic settings and preservation potential (Megill, 1988; Wyborn et al., 1994; Knox-Robinson and Wyborn 1997; McCuaig and Hronsky, 2014; Occhipinti et al., 2016; Groves et al., 2022). Although the source of metal is widely debated, the presence of red beds (a permeable aquifer), reduced lithology, a favourable deformation pattern, a chemical or structural trap, respectivey, as well as evaporites, a S source and a potential seal, can be considered the critical componentsof the sediment-hosted copper mineral system (Hitzman et al., 2005; Hitzman et al., 2012).

7 CONCLUSION

The world-class Kamoa – Kakula copper deposit is located directly to the west of the traditional, fragmented host rocks of the Congolese Copperbelt, characterised by Pan-African Lufilian deformation and salt-tectonics resulting in the diapiric extrusion of the Roan Group sediments. The regional stratigraphic correlation within this study shows that the Mine Series Subgroup (R2) in DRC occurs at an equivalent stratigraphic level to the sedimentary sequence the Kitwe Fm. in Zambia. Sediments of the Mwashya Subgroup (R4 in DRC and Mwashya in Zambia) were deposited during prominent regional extension in the Neoproterozoic Katanga basin. Overlying the Mwashya Subgroup is the Cryogenian Grand Conglomérat Fm., hosting the Kamoa Cu deposit. This Sturtian glaciogenic formation is observed to continue into Zambia, hosting ore deposits such as Kansanshi (Cu-Au; Domes region) and Fishtie (Cu; eastern basin). Observations from this study recognise the polymictic subrounded to subangular clasts and dropstones within the diamictite, supporting its glacial origin with later tectonic overprint demonstrated by elongate strain development in the clasts.

The range of the $\delta^{34}S$ values indicates that a significant portion of the reduced sulphur in rocks originated from early bacterial sulphate reduction reflected by the light S isotopic signatures of framboidal pyrite (to -19.9 ‰). The similar while narrower range of the $\delta^{34}S$ values for chalcopyrite suggests inheritance and homogenization of the initial S isotope composition during a relatively high-temperature hydrothermal event. The S isotope composition of later generations of pyrite indicate a contribution from a source enriched in the heavy isotope (up to 22.4 ‰ in Py2+Py3), whereas the highly negative $\delta^{34}S$ values for chalcocite (to -35.1 ‰) argue for extreme isotope fractionation under low-temperature conditions. This study recognises that economic sulphide mineralisation occurs due to the redox processes resulting from the breach of the boundary between the Grand Conglomérat diamictite package and underlying Mwashya sandstone. This results in the formation of disseminated copper sulphide mineralisation by the replacement of diagenetic pyrite and precipitation of hydrothermal sulphides. The distinct mineral zonation pattern is exhibited by replacement textures involving Py → Cpy → Bn + Cov → Cc. Minor amounts of carrollite and Co sulpho-arsenides are observed and their occurrence determined to be subeconomic. Geophysical forward-modelling indicates that sulphide mineralisation is responsible for signals in geophysical methods such as gravity, magnetics and resistivity, producing observable anomalies and demonstrating that these methods are suitable for the detection of concealed ore bodies.

8 REFERENCES

Annels, A.E. and Simmonds, J., (1984). Cobalt in the Zambian Copperbelt. Precambrian Research, 25, p.75-98.

Annels, A.E., (1989). Ore genesis in the Zambian Copperbelt, with particular reference to the northern sector of the Chambishi Basin, in Boyle, R.W., et al., eds., Sediment-hosted stratiform copper deposits: Geological Association of Canada Special Paper 36, p. 427-452.

Allen, P., Bowring, S., Leather, J., Brasier, M., Cozzi, A., Grotzinger, J.P., McCarron, G. and Amthor, J.J., (2002). Chronology of Neoproterozoic glaciations: New insights from Oman. 16th International Sedimentological Congress, p.7-8.

Bacha, R.R., Mungall, J. and Ernst, R.E., (2023). Petrogenesis of the Katangan mafic rocks, Zambia: Insights from lithogeochemistry, LIP classification, and petrological modeling. Results in Geochemistry, 12, 100027.

Batumike, J., Cailteux, J., and Kampunzu, A., (2007). Lithostratigraphy, basin development, base metal deposits, and regional correlations of the Neoproterozoic Nguba and Kundelungu rock successions, central African Copperbelt. Gondwana Research 11. p.432-447.

Barron, J., (2003). The Stratigraphy, metamorphism, and tectonic history of the Solwezi Area, Northwest Province, Zambia: integrating geological field observations and airborne geophysics in the interpretation of regional geology. Colorado School of Mines. PhD Thesis.

Bechtel, A., Sun, Y., Püttmann, W., Hoernes, S. and Hoefs, J., (2001). Isotopic evidence for multi-stage base metal enrichment in the Kupferschiefer from the Sangerhausen Basin, Germany. Chemical Geology, 176, p.31-49.

Begg, G., Griffin, W., Natapov, L., O'Reilly, S., Grand, S., O'Neill, C., Hronsky, J., Djomani, Y., Swain, C., Martin, T. and Bowden, P., (2009). The lithospheric architecture of Africa: Seismic tomography, mantle petrology, and tectonic evolution. Geosphere, 5, p.23-50.

Bernau, R., (2007). The geology and geochemistry of the Lumwana Basement hosted copper-cobalt (uranium) deposits, NW Zambia. University of Southampton. MSc. Thesis.

Bernau, R., Roberts, S., Richards, M., Nisbet, B., Boyce, A. and Nowecki, J., (2013). The Geology and Geochemistry of the Lumwana Cu (± Co ± U) deposits, NW Zambia. Mineralium Deposita, 48, p.137-153.

Bowen, R., & Gunatilaka, A., (1976). The Zambian Copperbelt. Science Progress (1933), p.87-109.

Bogdanova, S., Pisarevsky, S. and Li, Z.-X., (2009). Assembly and Breakup of Rodinia (Some results of IGCP project 440). Stratigraphy and Geological Correlation, 17, p.259-274.

Broughton, D., Hitzman, M. and Stephens, A.J., (2002). Exploration history and geology of the Kansanshi Cu-(Au) deposit, Zambia. Society of Economic Geologists Special Publication 9, 9, p.141-153.

Broughton, D. W., (2014). Geology and Ore deposits of the Central African Copperbelt. Colorado School of Mines. PhD Thesis.

Broughton, D., and Rogers, T., (2010). Discovery of the Kamoa copper deposit, Central Africa Copperbelt, D.R.C. Society of Economic Geologists, Special Publication 15, v. 1, p.287-297.

Brown, A.C., (2018). Latent volcanic heat and further unique aspects of early diagenetic stratiform copper mineralization in the White Pine-Presque Isle District, northern Michigan. Mineralium Deposita, v.53, 5, p.721-728.

Bull, S., Selley, D., Broughton, D., Hitzman, M., Cailteux, J., Large, R. and McGoldrick, P., (2011). Sequence and carbon isotopic stratigraphy of the Neoproterozoic Roan Group strata of the Zambian Copperbelt. Precambrian Research, 190, p.70-89.

Burnard P.G., Sweeney M.A., Vaughan D.J., Spiro B., Thirlwall M.F., (1993). Sulfur and isotope constraints on the genesis of a southern Zambian massive sulfide deposit. Economic Geology 88: p.418-436

Burnie S. W., Schwartz H. P. and Crocket J. H., (1972). A sulfur isotopic study of the White Pine Mine, Michigan. Econ. Geology 67, p.895-914.

Cailteux, J., Binda, P., Katekesha, W., Kampunzu, A., Intiomale, M., Kapenda, D., Kaunda, C., Ngongo, K., Tshiauka, T., Wendorff, M., (1994). Lithostratigraphical correlation of the Neoproterozoic Roan Supergroup from Shaba (Zaire) and Zambia, in the central African copper-cobalt metallogenic province. Journal of African Earth Sciences. 19. p.265-278.

Cailteux, J., Kampunzu, A.B., Catherine, L., Alphonse, K. and Milesi, J.-P., (2005). Genesis of sediment-hosted stratiform copper - Cobalt deposits, central African Copperbelt. Journal of African Earth Sciences, 42, p.134-158.

Cailteux, J.L.H., Muchez, P., De Cuyper, J., Dewaele, S. and De Putter, T., (2018). Origin of the megabreccias in the Katanga Copperbelt (D.R.Congo). Journal of African Earth Sciences, 140, p.76-93.

Cailteux, J. and Putter, T., (2019). The Neoproterozoic Katanga Supergroup (D. R. Congo): State-of-the-art and revisions of the lithostratigraphy, sedimentary basin and geodynamic evolution. Journal of African Earth Sciences Volume 150, p.522-531.

Capistrant, P., Hitzman, M., Wood, D., Kelly, N., Williams, G., Zimba, M., Kuiper, Y., Jack, D. and Stein, H., (2014). Geology of the Enterprise Hydrothermal Nickel Deposit, North-Western Province, Zambia. Economic Geology, 110, p.9-38.

Castroviejo, R., (2023). A Practical Guide to Ore Microscopy—Volume 1: Mineral Identification. Cham, Springer International Publishing, p.211-213.

Caruso, A.S., Clarke, K.D., Tiddy, C.J., Delean, S. and Lewis, M.M., (2018). Objective Regolith-Landform Mapping in a Regolith Dominated Terrain to Inform Mineral Exploration. Geosciences, 9, p.318.

Chávez, W.X., Jr., (2021). Weathering of Copper Deposits and Copper Mobility: Mineralogy, Geochemical Stratigraphy, and Exploration Implications. SEG Discovery, p.16-27.

Cooper, G.R.J., (1997). Forward modelling of magnetic data. Computers & Geosciences, 23, p.1125-1129.

Cox, D. P., Lindsey, D. A., Singer, D. A., Moring, B. C., Diggles, M. F. (2003) Sediment-Hosted Copper Deposits of the World: Deposit Models and Database. U.S. Geological Survey, Open-File Report 03-107.

Crundwell, F.K., Du Preez, N.B., Knights, B.D.H., (2020). Production of Cobalt from Cu-Co ores on the African Copperbelt—An overview. Miner. Eng. 2020, 156, 106450.

Dechow, E., Jensen, M., (1965). Sulfur isotopes of some central African sulphide deposits: Economic Geology 60, p.894–941.

Dentith, M., & Mudge, S., (2014). Geophysics for the Mineral Exploration Geoscientist. Cambridge: Cambridge University Press. doi:10.1017/CBO9781139024358.

Dewaele, S., Muchez, Ph., Vets, J., Fernandez-Alonzo, M. and Tack, L., (2006). Multiphase origin of the Cu–Co ore deposits in the western part of the Lufilian fold-and-thrust belt, Katanga (Democratic Republic of Congo). Journal of African Earth Sciences, 46, p.455–469.

El Desouky, H., Muchez, P. and Cailteux, J., (2009). Two Cu–Co sulphide phases and contrasting fluid systems in the Katanga Copperbelt, Democratic Republic of Congo. Ore Geology Reviews, 36, p.315-332.

Erickson, L.E., (2017). Reducing greenhouse gas emissions and improving air quality: Two global challenges. Environ. Prog. Sustainable Energy, 36, p.982-988.

Farquhar, J. and Wing, B.A., (2003). Multiple sulfur isotopes and the evolution of the atmosphere. Earth and Planetary Science Letters, 213, p.1-13.

Fay, I. and Barton, M., (2011). Alteration and ore distribution in the Proterozoic Mines Series, Tenke-Fungurume Cu–Co district, Democratic Republic of Congo. Mineralium Deposita, 47-5, p.501-519.

François, A., (1973). L'extrémité occidentale de l'Arc cuprifere shabien. Étude Géologique: Bureaux d'Études Géologiques, Gécamines-Exploitation, Likasi, Zaire, p.65.

François, A., (1974). Stratigraphie, tectonique et minéralisations dans l'Arc cuprifére du Shaba (Rép.du Zaïre), in Bartholomé, P. (ed.), Gisements stratiformes et provinces cupriféres: Centenaire de la Société Géologique de Belgique, Liège, p.79-101.

François, C., Debaille, V., Paquette, J.-L., Baudet, D. and Javaux, E.J. 2018. The earliest evidence for modern-style plate tectonics recorded by HP–LT metamorphism in the Paleoproterozoic of the Democratic Republic of the Congo. Scientific Reports, 8, 15452.

Gilchrist, G., (2019). Evolving estimation techniques for an evolving world class stratiform copper deposit at Kamoa-Kakula, Democratic Republic of the Congo. Mining Goes Digital, p.192-200.

Graedel, T., Barr, R., Chandler, C., Chase, T., Choi, J., Christofferson, L., Friedlander, E., Henly, C., Jun, C., Nassar, N., Schechner, D., Warren, S., Yang, M.Y. and Zhu, C., (2012). Methodology of Metal Criticality Determination. Environmental science & technology. 46, p.1063-70.

Green, R., (2006). Remanent Magnetization and the Interpretation of Magnetic Anomalies. Geophysical Prospecting. Geophysical Prospecting, 8, 1, p. 98-110.

Grohol, M. and Veeh, C., (2023). Study on the critical raw materials for the EU 2023, Final report. 10.2873/725585.

Groves, D.I., Santosh, M., Müller, D., Zhang, L., Deng, J., Yang, L.Q. and Wang, Q.F., (2022). Mineral systems: Their advantages in terms of developing holistic genetic models and for target generation in global mineral exploration. Geosystems and Geoenvironment, 1, 100001.

Haest, M., Muchez, P., Dewaele, S., Boyce, A., von Quadt, A., Schneider, J., (2009). Petrographic, fluid inclusion and isotopic study of the Dikulushi Cu-Ag deposit, Katanga (D.R.C.): implications for exploration. Mineralium Deposita 44, p.505–522.

Hayes, T.S., Cox, D.P., Bliss, J.D., Piatak, N.M. and Seal II, R.R., (2015). Sediment-hosted stratabound copper deposit model. U.S. Geological Survey, Scientific Investigations Report 2010-5070-M.

Heinrich, C.A. and Candela, P., (2013). Fluids and Ore Formation in the Earth’s Crust. Treatise on Geochemistry: Second Edition, 13, p.1–28.

Hendrickson, M.D., (2013). Geology of the Fishtie copper deposit, Central Province, Zambia. Colorado School of Mines. MSc Thesis.

Hendrickson, M.D., Hitzman, M., Wood, D., Humphrey, J. and Wendlandt, R., (2015). Geology of the Fishtie deposit, Central Province, Zambia: iron oxide and copper mineralization in Nguba Group metasedimentary rocks. Mineralium Deposita, 50, p.717-737.

Herman, R., (2001). An introduction to electrical resistivity in geophysics. American Journal of Physics, 69, p.943-952.

Hirt, C., (2016), Gravity forward modelling. In: Encyclopaedia of Geodesy (Ed. E. Grafarend), 9 p., doi: 10.1007/978-3-319-02370-0_106-1.

Hitzman, M., Kirkham, R., Broughton, D., Thorson, J. and Selley, D., (2005). The Sediment-Hosted Stratiform Copper Ore System. Economic Geology, 100, p.609-642.

Hitzman, M., Selley, D. and Bull, S., (2010). Formation of Sedimentary Rock-Hosted Stratiform Copper Deposits through Earth History. Economic Geology, 105, p.627-639.

Hitzman, M., Broughton, D., Selley, D., Woodhead, J., Wood, D. and Bull, S., (2012). The Central African Copperbelt: Diverse stratigraphic, structural and temporal settings the world's largest sedimentary copper district. SEG Spec. Publ., 16, p.487–514.

Hoffman, P.F., Kaufman, A.J., Halverson, G.H., Schrag, D.P., (1998). A Neoproterozoic Snowball Earth. Science 281(5381), p.1342–1346.

Hoffman, P.F., 1999, The break-up of Rodinia, birth of Gondwana, true polar wander and the snowball Earth: Journal of African Earth Sciences, v. 28, p.17–33.

Hoffmann, K.-H., Condon, D. J., Bowring , S. A. & Crowley , J. L.(2004). U–Pb zircon dates for the Neoproterozoic Ghaub Formation, Namibia: constraints on Marinoan glaciation. Geology, 32, p.817– 820.

Hoffman, P., Abbot, D., Ashkenazy, Y., Benn, D., Brocks, J., Cohen, P., Cox, G., Creveling, J., Donnadieu, Y., Erwin, D., Fairchild, I., Ferreira, D., Goodman, J., Halverson, G., Jansen, M., Hir, G., Love, G., Macdonald, F., Maloof, A. and Warren, S., (2017). Snowball Earth climate dynamics and Cryogenian geology-geobiology. Science Advances, 3, 1.

Hoffman, P. F., Abbot, D. S., Ashkenazy, Y., Benn, D. I., Brocks, J. J., Cohen, P. A., Cox, G. M., Creveling, J. R., Donnadieu, Y., Erwin, D. H., Fairchild, I. J., Ferreira, D., Goodman, J. C., Halverson, G. P., Jansen, M. F., Hir, G. L., Love, G. D., Macdonald, F. A., Maloof, A. C., Partin, C. A., Ramstein, G., Rose, B. E. J., Rose, C. V., Sadler, P. M., Tziperman, E., Voigt, A., and Warren, S. G., (2017). Snowball Earth climate dynamics and Cryogenian geology-geobiology, Science Advances, 3, 1, e1600983.

Hronsky, J. and Groves, D., (2008). Science of targeting: Definition, strategies, targeting and performance measurement. Australian Journal of Earth Sciences - AUST J EARTH SCI, 55, p.3–12.

Hund, K., Porta, D., Fabregas, T., Laing, T. and Drexhage, J., (2023). Minerals for Climate Action: The Mineral Intensity of the Clean Energy Transition. Climate-Smart Mining Facility. World Bank Group. 10.1596/40002.

John, T., Schenk, V., Mezger, K. and Tembo, F., (2004). Timing and PT Evolution of Whiteschist Metamorphism in the Lufilian Arc-Zambezi Belt Orogen (Zambia): Implications for the Assembly of Gondwana. Journal of Geology - J GEOL, 112, p.71–90.

Johnston, D.T., (2011). Multiple sulfur isotopes and the evolution of Earth's surface sulfur cycle. Earth-Science Reviews, 106, p.161–183.

Kampunzu, A.B. and Cailteux, J.L., (1999). Tectonic Evolution of the Lufilian Arc (Central Africa Copperbelt) During Neoproterozoic Pan-African Orogenesis. Gondwana Research, 2, p.401-421.

Kampunzu, A.B., Cailteux, J.L.H., Kamona, A.F., Intiomale, M.M. and Melcher, F., (2009). Sediment-hosted Zn–Pb–Cu deposits in the Central African Copperbelt. Ore Geology Reviews, 35, p.263–297.

Kennedy, K., Eyles, N. and Broughton, D., (2018). Basinal setting and origin of thick (1.8 km) mass-flow dominated Grand Conglomérat diamictites, Kamoa, Democratic Republic of Congo: Resolving climate and tectonic controls during Neoproterozoic glaciations. Sedimentology, 66, 2, p.556-589.

Knox-Robinson, C. and Wyborn, L.A.I., (1997). Towards a holistic exploration strategy: Using Geographic Information Systems as a tool to enhance exploration. Australian Journal of Earth Sciences, 44, p.453–463.

Kröner, A. and Stern, B., (2004). Pan-African Orogeny. Encyclopedia of Geology (Second Edition). pp.259-270.

Lelièvre, P.G. and Oldenburg, D.W., (2006). Magnetic forward modelling and inversion for high susceptibility. Geophysical Journal International, 166, p.76–90.

Lerouge, C., Cailteux, J., Kampunzu, A.B., Milesi, J.P., Flehoc, C., (2004). Preliminary sulfur isotope data of the Luswishi ore deposit, RDC. In: CAG20, 20th Colloquium of African Geology, Orleans, France, 1–261.

Lerouge, C., Cailteux, J., Kampunzu, A., Milesi, J., Flehoc, C., (2005). Sulfur isotope constraints on formation conditions of the Luswishi ore deposit, Democratic Republic of Congo (DRC). Journal of African Earth Sciences 42, p.173–182.

Li, Z.X., Bogdanova, S.V., Collins, A.S., Davidson, A., De Waele, B., Ernst, R.E., Fitzsimons, I.C.W., Fuck, R.A., Gladkochub, D.P., Jacobs, J., Karlstrom, K.E., Lu, S., Natapov, L.M., Pease, V., Pisarevsky, S.A., Thrane, K. and Vernikovsky, V., (2008). Assembly, configuration, and break-up history of Rodinia: A synthesis. Testing the Rodinia Hypothesis: Records in its Building Blocks, 160, p.179–210.

Lur'ye A.M., Gablina I.F., (1982). Controlling factors of copper concentration during the exogenetic process. In: Factors controlling the formation of rare and nonferrous metallic mineral deposits. Nauka, Moscow, p.256.

Machel, H.G., (2001). Bacterial and thermochemical sulfate reduction in diagenetic settings – old and new insights. Sedimentary Geology, 140, p.143-175.

MacIntyre, T., (2019). Geology and geochemistry of the Kansanshi cu-(au) deposit, North-western province, Zambia. Colorado School of Mines. PhD Thesis.

Malehmir, A. and Juhlin, C., (2023). Complex Overburden, Stratigraphy and Fault Systems of the Kansanshi Copper-Gold Deposits (Zambia): Reflection Seismic Challenges. p.1-5.

Mambwe, P., Milan, L., Batumike, J., Lavoie, S., Jébrak, M., Kipata, L., Chabu, M., Mulongo, S., Lubala, T., Delvaux, D. and Muchez, P., (2017). Lithology, petrography and Cu occurrence of the Neoproterozoic glacial Mwale Formation at the Shanika syncline (Tenke Fungurume, Congo Copperbelt; Democratic Republic of Congo). Journal of African Earth Sciences, 129, p.898–909.

Mambwe, P., Delpomdor, F., Lavvoie, S., Kapya Philippe, M., Batumike, J. and Muchez, P., (2020). Sedimentary evolution and stratigraphy of the ~765–740 Ma Kansuki-Mwashya platform succession in the Tenke-Fungurume Mining District, Democratic Republic of the Congo. Geologica Belgica, 23, p.69.

Master, S., Wendorff, M., (2011). Neoproterozoic glaciogenic diamictites of the Katanga Supergroup, Central Africa. Chapter 12. Geological Society, London, Memoirs 36, p.173–184.

McGowan, R., Roberts, S., Foster, R.P., Boyce, A. and Coller, D., (2003). Origin of the copper-cobalt deposits of the Zambian Copperbelt: An epigenetic view from Nchanga. Geology, 31, p.497-500.

McGowan, R., Roberts, S. and Boyce, A., (2006). Origin of the Nchanga copper–cobalt deposits of the Zambian Copperbelt. Mineral Deposit Research: Meeting the Global Challenge. Mineralium Deposita, 40, p.617–638.

McCuaig, T. and Hronsky, J., (2014). The mineral system concept: The key to exploration targeting. Society of Economic Geologists Special Publication, 18, p.153–175.

McCuaig, T., Scarselli, S., O’Connor, T., Busuttil, S., and McCormack, N., (2018). The Power of a Systems Approach to Mineral and Petroleum Exploration in Sedimentary Basins. SEG Special Publication Metals, Minerals, and Society, Volume 21, Chapter 3, p.39-62.

McNulty, B.A. and Simon M. Jowitt, J.M., (2021). Barriers to and uncertainties in understanding and quantifying global critical mineral and element supply, iScience, Volume 24, Issue 7,102809, 10.1016/j.isci.2021.102809.

Megill, R.E., (1988). Exploration economics: Tulsa. PennWell, 238p.

Morgan, L., (2012). Geophysical Characteristics of Volcanogenic Massive Sulphide Deposits. U.S. Geological Survey. Scientific Investigations Report 2010–5070–C.

Muchez, Ph., Brems, D., Clara, E., De Cleyn, A., Lammens, L., Boyce, A., De Muynck, D., Mukumba, W. and Sikazwe, O., (2010). Evolution of Cu–Co mineralizing fluids at Nkana Mine, Central African Copperbelt, Zambia. Journal of African Earth Sciences, 58, p.457–474.

Nowecki, J., (2014). Tracing seawater evaporation and its role in the formation of sediment-hosted stratiform copper deposits. University of Southampton. PhD Thesis.

Occhipinti, S.A., Metelka, V., Lindsay, M.D., Hollis, J.A., Aitken, A.R.A., Tyler, I.M., Miller, J.M. and McCuaig, T.C., (2016). Multicommodity mineral systems analysis highlighting mineral prospectivity in the Halls Creek Orogen. Ore Geology Reviews, 72, p.86–113.

Ohmoto, H., (1986). Stable isotope geochemistry of ore deposits. In: J.W. Valley, H.P. Taylor and J.R. O’Neil (eds.): Stable isotopes in high temperature geological processes. Reviews in Mineralogy. Vol. 16, p.491-556

Ohmoto, H., Kaiser, C. J., Geer, K. A., (1990). Systematics of sulphur isotopes in Recent marine sediments and ancient sediment-hosted base metal deposits, in Herbert, H. K., and Ho, S. E., eds., Publication - Geology Department and Extension Service, University of Western Australia, vol.23: Geology Department and Extension Service, University of Western Australia, p.70–120.

Ohmoto, H., Rye, R., (1997). Sulfur and carbon isotopes, in Barnes, H., ed. Geochemistry of Hydrothermal Ore Deposits: New York, John Wiley & Sons Inc, p.509–567.

Okitaudji, L.R., (1989). Geologie sedimentaire et concentration syndiagenetique du cuivre et du cobalt dans la serie des Mines du Shaba, Zaire. These de Doctorat en Sciences. Polytechnic National Institute of Lorraine (France), 476p.

OreWin Independent Consultants, (2023). Kamoa – Kakula Integrated Development Plan 2023, Job No 22005.

Oszczepalski, S., Speczik, S., Zieliński, K. and Chmielewski, A., (2019). The Kupferschiefer Deposits and Prospects in SW Poland: Past, Present and Future. Minerals, 9, p.592.

Parker, H.M., Seibel, G., David, D., Peters, B., Jakubec, J., Lawson, M., (2013). NI 43-101. Technical Report of Kamoa Copper Project, Democratic Republic of Congo (DRC). AMEC. NI43-101 Technical report and 172449. Katanga. 371p.

Pirard, C. and Hatert, F., (2008). The sulfides and selenides of the Musonoi mine, Kolwezi, Katanga, Democratic Republic of Congo. Canadian Mineralogist - CAN MINERALOG, 46, p.219–231.

Porada, H., (1989). Pan-African rifting and orogenesis in southern to equatorial Africa and eastern Brazil. Precambrian Research, 44, p.103–136.

Porada, H. and Berhorst, V., (2000). Towards a new understanding of the Neoproterozoic-Early Palaeozoic Lufilian and northern Zambezi Belts in Zambia and the Democratic Republic of Congo. Journal of African Earth Sciences, 30, p.727–771.

Qiaofan, H., Zuohai, F., Jiangping, M. and Ke, F., (2021). Fluid inclusions, H-O-S isotopic characteristics and genesis of the Chambishi copper deposit, Zambia. E3S Web of Conferences, 290, 03016.

Ripley E., Merino E., Moore C., Ortoleva P., (1985) Mineral zoning in sediment-hosted copper deposits. In: Wolf KH (ed) Handbook of strata-bound and stratiform ore deposits, vol XIII. Elsevier, New York, p.237–260.

Saintilan, N., Selby, D., Creaser, R. and Stijn, D., (2018). Sulphide Re-Os geochronology links orogenesis, salt, and Cu-Co ores in the Central African Copperbelt. Scientific Reports, 8-1, 14946.

Schmandt, D., (2013). Stratigraphy and mineralization of the Kamoa copper deposit, Katanga, Democratic Republic of Congo. Colorado School of Mines. MSc Thesis.

Schmandt, D., Broughton, D., & Hitzman, M., & Plink-Bjorklund, P. & Edwards, D. and Humphrey, J., (2013). The Kamoa Copper Deposit, Democratic Republic of Congo: Stratigraphy, Diagenetic and Hydrothermal Alteration, and Mineralization. Economic Geology. 108. p.1301-1324.

Schuh, W., Leveille, R.A., Fay, I. and North, R., (2012). Geology of the Tenke-Fungurume Sediment-Hosted Strata-Bound Copper-Cobalt District, Katanga, Democratic Republic of Congo. In: J.W. Hedenquist, M. Harris and F. Camus (Editors), Geology and Genesis of Major Copper Deposits and Districts of the World: A Tribute to Richard H. Sillitoe. Society of Economic Geologists, Special Publication 16, p.268-301.

Schwarcz, H.P. and Burnie, S.W., (1973). Influence of sedimentary environments on sulfur isotope ratios in clastic rocks: a review. Mineralium Deposita, 8, p.264–277.

Seal, R.R., (2006). Sulfur Isotope Geochemistry of Sulphide Minerals. Reviews in Mineralogy & Geochemistry 61, p.633–677.

Selley, D., Broughton, D., Scott, R., Hitzman, M., Bull, S., Large, R., McGoldrick, P., Croaker, M., Pollington, N. and Barra, F., (2005). A New Look at the Geology of the Zambian Copperbelt. Economic Geology. 100th Anniversary Volume, p.965–1000.

Selley, D., Scott, R., Emsbo, P., Koziy, L., Hitzman, M., Bull, S., Duffett, M., Sebagenzi, S.M.N., Halpin, J., and Broughton, D., (2018). Structural Configuration of the Central African Copperbelt: Roles of Evaporites in Structural Evolution, Basin Hydrology, and Ore Location. SEG Special Publications No. 21, p.115-156.

Sillitoe, R.H., and Gappe, I.M., Jr., (1984). Philippine porphyry copper deposits. Geologic setting and characteristics: Committee for Co-ordination of Joint Prospecting for Mineral Resources in Asian Offshore Areas (CCOP), CCOP Technical Publication 14, p.89.

Sillitoe, R.H., (2010). Porphyry Copper Systems. Economic Geology, 105, p.3–41.

Sillitoe, R., Perelló, J., Creaser, R., Wilton, J. and Dawborn, T., (2015). Two Ages of Copper Mineralization in the Mwombezhi Dome, Northwestern Zambia: Metallogenic Implications for the Central African Copperbelt. Economic Geology, 110, p.1917–1923.

Sillitoe, R., Perelló, J., Creaser, R., Wilton, J., Wilson, A., and Dawborn, T., (2017). Age of the Zambian Copperbelt. Mineralium Deposita, 52, p.1245–1268.

Simabwachi, M., (2022). Creation and Preservation of Business History: The Selection Trust and Anglo-American Corporation Archives in Zambia's Copperbelt. Historia, vol.67, n.2 p.90-115

Simusokwe, M., (2021). Lithology, Alteration and Mineralization of the Fishtie Cu-Co Deposit, Zambian Copperbelt. Akita University. PhD Thesis.

Slack, J.F., Kimball, B.E. and Shedd, K.B., (2017). Cobalt. U.S. Geological Survey (USGS), Critical Mineral Resources of the United States – Economic and Environmental Geology and Prospects for Future Supply, Professional Paper 1802–F.

Squire, R.J. and Keays, R.R., (2023). The role of super mountain belts and climatic controls on the genesis of copper deposits in the Kupferschiefer and the Central African Copperbelt. Mineralium Deposita, 4, p.717-732.

Steel, R. W., (1957). The Copperbelt of Northern Rhodesia. Geography, vol. 42, no. 2, p.83–92. JSTOR.

Steven, N. and Armstrong, R., (2003). A metamorphosed Proterozoic carbonaceous shale hosted Co-Ni-Cu deposit at Kalumbila, Kabompo Dome: the Copperbelt ore shale in Northwestern Zambia. Economic Geology 98, p.893-909.

Stephens, A.J. and Newall, G.C., (2003). The Lonshi Copper Mine, Katanga Province, Democratic Republic of the Congo. NI 43-101 Technical Report prepared for First Quantum Minerals Ltd., 35p.

Sucipta, S., Bella, L., Risdiana, S., and Sutrisno, S., (2019). Identification of Sandstone Layer beneath the Demonstration Disposal Site at Nuclear Serpong Area Using Resistivity Geo-electrical Method. Journal of Physics: Conference Series, 1198, 072001.

Sweeney R. E. and Kaplan I. R., (1973). Pyrite framboid formation: laboratory synthesis and marine sediments. Econ. Geol. 68, p.618-634.

Sweeney, M.A., Turner, P., Vaughan, D.J., (1986). Stable isotope and geochemical studies of the role of early diagenesis in ore formation, Konkola basin, Zambian Copperbelt. Economic Geology 81, p.1838–1852.

Sweeney, M., Binda, P., (1989). The role of diagenesis in the formation of the Konkola Cu-Co ore-body of the Zambian Copperbelt in Boyle, R. et al., eds., Sediment hosted stratiform copper deposits: Geological Association of Canada Special Paper 36, p.427-452.

Telford, W.M., Geldart, L.P. and Sheriff, R.E., (1990). Applied Geophysics. 2nd Edition, Cambridge University Press, Cambridge, 770p.

Twite, F., Broughton, D. & Nex, P. and Kinnaird, J., (2015). Controls of Sulphide Mineralization at the Kamoa Copper Deposit, with an Emphasis on Structural Controls, SE Democratic Republic of Congo. Conference Poster abstract, SEG 2015: World Class Ore Deposits: Discovery to Recovery.

Twite, F., (2016). Controls of sulphide mineralisation at the Kamoa copper deposit, with an emphasis on structural controls. University of the Witwatersrand. MSc Thesis.

Twite, F., Broughton, D., Nex, P., Kinnaird, J., Gilchrist, G. and Edwards, D., (2019). Lithostratigraphic and structural controls on sulphide mineralisation at the Kamoa copper deposit, Democratic Republic of Congo. Journal of African Earth Sciences. Volume 151, p.212-224.

Twite, F., Nex, P. and Kinnaird, J., (2020). Strain fringes and strain shadows at Kamoa (DRC), implications for copper mineralisation. Ore Geology Reviews, 122, 103536.

Turner, E.C., Dabros, Q., Broughton, D.W. and Kontak, D.J., (2023). Textural and geochemical evidence for two-stage mineralisation at the Kamoa-Kakula Cu deposits, Central African Copperbelt. Mineralium Deposita, 58, p.825–832.

Van Wilderode, J., Heijlen, W., De Muynck, D., Schneider, J., Vanhaecke, F. and Muchez, Ph., (2013). The Kipushi Cu–Zn deposit (DR Congo) and its host rocks: A petrographical, stable isotope (O, C) and radiogenic isotope (Sr, Nd) study. Journal of African Earth Sciences, 79, p.143–156.

Velivetskaya, T.A., Ignatiev, A.V., Yakovenko, V.V. and Vysotskiy, S.V., (2019). An improved femtosecond laser-ablation fluorination method for measurements of sulfur isotopic anomalies (Δ33S and Δ36S) in sulphides with high precision. Rapid Commun. Mass Spectrom. 33, p.1722–1729.

Vérard, C., (2021). 888-444 Ma Global Plate Tectonic Reconstruction With Emphasis on the Formation of Gondwana. Frontiers in Earth Science. Volume 9, id.404.

Wendorff, M., (2005). Evolution of Neoproterozoic-Lower Palaeozoic Lufilian arc, Central Africa: A new model based on syntectonic conglomerates. Journal of The Geological Society - J GEOL SOC. 162. p.5-8.

Wendorff, M. and Key, R.M., (2009). The relevance of the sedimentary history of the Grand Conglomérat Formation (Central Africa) to the interpretation of the climate during a major Cryogenian glacial event. Precambrian Research, 172, p.127–142.

Wilkin, R.T., Barnes, H.L. and Brantley, S.L., (1996). The size distribution of framboidal pyrite in modern sediments: An indicator of redox conditions. Geochimica et Cosmochimica Acta, 60, p.3897–3912.

Winter, J., (2020). Metamorphism, Metamorphic Rocks and Classification of Metamorphic Rocks. In: Reference Module in Earth Systems and Environmental Sciences. 10.1016/B978-0-12-409548-9.12542-4.

Wyborn, L.A.I., Heinrich, C.A., Jaques, A.I., (1994). Australian Proterozoic mineral systems: essential ingredients and mappable criteria. Australian Institute of Mining and Metallurgy Annual Conference, p.109–115.

Yantambwe, M. and Cailteux, J., (2019). Geological observations in the Five-Klippes area, Northwestern Katanga Copperbelt (Democratic Republic of the Congo). Geologica Belgica, 22, p.111–119.

Zientek, M. Bliss, J. & Broughton, D. & Christie, M., Denning, P., Hayes, T., Hitzman, M., Horton, J., Frost-Killian, S., Jack, D., Master, S., Parks, H., Taylor, C., Wilson, A., Wintzer, N. and Woodhead, J., (2014). Sediment-Hosted stratabound copper assessment of the Neoproterozoic Roan Group, Central African Copperbelt, Katanga Basin, Democratic Republic of the Congo and Zambia. U.S. Geological Survey, Scientific Investigations Report-5090-T.

Internet sources:

Ivanhoe Mines, (2023). OreWin Development Plan: Kamoa – Kakula, (2023). https://www.ivanhoemines.com/wp-content/uploads/22005kkidp23_230316rev1.pdf

https://ivanhoemines.com/news/2023/ivanhoe-mines-issues-2023-first-quarter-financial-results-and-overview-of-construction-and-exploration-activities/

https://www.ivanhoemines.com/news-stories/news-release/ivanhoe-mines-announces-outstanding-economic-results-of-updated-independent-integrated-development-plan-2023-idp-for-world-leading-kamoa-kakula-copper-complex/

Downhole log (Fig. 37), is on p.5 of this press release; https://ivanhoemines.com/site/assets/files/4478/2019-09-08-ivn-nr-fr.pdf

JOGMEC, (2013). Petroleum system analysis. https://www.jogmec.go.jp/english/oil/oilgas_10_000012.html

Kettle, J., (2021). Will a lack of supply growth come back to bite the copper industry? https://www.woodmac.com/news/opinion/will-a-lack-of-supply-growth-come-back-to-bite-the-copper-industry/

Porter, M., (2015). Lonshi, Mwenso, Democratic Republic of Congo. https://portergeo.com.au/database/mineinfo.asp?mineid=mn155

Porter, M., (2015). Frontier, Lufua, Democratic Republic of Congo. https://portergeo.com.au/database/mineinfo.asp?mineid=mn155

Porter, M., (2015). Central African Copperbelt – Zambia Copperbelt. https://portergeo.com.au/database/mineinfo.asp?mineid=mn126

Porter, M., (2019). Kamoa and Kakula, Katanga, Dem. Rep. Congo. https://portergeo.com.au/database/mineinfo.asp?mineid=mn1397

Statistica, (2023). Global CO_2 emissions statistics. https://www.statista.com/statistics/276629/global-co2-emissions/

9 APPENDICES

APPENDIX A: GEOLOGY / STRATIGRAPHY CODES

Stratigraphic Codes			Description	Thickness
Grand Conglomérat (Ng 1.1)	**Uppermost diamictite Ng 1.1.6**		Thick generally chloritic clast poor, slightly sandy diamictites containing 7-15% clasts; occasionally up to 20%. Occasionally contains thin sandstone beds +/- thin siltstone and reworked diamictite intercalated with clast to matrix supported conglomerate, sandstone beds and thin siltstone.	100-350 m
	Upper diamictite Ng 1.1.5		Diamictite with 7 to 15% clasts, quartzite +argillites (>locally mafics to the north) with frequent rim replacement by pyrite >pyrrhotite>>chalcopyrite. 1-4% sulphides. Contains zones of reworking. Matrix-supported conglomerates near top at Kansoko.	<200->550 m
	Upper laminated pyritic siltstone Ng 1.1.4		Pyritic sandy siltstone, bedded, laminated with planar >>irregular bedding. Minor pebbly bands. Soft sediment slumping. 1-12% mostly bedded pyrite. Gradational upper and lower contacts, often reworked at the base.	+/- 20 m
	Middle diamictite package Ng 1.1.3		Typical diamictite. Often weakly carbonaceous and generally clast rich ranging from 20-40% pebbles>>cobbles. General clast assemblage quartzite > argillite > mafic with occasional exotics (mica schist, dolomite, shale) in argillaceous matrix. Often contains weak minor reworked zones. Thin weakly pyritic siltstone. ± pyrrhotite + trace chalcopyrite. Sandy pebbly siltstone with thin zones of reworked diamictite. 0.5-1% replacement pyrite increasing to 5% in bottom +/- 5m. Often contains weakly reworked zones.	100-200m
	Lower laminated pyritic siltstone Ng 1.1.2		Laminated pyritic siltstone containing 15-30% pyrite occurring in bedding or as blebs and disseminations in sandy areas. Kamoa Pyritic Siltstone (KPS). Normally with slightly sandy graded beds towards base with shale rip-up clasts. Always decrease in pyrite over the basal 3-5m.	20-46 m
	Basal diamictite Ng 1.1.1	***Ng 1.1.1.3***	Argillaceous >> sandy and often chloritised. Diamictite generally clast poor but not in all cases. <20% clasts of quartzite > mafics>argillite >> quartz < 100mm. Significant copper mineralisation occurs. Gradational base.	40->100 m
		Ng 1.1.1.2	Siltstone, massive to weakly bedded. Can be preferentially mineralised. Often more than one band 1-11m thick intercalated with "reduced > "oxidised" facies diamictite.	Up to +50 m
		Ng 1.1.1.1	Maroon to light grey diamictite >20-35% subangular-subrounded clasts < 70mm of sandstone + quartzites + quartz with occasional large mafic pebbles. Frequently matrix & replacement hematite alteration. Sandy irregular base. Normally oxide copper + chalcocite mineralisation	<10-25 m
Mwashya Subgroup (R.4)	**R.4.2**		Feldspathic sandstone, fine- to coarse-grained with minor intercalations of hematite rich siltstone bands. Occasionally slightly pyritic but generally containing detrital specularite grains in the matrix. Varies from grey when fresh to pink when weathered.	30-300 m +

(Ivanhoe Mines)

APPENDIX B; SAMPLE LIST

Polished blocks, polished thin sections and sulphur isotopes sulphide grain sample list

Sample	BHID	Depth	Lithology	Strat 1	Strat 2	Mineral	Polished block
1	DKMC_DD624	302.00	SSL	Ng1.1.2		Py	Block 1
2	DKMC_DD624	302.00	SSL	Ng1.1.2		Py	Block 1
3	DKMC_DD624	303.50	SSL	Ng1.1.2		Cpy	Block 1
4	DKMC_DD624	303.50	SSL	Ng1.1.2		Cpy	Block 1
5	DKMC_DD624	303.50	SSL	Ng1.1.2		Cpy	Block 1
6	DKMC_DD956	278.00	SDT	Ng1.1.1	Ng1.1.1.3	Cpy	Block 1
7	DKMC_DD956	278.00	SDT	Ng1.1.1	Ng1.1.1.3	Cpy	Block 1
8	DKMC_DD624	297.80	SSL	Ng1.1.2		Py	Block 1
9	DKMC_DD624	297.80	SSL	Ng1.1.2		Py	Block 1
10	DKMC_DD624	298.80	SSL	Ng1.1.2		Py	Block 1
11	DKMC_DD624	298.80	SSL	Ng1.1.2		Py	Block 1
12	DKMC_DD624	304.30	SSL	Ng1.1.2		Cpy	Block 2
13	DKMC_DD624	304.30	SSL	Ng1.1.2		Cpy	Block 2
14	DKMC_DD1044	342.80	SSL	Ng1.1.1	Ng1.1.1.2	Cc	Block 2
15	DKMC_DD1044	342.80	SSL	Ng1.1.1	Ng1.1.1.2	Cc	Block 2
16	DKMC_DD1044	342.80	SSL	Ng1.1.1	Ng1.1.1.2	Hem	Block 2
17	DKMC_DD624	309.70	SDT	Ng1.1.1	Ng1.1.1.1	Bor	Block 2
18	DKMC_DD624	309.70	SDT	Ng1.1.1	Ng1.1.1.1	Cc	Block 2
19	DKMC_DD1044	343.30	SSL	Ng1.1.1	Ng1.1.1.2	Cc	Block 2
20	DKMC_DD1044	343.30	SSL	Ng1.1.1	Ng1.1.1.2	Cc	Block 2
21	DKMC_DD1044	327.00	SDT	Ng1.1.1	Ng1.1.1.1	Cc	Block 2
22	DKMC_DD956	274.50	SDT	Ng1.1.1	Ng1.1.1.3	Cpy	Block 2
23	DKMC_DD1044	343.7-3	SSL	Ng1.1.1	Ng1.1.1.2	Cc	Block 3
24	DKMC_DD1044	343.7-3	SSL	Ng1.1.1	Ng1.1.1.2	Cc	Block 3
25	DKMC_DD1044	343.7-2	SSL	Ng1.1.1	Ng1.1.1.2	Cc	Block 3
26	DKMC_DD1044	319.20	SSL	Ng1.1.1	Ng1.1.1.2	Bor	Block 3
27	DKMC_DD1044	319.20	SSL	Ng1.1.1	Ng1.1.1.2	Bor	Block 3
28	DKMC_DD1044	319.20	SSL	Ng1.1.1	Ng1.1.1.2	Cc	Block 3
29	DKMC_DD1044	336.40	SDT	Ng1.1.1	Ng1.1.1.1	Bor	Block 3
30	DKMC_DD1044	336.40	SDT	Ng1.1.1	Ng1.1.1.1	Cc	Block 3
31	DKMC_DD1044	322.70	SDT	Ng1.1.1	Ng1.1.1.1	Py	Block 3
32	DKMC_DD1044	322.70	SDT	Ng1.1.1	Ng1.1.1.1	Cpy	Block 3
33	DKMC_DD1044	333.40	SDT	Ng1.1.1	Ng1.1.1.1	Cc	Block 3
34	DKMC_DD1044	333.40	SDT	Ng1.1.1	Ng1.1.1.1	Bor	Block 3
35	DKMC_DD1044	333.40	SDT	Ng1.1.1	Ng1.1.1.1	Cc	Block 3
36	DKMC_DD627	488.80	SDT	Ng1.1.1	Ng1.1.1.3	Cpy	Block 4
37	DKMC_DD627	488.80	SDT	Ng1.1.1	Ng1.1.1.3	Py	Block 4
38	DKMC_DD627	488.80	SDT	Ng1.1.1	Ng1.1.1.3	Py	Block 4
39	DKMC_DD627	488.80	SDT	Ng1.1.1	Ng1.1.1.3	Cpy	Block 4
40	DKMC_DD627	492.50	SDT	Ng1.1.1	Ng1.1.1.3	Cob	Block 4
41	DKMC_DD627	492.50	SDT	Ng1.1.1	Ng1.1.1.3	Cob	Block 4
42	DKMC_DD627	492.50	SDT	Ng1.1.1	Ng1.1.1.3	Py	Block 4
43	DKMC_DD627	492.50	SDT	Ng1.1.1	Ng1.1.1.3	Cpy	Block 4

Sample	BHID	Depth	Lithology	Strat 1	Strat 2	Mineral	Polished block
44	DKMC_DD627	494.30	SDT	Ng1.1.1	Ng1.1.1.3	Cpy	Block 4
45	DKMC_DD1044	311.70	SSL	Ng1.1.1	Ng1.1.1.2	Py	Block 4
46	DKMC_DD1044	311.70	SSL	Ng1.1.1	Ng1.1.1.2	Py	Block 4
47	DKMC_DD1044	311.70	SSL	Ng1.1.1	Ng1.1.1.2	Cpy	Block 4
48	DKMC_DD624	288.50	SSL	Ng1.1.2		Py	Block 4
49	DKMC_DD624	288.50	SSL	Ng1.1.2		Py	Block 4
50	DKMC_DD627	474.70	SSL	Ng1.1.2		Py	Block 4
51	DKMC_DD627	474.70	SSL	Ng1.1.2		Py	Block 4
52	DKMC_DD627	498.30	SDT	Ng1.1.1	Ng1.1.1.1	Bor	Block 5
53	DKMC_DD627	498.30	SDT	Ng1.1.1	Ng1.1.1.1	Cpy	Block 5
54	DKMC_DD627	469.70	SSL	Ng1.1.2		Py	Block 5
55	DKMC_DD627	469.70	SSL	Ng1.1.2		Py	Block 5
56	DKMC_DD624	304.50	SDT	Ng1.1.1	Ng1.1.1.3	Cpy	Block 5
57	DKMC_DD624	304.50	SDT	Ng1.1.1	Ng1.1.1.3	Cc	Block 5
58	DKMC_DD1044	339.20	SDT	Ng1.1.1	Ng1.1.1.1	Cc	Block 5
59	DKMC_DD1044	328.80	SDT	Ng1.1.1	Ng1.1.1.1	Cc	Block 5
60	DKMC_DD1044	328.80	SDT	Ng1.1.1	Ng1.1.1.1	Bor	Block 5
61	DKMC_DD571	545.50	SDT	Ng1.1.1	Ng1.1.1.3	Cpy	Block 5
62	DKMC_DD627	490.00	SDT	Ng1.1.1	Ng1.1.1.3	Cpy	Block 6
63	DKMC_DD627	490.00	SDT	Ng1.1.1	Ng1.1.1.3	Cpy	Block 6
64	DKMC_DD571	546.10	SDT	Ng1.1.1	Ng1.1.1.3	Cob	Block 6
65	DKMC_DD571	546.10	SDT	Ng1.1.1	Ng1.1.1.3	Cpy	Block 6
66	DKMC_DD571	550.50	SDT	Ng1.1.1	Ng1.1.1.3	Bor	Block 6
67	DKMC_DD571	532.20	SSL	Ng1.1.2		Py	Block 6
68	DKMC_DD571	532.20	SSL	Ng1.1.2		Py	Block 6
69	DKMC_DD571	532.20	SSL	Ng1.1.2		Py	Block 6
70	DKMC_DD571	526.00	SSL	Ng1.1.2		Cc	Block 6
71	DKMC_DD571	526.00	SSL	Ng1.1.2		Py	Block 6
72	DKMC_DD1039	343.25	SSL	Ng1.1.1	Ng1.1.1.2	Cc	Block 7
73	DKMC_DD1039	342.20	SSL	Ng1.1.1	Ng1.1.1.2	Cc	Block 7
74	DKMC_DD956	235.60	SSL	Ng1.1.2	Ng1.1.2.2	Py	Block 7
75	DKMC_DD1039	329.00	SDT	Ng1.1.1	Ng1.1.1.3	Cc	Block 7
76	DKMC_DD1044	344.60	SSL	Ng1.1.1	Ng1.1.1.2	Cc	Block 7
77	DKMC_DD1039	329.00	SDT	Ng1.1.1	Ng1.1.1.3	Py	Block 7
78	DKMC_DD1044	345.70	SDT	Ng1.1.1	Ng1.1.1.1	Cc	Block 7
79	DKMC_DD1039	324.40	SDT	Ng1.1.1	Ng1.1.1.3	Cc	Block 8
80	DKMC_DD1039	324.40	SDT	Ng1.1.1	Ng1.1.1.3	Cc	Block 8
81	DKMC_DD1039	335.30	SDT	Ng1.1.1	Ng1.1.1.3	Cc	Block 8
82	DKMC_DD571	525.10	SDT	Ng1.1.3		Py	Block 8
83	DKMC_DD571	525.10	SDT	Ng1.1.3		Py	Block 8
84	DKMC_DD956	242.40	SSL	Ng1.1.2	Ng1.1.2.2	Py	Block 8
85	DKMC_DD956	242.40	SSL	Ng1.1.2	Ng1.1.2.2	Py	Block 8
86	DKMC_DD627	481.00	SSL	Ng1.1.2		Py	Block 8

Sample	BHID	Depth	Lithology	Strat 1	Strat 2	Mineral	Polished block
87	DKMC_DD627	481.00	SSL	Ng1.1.2		Py	Block 8
88	DKMC_DD1039	342.60	SSL	Ng1.1.1	Ng1.1.1.2	Cc	Block 8
89	DKMC_DD571	536.00	SSL	Ng1.1.2		Cpy	Block 9
90	DKMC_DD571	536.00	SSL	Ng1.1.2		Py	Block 9
91	DKMC_DD571	536.00	SSL	Ng1.1.2		Py	Block 9
92	DKMC_DD571	536.00	SSL	Ng1.1.2		Py	Block 9
93	DKMC_DD956	277.50	SDT	Ng1.1.1	Ng1.1.1.3	Cpy	Block 9
94	DKMC_DD627	493.50	SDT	Ng1.1.1	Ng1.1.1.3	Cpy	Block 9
95	DKMC_DD571	531.80	SSL	Ng1.1.2		Py	Block 9
96	DKMC_DD571	531.80	SSL	Ng1.1.2		Py	Block 9
97	DKMC_DD1039	338.30	SDT	Ng1.1.1	Ng1.1.1.3	Cc	Block 9
98	DKMC_DD1044	309.70	SSL	Ng1.1.1	Ng1.1.1.2	Py	Block 10
99	DKMC_DD1044	309.70	SSL	Ng1.1.1	Ng1.1.1.2	Cpy	Block 10
100	DKMC_DD571	528.90	SSL	Ng1.1.2		Py	Block 10
101	DKMC_DD571	528.90	SSL	Ng1.1.2		Py	Block 10
102	DKMC_DD571	528.90	SSL	Ng1.1.2		Py	Block 10
103	DKMC_DD624	303.10	SSL	Ng1.1.2		Cpy	Block 10
104	DKMC_DD624	303.10	SSL	Ng1.1.2		Py	Block 10
105	DKMC_DD624	303.10	SSL	Ng1.1.2		Bor+Cov	Block 10
106	DKMC_DD624	303.10	SSL	Ng1.1.2		Cpy	Block 10
107	DKMC_DD624	303.10	SSL	Ng1.1.2		Bor+Cov	Block 10
108	DKMC_DD571	525.10	SDT	Ng1.1.3		Py	Block 10
109	DKMC_DD1039	344.90	SDT	Ng1.1.1	Ng1.1.1.1	Cc	Block 10
110	DKMC_DD1039	336.50	SDT	Ng1.1.1	Ng1.1.1.3	Cc	Block 10

APPENDIX C; POLISHED THIN SECTION PHOTOMICROGRAPHS

DKMC_DD627	492.50m	1	Description
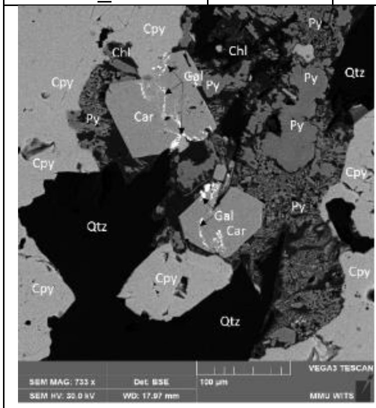			627-492.5-1 Pyrite + chalcopyrite + carrollite + galena in quartz-sericite-chlorite matrix
			The photomicrograph contains euhedral and irregular chalcopyrite with sharp and corroded margins. There is possible diagenetic alteration of the copper sulphide. There are black inclusions within the cpy crystals that may have formed during crystallisation or early diagenesis. Well-developed euhedral carrollite crystals (50 – 60 µm) indicate their diagenetic nature and are predating an internal growth of galena veinlets. Irregular and disseminated pyrite is present. There is the presence of a (sericite)-quartz-chlorite matrix. The carrollite-galena assemblage suggests highly acidic, diagenetic conditions of the sulphides.

DKMC_DD627	492.50m	2	Description
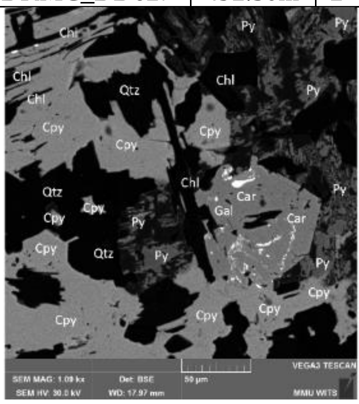			627-492.5-2 Pyrite + chalcopyrite + carrollite + galena in quartz-chlorite-(sericite) matrix
			The photomicrograph displays crystals with texture that showing sharp edges as well as corroded boundaries. Irregular cpy dominates the left of the image, with euhedral carrollite in the central part of the image. Disseminated pyrite is observed within the matrix, intergrown within a quartz-chlorite in the matrix. Potentially the pyrite fabric can be attributed to pre-existing framboidal pyrite. The absence of potassic-alteration although (sericite) – chlorite alteration is distinct and present. Irregular quartz is observed in the matrix. Whilst cross cutting chlorite is observed crosscutting cpy + car.

DKMC_DD627	492.50m	3	Description
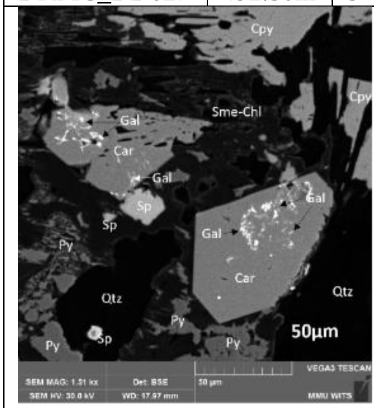			627-492.5-3 Pyrite + chalcopyrite + carrollite + galena + sphalerite in quartz-chlorite-smectite + matrix
			The photomicrograph is an alternate view of sample from drillhole DKMC_DD627. This sample also displaces both sharp edges around what appears to have been euhedral carrollite, with corroded edges (centre - right). Galena veinlets are distinct within the euhedral carrollite grain. The irregular and disseminated pyrite crystals support sulphide dissolution during the later chloritisation phase (within the matrix). Sphalerite has a wide range of occurrences and therefore and can be interpreted to be an associated mineral. Sphalerite appears to be enclosed in the quartz and chlorite-smectite matrix and may be of sedimentary origin.

DKMC_DD627	492.50m	4	Description
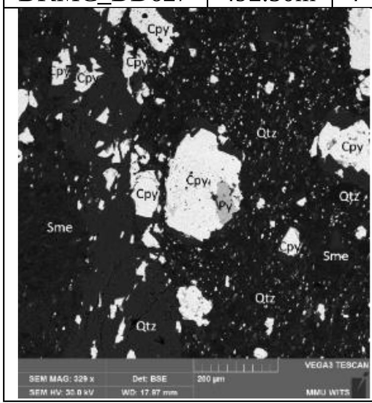			627-492.5-4 Chalcopyrite + pyrite in quartz-smectite matrix
			The photomicrographic displays chalcopyrite grains with irregular margins floating in a chlorite-smectite-quartz matrix. There appears to be a crude vertical alignment in the sample suggesting an original sedimentary stratification of poorly sorted diamictite (the basal diamictite). The chalcopyrite grains have crude diagenetic envelopes of chlorite / silica. Diagenetic pyrite is also visible in the central grain (medium grey), which has been almost completely replaced by the surrounding chalcopyrite.

DKMC_DD627	492.50m	5.1	Description

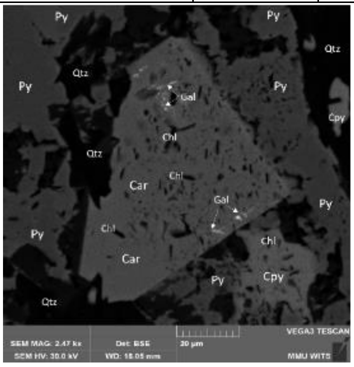

627-492.5-5-1 Pyrite + chalcopyrite + carrollite + galena + chlorite + quartz

The present view displays euhedral carrollite crystal in the centre of the photomicrograph, with a corrosive growth texture on its margins. The presence of galena and chlorite within the carrollite grain and corrosion of the left margin of the crystal support later diagenetic processes. Chalcopyrite is present in the lower-right bottom of the photo and which appears to be replacing pyrite which is surrounding carrollite. The black parts surrounding and interstitial are bladed chlorite and irregular quartz.

DKMC_DD627	492.50m	5.2	Description

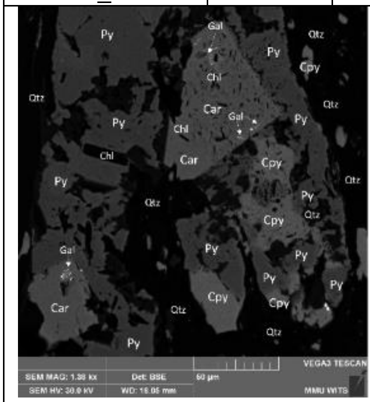

627-492.5-5-2 Pyrite + chalcopyrite + pyrite + carrollite + galena + quartz-chlorite

This view is a zoomed-out perspective of the previous photomicrograph and displays an elongated concentration of sulphide mineralogy (py + cpy + euhedral and subangular carrollite), bound by a silica-chlorite matrix. Bladed chlorite crystals also occur within the sulphide crystals. This geometry is likely associated to the strain shadow orientation that is associated to mineralisation surrounding clasts. Chalcopyrite is observed and is replacing pyrite, thus secondary in origin. The timing of the galena post-dates carrollite and thus may represent its formation during late-stage hydrothermal activity.

DKMC_DD627	492.50m	5.6	Description

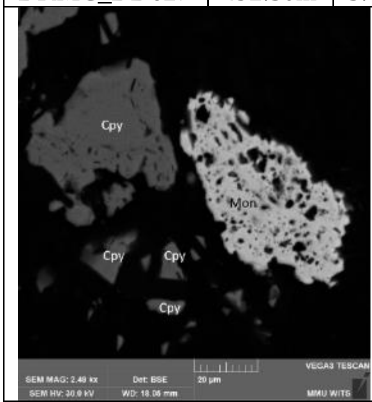

627-492.5-6 Chalcopyrite + monazite

Chalcopyrite and monazite are shown in this photomicrograph and appear to be sitting within a quartz-chlorite matrix. Corroded margins of the chalcopyrite grain indicates diagenetic / hydrothermal alteration. Solution cavities within the monazite reflect intensive alteration of the grain, potentially due to diagenetic / hydrothermal brines. The grain boundary of the monazite is irregular, although the central part of the grain has been more resistive to this disruption.

DKMC_DD627	492.50m	4	Description

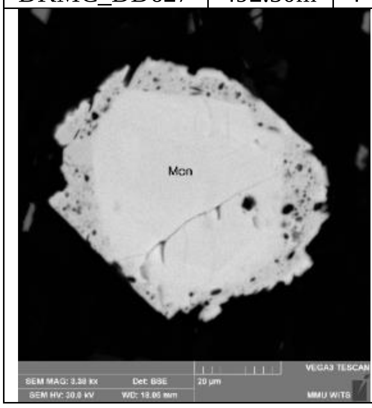

627-492.5-7 Monazite

The photomicrograph displays a zoomed-in perspective of a monazite grain which is ~50 – 60 µm in size. The grain boundary is irregular and pitted, showing intense alteration that is similarly observed in the previous sample. The central part of the grain shows little effect from hydrothermal dissolution. It is likely that the texture of this grain was predominantly controlled by diagenetic / hydrothermal processes, which caused the development of this cavity-like texture in the margins.

DKMC_DD1044	319.20m	1	Description
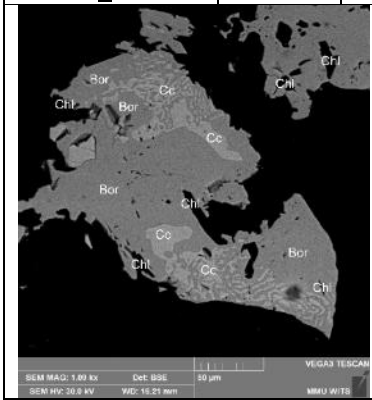			1044-319.2-1 Bornite + chalcocite The centre of the photomicrograph displays a large grain of bornite. It displays a corrosive texture in the top part, with smooth corroded edges in the bottom right. Also present is the distinct myrmekitic texture and wavy light grey bands indicating the replacement of bornite by chalcocite. This myrmekitic-like texture between the bornite and chalcocite, and limited development of chalcocite indicates a weak supergene sulphide enrichment at the expense of the bornite margins, likely associated to hydrothermal processes.
DKMC_DD1044	319.20m	2.1	Description
			1044-319.2-2-1 Magnetite in chlorite-sericite matrix Angular magnetite grain (~200 µm x 200 µm) is observed in the top part of the photomicrograph. Further below is corroded magnetite grains with a bladed texture. The different magnetite grains are distinguishable and are likely to occur in a zone in which hydrothermal processes have acted preferentially to the bottom of the grain, where the most corrosion is observed. These corroded margins and dissolved / replaced interior suggest later diagenetic alteration. The grains of magnetic appear to be surrounded by a distinct chlorite-sericite matrix.
DKMC_DD1044	319.20m	2.2	Description
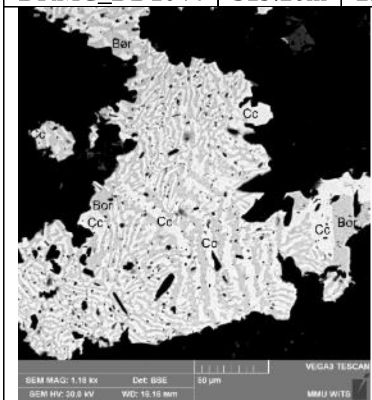			1044-319.2-2-2 Bornite + chalcocite Displayed is an irregular shaped grain of bornite + chalcocite exhibiting widespread development of myrmekitic-like texture indicates. This suggests the systematic replacement of bornite by chalcocite. This grain points towards a mature supergene sulphide enrichment process. The strong corrosion at the margin of the original bornite grain may suggest sulphide-rich reducing dissolution conditions.
DKMC_DD1044	319.20m	2.3	Description
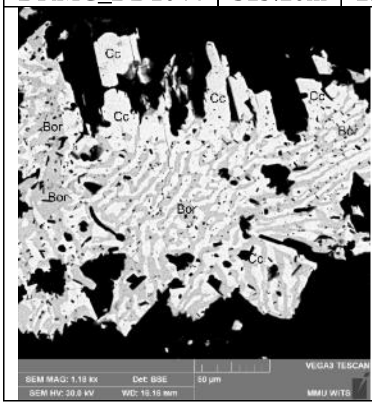			1044-319.2-3 Bornite + chalcocite The photomicrograph shows bornite + chalcocite and intense myrmekitic texture throughout the grain. The grain boundaries exhibit substantial corrosive form, with the top part of the grain hosting the most abundant replacement of bornite by chalcocite, shown by the occurrence of chalcocite in the elongate fingers at the top part of the grain. It is likely that this grain belongs to the supergene sulphide enrichment zone.

DKMC_DD1044	319.20m	2.4	Description
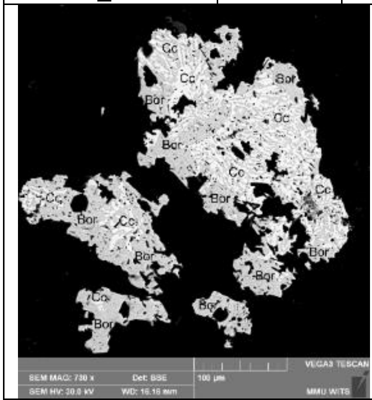			1044-319.2-4 Bornite + chalcocite The photomicrograph shows a zoomed-out view of bornite + chalcocite grains. This exhibits an extensive myrmekitic texture. This texture is a result of replacement of bornite by chalcocite. The present view indicates differentially more chalcocite formation in the upper right diagonal parts of both grains. Thus, the lower left diagonal parts have comparatively survived the alteration. This may provide an indication of the directional circulation path that hydrothermal fluids may have taken.
DKMC_DD1044	319.20m	2.6	Description
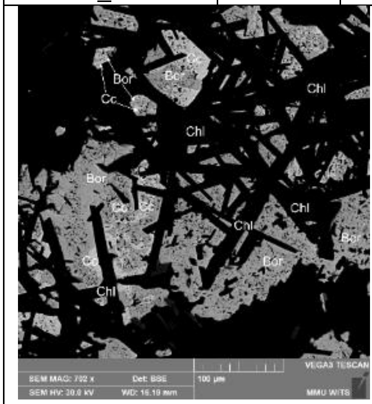			1044-319.2-6 Bornite + chalcocite + chlorite Bornite appears to have a granular pitted texture with a close textural relationship with lighter grey chalcocite on the grain edges. The bornite and chalcocite are cross-cut by widespread chlorite, exhibiting a bladed texture. The textures and sulphide + chlorite relationship suggests a paragenesis of replacement of bornite by chalcocite during the supergene enrichment → to late-stage overprinting of chlorite on bornite + chalcocite → The late-stage alteration appears to have had a negative impact on the Cu sulphide abundance.
DKMC_DD1044	319.20m	2.7	Description
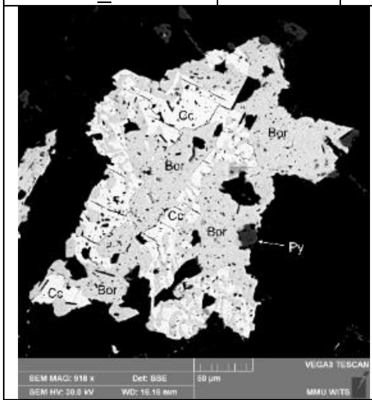			1044-319.2-7 Bornite + chalcocite Irregular grain of bornite with intergrown light grey chalcocite. Bornite exhibits a granular pitted texture whilst chalcocite has bladed fractures. Textural relationship suggests → replacement of bornite by chalcocite (supergene sulphide enrichment stage) → potential late-stage silica-chlorite alteration → subangular pyrite forming during this late stage. The formation of late-stage pyrite may have a negative impact on mineralisation.
DKMC_DD571	550.50m		Description
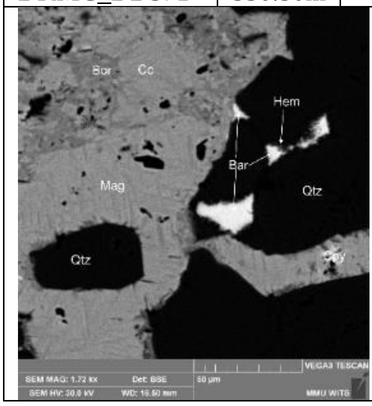			571-550.5 Bornite + chalcocite + hematite +barite + quartz Dark grey bornite with pore spaces developed from the pitted texture, with intergrown well developed chalcocite surround quartz, which may be qtz fragments or silica rich inclusions within the diamictite. Barite with intensely corroded edges is observed. The well-developed sulphide proximal to barite and its co-occurrence with quartz and hematite suggests that this barite is likely to be of an early-stage origin.

<table>
<tr><td>DKMC_DD571</td><td>550.50m</td><td></td><td>Description</td></tr>
<tr><td colspan="3" rowspan="2">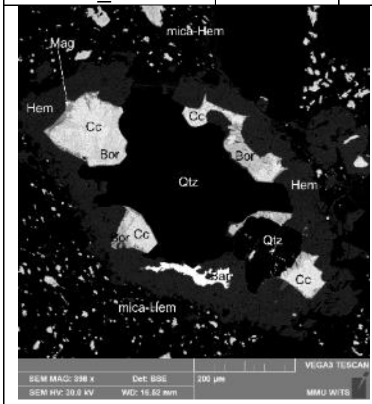
</td><td>571-550.5 Chalcocite + bornite + in quartz-hematite-mica matrix</td></tr>
<tr><td>This sample displays the co-occurrence of Cu-sulphides irregular shaped grains of bornite and chalcocite. It appears to be in the later stages of supergene enrichment as there is dominantly more well-developed chalcocite. A medium grained granular groundmass predominantly comprising hematite and mica sounds the grain. Irregular shaped quartz is located in the central portion. Barite with severely corroded margins is present enveloped by a hematite-mica matrix and the extent of its corrosion suggests its early formation. It is likely bornite and quartz as pore space-filling to start with followed by chalcocite replacement at the cost of bornite.</td></tr>
<tr><td>DKMC_DD571</td><td>550.50m</td><td>1</td><td>Description</td></tr>
<tr><td colspan="3" rowspan="2">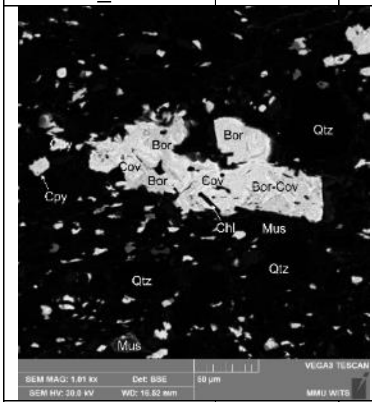
</td><td>571-550.5-1 Chalcopyrite + bornite + covellite in quartz-mica matrix</td></tr>
<tr><td>The irregular shaped, granular edged bornite-covellite-chalcopyrite assemblage is presently enclosed in a matrix of quartz-chlorite-mica. Bornite and chalcopyrite are generally the hypogene minerals that are altered to chalcocite and covellite during the supergene enrichment. It is likely covellite was formed as a result of supergene / hydrothermal replacement of bornite. The scattered nature of chalcopyrite quartz-clay-mica assemblage may support the proposal of its formation during the hydrothermal alteration stage.</td></tr>
<tr><td>DKMC_DD571</td><td>550.50m</td><td>2</td><td>Description</td></tr>
<tr><td colspan="3" rowspan="2">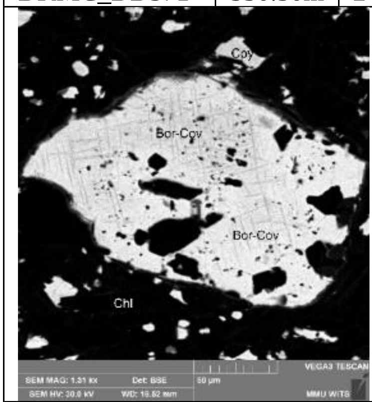
</td><td>571-550.5-2 Chalcopyrite + bornite + covellite in chlorite matrix</td></tr>
<tr><td>This photomicrograph displays the development of hydrothermal solution lamella. The original bornite grain (> 100 μm) has been converted into covellite during hydrothermal alteration. The corroded margins and internal dissolution in the grain reflect the intensity of this replacement. A thin chlorite-silica rim around the grain indicates corrosion during chloritisation.</td></tr>
<tr><td>DKMC_DD571</td><td>550.50m</td><td>3</td><td>Description</td></tr>
<tr><td colspan="3" rowspan="2">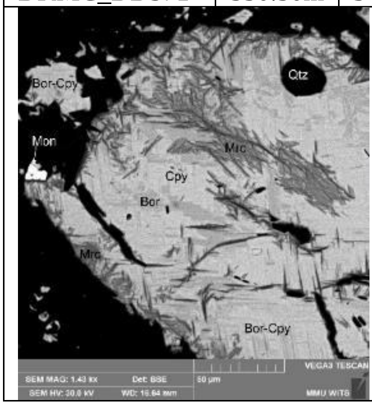
</td><td>571-550.5-3 Chalcopyrite -+ bornite + marcasite + monazite + quartz</td></tr>
<tr><td>Displayed in the photomicrograph is a dominant copper sulphide assemblage of chalcopyrite and bornite-chalcopyrite. The grain has fragmented crenulate margins, indicating the acidic nature of the hydrothermal / diagenetic fluids of white it was exposed to. The development of marcasite along fractures and grain margins suggests a late-stage alteration development. The presence of monazite supports the proposal of an acidic source nature.</td></tr>
</table>

DKMC_DD571	550.50m	4	Description

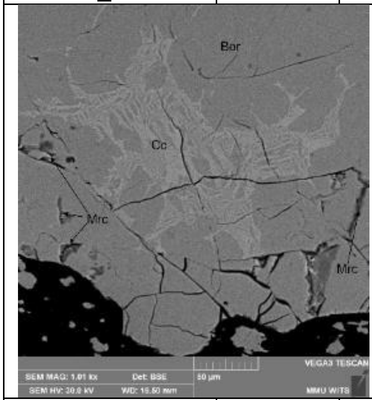

571-550.5-4 Bornite + chalcocite

The photomicrograph shows the presence of a moderately fractured grain of bornite. Chalcocite development started from the central part of the bornite rather than its margin, indicating replacement of bornite by chalcocite. This intergrowth style may be linked to the solid-solution series-like nature of the hydrothermal fluids. Alternatively, the chalcocite concentration in the central part may have been controlled by the fractures present. The development of marcasite potentially indicates late-stage hydrothermal alteration.

DKMC_DD571	550.50m	5	Description

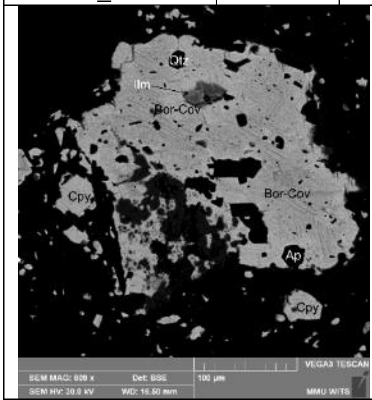

571-550.5-5 Chalcopyrite + bornite + covellite + quartz + ilmenite + apatite aluminosilicates

The granular pitted texture of this grain is observed to be associated to hydrothermal activity and is a mineral replacement texture. The main sulphide are bornite and covellite, exhibiting a bladed texture. Whilst the corroded margins and dissolution within the grain can be linked to the late-stage hydrothermal fluids infiltration that introduced quartz-aluminosilicates-apatite and ilmenite-like minerals. The presence of quartz-apatite may indicate an acidic source.

DKMC_DD571	550.50m	6	Description

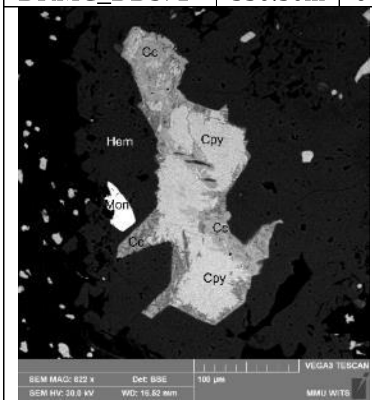

571-550.5-6 Chalcopyrite + chalcocite in hematitic matrix

In the centre of the photomicrograph, an elongate irregular grain comprising of a chalcopyrite core and a margin showing of chalcocite. These occur with a hematite-clay-quartz rich matrix. The geometrical arrangement of chalcopyrite and chalcocite may indicate genetic relationship originating from the infilling of pore space, with subsequent replacement of chalcopyrite by chalcocite. A sub-rounded to irregular inclusion of monazite is observed within the hematite-clay-silica matrix that envelops the chalcopyrite-chalcocite, which suggests its early-stage formation.

DKMC_DD952	131.80m	1.1	Description

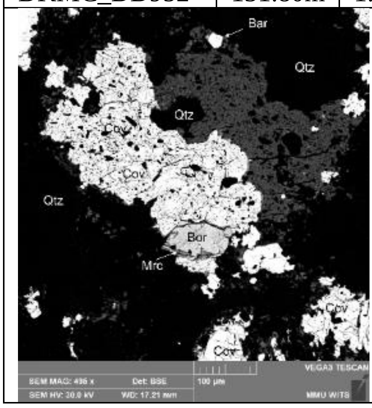

KKW005-1-1 Bornite + covellite + barite + marcasite + quartz

This photomicrograph shows a relict sub-angular grain of bornite in the central/bottom part. This grain is engulfed in irregular pitted covellite. This suggests that bornite was the original hypogene sulphide, subsequently replaced by covellite. Bornite displays marcasite development likely during injection of acidic hydrothermal solutions. Barite doesn't display a distinct cross-cutting relationship and is difficult to be linked to a particular stage. Its occurrence in the quartz-chlorite-clay matrix may be related to its early-stage development. The strong corrosion of grains and the pitted fabric may be due to acidic solutions.

DKMC_DD952	131.80m	1.2	Description

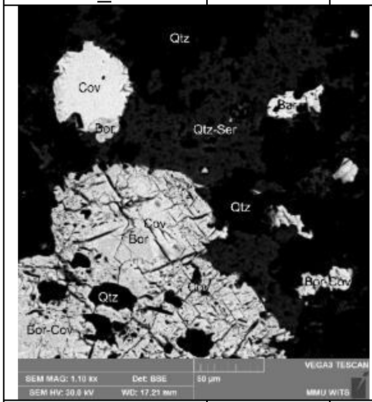

KKW-005-1-2 Bornite + covellite + barite in quartz-sericite matrix

Bornite engulfed within growth of covellite. Covellite exhibits a granular pitted texture, with occasional bladed structure. The bladed texture cross-cuts bornite and may be a texture associated to the replacement of bornite by covellite. The hypogene bornite has undergone supergene sulphide enrichment, subsequently being affected by alteration during the sericite-like alteration. Evidence of this alteration is exhibited by the extremely corroded grain margins. Barite is also present but lacks a cross-cutting relationship with sulphides, instead constrained to the quartz-sericite matrix.

DKMC_DD952	131.80m	2	Description

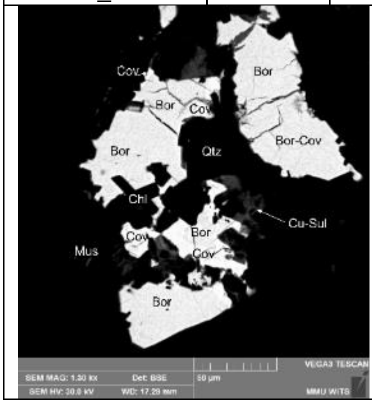

KKW005-2 Bornite + covellite + quartz + mica + Cu sulphate

The photomicrograph shows bornite which is being converted into covellite, as a result of the supergene enrichment process. Sulphide alteration into Cu-sulphate is also visible which exhibit a close association of the corroded margins to the grains. Fractures occur in the grain but the absence of alteration minerals suggest a lack any significant association to alteration. It is likely that these fractures occur late in bornite development or my post-date mineralisation and alteration stages. A quartz-mica-sericite assemblage surrounds the grains.

DKMC_DD952	131.80m	3.1	Description

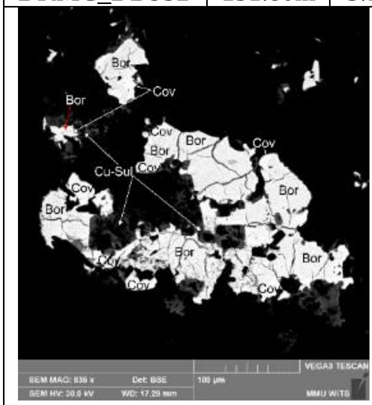

KKW005-3-1 Bornite + covellite + Cu sulphate

Fragmented grain of bornite. Distinctly corroded grain boundaries. Granular textured covellite forming a rim surround the bornite grain. This suggest development of covellite from the outer parts of the grain inward (bornite replacement by covellite). Cu sulphates occur as a dissolution fabric intimately associated to the grain margin. Absence of the pitted fabric, indicated that this bornite grain was at the early stages of replacement by covellite. The high intensity of fractures may postdate the precipitation of bornite or may be a precursor-texture associated to bornite-covellite replacement.

DKMC_DD952	131.80m	3	Description

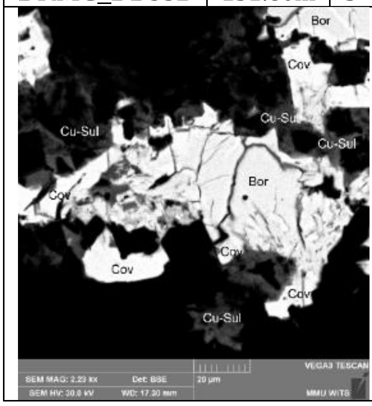

KKW005-3-3 Bornite + covellite + Cu sulphates

Moderately fractured bornite and parts of the grain show it conversion to covellite. This replacement is a supergene enrichment process. Observed is sulphide alteration into Cu-sulphate, this is the medium grey corroded margins to the grains. Fractures occur in the grain but no noticeable alteration or secondary mineralisation appears to be associated to the fractures. It is possible that the fractures are part of the most recent event the grain has undergone and may be coincident or postdate any mineralisation and alteration stages. A quartz-mica-sericite assemblage is likely the matrix, though not confirmed.

<table>
<tr><td>DKMC_DD952</td><td>131.80m</td><td>4</td><td>Description</td></tr>
<tr><td colspan="3" rowspan="2">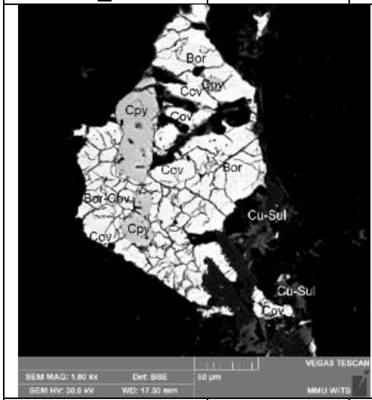
</td><td>KKW005-4 Chalcopyrite + bornite + covellite + Rutile + Cu sulphates</td></tr>
<tr><td>Displayed is a fragmented bornite-covellite assemblage. The left of the grain has chalcopyrite with an elongate geometry, its grain boundary is moderately corroded. Despite fractures, the grain boundary exhibits limited corrosion. Dissolution by Cu sulphates is apparent and has an affinity to the grain boundary. Whilst chalcopyrite occurs earlier in the paragenesis, chalcopyrite appears to exploit the fractures in the grain, it is proposed that is occurrence represents a mineralisation episode postdating the fractures. Dark grey rutile grains may be present in the lower part of the grain but are indistinct.</td></tr>
<tr><td>DKMC_DD952</td><td>131.80m</td><td>5</td><td>Description</td></tr>
<tr><td colspan="3" rowspan="2">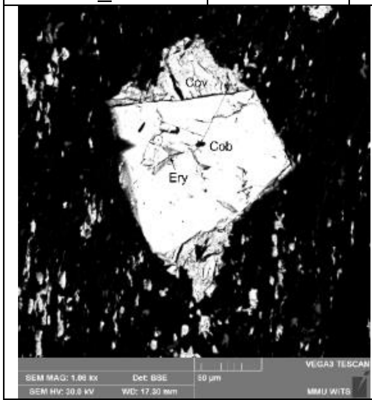
</td><td>KKW005-5 Cobaltite + covellite + erythrite</td></tr>
<tr><td>A central grain of cobaltite that is weakly fractured is observed. A close association to granular covellite with corroded edges occurs along straight elongated edges of the cobaltite grain. Fractures within the cobaltite grain are likely infilled by erythrite. Erythrite suggests alteration of cobaltite due to oxidation and as covellite formation is associated to reduced conditions, it is difficult to explain this simultaneous existence of minerals. Unless covellite and erythrite are potentially linked to two distinct processes.</td></tr>
<tr><td>DKMC_DD952</td><td>131.80m</td><td>6</td><td>Description</td></tr>
<tr><td colspan="3" rowspan="2">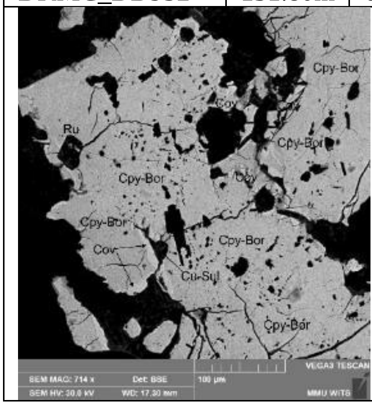
</td><td>KKW005-6 Chalcopyrite + bornite + covellite + rutile + Cu sulphates</td></tr>
<tr><td>A granular chalcopyrite – bornite assemblage is observed in the central parts of the grain. This central part is associated to a pitted, granular texture that appears to be curvilinear towards the top. The grain margins develop weak fracturing, this texture is likely associated to covellite (after chalcopyrite – bornite). This is a result of the supergene enrichment stage. The occurrence of rutile suggest acidic parent rocks, whilst the Cu-sulphates (dull grey dissolution textures) are the possibly products of late-stage oxidation.</td></tr>
</table>

Polished thin sections; Kakula, Kakula west, Kansoko Centrale, Kansoko Sud

APPENDIX D; POLISHED BLOCKS PHOTOMICROGRAPHS

Polished blocks and polished thin sections

Polished block 1: DKMC_DD624 and DKMC_DD956

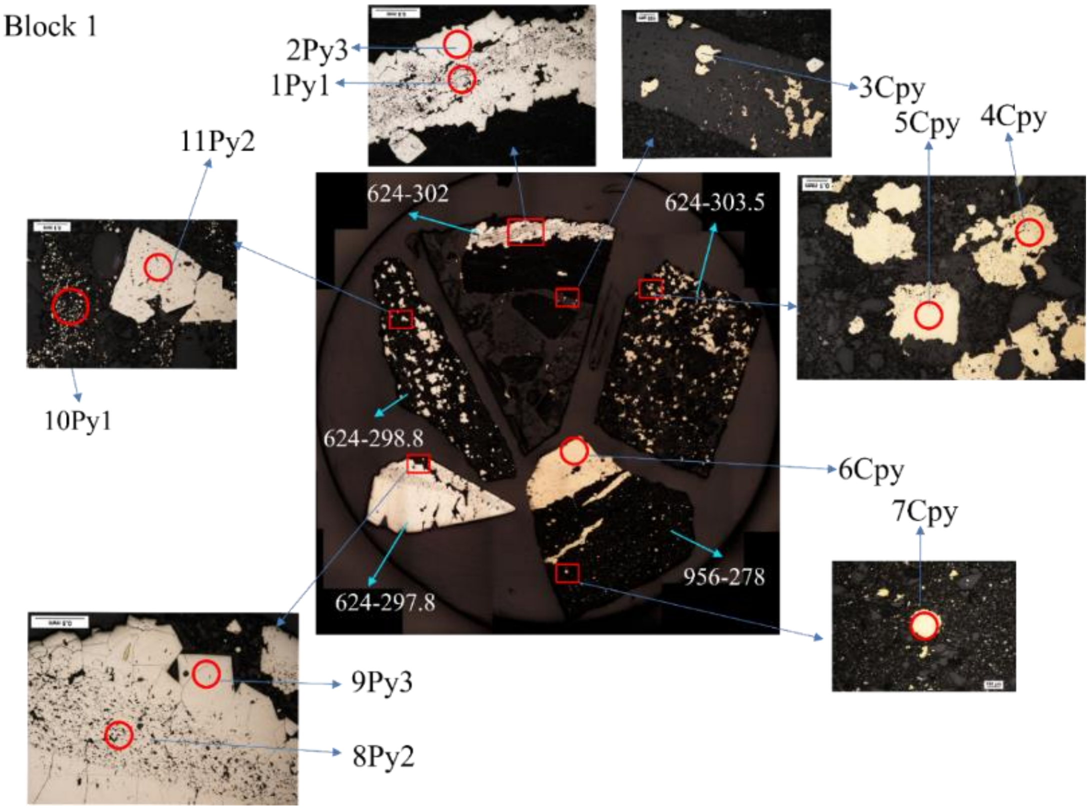

Polished block 2: DKMC_DD624, DKMC_DD956, DKMC_DD1044

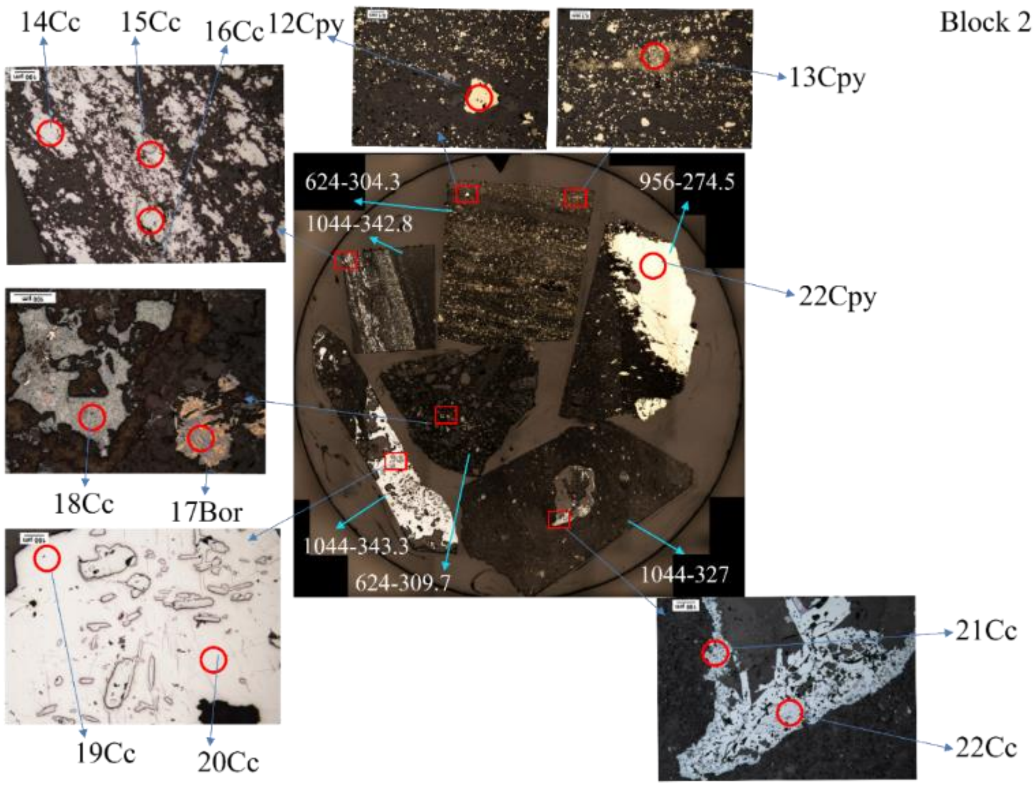

Polished block 3: DKMC_DD1044

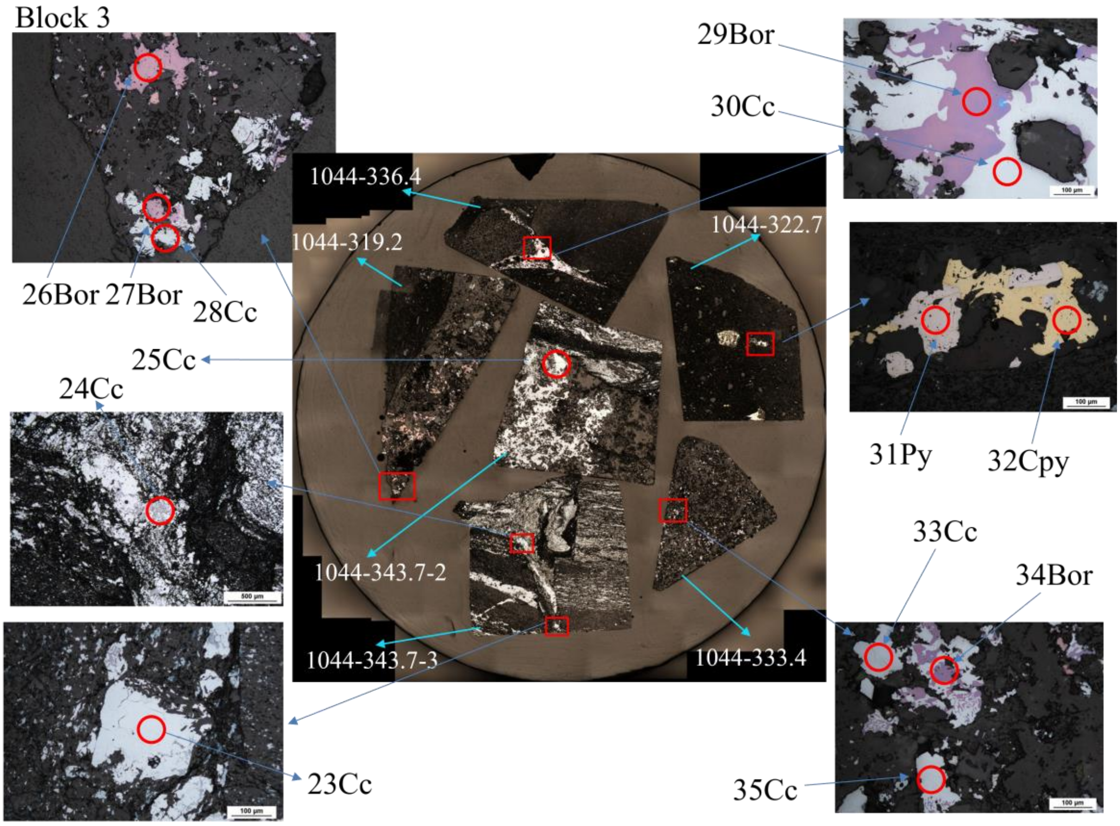

Polished block 4: DKMC_DD624, DKMC_DD627, DKMC_DD956, DKMC_DD1044

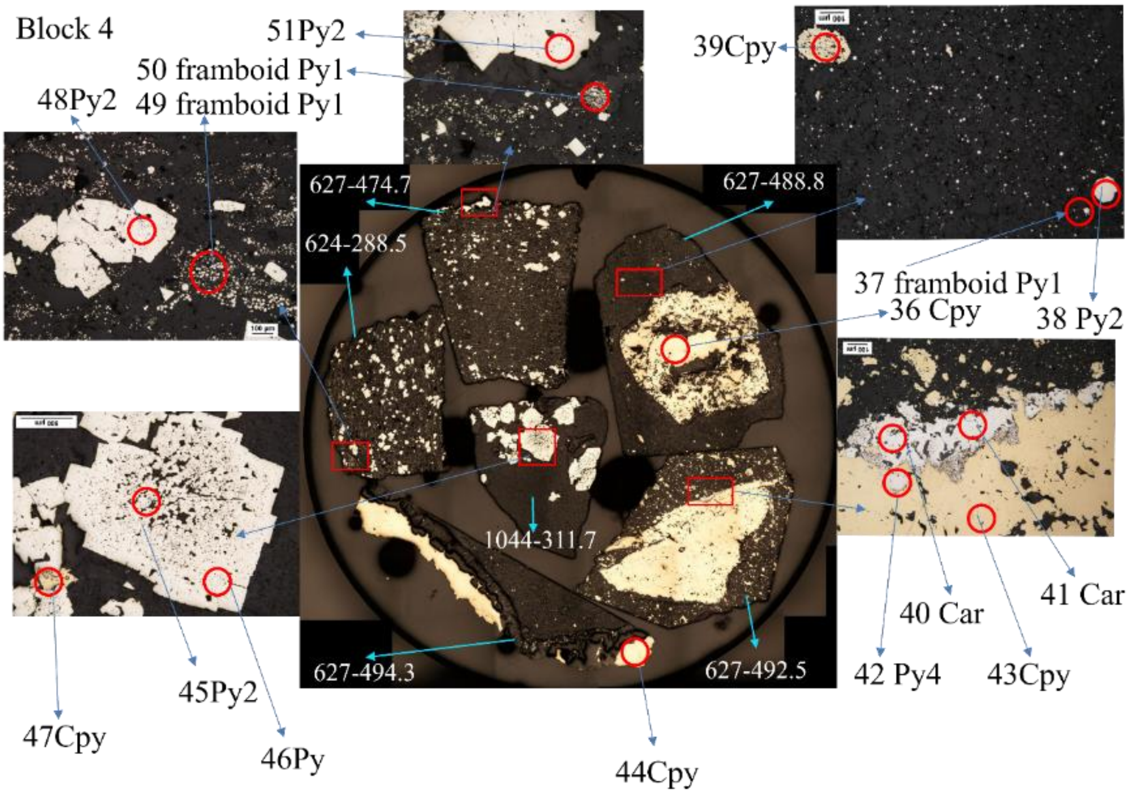

Polished block 5: DKMC_DD571, DKMC_DD624, DKMC_DD627, DKMC_DD956, DKMC_DD1044

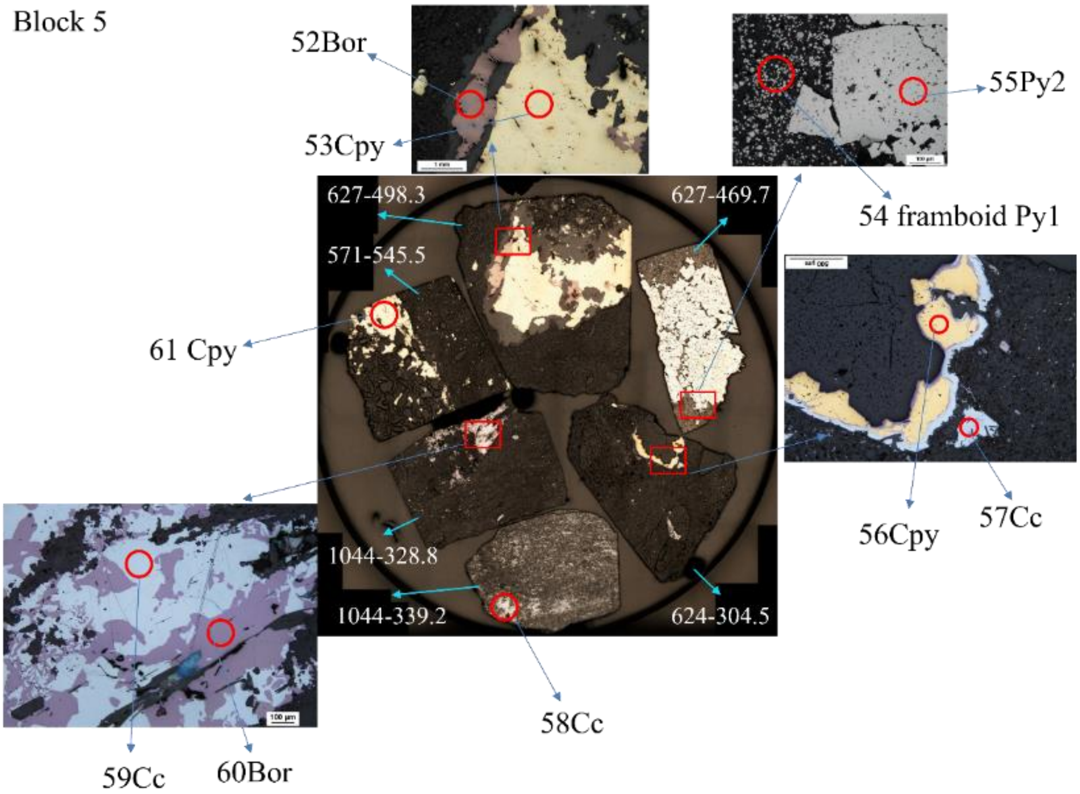

Polished block 6: DKMC_DD571, DKMC_DD627

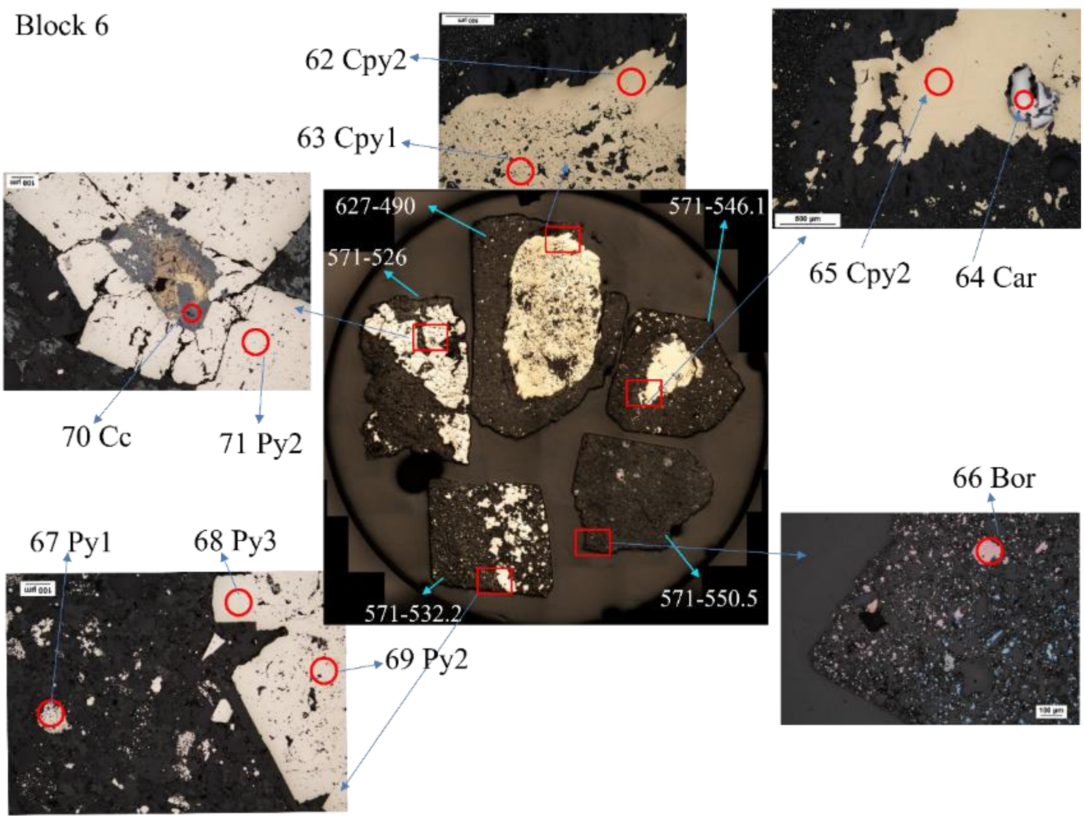

Polished block 7: DKMC_DD956, DKMC_DD1039, DKMC_DD1044

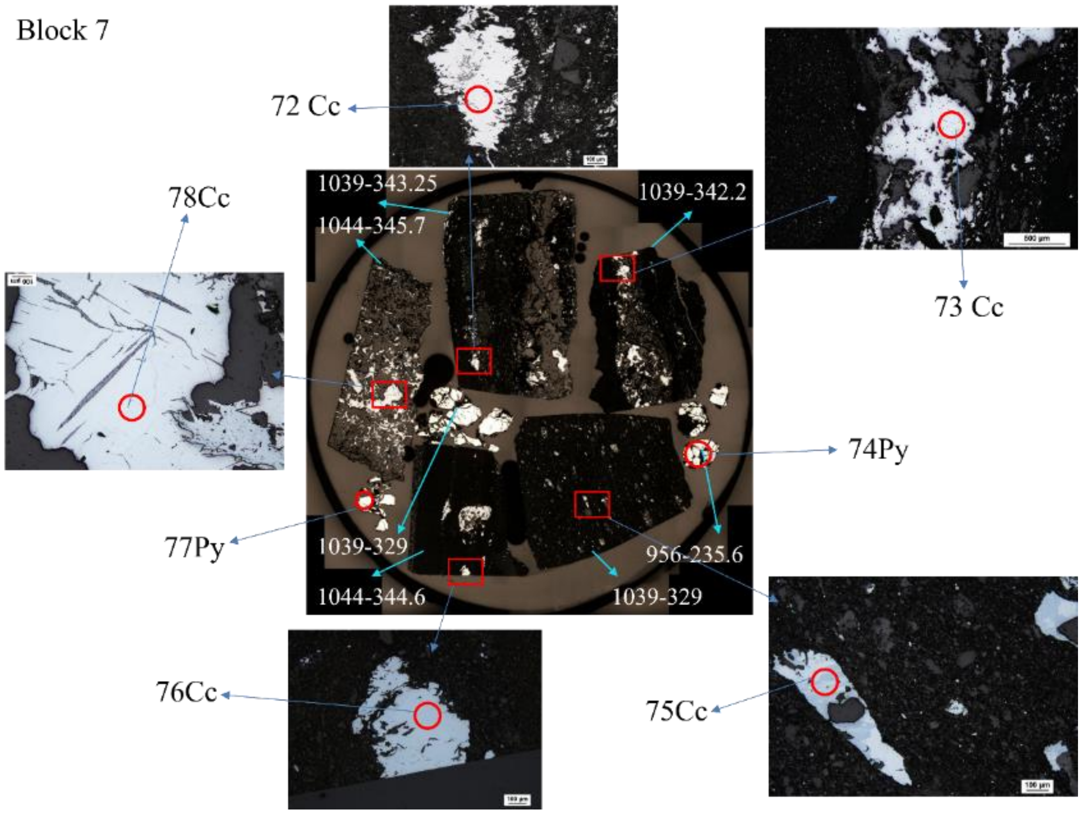

Polished block 8: DKMC_DD571, DKMC_DD627, DKMC_DD956, DKMC_DD1039

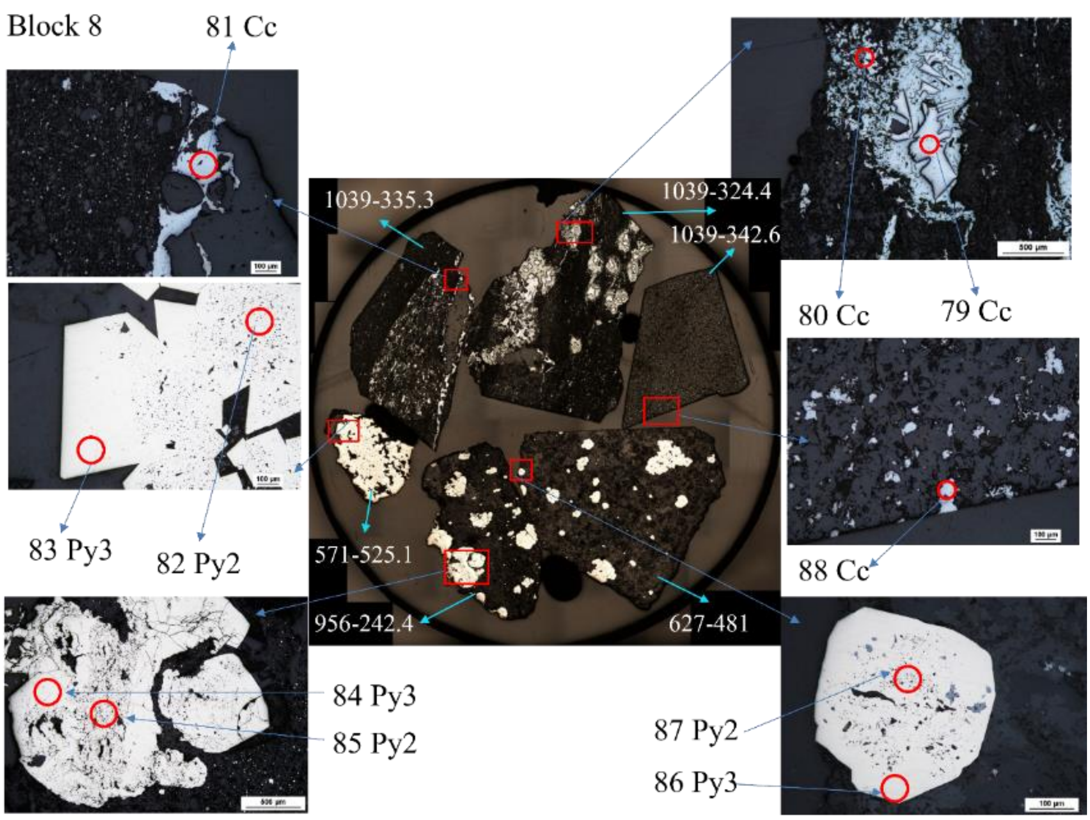

Polished block 9: DKMC_DD571, DKMC_DD627, DKMC_DD956, DKMC_DD1039

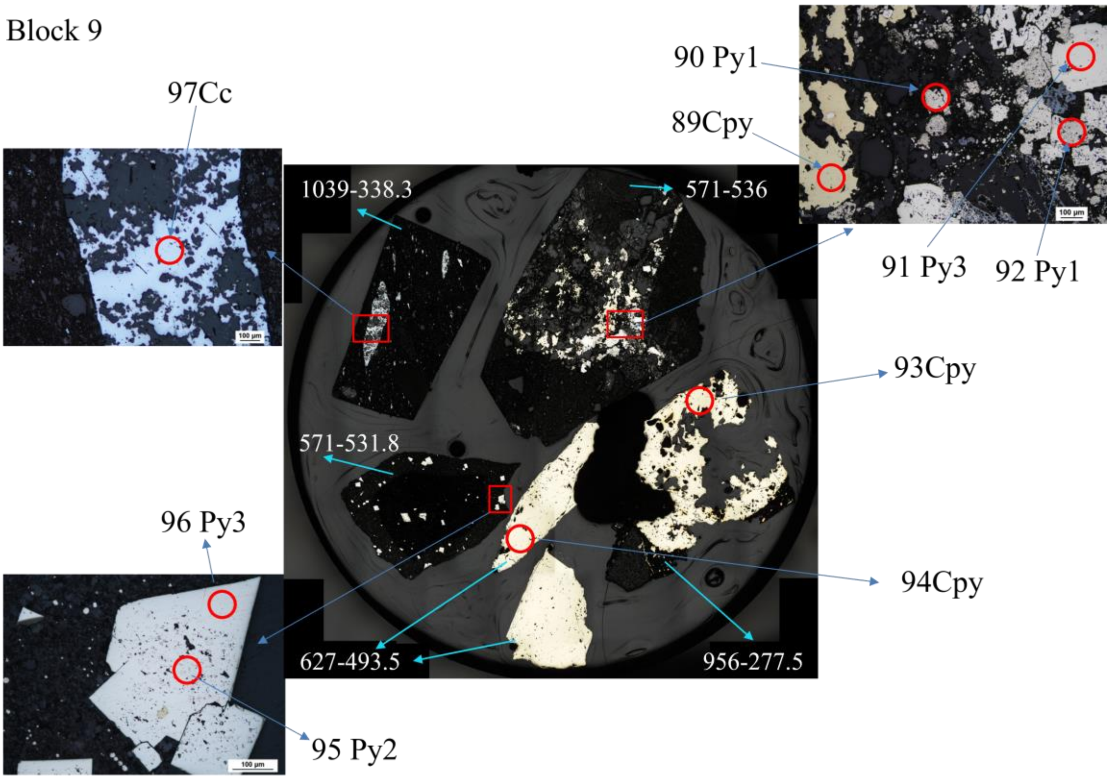

Polished block 10: DKMC_DD571, DKMC_DD624, DKMC_DD1039, DKMC_DD1044

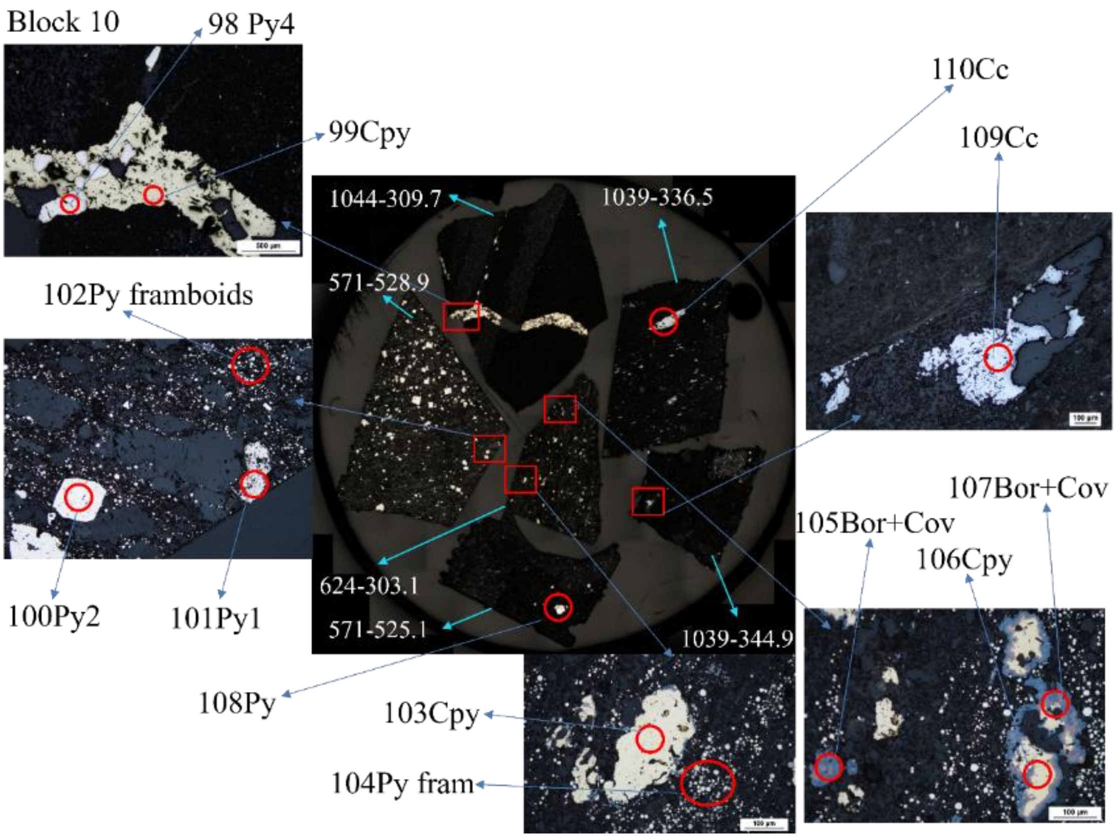

APPENDIX E; SULPHUR ISOTOPE RESULTS

Sample_ID	Mineral	$\delta^{34}S$, ‰	S content in mineral
1	Py2	20	53.2
2	Py3	22.4	53.2
3	Cpy	-13.8	34.95
4	Cpy	-12.3	34.95
5	Cpy	-11.6	34.95
6	Cpy	-11.6	34.95
7	Cpy	-11.9	34.95
8	Py2	-9.2	53.2
9	Py3	-10.0	53.2
10	Py1	-10.0	53.2
11	Py2	-11.7	53.2
12	Cpy	-9.2	34.95
13	Cpy	-11.2	34.95
14	Cc	-34.7	20.1
15	Cc	-35.1	20.1
16	Hem	no signal	20.1
17	Bor	8.1	25.6
18	Cc	9.1	20.1
19	Cc	-33.1	20.1
20	Cc	-33.1	20.1
21	Cc	no signal	20.1
22	Cpy	-12.2	34.95
23	Cc	-32.4	20.1
24	Cc	-32.3	20.1
25	Cc	-32.6	20.1
26	Bor	-6.3	25.6
27	Bor	-6.7	25.6
28	Cc	no signal	20.1
29	Bor	-17.5	25.6
30	Cc	-18.0	20.1
31	Py4	-8.1	53.2
32	Cpy	-2.4	34.95
33	Cc	-12.6	20.1
34	Bor	-13.3	25.6
35	Cc	-14.8	20.1
36	Cpy	-11.8	34.95
37	Py1	no signal	53.2
38	Py2	4.3	53.2
39	Cpy	-13.6	34.95
40	Cob	-12.7	20.6
41	Cob	-12.0	20.6
42	Py4	-14.4	53.2
43	Cpy	-13.2	34.95

Sample_ID	Mineral	$\delta^{34}S$, ‰	S content in mineral
44	Cpy	-12.2	34.95
45	Py2	15.0	53.2
46	Py3	15.4	53.2
47	Cpy	-3.2	34.95
48	Py2	-8.5	53.2
49	Py1	-11.1	53.2
50	Py1	-10.9	53.2
51	Py3	-8.7	53.2
52	Bor	2.0	25.6
53	Cpy	5.4	34.95
54	Py1	-10.9	53.2
55	Py2	-8.8	53.2
56	Cpy	-8.1	34.95
57	Cc	-9.4	20.1
58	Cc	-27.7	20.1
59	Cc	-11.4	20.1
60	Bor	-10.5	25.6
61	Cpy	-9.9	34.95
62	Cpy	-11.1	34.95
63	Cpy	-12.3	34.95
64	Cob	-8.0	20.6
65	Cpy	-10.4	34.95
66	Bor	-10.6	25.6
67	Py1	-19.9	53.2
68	Py3	-10.0	53.2
69	Py2	-9.6	53.2
70	Cc	no signal	20.1
71	Py2	-9.4	53.2
72	Cc	-32.6	20.1
73	Cc	-34.0	20.1
74	Py3	-10.0	53.2
75	Cc	-11.3	20.1
76	Cc	-32.4	20.1
77	Py3	-9.4	53.2
78	Cc	-30.4	20.1
79	Cc	-5.0	20.1
80	Cc	-5.3	20.1
81	Cc	-21.7	20.1
82	Py2	-10.0	53.2
83	Py3	-9.4	53.2
84	Py3	-8.5	53.2
85	Py2	-9.6	53.2
86	Py3	-9.9	53.2
87	Py2	-13.0	53.2

Sample_ID	Mineral	$\delta^{34}S$, ‰	S content in mineral
88	Cc	-33.2	20.1
89	Cpy	-12.3	34.95
90	Py1	-11.3	53.2
91	Py3	-7.8	53.2
92	Py1	-10.9	53.2
93	Cpy	-11.4	34.95
94	Cpy	-12.9	34.95
95	Py2	-9.2	53.2
96	Py3	-9.9	53.2
97	Cc	-28.0	20.1
98	Py4	8.5	53.2
99	Cpy	4.5	34.95
100	Py2	-10.4	53.2
101	Py2	-0.4	53.2
102	Py1	-11.1	53.2
103	Cpy	-12.2	34.95
104	Py1	-13.4	53.2
105	Bor+Cov	no signal	30
106	Cpy	-12.9	34.95
107	Bor+Cov	-13.2	30
108	Py2	-9.3	53.2
109	Cc	-29.6	20.1
110	Cc	-24.2	20.1

APPENDIX F; SULPHUR ISOTOPE HISTOGRAMS

Frequency plot of sulphide mineral sulphur isotopic data (bin size = 2); DKMC_DD571

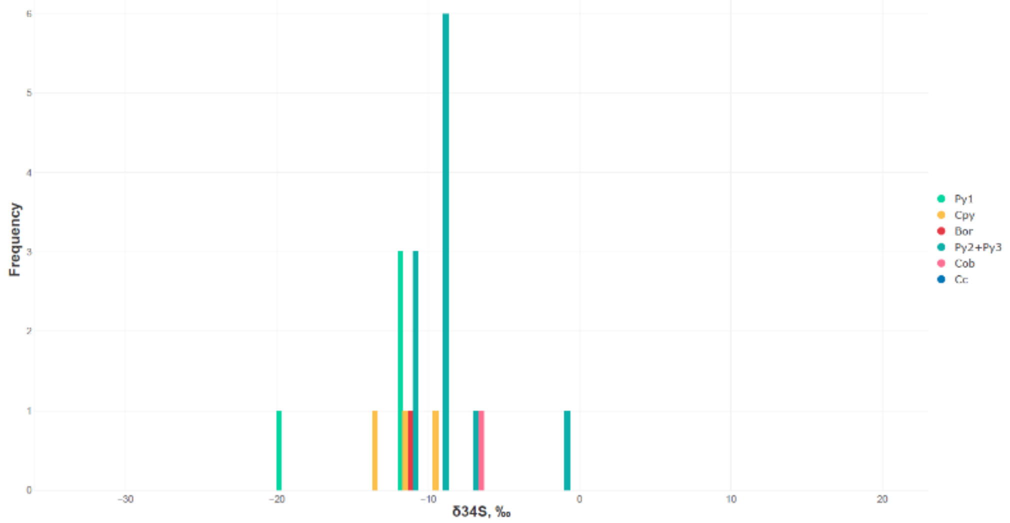

Frequency plot of sulphide mineral sulphur isotopic data (bin size = 2); DKMC_DD624

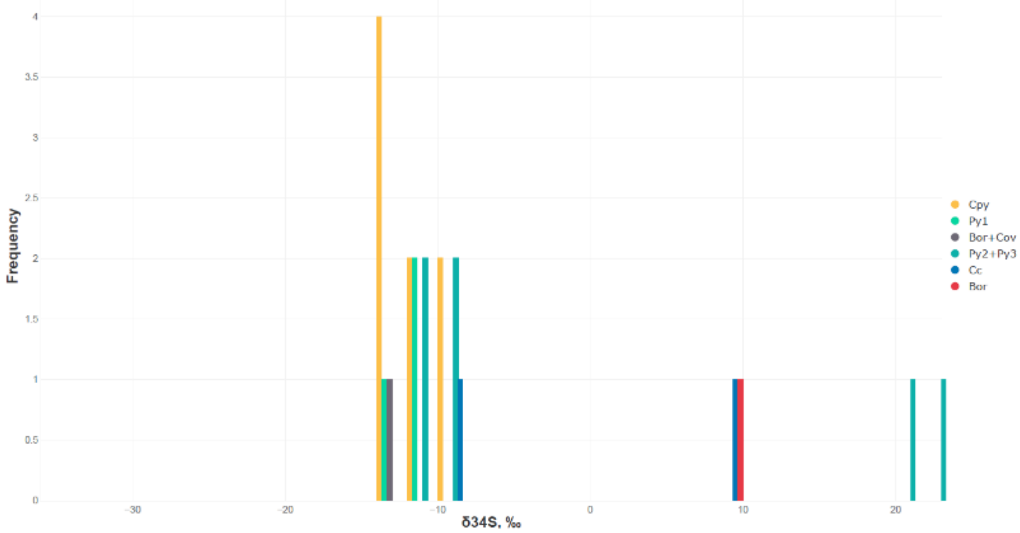

Frequency plot of sulphide mineral sulphur isotopic data (bin size = 2); DKMC_DD627

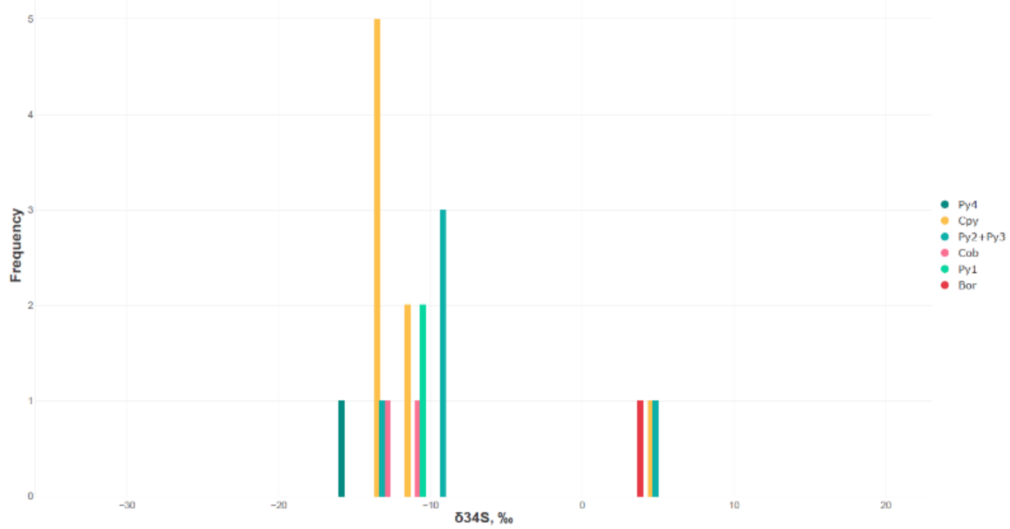

Frequency plot of sulphide mineral sulphur isotopic data (bin size = 2); DKMC_DD956

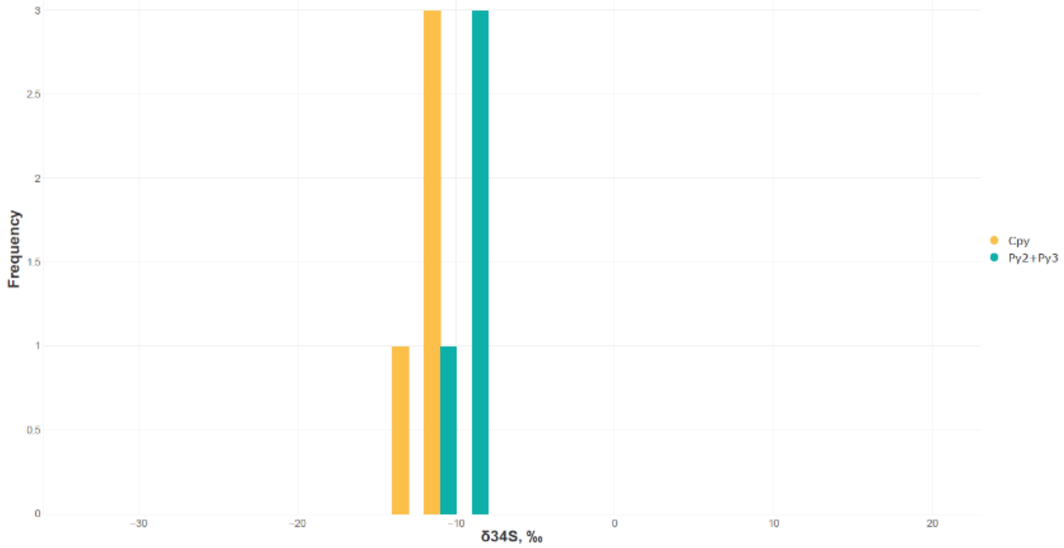

Frequency plot of sulphide mineral sulphur isotopic data (bin size = 2); DKMC_DD1039

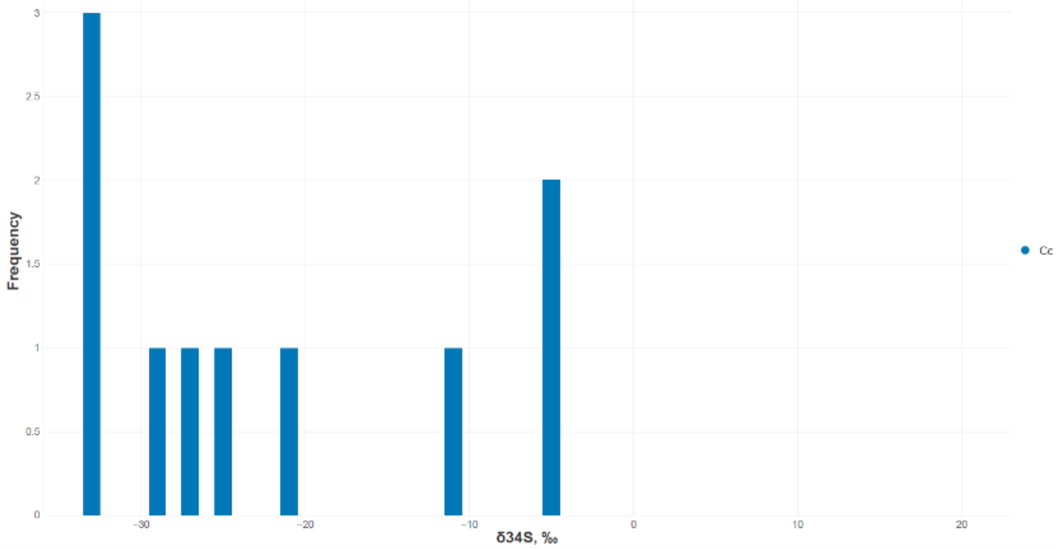

Frequency plot of sulphide mineral sulphur isotopic data (bin size = 2); DKMC_DD1044